UNDERSTANDING THE NANOTUBE GROWTH MECHANISM: A STRATEGY TO CONTROL NANOTUBE CHIRALITY DURING CHEMICAL VAPOR DEPOSITION SYNTHESIS

A Dissertation

by

DIEGO ARMANDO GOMEZ GUALDRON

Submitted to the Office of Graduate Studies of
Texas A&M University
in partial fulfillment of the requirement for the degree of

DOCTOR OF PHILOSOPHY

Approved by:

Chair of Committee,	Perla B. Balbuena
Committee Members,	Yue Kuo
	Hae-Kwon Jeong
	Choongho Yu
	Daniel Resasco
Intercollegiate Faculty Chair,	Ibrahim Karaman

December 2012

Major Subject: Materials Science and Engineering

ABSTRACT

For two decades, single-wall carbon nanotubes (SWCNTs) have captured the attention of the research community, and become one of the flagships of nanotechnology. Due to their remarkable electronic and optical properties, SWCNTs are prime candidates for the creation of novel and revolutionary electronic, medical, and energy technologies. However, a major stumbling block in the exploitation of nanotube-based technologies is the lack of control of nanotube structure (chirality) during synthesis, which is intimately related to the metallic or semiconductor character of the nanotube.

Incomplete understanding of the nanotube growth mechanism hinders a rationale and cost-efficient search of experimental conditions that give way to structural (chiral) control. Thus, computational techniques such as density functional theory (DFT), and reactive molecular dynamics (RMD) are valuable tools that provide the necessary theoretical framework to guide the design of experiments. The nanotube chirality is determined by the helicity of the nanotube and its diameter. DFT calculations show that once a small nanotube 'seed' is nucleated, growth proceeds faster if the seed corresponds to a high chiral angle nanotube. Thus, a strategy to gain control of the nanotube structure during chemical vapor deposition synthesis must focus on controlling the structure of the nucleated nanotube seeds.

DFT and RMD simulations demonstrate the viability of using the structures of catalyst particles over which nanotube growth proceeds as templates guiding nanotube growth toward desired chiralities. This effect occurs through epitaxial effects between the nanocatalyst and the nanotube growing on it. The effectiveness of such effects has a non-monotonic relationship with the size of the nanocatalyst, and its interaction with the support, and requires fine-tuning reaction conditions for its exploitation.

RMD simulations also demonstrate that carbon bulk-diffusion and nanoparticle supersaturation are not needed to promote nanotube growth, hence reaction conditions that increase nanoparticle stability, but reduce carbon solubility, may be explored to achieve nanotube templated growth of desired chiralities. The effect of carbon

dissolution was further demonstrated through analyses of calculated diffusion coefficients. The metallic nanocatalyst was determined to be in viscous solid state throughout growth, but with a less solid character during the induction/nucleation stage.

DEDICATION

To Elsa Gualdrón and Paola León

ACKNOWLEDGEMENTS

I would like to thank my advisor Dr. Perla Balbuena for their support and guidance throughout the course of my doctoral studies; and my committee members Dr. Daniel Resasco, Dr. Choongho Yu, Dr. Hae-kwon Jeong, and Dr. Yue Kuo for being part of this endeavor.

I also would like to thank coworkers and friends for their support and friendship, which made my time at Texas A&M University a wonderful experience. I also would like to extend my gratitude to the DEPARTMENT OF ENERGY, grant DE-FG02-06ER15836, which provided financial support for my research and studies; and to TEXAS A&M UNIVERSITY SUPERCOMPUTER CENTER, NATIONAL ENERGY RESEARCH SCIENTIFIC COMPUTING CENTER, and University of Texas at Austin TACC system, which provided computational resources for my research.

NOMENCLATURE

CC	Carbon-carbon
CVD	Chemical vapor deposition
CS	Carbon-support
DFT	Density functional theory
HOMO	Highest occupied molecular orbital
HRTEM	High resolution electron microscopy
LUMO	Lowest unoccupied molecular orbital
MC	Metal-carbon
MM	Metal-metal
MS	Metal-support
RDF	Radial distribution function
RMD	Reactive classical molecular dynamics
SWCNT	Single-walled carbon nanotube
TEM	Transmission electron microscopy

TABLE OF CONTENTS

Page

Page

LIST OF FIGURES

FIGURE Page

FIGURE Page

FIGURE Page

FIGURE Page

FIGURE Page

LIST OF TABLES

1. INTRODUCTION AND LITERATURE REVIEW

Carbon nanotubes (CNTs) are allotropic forms of carbon that have captured the imagination of the scientific community since their official discovery in 1991 [1]. Such excitement about this material, especially about the single-walled nanotube form (SWCNT), mainly arises from the outstanding electronic and optical properties that make them promising candidates for revolutionary applications in a number of fields [2-5]. Nevertheless, the specific properties of a SWCNT such as its metallic, or semiconductor character and (relevant band gap) are tightly related to its structure [6], which is uniquely defined by its chirality, with the latter defining the nanotube diameter, and the degree of helicity of the nanotube wall hexagonal pattern.

From a geometric point of view, a SWCNT is formed by rolling a graphene sheet into a seamless cylindrical structure, with different ways of performing said rolling resulting in different nanotube chiralities, and thus nanotube properties. Chiral indexes *(n,m)* are used to identify a SWCNT according to its chirality, and are uniquely related to the tube diameter *d* and the helicity of the wall as numerically given by the so-called 'nanotube chiral angle θ_c' (Equation 1-1 and 1-2), where the latter is related to the helicity of the hexagonal pattern of the nanotube wall. Solution of the nanotube electronic structure shows that for cases where *n-m* is a multiple of three (3) the nanotube has metallic character, and semiconductor one otherwise [6].

$$d = \left(\frac{a}{\pi}\right)(n^2 + nm + m^2)^{1/2} \qquad (1 - 1)$$

$$\theta_c = tan^{-1}(\sqrt{3}m/(m + 2n) \qquad (1 - 2)$$

Full exploitation of nanotube-based technologies requires the production of high SWCNT quantities of desired properties (i.e. selected chirality). While synthesizing SWCNTs by chemical vapor deposition (CVD) methods seems a viable option for scale-up production, controlling the nanotube chirality during their synthesis has posed one of the most challenging research problems in nanotechnology. It has become evident that

tuning synthesis conditions in search of chiral selectivity is a formidable task due to the notoriously wide parameter-space characteristic of nanotube growth, and the controversial nature of the nanotube growth mechanism [7, 8].

In this dissertation, computational efforts addressed to elucidate the nanotube growth mechanism, and develop a strategy to control nanotube chirality are presented. (An introductory review of literature relevant to these two research problems is presented is presented in subsection 1.1, whereas more specific literature reviews are presented in each corresponding Section throughout this dissertation). Computational studies allow uncoupling the effect of different parameters impacting nanotube growth, isolating their individual effects in a manner that is not possible through experimental means, while also permitting to analyze the dynamics of nanotube growth with a resolution that, given the (short) time and (small) size scales characteristic of nanotube growth, is not possible to achieve through direct observation via transmission electron microscopy (TEM).

Nonetheless, the implementation of a computational methodology to study nanotube growth cannot be done carelessly since the significance of results obtained through these methods depends on the accuracy with which the interactions involving atoms (nuclei) and electrons is calculated, and the connection of the constructed simulation models to the actual system. Quantum mechanics can be used to describe the electronic interactions that play a fundamental role in nanotube growth via *ab-initio* calculations that look for approximate solutions to the Schrödinger equation [9]. However the current computational power typically limits these methods to nearly one hundred atoms. On the other hand, classical mechanics can be used to describe the dynamics of nuclei, provided that appropriate *force fields* can be developed to implicitly account for electronic interactions, although current computational power limits the dynamics of up to millions of atoms to several nanoseconds.

1.1. Literature review

Iijima officially discovered carbon nanotubes in 1991 [1]. Since then, they rapidly gained the attention of the scientific community due to their outstanding properties, and become one of the main exponents of the nanotechnology era. Accordingly, there is a tremendous amount of nanotube-related literature. Nonetheless, the literature presented here mainly focuses on efforts to understand the nanotube growth mechanism and control nanotube chirality.

1.1.1. Nanotube growth mechanism

The nanotubes discovered by Iijima were obtained by an arc-discharge (AC) method, where an electric current is passed through two graphite electrodes separated about one millimeter. In this high-temperature process, carbon atoms are vaporized on one electrode, and then self-assemble into multi-walled carbon nanotubes (and other carbon forms) on the other electrode. Notably, doping the electrodes with traces of metal permits the formation of single-wall carbon nanotubes (SWCNTs) as well [10]. The next successful method to synthesize SWCNT was laser ablation (LA), where a laser beam hits a graphite target doped with metal [11]. Carbon and metal atoms vaporize, with the metal atoms assembling into nanoparticles, and carbon atoms self-assembling into SWCNTs on the nanoparticles. AC and LA synthesis are very energetically demanding, thus chemical vapor deposition (CVD) synthesis, which can be done at comparatively low temperatures (~1000 K), appears as a suitable alternative for scaled-up production of SWCNTs.

Traditionally, CVD nanotube synthesis has used transition metals iron [12-14], nickel [15-18], and cobalt [19-21] as nanocatalysts, which have been shown to achieve higher yields in comparison to other catalytic materials. The catalyst nanoparticle may be unsupported (floating catalyst) [13], or may be supported on a suitable substrate such as silica, alumina, or magnesia [17, 20]. Floating nanocatalysts are usually obtained by introducing a metal-organic gas into the reactor at a suitable temperature (~1000 K), whereas supported nanocatalyst are usually obtained by the annealing of a metal film deposited on the support, or treatment (calcination, reduction) of a support impregnated

with a precursor catalyst solution. Once the nanocatalyst has formed, the system is taken to a target temperature, and a gas mixture containing a carbon-containing gas (and inert gases) is introduced to the reactor. After several minutes, SWCNTs are produced if the synthesis conditions were suitable for nanotube growth.

In light of the typical synthesis conditions (i.e. catalyst composition, temperature, gas partial pressures, pre-growth treatments) for successful nanotube growth, and observed similarities between the latter and nanofibers growth, the vapor-liquid-solid (VLS) mechanism was originally proposed by Gavillet *et al* in 2001 [22]. In the growth scenario proposed by the VLS model, the nanoparticle is in *liquid* state, the precursor *gas* molecules decompose on the nanoparticle surface with the liberated carbon atoms dissolving into the nanoparticle until the supersaturation is achieved, and carbon precipitates onto the nanoparticle surface to self-assemble into a *solid* nanotube.

Nonetheless, since the VLS model was proposed, experimental and theoretical results have seemingly both supported [13, 16, 23-25] and contradicted [17, 26-30] the VLS model. An implication of the VLS model is that bulk-diffusion processes control the nanotube growth rate. Accordingly, agreement between calculated activation energies of nanotube growth in some experiments (~1.0 – 2.0 eV) [15], and calculated activation energies for diffusion of carbon through bulk metals [31] seem to support the VLS model. However, it has been argued that the experimental activation energies also agree with the activation energies of precursor decomposition [28], or the activation energy for the addition of carbon to the nanotube rim [32]. On the other hand, diffusion activation energies, although calculated for solid models, show a much lower activation for surface diffusion than bulk diffusion. Nevertheless, in a number of experiments, carbon is detected within the nanoparticle [7, 14, 24].

On the other hand, the hypothesis of a liquid nanoparticle seems to originate in the observed deformation of the nanoparticle during nanotube growth [16, 33], related to the established fact that nanoparticles undergo a reduction in melting points due to size effects in comparison to their bulk counterparts [34, 35]. Moreover, it has been argued that a typical phase diagram for a metal carbon system suggests a further reduction in the

melting point due to the presence of an eutectic point [36]. However, whether such melting point reduction is large enough to maintain the nanoparticle in the liquid state at the typical synthesis conditions is uncertain since the study of nanoparticle phase-diagrams is still in its early stages. Moreover, supporting the nanoparticle has been shown to counteract in some extent the melting point reduction effect [36, 37].

It has also been noted that transmission electron microscopy (TEM) images of experimental growth show the nanoparticle to maintain crystallinity, and long-range order despite the observed deformation during nanotube growth [17, 19, 24, 38]. Accordingly, it has been proposed that the nanoparticle is either in a solid or viscous state, with the observed deformation occurring through a creep mechanism [17]. This crystallinity has, however, a periodic character as revealed by frame-by-frame analysis of nanotube growth via in-situ TEM, where frames where the nanoparticle lattice is clearly defined are alternated with frames where the nanoparticle structure appears blurry.

It has also been argued that the dissolution of carbon inside the nanoparticle results in formation of a carbide, whose decomposition yields precipitation of carbon to the nanoparticle surface, and self-assembly into a carbon nanotube. Under this premise, materials forming metastable carbides (e.g. nickel, cobalt, and iron) are good candidates as nanotube growth catalyst, whereas materials not forming carbide (e.g. gold, copper) or forming stable carbides (e.g. molybdenum) are not. However, while (pure) molybdenum is known to be inactive [7, 20], coinage metals such as gold and copper have been shown to be active for nanotube growth by Homma *et al* [26]. Bulk gold and copper do not form carbides since they negligibly dissolve carbon. Thus, not only does the successful growth on nanoparticles of these materials challenge the notion of carbide formation as requirement for nanotube growth, but also the notion of a bulk diffusion-controlled nanotube growth. Nonetheless, based on experimental data, Homma *et al* [23] have proposed that gold, and copper do dissolve carbon when in nanoparticle form.

The most common method to evaluate the formation of particle carbide or not during growth is through X-ray diffraction (XRD), although results have varied through

different reported experiments. XRD analyses of successful growth experiments have supported both the presence [14, 24], and the absence of the carbide particle [14]. Whereas other experiments have suggested that particles that were inactive for growth corresponded to carbides, whereas those that were active corresponded to metallic ones [39].

In summary, three outstanding questions in regard to the nanotube growth mechanism are: 1) what is the state of the nanoparticle? 2) what is the carbon transport mechanism? and 3) does a carbide particle forms during nanotube growth?

1.1.2. Strategies for chirality control

Since the realization that the properties of SWCNTs depend on structural features such as their chirality, there has been a tremendous interest in devising a strategy to obtain commercial quantities of nanotubes of a specific chirality, or alternatively pure samples of either metallic or semiconducting nanotubes. CVD synthesis typically produces a heterogeneous mixture of nanotubes of various chiralities, thus an additional separation process is needed to purify a targeted chirality. While these post-synthesis techniques have become useful and efficient [40], there are still concerns about their cost in a commercial setting, as well as considerable damage suffered by the nanotubes during these typically complex treatments.

Alternatively, nanotube 'cloning' (where growth proceeds from a 'carbon seed' of the desired chirality) has been proposed to produce nanotubes of selected chirality [41]. However, the production rate characteristic of this method is far below that characteristic of CVD synthesis. Accordingly, achieving chirality control during nanotube synthesis has been established as one the most coveted goals in the field of nanotube synthesis. As Equation 1-1 shows, a particular nanotube diameter d corresponds to a finite combination of the chiral indexes n and m. Thus, controlling the nanotube diameter during synthesis has been considered a stepping-stone toward chirality control [20, 42]. Diameter control strategies are based upon the observed correlation between nanoparticle size and nanotube diameter.

Among CVD processes, CoMoCAT synthesis as developed by Resasco *et al* [20] stands out as one the processes with better chirality control, with a predominant synthesis of (6,5) (and (7,5)) nanotubes. CoMoCAT uses a cobalt-molybdenum mixture on silica or magnesia supports. Pre-growth treatment has been determined to produce reduced metallic cobalt nanoparticles, on which precursor decomposition and nanotube growth occur. Using a cobalt catalyst as well, but dispersed on zeolite, Yuan *et al* [21] were able to synthesize predominantly (9,8) nanotubes. On the other hand, using iron-copper catalysts on magnesia, Kraus *et al* [43] synthesized predominantly (6,5) nanotubes. Nevertheless, the origin of the observed selectivity in these processes is not completely understood, although a control in the dispersion of the nanoparticles seems to play a significant role.

Notably, the chiral angles of the nanotubes predominantly produced in the previously discussed processes correspond to near-armchair nanotubes. Moreover, near-armchair nanotubes seems to be recurrently synthesized in a number of nanotube growth experiments [20, 21, 44, 45]. However, a reduction of the average chiral angle of produced nanotubes (i.e. increasing production of near-zigzag nanotubes) has been shown to occur with changes in type of precursor gas used [20]. Similarly, multi-walled carbon nanotubes (MWCNTs) synthesized on nitrogen-containing atmospheres feature walls that have been identified as either armchair or zigzag, although it has been pointed out that such effect may arise from a carbide stabilization assisted by nitrogen, and a subsequent epitaxial effect between the carbide particle and the nanotube [46].

An epitaxial effect between the nanoparticle and the nanotube, where the nanoparticle structures templates the nanotube growth has been proposed as a means to control nanotube chirality, and it is the overarching theme throughout this dissertation. Reich *et al* [47] has calculated the interactions between nanotube caps of selected chiralities, and a flat (111) fcc-nickel surface, where the lattice matching between the cap rim and the surface sites seemed to correlate to the cap/surface binding energy.

Zhu *et al* [38] observed through high-resolution TEM techniques a correlation between the orientation of the hexagonal pattern of the nanotube wall and that of the

nanoparticle lattice as indicated by the orientation of the particle (100) planes, and pointed the matching between CC bond distances in nanotubes, and the distance between adjacent hollow sites on a fcc-cobalt (111). They proposed that a step in the nanoparticle surface would form aligned with the crystallographic orientation of the nanoparticle, and that the relative orientation of the nanotube growth axis to the step would determine the chirality of the resulting nanotube. A major concern, however, is whether this strategy is compatible with the nanoparticle state (liquid or solid) that is best suited for nanotube growth.

A structural connection between the nanoparticle and the nanotube has also been explored experimentally. Chiang and Sankaran [48] demonstrated changes in the chiral distribution of nanotubes synthesized on floating nickel-iron bimetallic nanoparticles as a result of changes in catalyst composition, which affected the lattice spacing in the nanoparticle. Moreover, in a related computational work, it was shown that the relative binding energy of relevant chiral caps on bimetallic nickel-iron surfaces was correlated to the relative abundances between chiralities in the original experiments.

Harutyunyan *et al* [45] demonstrated a correlation between the nanoparticle faceting of iron catalysts and the relative abundance of nanotubes chiralities of metallic character. The faceting, or lack thereof, observed via TEM, was linked to the type of inert gas present during the pre-growth catalyst treatment stage. Although it must be noted that the analysis presented centered on the structure of the nanoparticle before growth was initiated and that the evolution of the nanoparticle during growth was not followed.

The quest for chiral selectivity has not focused only on the obtaining nanotubes of a single chirality, but also on obtaining several chiralities as long as all them have the same electronic character (i.e. metallic or semiconducting). While Harutyunyan *et al* [45] obtained majority of metallic nanotubes, Liu *et al* [49] has demonstrated the growth of majority semiconducting nanotubes using a mixture of alcohols (and water) as a precursor gas. Notably, the presence of methanol seems to play a role in the growth mechanism of these *horizontally* grown nanotubes. Synthesis strategies that result on the

aligned growth on electronically relevant support can be useful for their direct application on electronic devices. Most recently, Zhou *et al* [50] have synthesized *horizontally-grown* nanotubes with higher than 90% abundances of semiconductor nanotubes using a mixture of isopropyl alcohol and water. It has been suggested that selective etching of metallic nanotubes by the reactive species may play a significant role in the abundance of semiconducting nanotubes.

In summary, despite significant advances in the field of nanotube synthesis, achieving chirality control has proven to be a challenging and elusive goal. One potential strategy to achieve this goal is the use of the nanoparticle structure as a template to control chirality, and is this strategy that is explored throughout this dissertation using molecular simulations.

1.2. Dissertation overview

This dissertation uses a multiscale approach to the study of nanotube growth, with Sections 3 through 6 centering on the use of density functional theory (DFT) toward the calculation of energetics, charge transfer phenomena, and structural optimizations of simulation models relevant to nanotube growth; and Sections 7 through 9 centering on the use of reactive classical molecular dynamics (RMD) toward the determination of a continuous picture of the nanotube growth mechanism, and the effect of parameters of interest on the latter, in particular those that could potentially facilitate chirality control.

Section 3 focuses on the thermodynamic and kinetic aspects intrinsic to the chiral structure of the carbon 'seeds' from which nanotube growth proceeds. These seeds correspond to the nanotube capped-end, and its formation outlines the earliest moments in which chirality may be determined. Section 3 shows evidence based in DFT calculations that without controlling the nucleation and formation of the nanotube cap, nanotubes with high chiral angles (near-armchair nanotubes) are kinetically favored over nanotubes with low chiral angles (near-zigzag nanotubes).

On the grounds of the evidence obtained in Section 3, the overarching theme to this dissertation is established, which is the utilization of the catalyst particle on which the nanotube grows on a CVD process as a means to creating a template effect that

guides the nucleation of the cap toward a desired chirality. Section 4 focuses on the interactions of selected nanotube caps with small metallic clusters to inquire about the nature and energetics of the cap/catalyst interactions, and its dependence on the chirality of the nanotube cap as calculated by DFT methods. An electronic charge analysis demonstrates that the interaction between the cap and the catalyst is dominated by the charge transfer between the catalyst and the nanotube (cap) rim, while determination of the electronic density of states reveals that the latter constitute the most reactive part of the nanotube (cap). On the other hand, structural optimizations show that the small cluster reshapes into different structures to maximize its interaction with the selected caps.

With the importance of the nanotube rim/catalyst interface having been established in Section 4, Section 5 focuses on the mechanism of addition of carbon atoms to the rim/catalyst interface for the formation of new hexagonal rings in selected chiral caps via DFT optimizations. The determination of energetic driving forces for two competing events (namely, dissolution of carbon into the nanoparticle, and addition of carbon to the cap rim) is performed demonstrating that while dissolution is an energetically favorable process, addition of carbon to the rim leads to an even more favorable energetic state. This finding motivates the work presented in Section 8, in which RMD simulations are used to directly study the competition between bulk diffusion (which is driven by the energetic of dissolution), and surface diffusion (which is driven by the energetics of carbon addition to the rim).

Section 6 builds on the observed reshaping of the catalyst structure in Section 3, and introduces the interaction of comparatively larger clusters with selected chiral caps. Upon DFT structural optimization, the larger cluster size allows to observe a correlation between the cap chirality and the orientation of the (100) crystallographic direction of the cluster. Although the effect is induced *by* the cap *on* the cluster (i.e. *inverse* template effect), it establishes a correlation between the cap/nanotube structure and the catalyst. The inverse template effect is explained on the basis of the calculated carbon-carbon (CC), metal-carbon (MC), and metal-metal (MM) bond energies, which are shown to

have a relative strength CC > MC > MM. On these grounds, the experimentally observed step formation on the nanoparticle surface is utilized to model different orientations of the nanoparticle surface on the premise that the orientation of the nanoparticle causes a variation of the step structure. Thus, nucleation of carbon structures on (211) and (321) surfaces is studied via DFT to demonstrate that the favored 'chirality' of early structures depends on the surface structure.

Section 6 proposes a method to control the nanoparticle structure (and promote a potential *direct* template effect) based on an adequate selection of the support so an appropriate interaction between the support and the catalyst is established. A change in the nanoparticle dynamics and preferred crystallographic orientation is demonstrated though RMD simulations. Section 7 explores in deeper fashion the effects of the catalyst/support interactions and particle size on the metal/carbon dynamics during nucleation and growth, and their repercussions on chirality control. It is shown via RMD simulations that in agreement with DFT calculations (where hollow sites in a (111) surface are shown to be the most stable sites for carbon ad-atoms) the nascent cap/nanotube structure tends to follow the underlying particle surface pattern via hollow-site occupation. Two necessary trade-offs emerge in the light of these simulations: i) A weak catalyst/support interaction that promotes atom mobility may improve defect healing, and better catalyst/nanotube contact, ii) A strong catalyst/support interaction that reduces atom mobility may help the nanoparticle to retain its surface structure for longer times. At the end of this Section, it becomes evident that a better understanding of the reaction mechanism is needed to find the region in the parameter-space that promotes growth of high-quality nanotubes, while maintaining a stable particle structure.

Aligned with the goal of gaining a better understanding of the nanotube growth mechanism, Section 8 shows RMD simulations addressed to elucidate the carbon transport mechanism (whose driving forces were estimated in Section 5 via DFT calculations), in particular whether surface diffusion or bulk diffusion is the dominant mechanism throughout different stages of nanotube growth. A comprehensive analysis of the trajectories of more than 3,000 carbon atoms is performed, which reveals that, for

a material with significant carbon solubility such as nickel, dissolution processes dominates during the early stages of growth. A dissolution model is proposed based on a driving force determined by the difference of the nanoparticle carbon content with respect to that of saturation. The saturation content, or carbon solubility, was determined to be dependent on nanoparticle size and shape with the latter being influenced by the strength of the metal/support interaction. The ratio between nickel and metal atoms was found to be consistent with known carbide compositions, which in addition to the identification of dissolved carbon atoms with comparatively long residence times within the nanoparticle could be a harbinger of carbide formation. Nonetheless, the most relevant results are the direct observation that surface diffusion dominates during the growth stage, and that cap nucleation, and carbon dissolution are competing mechanisms (since they start occurring simultaneously).

Following-up on a possible formation of carbide in carbon-dissolving catalysts such as nickel, Section 9 shows an analysis of the nanoparticle state during RMD nanotube growth using two types of precursor gases: one whose catalysis generates a single carbon atom (a C(1) precursor), and another whose catalysis generates a carbon dimer (a C(2) precursor). Independently of the type of precursor, visualization of the growth process shows that nickel nanoparticles increased their carbon content seemingly until a relatively stable situation where the nanoparticle surface layer encloses a carbon-metal core. In that state, analyses of density profile reveal a layered (in average) metal-carbon-metal structure along the direction normal to the support. However, indications of phase-separation are observed within the nanoparticle due to aggregation of carbon atoms into it, with the type of precursor gas used affecting the extent of such aggregation. Calculation of diffusion coefficients shows the nanoparticle to be in a more or less solid viscous state depending on the strength of the metal support interaction, the particle size, and the growth stage at which the coefficient is determined. Section 10 concludes, and summarizes the findings discussed throughout this dissertation, while also recommending what research directions should be followed based on the presented work.

2. COMPUTATIONAL METHODS

DFT and RMD constitute the two simulation methods on which this work is based on, with their corresponding theoretical background being presented in the following subsections.

2.1. Density functional theory calculations

DFT is a computational method to find an approximate solution of the Schrödinger equation that is central to quantum mechanics theory [51]. Equations 2-1 and 2-2 give the time-dependent and time-independent forms of this equation, respectively.

$$i\hbar\frac{\partial}{\partial t}\Psi = H\Psi \qquad (2-1)$$

$$H\Psi = E\Psi \qquad (2-2)$$

The time-independent form (Equation 2-2) is an eigenvalue equation, where the operation of H on the wave function Ψ results in an eigenvalue corresponding to the energy of the system. Hence, the Hamiltonian H corresponds to the quantum operator of energy. The Hamiltonian that describes a system with K nuclei and N atoms is given by Equation 2-3.

$$H = \sum_{i=1}^{N}\frac{{p_i}^2}{2m} + \sum_{n=1}^{K}\frac{{P_n}^2}{2M_n} + \frac{1}{4\pi\varepsilon_o}\frac{1}{2}\sum_{i,j=1,i\neq j}^{N}\frac{e^2}{|r_i - R_n|}$$
$$- \frac{1}{4\pi\varepsilon_o}\sum_{n=1}^{K}\sum_{i=1}^{N}\frac{Z_n e^2}{|r_i - R_n|} + \frac{1}{4\pi\varepsilon_o}\frac{1}{2}\sum_{n,n'=1,n\neq n'}^{N}\frac{Z_n Z_{n'} e^2}{|R_n - R_{n'}|} \qquad (2-3)$$

The first and second term in 2-3 describe the kinetic energies of electrons and nuclei, respectively, whereas the third, fourth, and fifth term describe electron-electron, nuclei-electron, and nuclei-nuclei coulomb interactions, respectively. Further simplification of the Hamiltonian is done via the Born-Oppenheimer approximation [9] in which the kinetics of the nuclei (which are comparatively much heavier and slower

than electrons) is neglected. Thus the approximated Hamiltonian is given by Equation 2-4.

$$H = \sum_{i=1}^{N} \frac{{p_i}^2}{2m} + \sum_{i,j=1,i\neq j}^{N} \frac{e^2}{|r_i - R_n|} - \frac{1}{4\pi\varepsilon_o} \sum_{n=1}^{K} \sum_{i=1}^{N} \frac{Z_n e^2}{|r_i - R_n|} \qquad (2-4)$$

Despite this approximation, solution of the Schrödinger equation in this manner represents a many-body problem with an inherent tremendous computational effort needed for its solution. Density functional theory can simplify this problem by focusing on the calculation of the electron density of the system (a function of three spatial variables). The importance of the electron density arises from the fact that according to the work of Hohenberg, Kohn, and Sham [52] "the ground-state energy from Schrödinger's equation is a unique functional of the electron density", where this functional is such that "the electron density that minimizes the energy of the overall functional is the true electron density corresponding to the full solution of the electron density". Thus for each electron:

$$\left[-\frac{\hbar^2}{2m}\nabla^2 + V(r) + V_H(r) + V_{XC}(r)\right]\psi_i(r) = \varepsilon_i \psi_i(r) \qquad (2-5)$$

The first two terms correspond to the electron kinetic energy, and the interaction of the electron with the nuclei. The third term, (the Hartree potential [53]) is defined by Equation 2-6, and corresponds to the Coulombic repulsion between the electron and the electron density.

$$V_H(r) = e^2 \int \frac{n(r')}{|r-r'|} d^3r' \qquad (2-6)$$

Since the electron itself is contributing to the electron density, there is a self-contribution interaction included in the Hartree potential. Thus the fourth term introduces the necessary correction due to self-contribution interactions in addition to exchange and correlation effects. This exchange correlation potential is defined by:

$$V_{XC}(r) = \frac{\delta E_{XC}(r)}{\delta n(r)} \qquad (2-7)$$

Although the existence of the exact exchange-correlation functional is guaranteed, its form is not known. Accordingly, several forms of the functional that have been known to reproduce correctly the properties of a large variety of systems have been proposed. In the work presented in this dissertation, the Perdew-Burke-Ernzerhof functional (PBE) [54] based on the generalized gradient approximation (GGA) [55] was used for periodic systems such as the surface models utilized in Section 6. Whereas the Becke three-parameter exchange functional [56] combined with the Lee-Yang-Parr correlation functional [57] (B3LYP), which includes a contribution of the exact Hartree-Fock functional was utilized for isolated systems such as the 'nanotube cap on a cluster' models described in Sections 3 through 6.

A set of functions known as the basis set is used to construct the approximate the real wave function through their linear combination. These functions must possess certain characteristics according to the characteristics of the studied system. For instance, periodic systems as the surface models in Section 6 require functions whose values repeat periodically according to the periodicity of the system. For such systems, Bloch plane waves are appropriate [58], and have a general form given by:

$$\phi_k(r) = e^{ik.r} u_k(r) \qquad (2-8)$$

On the other hand, for isolated systems the basis set requires functions that are centered on specific points in space, and are typically set to represent atomic orbitals. For both periodic and isolated systems, a larger basis set allows for more accurate solutions since there is more flexibility to accommodate a linear combination that accurately represents the actual wave function. For periodic systems, the basis set size is determined by selection of an energy cutoff associated with the kinetic energy of the basis set plane waves. However, for isolated systems, the basis set size depends on the basis set chosen to perform the calculation. The minimum basis set that can be used for a calculation is one that uses one basis function for each electron in the system. In this

case, typically a Slater-type orbital (function) (STO) [59] that rapidly decays away from the nucleus is used. A larger basis set can use more and other types of functions for each electron, especially if they are valence electrons. In this work, periodic systems used a 450 eV cutoff for the basis set, whereas isolated systems used the Los Alamos National Laboratory basis set (LANL2dz) [60, 61].

Valence electrons are typically the most relevant electrons in simulation systems; hence it is customary to reduce computational time by 'freezing' the core electrons, and approximating the interaction between core and valence electrons via a pseudopotential function. The isolated systems presented in this dissertation used the pseudopotential function included in the LANL2dz basis set. Equivalently, the periodic systems used a 'frozen' core approximation in conjunction with the projector augmented wave method (PAW) [62].

In the process of finding the solution of the Schrödinger equation, a number of integrals have to be solved in numerical fashion. Expectedly, the way in which the integration grid is set up impacts the accuracy of the calculations. For periodic systems, these integrals are solved in the reciprocal space, specifically within the Brillouin zone. Accordingly, the necessary number of grid points for the integration grid is proportional to the dimensions of the reciprocal cell. In the periodic calculations presented in this work, the grids were created according to the method developed by Monkhorst and Pack [63], using a 9 x 9 x 1 scheme.

In summary, DFT methods focus in the calculation of the electron density to derive all the electronic properties of the systems. The selection of an exchange correlation functional is central to DFT methods, and the accuracy of the calculations. Periodic DFT calculations in this work used a GGA-PBE functional with Bloch waves using a 450 eV cutoff, and a 9x9x1 integration scheme, while isolated DFT calculations used the B3LYP functional with LANL2dz as the basis set.

2.2. Reactive classical molecular dynamics

Classical molecular dynamics (MD) is a computational methodology that calculates the dynamic evolution of a system based in classical Newtonian mechanics. The Hamiltonian corresponding to the energy of a system of N particles is:

$$\sum_{i=1,i\neq j}^{N}\sum_{j=1}^{N}E_{ij_{VDW}}+\sum_{i=1,i\neq j}^{N}\sum_{j=1}^{N}\frac{q_iq_j}{r_{ij}^2}+\sum E_{ij}+\sum E_{ijk}+\sum E_{ijkl}+\sum_{i=1}^{N}\frac{M_iV_i^2}{2}\quad(2-9)$$

The first and second terms correspond to Van der Waals and Coulombic interactions, respectively. The third, fourth, and fifth term describe the energy due to bond energies, angles, and torsion angles, whereas the last term represents the total kinetic energy of the system, and is intimately connected to the temperature of the system.

The form and parameters of the functions that describe the different interactions can be modified and tuned to represent the system more accurately, and constitute the so-called force field. Force fields can be derived and parameterized using experimental information (conferring them an empirical character), or can be derived and parameterized based on *ab-initio* calculations. A force field expression that allows for the breaking and formation of bonds confers the reactive character of reactive classical molecular dynamics (RMD). Besides being used to determine the energy of the system for a particular configuration, the force field is used to calculate the force on each particle. The force on particle *i* due to interactions with other particles is given by:

$$F_i=\sum_{j=1,j\neq i}^{N}\frac{\partial E_{ij}}{\partial r_{ij}}\quad(2-10)$$

The RMD simulations presented in this dissertation use the predictor-corrector algorithm (PC) [64] to model the dynamics of the systems. Velocity Verlet and leapfrog algorithms are alternative algorithms often used in MD simulations [65]. In the PC scheme, positions, velocities, and accelerations (F_i/M_i) at time *t* are used to *predict* the

positions, velocities, and accelerations at time $t + \Delta t$ using a series expansion. At the new positions, the acceleration (force) is calculated again using Equation 2-10. Typically, the two calculated accelerations are different; and the positions, velocities, and accelerations at time $t + \Delta t$ are *corrected* proportionally to such difference.

Since the particles kinetic energy and temperature are intimately connected, the velocities have to be continuously rescaled to ensure that the temperature T of the simulation system is maintained constant [66]. The instantaneous temperature is calculated by Equation 2-11, and the velocity of each particle corrected by Equation 2-12.

$$T_{ins} = \frac{\sum_{i=1}^{N} M_i V_i^2}{3Nk_B} \qquad (2-11)$$

$$V_{i_{corrected}} = V_i \sqrt{\frac{T}{T_{ins}}} \qquad (2-12)$$

In addition to the velocity rescaling, the simulation temperature must be controlled using a thermostat algorithm. Berendsen [67], Nosé-Hoover [68], and Langevin [69] are common thermostats used in MD simulations. In this dissertation, Langevin dynamics is used to control the temperature through the introduction of random temperature-dependent, and frictional forces. Thus the corrected force on particle i is given by Equation 2-13, wherein a careful selection of the friction factor γ must be done.

$$F_{i_{corrected}} = F_i + \gamma M_i V_i + \sqrt{2\gamma k_B T M_i n_{random}} \qquad (2-13)$$

Molecular dynamics simulations are often performed to study the equilibrium properties of a system of interest. In such case, the dynamics of the system is simulated for an appropriate time that allows the system for equilibration. Once the system is equilibrated, the dynamics of the system must be simulated long enough to allow sampling a significant number of microstates that permit to meaningful calculate

relevant properties. In other cases, such as in the RMD simulations of nanotube growth presented in this dissertation, the interest is on the dynamic evolution of the system without necessarily evolving through equilibrated states. Accordingly, non-equilibrium RMD simulations were performed in this work.

RMD simulations in this dissertation are addressed to simulate the growth of single-wall carbon nanotubes (SWCNTs). These simulations were performed using a specialized Fortran code (SIMCAT) developed by Professor Balbuena's group at Texas A&M University to simulate the nanotube growth process in a CVD process [70]. In a typical simulation, a metallic nanoparticle is placed on a graphene support within an appropriate orthorhombic simulation supercell. A hard-wall potential is placed on the XY plane to eliminate the periodicity of the system in the Z direction perpendicular to the substrate. As the simulation starts, particles modeling the precursor gas fill the simulation supercell according to a preset value of gas density. The precursor gas particles constitute a vapor phase, and metal and carbon atoms constitute a condensed phase. The velocity rescaling is done separately for each phase, as well as the selection for the friction factor γ.

A simple scheme is used to model the catalytic process relevant to CVD synthesis. The dynamics of the precursor gas particles is unperturbed by interactions with other atoms in the systems, but when a precursor gas particle bumps onto the metallic nanoparticle surface, it is converted into a regular carbon atom. The conversion scheme produces only one atom when catalysis of a C(1) precursor gas (e.g. CH_4, or CO) is modeled, and a carbon dimer when catalysis of a C(2) precursor gas (e.g. C_2H_2, or C_2H_5OH). For each catalytic event, a new precursor gas particle is added at a random position within the simulation supercell, with a velocity equal to the average velocity characteristic of the gas phase at the moment of addition.

The set of force fields used in the RMD simulations presented in Section 6 through 9 model the energetics of the five types of interactions central to nanotube growth, namely, metal-metal (MM), carbon-carbon (CC), metal-carbon (MC), metal-

support (MS), and carbon-support (CS) interactions. The Sutton-Chen potential [71] as described by Equations 2-14 and 2-15 models MM interactions in the nanoparticle.

$$E_i = \varepsilon \left[\frac{1}{2} \sum_{j \neq i} \left(\frac{a}{r_{ij}} \right)^n - c\sqrt{\rho_i} \right] \qquad (2-14)$$

$$\rho_i = \sum_{j \neq i} \left(\frac{a}{r_{ij}} \right)^m \qquad (2-15)$$

The parameter calculated in Equation 2-15 corresponds to the local density around the metal atom of interest, and (as shown in Equation 2-14) affects its interactions with other metal atoms. On the other hand, a force field developed by Balbuena *et al* [72] based on the Tersoff-Brenner potential [73], models MC and MS interactions as described in Equations 2-16 through 2-18. Repulsive contributions are calculated by Equation 2-17, and attractive contributions by Equation 2-18.

$$E_{ij} = \alpha_{ij} V^R(r_{ij}) - \alpha_{ij}^{1.1} V^A(r_{ij}) \qquad (2-16)$$

$$V_{ij}^R = f(r_{ij}) \frac{D_e}{S-1} e^{\{-\beta\sqrt{2S}(r_{ij}-R_e)\}} \qquad (2-17)$$

$$V_{ij}^A = f(r_{ij}) \frac{D_e S}{S-1} e^{\{-\beta\sqrt{2/S}(r_{ij}-R_e)\}} \qquad (2-18)$$

The function defined by parts $f(r_{ij})$ serves as a distance-dependent weighting factor. The parameter α_{ij} in Equation 2-16, on the other hand, is central to the RMD simulations presented in this work, because the variation of this parameter is utilized to modify the interaction between the graphene support and metallic nanoparticles (MS interactions) to study its effect on nanotube growth. Also, the parameter α_{ij} can be utilized to modify the interactions between the nanotube rim and the particle, and the body of the nanotube and the particle (MC interactions). However, all the simulations presented in this dissertation utilize the same values of α_{ij} to describe MC interactions,

which have demonstrated the best performance based on the quality of the simulated nanotube growth.

The CC, and CS interactions are described using a modified Tersoff-Brenner potential [72] as described by Equations 2-19 through 2-21:

$$E_{ij} = \alpha_{ij} V^R(r_{ij}) - \alpha_{ij}^{1.1} V^A(r_{ij}) \qquad (2-19)$$

$$V_{ij}{}^R = f(r_{ij})\left(1 + \frac{Q}{r_{ij}}\right) A e^{-ar} \qquad (2-20)$$

$$V_{ij}^A = b_{ij}\left(f(r_{ij}) \sum_{n=1}^{3} B_n e^{-\beta_n r_{ij}}\right) \qquad (2-21)$$

The modification in (2-20) accounts for the weakened CC interactions inside the metal nanoparticle as determined by DFT calculations. As for MC interactions, $f(r_{ij})$ is a function defined by parts that serves as a distance-dependent weighting factor. The parameters b_{ij} and α_{ij} are parameters that depend on the local environment around atoms *i*, and *j*. Specifically, b_{ij} accounts for the bonding of *i*, and *j* to other carbon atoms, whereas α_{ij} accounts for coordination of metals atoms around *i*, and *j*. The latter parameter is particularly important to screen the interaction between carbon atoms dissolved within the metal nanoparticle.

In summary, RMD methods focus either in the calculation of the system dynamics to calculate equilibrium properties, or on following the evolution of the system via a non-equilibrated path. The selection of an appropriate force field form, and a meaningful determination of its parameters through experiments or *ab-initio* calculations are central to RMD methods, and the accuracy of the calculations. Periodic RMD calculations presented in this work use the Sutton-Chen potential, and modified versions of the Tersoff-Brenner potentials to study the evolution of a reaction system during nanotube growth.

3. THE ROLE OF CAP CHIRALITY IN THE MECHANISM OF GROWTH OF SINGLE-WALL CARBON NANOTUBES*

3.1. Summary

Addition of C_2 radicals to rim sites of carbon nanotube caps with different chiral angles and its relation to the catalyzed growth of single-wall carbon nanotubes are investigated using DFT calculations. It is shown that high chiral angle (near-armchair) caps are thermodynamically more stable than low chiral angle (near-zigzag) ones. On the other hand, it is demonstrated that the rim structure of armchair and near-armchair caps favors their kinetics of growth in comparison to that of near-zigzag and zigzag caps. Our findings explain several features of nanotube growth found in experimental synthesis.

3.2. Introduction

The chiral angle of a single-wall carbon nanotube (SWCNT) is geometrically determined by rolling over a hypothetical graphite sheet to form the nanotube structure [74]. A cap-ended nanotube is a one that features an open end (nanotube rim), and an end close by a cap structure. The cap is defined as a hemispherical structure constituted by a number of hexagonal rings, and six pentagonal rings arranged according to the isolated pentagon rule [75]. The structure and properties of open-ended nanotubes are unique for a given chirality, but for a cap-ended nanotube there is typically several cap structures that are compatible with a given chirality. As a rule-of-thumb, the larger the nanotube diameter increases, the more cap structures can fit the nanotube. It must be noted, however, that although a single chirality may be fit by different cap structures, each particular cap structure can only fit a single chirality [76].

SWCNTs are produced by different methods [77], with the most popular being chemical vapor deposition (CVD) methods, wherein a C-containing precursor gas is decomposed over a transition metal nanocatalyst at relatively high temperatures (~ 1000

*Diego A. Gomez-Gualdron, and Perla B. Balbuena. "The role of cap chirality in the mechanism of growth of single-wall carbon nanotubes", Nanotechnology, 19, 485604, (2008). DOI:10.1088/0957-4484/19/48/485604. Printed with permission of the Institute of Physics (IOP).

K) and moderate pressures [78] . Some CVD methods have been reported to produce of SWCNTs of selected chiralities in the near-armchair range [20, 79], but the reasons for such selectivity are not clear. The abundance of (n,m) species obtained by a CVD method (CoMoCAT) that uses Co nanocatalysts grown over molybdenum carbide surfaces and deposited on SiO_2 or MgO substrates [79] has been found to depend on temperature and on the nature of the substrate [20]. Optical absorption analyses show that on SiO_2 substrates, at temperatures between 700 and 800 ◦C, approximately 50% of the tubes are (6,5), followed by ∼30% of (6, 6) and (7,7) armchair tubes, and relatively small amounts of (8, 4), (7, 5), and (7, 6) near-armchair tubes. As temperature increases to 850 ◦C, the percent of the smallest (6,5) nanotube decreases significantly. It is also interesting that the relative percentages of abundance change shifting the distribution towards the largest near-armchair tubes when a different substrate (MgO) is used at a relatively low temperature, 750 ◦C [20]. Another interesting finding is that when CO is used as a precursor gas, none of the detected tubes belong to the zigzag or near-zigzag type, however when CH_4 is used at the same temperature, tubes of larger diameters and a wider distribution of chiralities, including a few zigzag tubes are found.

It is generally accepted that caps nucleate at the beginning of the nanotube growth reaction, emerging from the small metal catalytic clusters involved in the reaction [78]. A possible mechanism has been described in [70, 80]: carbon atoms dissolve inside the cluster and eventually popup outside the cluster forming the cap. Here, it is proposed that chirality selectivity is primarily determined by two factors: 1) the formation and stability of the cap on the nanocatalyst surface, and the thermodynamics and kinetics of growth via formation of new hexagonal rings through the progressive addition of carbon to the cap structure. Under this hypothesis, the dominant chirality is likely to be defined by the type of cap that is favored at the early stages of the SWCNT growth process.

Here we use DFT calculations to investigate the role of the cap chirality on the growth mechanism, assuming that such growth proceeds by addition of C_2 radicals to the cap rim. Our analysis involves the C_2 addition to caps, starting with the smallest one-

end closed structures for which nanotube chirality can be defined. This smallest chiral unit can in fact be considered as a cap-ended SWCNT of length equal to zero [75].

3.3. Computational methods

Figure 3-1 depicts a few of these structures for various chiral angles: from an armchair structure (6, 6) and decreasing the chiral angle toward a near-zigzag structure (9, 1). The caps are shown in a position that matches a vertically aligned carbon nanotube. We emphasize that the caps edges in **Figure 3-1** do not resemble what is usually pictured as the edges of either an armchair or a zigzag nanotube. The reason is that to define these minimal chiral units we have chosen to end a given cap as soon as all the six pentagons are incorporated, thus the last row may contain pentagons; in contrast, the nanotube rim is usually characterized by a row entirely composed by hexagonal rings. For instance, the edges of a (6, 6) cap rather resemble those of a typical zigzag picture; however, once enough carbon atoms are added to this (6, 6) unit forming new hexagons, the armchair edge is recovered. Thus, other features contribute to the nanotube chirality besides the nanotube edge, such as the cap structure, which is particularly important during nanotube growth using CVD methods. Caps having chirality close to armchair (near-armchair) resemble paraboloids of revolution truncated at approximately 45◦, whereas the nearly zigzag ones show hook-like structures.

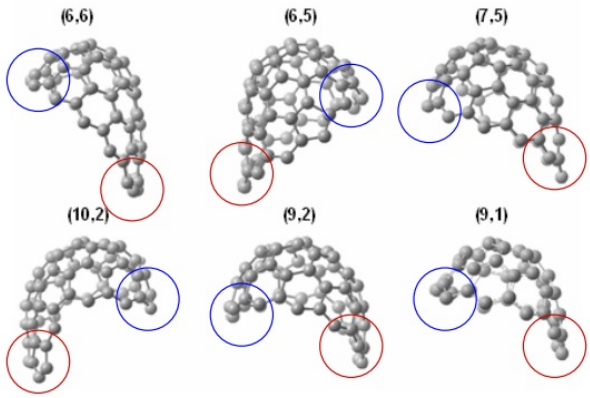

Figure 3-1. Structures of selected caps of several chiralities fulfilling the isolated pentagon rule. Nanotubes (6,5) and (9,1) have identical diameter, and for them there is only one possible cap compatible with their respective chiralities. The regions circled in blue are referred as the rear, and those in rear as the tip of cap.

We identify two regions in the cap, as shown in **Figure 3-1**, a 'rear' region, and a 'tip' region. Due to the specific distribution of pentagons and hexagons, the rim structure is dependent on the chirality. Most of the rim sites in each cap shown in **Figure 3-1** are zigzag sites; however a few of them are armchair (*ac*) sites where a new hexagon may be completed by addition of a C_2 radical. **Figure 3-2** shows that the *ac* site is located in the rear region for a near-armchair cap, and in the tip region for a near-zigzag one. This different site distribution has an effect on the growth as discussed in subsection 3.4.

The smallest chiral units were fully optimized using density functional theory with the Becke 3-parameter exchange functional [56, 81] and the Lee *et al* [57] correlation functional B3LYP and the 6-31G basis set. The Gaussian 03 program [82] was used for all the calculations.

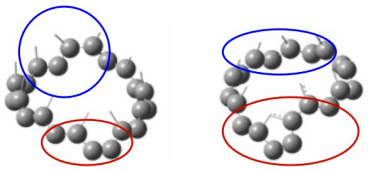

Figure 3-2. Rim structure of typical armchair-like and zigzag-like caps. Left: (6, 5). Right: (9, 1). Note that the armchair site where a new hexagon may be formed by addition of a C_2 radical is located in the rear (circled in blue) for the armchair-like, but in the tip (circled in red) for the zigzag-like.

3.4. Results and discussion

The CC bond distances in the optimized caps are not as regular as for the open-ended nanotubes due to strain generated by the presence of the pentagons that give the curvature to the cap. The CC bond length in the caps ranges from 1.38 to 1.47 °A in the inner rings, whereas in the edges is ~1.41 Å for zigzag-like (3 atoms) endings and ~1.24 Å for armchair-like endings (4 atoms). **Table 3-1** displays the absolute energies of optimized (7, 5) caps of different spin multiplicities. The cap energy shows small differences in terms of multiplicity; for example there is a difference of 0.0024 a.u. (1.38 kcal mol^{-1}) between the total energy of caps of multiplicity one (1), and three (3), and 0.0108 a.u. (6.91 kcal mol^{-1}) between multiplicities one (1) and eleven (11). The most

stable cap corresponds to multiplicity three, that is, there are two unpaired electrons. Saturating carbon nanotube edges with hydrogen is sometimes used in calculations to stabilize the nanotube and to resemble the behavior of an infinite length nanotube; this approach was not adopted to keep the cap structure/reactivity as in the early stages of nanotube growth.

Table 3-1. Minimum energies of (7,5) caps of different spin multiplicities. Multiplicity 3 yields the lowest energy value, corresponding to a cap with two unpaired electrons. Similar energy differences were obtained for the other caps in Figure 3-1.

Multiplicity	Energy (a.u.)
1	-2437. 127 12
3	**-2437.129 52**
5	-2437.128 88
11	-2437.116 32

Table 3-2 shows the energies per C atom of the optimized caps and the energy differences calculated with respect to the lowest energy per C atom of this group, found for a (7, 5) cap. For a given chirality the effect of the different cap structure does not yield a significant energy difference, however very different energies per C atom are observed for different chiralities, for example the cap compatible with the (9,1) chirality has the less favorable energy, presenting a difference of 0.23 eV/C atom (5.30 kcal mol^{-1} per C atom) with the most stable (7, 5) cap. Although not completely monotonic, there is a trend where the energy per carbon atom increases as the chiral angle decreases becoming closer to zero (zigzag), that is armchair-like caps are more stable than zigzag-like, in agreement with previous theoretical studies [47].

It is interesting to note the 0.21 eV difference between (6,5) and (9, 1) caps, both of which have only one matching cap. Besides the (6, 5) and the (9, 1), in the rest of this Section, we analyze the most stable (7, 5), (10, 2), and (6, 6) cap structures. The spin multiplicity of 3 found for the caps suggests a growth reaction mechanism based on reaction with a species with two unpaired electrons such as a C_2 radical

Table 3-2. Energies per carbon atom (eV) and energy differences (in eV) with respect to the most stable (7, 5) of the set of caps of similar-diameter and different chiralities (see Figure 3-1). Except (6,5) and (9, 1) all other caps have more than one cap compatible with their chirality. Cases a, b, c, d, represent different caps of the same chirality, but they are only a subset of the possible caps available in each case.

Cap	Energy/C atom (eV/C atom)	Relative energies (eV)
(6,6)a	-1036.20	0.02
(6,6)b	-1036.17	0.05
(6,6)c	-1036.19	0.03
(6,5)	**-1036.20**	0.02
(7,5)a	-1036.22	0.00
(7,5)b	-1036.20	0.02
(7,5)c	-1036.17	0.05
(7,5)d	-1036.21	0.01
(10,2)a	-1036.12	0.10
(10,2)b	-1036.17	0.05
(10,2)c	-1036.19	0.03
(9,2)a	-1036.13	0.09
(9,2)b	-1036.03	0.19
(9,2)c	-1036.05	0.17
(9,1)	**-1035.99**	0.23

Experimental reports also suggest a correlation between the abundance of C_2 species and the production of single-wall carbon nanotubes [83]. Since C_2 is a nucleophilic species and the unsaturated cap is an electrophilic one, the addition reaction may occur via interaction of the lowest unoccupied molecular orbital (LUMO) of a cap with the highest occupied molecular orbital (HOMO) of a C_2 radical. **Figure 3-3**-top displays the calculated LUMO and HOMO orbital energy levels of five of the caps shown in **Figure 3-1**. According to the proposed reaction mechanism the C_2 radical affinity of the cap would be higher as the cap LUMO level lays closer to the radical HOMO level; therefore, it is apparent from **Figure 3-3** that the (6, 5) chirality is favored in that sense. LUMO orbital isosurfaces displayed in **Figure 3-3** indicate that this orbital is generally spread out on the surface of the caps except for (10, 2) and (6, 6) whose LUMO orbitals are rather localized.

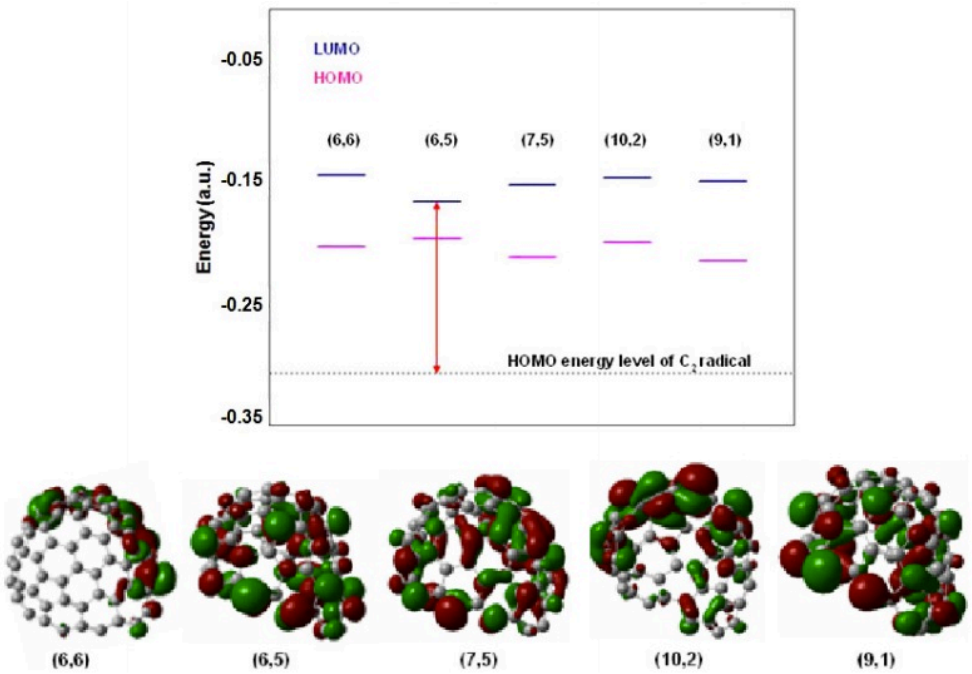

Figure 3-3. Top: schematic of the LUMO and HOMO energies (in a.u.) of caps of different chiralities, a base line is drawn corresponding to the energy level of the HOMO orbital of a C_2 radical. Notice that the (6, 5) LUMO is the closest one to the C2 HOMO. Bottom: LUMO orbital isosurfaces (isovalue = 0.02 electrons au−3) of the caps showing higher localization of the LUMO orbitals in the (6, 6), and (10, 2) caps.

The shape of the LUMO orbital reveals that is composed mainly by p_z orbitals forming the π cloud of delocalized electrons. The localization of the LUMO is on the rear of the (10,2) cap and on one side (covering both half of the tip and half of the rear) for the (6,6) cap. The LUMO localization on the (6,6) cap occurs in spite of the symmetry plane bisecting the right-hand and left-hand parts of the cap where the rim sites look exactly the same at either side. For the (10,2) cap, the localization of the LUMO orbital (rear region) and the location of the favorable sites for C_2 addition leading to completion of a new hexagon (rim sites in the tip region) do not match.

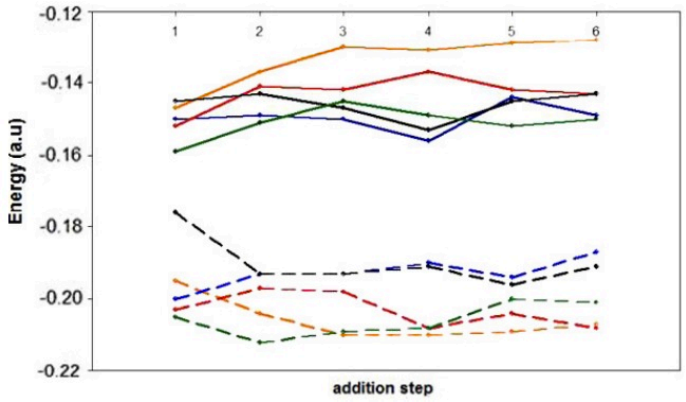

Figure 3-4. Energy (in a.u.) of the frontier orbitals after several steps in the C_2 addition reaction to form a new hexagon in a cap. Orange: (6,6), blue: (6, 5); red: (7, 5), black: (10, 2), green: (9, 1).

On the other hand, it is seen from **Figure 3-3** that the π cloud is more spread out for the species (6,5), (7,5) and (9,1). For the near-armchair caps (6,5) and (7,5), there is a minor mismatch given by a slightly higher contribution to the LUMO observed in the carbon atoms located near the tip of the cap even when the site favorable for C_2 addition is located in the rear of the cap, but this mismatch is much less dramatic than that observed for (10, 2). As the nanotube grows by adding C_2 species to the available sites, the energetic of the LUMO and HOMO is expected to vary moderately. This variation is depicted up to the sixth step of C_2 addition in **Figure 3-4**. The (6,6) chirality undergoes a rising of the energy of the LUMO as C_2 is added, therefore increasing the gap between this latter orbital and the C_2 HOMO, which can be interpreted as a decrease in cap affinity for the radical. The energy of the LUMO level of the (6,6) cap is over the LUMO level of the rest of the caps, this can be related to a rapid increase of the stability of the (6,6) cap when the (6,6) nanotube is growing and recovering the characteristic rim and symmetry of the armchair tube.

One common feature for all the cases is the somewhat constant Fermi level, (which is approximately located halfway between the LUMO and HOMO) because most C_2 additions cause an increase of the LUMO energy accompanied by a decrease in the HOMO energy. **Figure 3-3** shows that the (6, 5) cap had the lowest LUMO, and the highest HOMO. This trend is disrupted as the caps are growing (**Figure 3-4**) with a

more disrupting effect on the LUMO than on the HOMO. Only after the first addition step the (6, 5) HOMO is relatively low. In the other addition steps, the (6, 5) HOMO is the highest one, although closely followed by the HOMO of (10, 2). The HOMO energy of the (6, 6) cap follows an inverse trend to the LUMO, as growth progresses. The HOMO of (7, 5) and (9, 1) clearly stand below that of (6, 5) for all the cases. On the other hand, the LUMO energies for all of the chiralities are above that of (6, 5) throughout growth, with the exception of that of (9, 1), which is below the (6, 5) LUMO after the first and fifth step. Thus, although **Figure 3-3** shows some preference for the addition reaction by the (6, 5), from analysis of the LUMO energies after addition of the C_2 radical (**Figure 3-4**), we conclude that this cannot be the only factor behind the preferential selectivity of (6, 5) nanotubes, since the rarely-detected (9, 1) nanotube shows similar features.

To further investigate this point, the first step of the C_2 addition growth mechanism is depicted in **Figure 3-5** for both (6,5) and (9,1) caps: the hypothetical C_2 radical (formed in some preceding step of the growth reaction) is headed toward an active site. We consider a site to remain active as long as the addition of a C_2 completes a hexagonal ring. A clean growth is maintained as long as no defects are added to the structure (formation of heptagons and other non-six-member rings). The addition of the C_2 radical to other sites would form a strained pentagonal ring that would not be energetically favorable because all the six pentagons are already incorporated into these caps, so forming other stable pentagons is not possible for a clean growth.

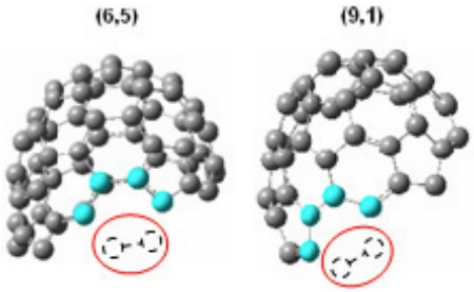

Figure 3-5. Example of CNT C_2-based growth mechanism for the (6, 5), and (9, 1) caps. The C_2 species is added in a location wherein its addition completes a new hexagon in the cap.

At this point we observe that due to the geometry of the cap interacting with the cluster which is deposited on a substrate surface (**Figure 3-6**) the hypothetical axis of the upcoming nanotube will not be perpendicular to the substrate surface but rather forming an angle close to 75˚; accordingly, the direction of nanotube growth is likely to be affected by the location of the active sites for formation of new hexagonal rings and by how this growth changes the inclination of the nanotube axis. For instance, filling the 'rear' of the cap (as in the near-armchair cases, see **Figures 3-1** and **3-2**) would straighten up the axis of growth by modifying the 'truncation' angle of the cap, as illustrated in the schematic **Figure 3-6**.

Among the hypotheses proposed to explain the stop of the nanotube growth during synthesis by CVD methods, it is argued that tubes might push against the catalyst pore walls finishing the growth due to mechanical reasons, or hindrance effects might exist because of bundling of neighbor growing nanotubes [78]. On the other hand, it is seen that if optimal conditions are present growth of several centimeters long nanotubes can be achieved [84]. 'Forest' growth [85, 86] has been defined as a collection of vertically aligned nanotubes of approximately the same length. Another microstructure defined as 'grass' is characterized by bundling of horizontally aligned tubes [86]. Our analysis suggests that forest-type bundling is likely to occur for near-armchair and armchair chiralities, since the sites available for the addition of C_2 are located at the rear of the cap, favoring the development of straight tubes. In contrast, for the near-zigzag caps these active sites are located at the tip, so at the beginning of the growth the angle of the nanotube axis with respect to the substrate would be rather enhanced and not corrected in anyway during the growth as illustrated in **Figure 3-6**; such growth may cause the formation of highly interconnected 'grass' structures.

Another interesting feature of this growth that contrasts the behavior of the near-armchair (6, 5) versus the near-zigzag (9, 1) tube (and supports our discussion about the change in the angle that the new tube forms with its substrate) is sketched in **Figure 3-7**. As discussed before, the near-armchair caps have the site for the first addition located in the rear of the cap, thus the C_2 addition leads to the completion of a hexagon and

immediately generates two available sites at either side of the site where the first addition occurred. This leads to two alternatives for the next step. Notice that these sites are still in the rear part, therefore, either possibility of addition of C_2 is going to help to regenerate the rear part of the cap.

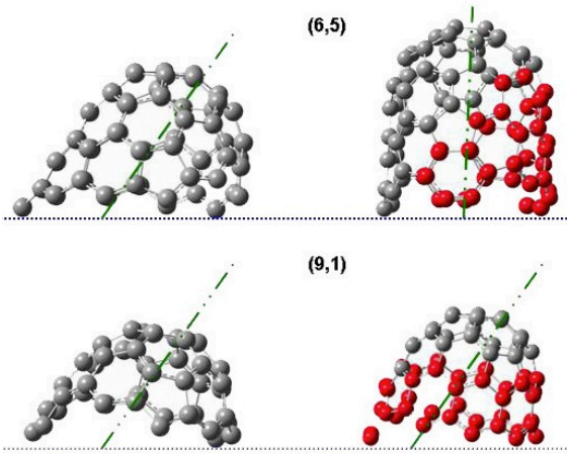

Figure 3-6. Schematic of the nanotube growth by C_2 addition to the rim sites to a near-armchair (6, 5) cap (top) and to a near-zigzag (9,1) cap (bottom). Note that the initial inclination of approximately 75◦ is changed by growth in the near-armchair tube, whereas remains about the same in the near-zigzag tube.

We tested both alternatives of adding the C_2 radical in either position by optimizing and calculating the addition energy and choosing the lowest one as the one to occur. As a result of the new additions the number of available sites is increased. For instance, in the (6, 5) chirality (**Figure 3-7**, left), after the second addition, the number of available sites increases to three. As the number of sites is increasing more tests were run to define the possible sites where the new hexagon is more likely to be completed. This sequence is summarized in **Figure 3-8**. In contrast, near-zigzag caps have their first available site near the tip, in the case of (9, 1) shown in **Figure 3-7**-right, once the first hexagon is completed only one new near site is created, and in fact none of the possible hexagon completions generates more than one new site for the next step. Since the completion of successive sites starts from the tip for this type of cap, no chance is left to recover the rear part of the cap. For the (9,1) chirality the addition-driven sites

appear in a helical fashion starting from the tip passing by the rear and coming back to the tip (**Figure 3-6**). Once in the tip again the same path is followed from that point on. Therefore, the inclination of the nanotube would be hardly corrected for near-zigzag chiralities.

For the (10, 2) cap (near-zigzag cap), the first addition step does generate two active sites, but no further increase of those available sites occurs later on. This behavior can be explained by analysis of the characteristics associated with a given chirality, notice that for the completion of a hexagon by adding a C_2 species an armchair termination is necessary. Then, although initially the armchair terminations are not very evident in (6, 6), (6, 5) and (7, 5) (the rims look zigzag-like), once the hexagons start to be completed, the 'typical' armchair structure starts to reveal in the (6, 6) nanotube, and the near-armchair (6, 5) and (7, 5) nanotubes. According to this, the highest the chiral angle (near-armchair), the more armchair sites are likely to be revealed as the nanotube grows.

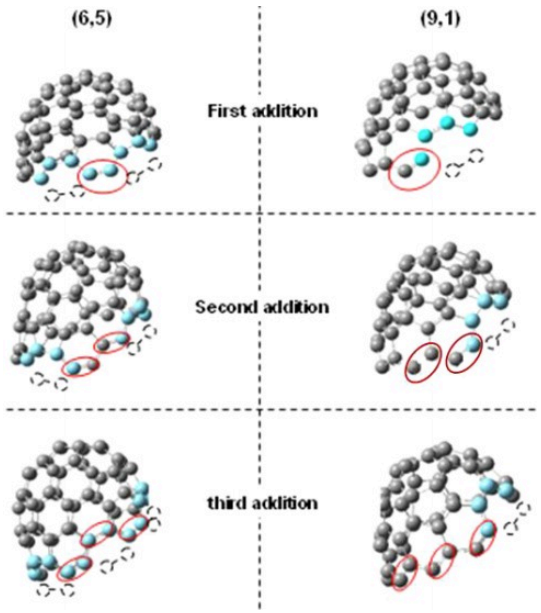

Figure 3-7. The number of favorable sites for the addition of a C_2 radical is kept constant as the nanotube grows out of the (9, 1) cap, but increases when nanotube grows out of the (6, 5) cap. The C_2 radicals added in a preceding step are circled in red, and the favorable sites for further addition of C_2 are highlighted in blue whereas the hypothetical attacking radical is drawn in dashed line.

Similarly, due to the near-zigzag nature of (9, 1) and (10, 2) nanotubes, less armchair sites are to be created. Now, the growth of the near-armchair nanotubes does not necessarily occur in a helical manner as that of the (9, 1) cap since many different available sites are created at different sites around the rim. Not only are there different available locations for reaction, but also those located by the rear of the cap are the ones that usually have better addition energies. This means that the growth in the near-armchair chiralities takes place by restoring the rear part and therefore correcting the initially present inclination of the nanotube axis. On the other hand, *the existence of more available sites have kinetic implications*. One of the concepts invoked in reaction kinetics relates to the number effective collisions necessary for a reaction to occur. The number of 'effective collisions' increases with temperature and concentration of reactant species, and relates to the frequency factor in the corresponding reaction rate constant expression [87] as shown by:

$$R(t) = A_{\infty} e^{\frac{E_a}{KT}} [C]^n \qquad (3-1)$$

$$A_{\infty} = k \times \{number\ of\ active\ sites) \qquad (3-2)$$

The growth of the nanotube could be regarded (in its final step) as the reaction between a C_2 radical and an armchair site. Therefore, if the cap shows an increase in the concentration of these sites as it undergoes the addition of C_2; then, the final effect should be an increase in the reaction rate (Equation 3-1 and 3-2). Since this effect would be more evident in near-armchair caps, it would be in agreement with the highest abundance of near-armchair nanotubes in most catalytic processes. **Figure 3-8** shows the energy of C_2 addition in each step for all the caps in this study, the most favorable path is marked in red. As previously mentioned, the (9, 1) nanotube has only one alternative in each step. Similarly, the (10, 2) nanotube has two alternative sites at each addition, whereas the abundance of favorable addition sites for (7, 5), (6, 5) and (6, 6) is evident from the figure. According to this criteria, the (7, 5) nanotube would have a slight advantage over (6, 5) since after the sixth step it leaves four available sites already whereas (6, 5) leaves three. However, notice in one of the alternatives for (7, 5) the

energy is −5.25 eV, much weaker than the typical values for (7, 5) which are larger than −8.00 eV.

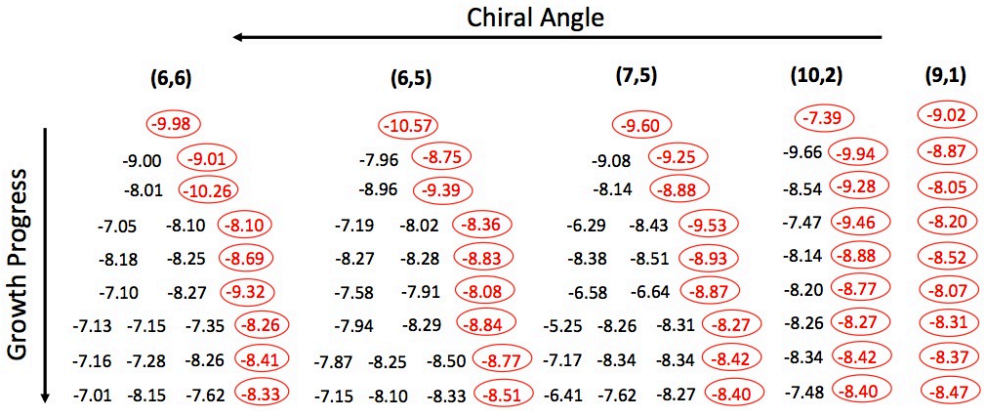

Figure 3-8. Energy of adsorption (eV) for the adsorption path of the C_2 radical, the path in red corresponds to the minimum energy path. Notice that as the chiral angle increases from zigzag to armchair also does the number of favorable additions in each step.

Furthermore, inspecting the geometry corresponding to the weakest addition energy, it is found that it corresponds to a defective structure with a strained hexagon formed. Similar situations are found for other values of the same magnitude in other addition steps (such as the −6.41 eV in the ninth addition step), and all of them correspond to defective structures. These defective structures arise due to high strain generated in the bonds of the caps, which affects cap stability (cap develops a tendency to bend over itself during the growth, particularly by merging its left and right sides in the rear part). This makes some armchair sites to change their ∼120◦ opening by a ∼90◦ opening, which would form a squared ring after the addition of C_2. Since this tendency was also observed during the optimizations of the (6, 5) and (6, 6) cases (for addition energy values around −7.00 eV), we suggest that the presence of the metallic cluster must play an important role in not allowing the structure to enclose in a fullerene-like manner and instead favoring the growth of the nanotube. Additional calculations presented in Section 4, and [88] reveal that since the cluster atoms tend to locate close to the rear part of the cap, they are able to stand in between the right and left sides of the

rear alleviating the tendency of the cap to close. It is also remarkable that if the additions with less favorable energy are ruled out, then the (6, 5) nanotube appears as the one with more favorable sites over the (6, 6), and (7, 5) nanotubes.

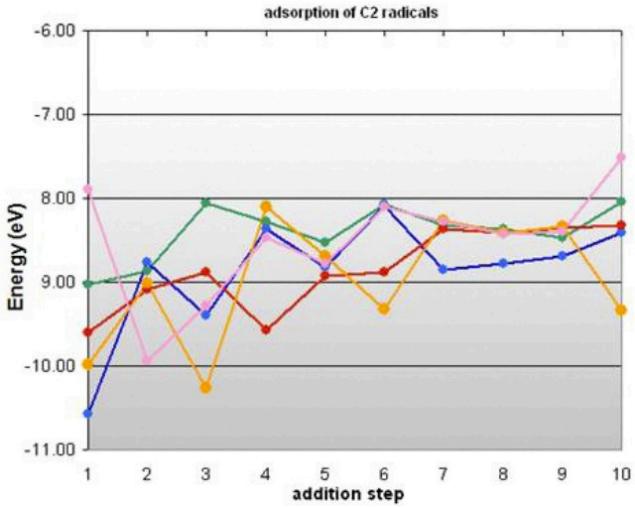

Figure 3-9. Best adsorption energies (red path in Figure 3-8) for the different caps. (6, 6) in orange, (6, 5) in blue, (7, 5) in red, (10, 2) in magenta and (9, 1) in green. The (9, 1) curve is never below the one for (6, 5). The near-armchair caps have better adsorption energies of the C_2 radical in the ten initial steps of the growth.

For each chirality, **Figure 3-9** displays the points corresponding to the 'red path' in **Figure 3-8**. It shows how the structure of the caps responds to the addition of the C_2 radical. For the first addition, the (6,5) cap is the one more energetically favored, followed by the (6,6) and (7,5) ones, whereas the near-zigzag (9, 1) and (10,2) caps are the least energetically favored. Comparing (6,5) and (9,1), it is observed how the adsorption energy of C_2 on the (9,1) cap in typically weaker than that on the (6,5) one. Up to the sixth step, they are fairly equal in the even steps, but as the tube grows this 'periodicity' is lost and the (6,5) adsorption energy becomes stronger than that of the (9,1). The (10,2) cap has the strongest energy in the second addition, and it follows closely the adsorption curve of (6,5) up to the sixth step, where the (10, 2) energies become weaker. The most irregular curve is the one for (6, 6), which follows an oscillatory pattern having very strong adsorption energies at the first, third, sixth and

tenth steps. These points correspond to situations where the (6,6) symmetry is recovered by completion of a new hexagon.

The oscillation period increases as the cap grows. For instance, there are two steps between the first and third minimum energy points and four steps between the sixth and the tenth steps. This is because as the nanotube is growing it takes more additions to recover the optimal geometry. The (7,5) cap shows good adsorption energies even outdoing the (6,5) in several steps before the sixth; after that point its adsorption energies are weaker. Thus, in average it could be said that there is a better energetic response to the C_2 addition for the near-armchair than in the near-zigzag caps. It is also observed that the C_2 adsorption energy tends to become weaker and more independent of chirality as the nanotube grows.

3.5. Conclusions

In summary, armchair and near-armchair caps facilitate thermodynamically and kinetically C_2 additions to their rim sites, offering more alternative reaction paths than near-zigzag caps do. The specific nanotube growth pattern of armchair and near-armchair caps may determine the growth of vertically aligned nanotubes, whereas near-zigzag caps may tend to grow tubes with an inclination with respect to the substrate. Findings are in agreement with the relative abundance of armchair and near-armchair tubes in CO decomposition CVD methods, and suggest that besides C_2, other species such as individual C atoms or C_3 species may be operative in the growth mechanism when CH_4 is used as precursor gas.

4. EFFECT OF METAL CLUSTER-CAP INTERACTIONS ON THE CATALYZED GROWTH OF SINGLE-WALL CARBON NANOTUBE*

4.1. Summary

Density functional theory is employed to investigate the interactions between a nine-atom cobalt cluster and single-wall carbon nanotube caps with chiral angles ranging from near zigzag to armchair. With the aim of analyzing the initial stages of nanotube growth, the caps used in our study are the minimal units for which chirality can be defined. Electrostatic potential maps, atomic charges, and electronic density of states are analyzed for the individual caps and cluster and for the cap/cluster coupled system to detect changes triggered by the cap/cluster interactions. It is observed that the metal cluster becomes oxidized, and significant changes are detected in its geometry; such changes are dependent on the cap chirality. Strong electrostatic interactions are found between the cap rim atoms and the cobalt atoms in contact with them. However, the bonding orbitals involved in such strong interactions are dominated by inner rather than by frontier orbitals, which are the ones that most likely would be able to participate in nanotube growth reactions. Among other findings, our results suggest that armchair and near-armchair systems should be the most favored when the growth mechanism is dominated by reactions such as C_2 addition to the cap rim atoms.

4.2. Introduction

Single-wall carbon nanotubes (SWCNTs) possess great technological importance as widely reported [89-92]. One third of the population of nanotubes is metallic, whereas the other two-thirds are semiconductor, but for some applications it is necessary a homogeneous mixture of either type [93-96]. The chiral indexes (*n*,*m*) determine the degree of helical twist of the graphite lattice along the nanotube axis[74], where the term chirality is derived from the left and right-handed helicity of the tubes defined by their

* Reprinted with permission from Diego A. Gomez-Gualdron, and Perla B. Balbuena, "The effect of metal Cluster-Cap interactions on the Catalyzed Growth of Single-Wall Carbon Nanotubes", J. Phys. Chem. C, 113, pp 698-709, (2009). DOI: 10.1021/jp808457j.

chiral indexes (*n*,*m*) and (*m*,*n*) respectively [97]. Since the chiral angle or chirality is related to the nanotube electronic, physical, and chemical properties, specific applications require production of nanotubes with a narrow distribution of chiralities. [96, 98-101].

SWCNTs are produced by various different methods [77]; among them, the chemical vapor deposition (CVD) methods are based on the catalyzed decomposition reaction of a C-containing precursor gas. The catalyst is usually a transition metal and the reaction proceeds at relatively high temperatures (about 1000 K) and moderate pressures [78]. One of the main challenges in the nanotube production process is the control of the chirality during the nanotube growth. Chirality selectivity is likely due to a combination of factors, making difficult the process of isolating and studying the effect of a single factor and even to determine if such effect is real. Despite this difficulty, it has been reported that some CVD synthesis processes are able to produce SWCNTs of selected chiral angles, especially in the near-armchair and armchair range, but currently, the reasons for such selectivity are not clear [20, 79].

The abundance of (*n*,*m*) species in the CoMoCAT process using Co nanocatalysts over Mo−carbide surfaces deposited on SiO_2 or MgO substrates has been found dependent on temperature--which in turn influences diameter--and on the nature of the substrate [20]. Optical absorption analyses show that on SiO_2 substrates, at temperatures between 700 and 800 °C, ~50% of the tubes are of the near-armchair (6,5) type, followed by ~30% of (6,6) and (7,7) armchair tubes and relatively small amounts of (8,4), (7,5), and (7,6) near-armchair tubes. As temperature increases to 850 °C, the percent of the smallest (6,5) tube decreases significantly. It is also interesting that the relative percentages of abundance change significantly, shifting the distribution toward the largest near-armchair tubes when a different substrate (MgO) is used at a relatively low temperature, 750 °C [20].

The fairly high selectivity of the CoMoCAT synthesis makes it adequate as a model process to be investigated in computational studies. Molecular simulation techniques are very useful (provided that the chemistry model is good enough) in the

attempt of isolating different factors believed to be involved with the chirality selectivity, mainly because they allow a thorough systematic observation not possible to be achieved experimentally. We believe that in a given process some factors can favor and others alter the growth of a given chirality, but in the end, it is the sum of the factors what will determine which chirality outgrows the others.

Even when the reaction mechanism of the catalyzed nanotube growth is very complex, we assume root growth, which has been suggested from experimental and theoretical studies [17, 102]. A critical point in the selection of chirality during the root-based process is the nucleation stage. It is generally accepted that caps nucleate at the beginning of the nanotube growth reaction, emerging from the small metal catalytic clusters involved in the reaction [78]. Due to the difficulties associated with experimentally observing the birth of the nanotube, the nucleation stage is generally studied theoretically [102-104], although HRTEM observations have been reported as well [16, 17]. A possible growth mechanism has been described in previous reports [70, 80]: carbon atoms dissolve inside the cluster and eventually lift-off outside the cluster initially forming a "minimal" cap. This minimal cap is defined as a collection of six pentagonal and a number of hexagonal rings arranged according to the isolated pentagon rule [75], which usually closes one of the nanotube ends during the growth process.

In this work, we focus on a system composed by a model catalyst particle and a minimal cap. Even when in many cases a (n,m) nanotube can be closed by several different cap structures, a given minimal cap can grow only into a unique (n,m) tube [76]. We hypothesize that three main factors affecting selectivity might be either intrinsic to cap features, related to the specific reaction mechanism, or determined by the minimal cap/catalyst nanoparticle interactions. Moreover, it is expected that the growth conditions must be also conditioned to the nature of the catalyst/cap interactions even when their exact relation to chiral selectivity is not clear yet.

It is the purpose of this work to study how the electronic and geometric properties of a cobalt cluster (Co was selected because of its use in the CoMoCAT process) and those of a minimal chiral cap might be affected when the cluster/cap

interaction takes place. Thus, we first describe the individual minimal caps and metal cluster to provide an insight on the features that would make the coupled system compatible and for further comparison to such coupled system. Density functional theory (DFT) was used to perform the simulations. The caps were selected from various chiralities ranging from armchair to near-zigzag ((6,6), (6,5), and (7,5), because of their abundance; and (9,1) and (10,2) due to their scarcity in the synthesis product). For the metal cluster we use Co_9, which contains the minimum number of atoms able to cover the cap rim for caps of small diameters (0.75−0.87 nm).

Other authors have studied such interaction using flat surfaces [47] or single atoms [103]; however, evidence from HRTEM [16, 17] pointing out to the existence of a small group of metal atoms active during the nucleation stage and also to the presence of defective rather than perfect catalyst surfaces suggests that a metal cluster may be a better model to understand the nature of the metal/cap interaction at the initial stages of growth. We describe the changes in the distribution of electronic density and in the cluster geometry induced by the chemical/electronic nature of specific cap chiralities, and we point out and discuss the differences of these changes for the distinct chiralities as they provide insights about the origin of the chirality selectivity. We also study the orbital population, especially of the frontier orbitals as they are related to the reactivity of the system.

4.3. Computational methods

To account for quantum effects in the nanotube growth, ab initio calculations using DFT with the three-parameter Becke [56, 81] gradient-corrected exchange functional in conjunction with the Lee−Yang−Parr correlation functional [57] (B3LYP) were carried out using the Gaussian 03 software [82]. The B3LYP functional has been widely used to describe similar interactions [105-114]. In particular, Polestshuk *et al* [112] reported a very detailed study of metal−benzene interactions involving a comparative analysis of the electronic structure and diabatic and adiabatic dissociation energies using a series of multiconfigurational methods such as multiconfigurational quasidegenerate perturbation theory (MCQDPT) and complete active space self-consistent field (CASSCF) among

others, as well as a group of single-configuration methods including Moller−Plesset second-order perturbation theory (MP2) and two DFT methods: B3LYP and PBE. It was concluded that B3LYP offers the best representation among the single configuration methods, outperforming both MP2 and the PBE functional, and yielding dissociation energies close to those of the best multiconfigurational method. Thus, we are confident that the B3LYP results are reasonably accurate and at least they should offer a good platform for comparison between the metal/cap interactions for caps of different chiralities, which is the main goal of this work.

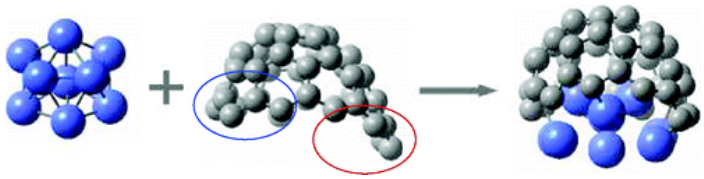

Figure 4-1. Structures of a nine-atom Co cluster and minimal caps of selected chiralities are optimized separately, and in a combined form.

The basis set 6-31G was used for the carbon atoms, whereas the LANL2DZ basis set and effective core potentials that incorporate relativistic effects [60, 61] were used for the cobalt atoms. The LANL2DZ provides a reasonably accurate description of the electronic structure of transition metal atoms as shown in numerous reports [115-117]. The first stage was the search of minima for the separate cluster and minimal caps. The starting structures for the optimization of the minimal caps were created using the CAGE program [75] following the isolated pentagon rule [90]. Different spin states were tested for the minimal caps; the triplet was the most stable one. A typical minimal cap can be observed in **Figure 4-1** (center). For the upcoming discussions we named some parts of the minimal cap. The outermost 'circumference' of the minimal cap is called the 'rim', while the rest is called the 'body' of the cap.

When the minimal cap is directed so it matches a vertically aligned nanotube the upper-half of the rim (circled in blue in **Figure 4-1**) is called the 'rear', whereas the lower half of the rim (circled in red) is called the 'tip'. The initial structure of the Co

cluster was built from FCC bulk Co; and optimized first with PM6 [118, 119] exploring several initial geometries and then with DFT methods. Different spin polarizations were also tried for the cobalt cluster; although the geometry dependence on the spin was negligible, the most stable electronic configuration was one with 17 unpaired electrons.

The initial geometry of the coupled system is shown in **Figure 4-1**, the optimized nine-atom Co cluster was located filling out the inner space of the cap. This cluster size has proven able to grow a nanotube structure using the reactive force field described in. [72], and briefly introduced in Section 2. Molecular dynamics-calculated structures grown with different cluster sizes are shown in the *supplementary information* in [88]; the quality of the grown nanotubes is similar for the different sizes. On the other hand, even if a larger cluster (~1 nm diameter) may be required for an adequate dissolution of carbon from the feedstock, HRTEM studies reveal that only a small number of atoms of such larger cluster directly interact with the minimal cap [17]. On the basis of this, we postulate that the Co_9 cluster used in this work is appropriate to provide a comparative study of the cap/cluster interactions for different cap chiralities. Both the cap and cobalt cluster separate optimizations were performed using tight convergence criteria (10^{-8} accuracy) for the self-consistent field (SCF) iterations. The optimization of the combined system was carried out at full criteria for forces and displacements, but the SCF calculations during optimization were performed with a tolerance of 10^{-6}; therefore, to increase the accuracy of the calculations somewhat further, single-point calculations were done with the tight convergence criteria on the previously optimized geometry.

The interaction energy for the coupled system shown in **Figure 4-1** is calculated as follows**:**

$$E = E_{cluster+cap} - \left(E_{cluster} + E_{cap}\right) \qquad (4-1)$$

This interaction energy is calculated with the purpose of comparing the interaction strength of the minimal cap and the cluster as the chirality varies. For each case, the cohesive energy of the cluster is estimated taking the final geometry of the

coupled system, removing all the cap atoms, and performing a single point calculation to obtain the energy corresponding to such geometry using the equation:

$$E_{cohesive} = \frac{n(E_{cobalt}) - E_{cluster}}{n} \qquad (4-2)$$

The cohesive energy reveals the strength of the Co−Co interactions and how it is affected by the interaction with carbon. This energy could be relevant since the 'fluidity' of the cluster might affect the diffusive motion of carbon atoms on the surface and inside the metal cluster during the catalytic process. The atomic charges are calculated according to the Merhz-Kollman scheme [120] to fit the electrostatic potential. The spin density is calculated according to the Mulliken population analysis [121]. Density of states (DOS) of the individual systems, partial contributions of the different molecular fragments to the DOS, as well as populations of the molecular orbitals, and overlap populations between molecular fragments were calculated using the AOMix software [122, 123]. We focused on contributions to the DOS of the cluster, cap rim, and cap body considered as distinct molecular fragments.

4.4. Results and discussion

4.4.1. Smallest chiral unit

As mentioned earlier, the key elements that determine chirality selectivity could be intrinsic to the nature of the cap or they could be governed by cap/cluster interactions; these aspects may gain or lose relevance depending on the growth reaction mechanism. In this subsection, we describe features of the minimal caps (from now on referred as 'caps') before they interact with the metal cluster. Additional information respect to the properties of caps in this study has been reported recently [124]. **Figure 4-2** compares the electronic density of states for the *armchair* (6,6) and for the *near-zigzag* (9,1) caps. The symmetry of the armchair cap is somewhat reflected in its electronic distribution, where the α and β density of states closely follow each other, and in consequence the lowest unoccupied molecular orbitals (LUMO) α/β are very close to each other, and so are the highest occupied molecular orbitals (HOMO) α/β levels (**Figure 4-2**, top). This

α/β gap at the HOMO or LUMO is of the order of 0.05 eV for the (6,6) cap, and it is also low for the near-armchair caps (7,5) and (6,5) with maximum values of the order of 0.13 eV except by the LUMO of the (6,5) whose α/β gap is 0.59 eV.

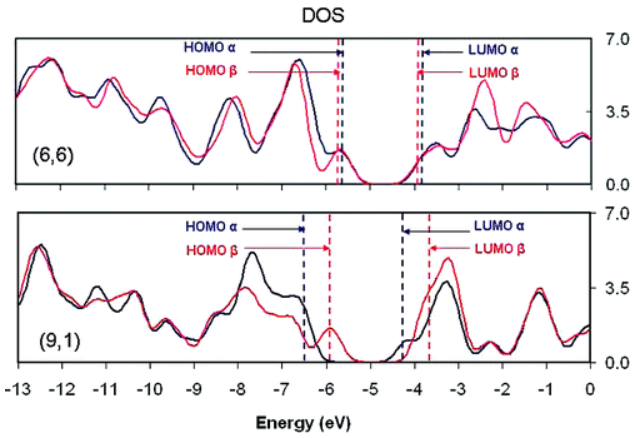

Figure 4-2. Electronic DOS of the (6,6) armchair cap (top) and the near-zigzag (9,1) cap (bottom). The α DOS is drawn in blue, whereas the β DOS is colored red. The HOMO and LUMO levels are marked by the vertical dashed lines; the color code is maintained as for the DOS curves. Notice how close are the α and β levels in the highly symmetric (6,6), whereas they split apart for the (9,1). Also, the dominant spins of the frontier orbitals appear inverted in the (9,1).

The frontier LUMO and HOMO orbitals provide information about reactivity of a molecular system. In a complex reaction such as the nanotube growth, which may involve a number of free radicals, it is likely that not only the LUMO and HOMO are involved, but also nearby orbitals. Our analysis suggests that *near-armchair* caps may have a large number of orbitals with energies similar to the LUMO and HOMO since both α and β orbitals have comparable populations around those energy values.

On the other hand, for a *near-zigzag* cap (**Figure 4-2**, bottom), the contribution around the LUMO is solely done by one kind of spin−orbital with an α/β gap of the order of 0.50 eV, thus a smaller number of potentially reactive orbital states are available at the frontier energy levels. Although at this point it is not clear how spin might affect growth, it is interesting to notice that the population of (9,1) cap spin states at the LUMO and HOMO levels have an opposite trend to those of the other caps studied, i.e. the

HOMO in (9,1) is dominated by β spin electrons (minority spin), whereas the (9,1) LUMO is dominated by α electrons.

In a later subsection we analyze the difference of the interactions between the cap body and the cap rim with the metal cluster. In the root-growth mechanism, the rim sites have great importance since the nanotube growth will proceed through them, but also the same sites will be exposed to the metal atoms. A difference is expected between the rim and body reactivities, otherwise lifting of the cap surrounding the cluster would not occur; this is also suggested by studies done for parameterization of MD force fields for nanotube growth [72].

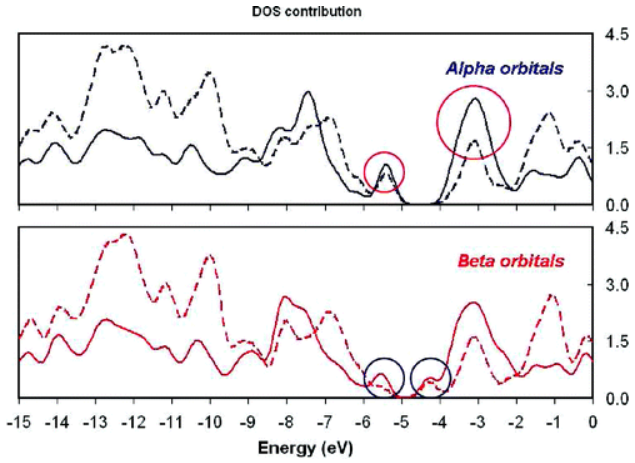

Figure 4-3. Partial DOS for α spin (top) and β spin (bottom) in the (6,5) cap. The peaks corresponding to frontier orbitals are circled to highlight the highest contribution of the rim atoms (solid line) compared to the rest of the cap atoms (dashed line).

Figure 4-3 shows the partial DOS of the rim and body atoms of the *near-armchair* (6,5) cap. The behavior of the DOS is similar for both α spin (top) and β spin orbitals (bottom). The atoms of the cap body dominate the inner energy levels (<−8.6 eV), whereas the rim atoms only contribute about 30%. At intermediate energies, between −8.6 and ≈ −6.0 eV, there is approximately equal population of the energy levels from the rim and the body atoms. Most importantly, at the HOMO and LUMO levels (circled in **Figure 4-3**) the rim DOS curve goes over the one for the atoms of the cap body contributing about 60% of the total DOS; this is even more relevant in account

of the smaller number of atoms in the rim than in the body, confirming that the cap rim is much more reactive than the body.

4.4.2. Metal cluster

A description of a Co_9 cluster is done in this subsection; the original geometrical features are examined so changes can be pointed out in the coupled cap/cluster system. The optimized cluster structure is shown in **Figure 4-4**. Co_9 consists of three layers, the bottom one composed by A, B, C, D, and E atoms; the middle layer by atoms F and G, and the top layer by H and I. The mean Co−Co bond length is ~2.6 Å, which is larger than the bond length in the cobalt dimer calculated at the B3LYP/LANL2DZ level (2.0 Å), but close to the 2.51 Å of the *a* parameter of the HCP unit cell of bulk Co [125]. A, B, C, and D form a rectangular frame with side lengths ~4.1 and ~2.6 Å, and atom E is located at the intersections of the rectangle diagonals. The DEC and AEB angles are about 120°, so the ABCDE plane resembles a typical (111) FCC plane. Bulk Co is an HCP structure, [125] but it has been found that small clusters of diameters lower than 20 nm tend to adopt FCC structure [126], and similarly at temperatures above 450 °C [127]. However, the optimized structure of Co_9 is neither FCC nor HCP. The tetragonal packing of the cluster is revealed by the frequency of occurrence of ~60° angles shown in **Figure 4-4**.

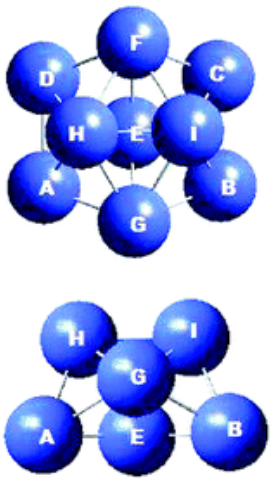

BOND LENGTH (Å)	
A-B	4.14
A-D	2.57
B-C	2.58
C-D	4.17
A-G	2.56
B-G	2.57
C-F	2.57
D-F	2.58
G-E	2.50
F-E	2.50
D-E	2.48
C-E	2.45
B-E	2.44
A-E	2.44
H-F	2.56

BOND LENGTH (Å)	
H-G	2.57
H-I	2.57
H-D	2.57
H-A	2.63
I-F	2.57
I-G	2.56
I-C	2.59
I-B	2.59

ANGLE (degrees)	
A-D-C	88.0
D-C-B	88.3
C-B-A	91.6
B-A-D	92.0
D-E-C	119.2
A-E-B	113.6
D-E-A	63.2
C-I-B	58.9
D-H-A	58.8
G-I-B	59.0
A-H-G	59.1
F-I-C	60.1
D-H-F	62.1
H-G-I	59.9
H-F-I	59.9

Figure 4-4. Co_9 top and side view, and geometric information. Atoms A, B, C, D, and E constitute the bottom layer; F and G the middle layer; and H and I are in the topmost part of the cluster.

The distance between the bottom and middle layers is 1.34 Å, and that between the middle and top layers is 0.81 Å. The cluster has two symmetry planes perpendicular to each other and to the ABCDE plane. The first plane passes through the atoms F and G, and the second symmetry plane passes through atoms H and I. A binary symmetry axis is centered at and normal to the H−I bond.

The cohesive energy of Co_9, calculated according to Equation 4-2, is 1.77 eV/atom, much lower than the 4.39 eV/atom experimental value of bulk Co [128]. This will determine a decrease in the cluster melting point and a more flexible structure especially at high temperatures such as those of the catalytic synthesis (~750 °C) that will facilitate the migration of C atoms inside the cluster, as well as their diffusion to the surface [80]. Although the cluster in the real process is set on a substrate, which restricts its mobility, the lack of thermal effects in our 0 K simulations would offer restrictions to the free cluster that may compensate the absence of the substrate in these studies.

Table 4-1 shows the charges fitted to the electrostatic potential and the spin multiplicity on each cluster atom. The cluster reveals a slight polarization; the most negative charge is on the central atom E whereas A, B, C, and D have somewhat positive charges so a radial polarization is observed on the bottom layer. F and G have smaller positive charges compared to the atoms beneath; H and I have a low negative charge that makes the cluster compatible with the interior of the nanotube cap as explained later. Nevertheless, the behavior of the cluster when exposed to the cap interaction is mainly dictated by polarization about atom E. Another feature related to the electronic distribution is the spin density; it is seen that the cluster has a fairly homogeneous distribution of spin density and an equal partition of unpaired electrons (there is an excess of the majority spin electrons in all atoms).

Table 4-1. Electronic charges and spin density on the Co_9 atoms.

Atom label	Charge (e)	Spin density	Atom label	Charge (e)	Spin density
A	0.055	1.83	F	0.043	1.94
B	0.067	1.91	G	0.012	1.92
C	0.079	1.91	H	-0.013	1.96
D	0.077	1.83	I	-0.014	1.97
E	-0.308	1.71			

4.4.3. Cluster/cap coupled system

4.4.3.1. Polarization effects

This subsection starts with a description of the electrostatic potential (ESP) around the separate cap and cluster that illustrates the electronic compatibility between them. ESP maps on total density isosurfaces are shown in **Figure 4-5** for the (9,1), (7,5), and (6,5) caps, and for Co_9. In agreement with the charges displayed in **Table 4-1**, **Figure 4-5** shows a negative potential on top of the cluster and positive potential in its bottom corners. On the other hand, the cap potential is positive inside and negative in some rim sites. Therefore, the favorable interaction between Co_9 and any of the caps arises from the matching negative cluster top/cap interior, and from that of the cluster corners/cap rim. A change in the cluster geometry could result in different polarization features anticipating less or more affinity with the cap. The different polarization strengths visualized in **Figure 4-5** correlate with the dipole moment of the caps: 3.27 D for (7,5), 2.99 D for (9,1), and 2.29 D for (6,5).

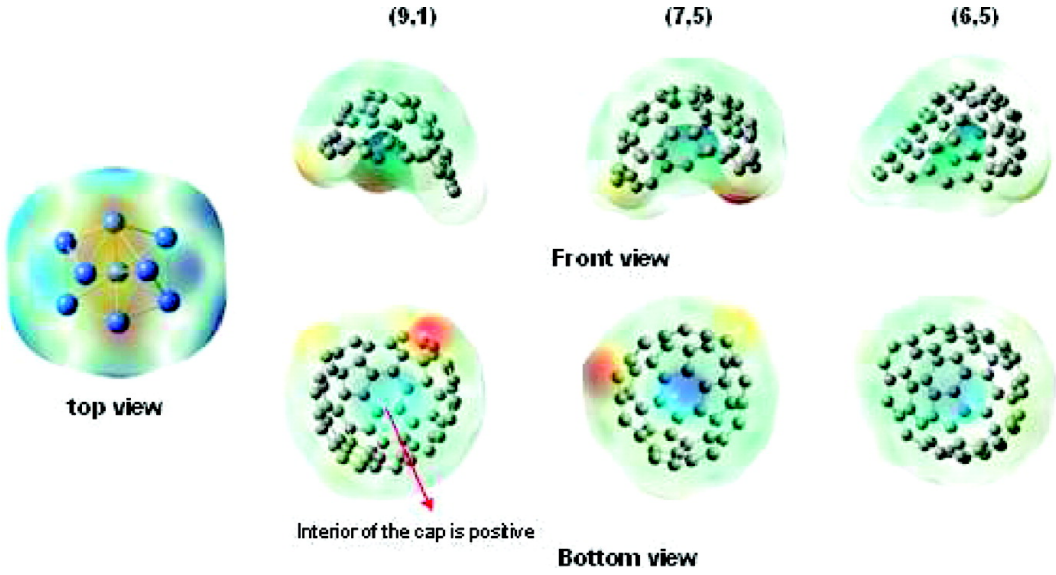

Figure 4-5. Electrostatic potential (negative, red; positive, blue) mapped on total density isosurface (0.0004 electrons/(a.u.)^3) for Co_9 and (9,1), (7,5), and (6,5) caps. The negative top part of the cluster offers a perfect fit for the positive region in the interior of the cap.

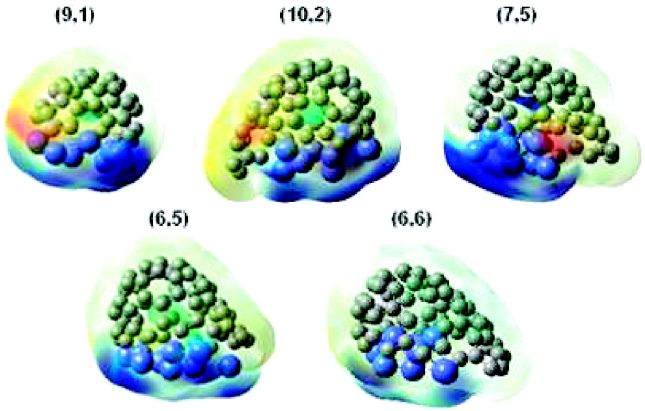

Figure 4-6. Electrostatic potential mapped on an electron density isosurface (0.0004 electrons/(a.u.)^3) for various cap-Co_9 systems. Notice how the polarization of the system decreases as the chiral angle increases from zigzag to armchair.

Although no clear correlation was found between chiral angle and polarization for the isolated caps (**Figure 4-5**), the ESP maps in the cap/cluster system shown in **Figure 4-6** do suggest a trend since the polarization is larger for the near-zigzag (9,1) cap and decreases as chirality approaches the (6,6) armchair cap. In fact, the

(6,6)/cluster pair has the lowest dipole (0.9 D), whereas, (9,1)/cluster and (10,2)/cluster have dipoles 7.0 and 7.8 D each. The higher dipole found for (10,2)/cluster compared to (9,1)/cluster is perhaps due to cap diameter differences. An additional insight on how the electronic cloud is distributed between cap and cluster can be gained looking at the orientation of the dipole vector. After optimization, one of the axes points from the cluster toward the inner part of the cap, with the dipole component in this direction being the one showing the largest cap/cluster charge separation, originated by oxidation of the cluster.

4.4.3.2. Cap/cluster interaction strength

Continuing our analysis of the coupled system, we evaluate the interaction strength of each cap with the metal cluster. The cap/luster interaction energies calculated using Equation 4-1 are shown in **Table 4-2**. As expected, these interaction energies depend on cap chirality, suggesting that *in the initial stages of nanotube growth* some of these caps may be more favored than others. Other studies have also revealed differences in the interaction of different chiralities with metal substrates; for example, Reich *et al* reported the variation of the interaction of caps with a flat Ni surface [100]. Our results indicate that the interaction energy of the (6,5)/Co_9 pair is the largest one among the group studied, whereas the (9,1)/Co_9 pair has the second one.

Table 4-2. Interaction energies (eV) calculated according to Equation 4-1, and cohesive energies (eV) calculated according to Equation 4-2 of the DFT fully optimized coupled systems Co_9-SWCNT cap.

Cap chirality	Interaction energy	Cohesive energy
(6,6)	-10.44	1.62
(6,5)	-15.36	1.32
(7,5)	-12.27	1.44
(10,2)	-13.04	1.39
(9,1)	-13.68	1.44

Certainly, due to their small diameter, the interactions of (6,5) and (9,1) caps with Co_9 might be the largest of this group of caps; however, the difference of 1.68 eV between the two of them is significant because both of them have the same diameter.

The energetic differences among the various chiralities are expected to be reduced as the metal cluster size increases. This does not mean that solely changing the cluster size the chirality can be controlled, since other factors may also play a role. For instance, the (7,5) and (10,2) diameters are larger than that of the (6,5), but the energetic difference of more than 2 eV between either one and the (6,5) might not be totally removed if the metal cluster size is increased assuming that the main interactions are given only by a small set of atoms.

However, the cluster size may indirectly induce an effect on chirality distribution as follows. Experimental results have suggested that the tube diameters increase when they are grown on larger clusters. An increase in the cluster size broadens the chirality distribution [20], but wider nanotubes have larger number of caps to grow from; therefore, increasing the chances that each chirality will be able to have at least one 'competitive' cap to start the growth from.

Diffusion effects could also have an impact on the growth rate. If the carbon species dissolve in the cluster before emerging to the surface and growing the cap, a higher diffusion rate would allow a more rapid growth. Thus, if diffusion rate differences arise from different cap chiralities, these could lead to selectivity. To prove this point, we recall that the weaker is the binding between metal atoms, the easier it is for a foreign species to diffuse through the structure (provided no reaction occurs). Indeed, after interaction with the (6,5) cap, the metal cluster has the lowest cohesive energy; thus, the weakest metal/metal interaction (**Table 4-2**). We note that changes in the cluster geometry could have effects both on the cap/cluster interaction and metal cohesive energies, as shown in **Table 4-2**. Zigzag rim terminations interact more strongly with the metal atoms than armchair terminations [103]; therefore, the basis for the larger interaction energy for the pair (6,5)/Co_9 might be the higher number of zigzag sites--10 for a (6,5) cap--interacting with cobalt atoms.

4.4.3.3. Evolution of the cluster geometry

The reorganization of the cluster is less drastic for near-zigzag systems than for near-armchair ones. For near-zigzag cases, it consists of the opening of the cluster while

basically retaining their relative position and original polarization pattern. For instance, in the (9,1)/Co_9 pair, the EFG symmetry plane is retained while the cluster flattens and the three original layers are no longer distinguishable. Similarly, in (10,2)/Co_9 the AED symmetry plane appears but the symmetry around the EFG plane is only slightly distorted, whereas the polarization pattern is also maintained. The distances EG, EC, and ED for (9,1) and ID, ED, and GD for (10,2), which go beyond 3.0 Å, show that some Co atoms gather around specific sites in the cap rim but one or two atoms are torn apart due to stronger metal/carbon than metal/metal interaction. With respect to characterization of cap/cluster interaction, the inverted curvature of the final cluster reveals the very weak interaction between metal and carbon atoms coordinated to three other carbon atoms.

In the case of near-armchair caps the relative initial positions are distorted, the overall migration of the cluster toward the 'rear' part of the cap shows the high activity of that zone. In (7,5)/Co_9, the cluster resembles a stepped surface (CEBGD one terrace, AFHI the other one), whereas for (6,5)/Co_9 the cluster becomes a defective (111) FCC monolayer. From **Figure 4-7**, changes in the polarization patterns can be observed. We suggest that these changes in the metal cluster geometry and polarization are the result of the effect of the surface mirroring the cap chirality. That is, chiral surfaces or clusters are needed to match chiral rims, and the generation of such chiral surfaces may be determined both by the effect of the growing cap and by the nature of the substrate over which the metal cluster is deposited. On the other hand, the highly symmetric (6,6) has barely deformed the cluster, but the polarization only occurs in the corner of the cluster interacting with the rim. On the basis of the observed low deformation of the cluster, the use of a highly symmetric cluster might be more suitable for the epitaxial growth of armchair tubes. The distribution of Co−Co distances before and after the interactions with caps is shown in **Figure 4-8**. The average Co−Co distance increases significantly from 3.18 Å in Co_9 to 4.61 Å for the (6,5)/Co_9, followed by 4.07 Å for the (7,5)/Co_9, 4.03 Å for the (10,2)/Co_9 and 3.91 Å for the (9,1)/Co_9, and 3.36 Å for the (6,6)/Co_9, the least affected system.

(6,6)

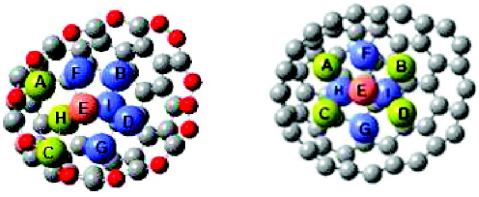

Label	Charge	S. Density	Charge C	
A	0.460	1.41	-0.628	-0.691
B	0.165	2.02		
C	0.507	2.31	-0.627	-0.557
D	0.197	2.13		
E	-0.255	-2.49		
F	0.061	1.98		
G	0.066	1.90	-0.795	
H	0.308	2.05		
I	0.066	1.97		
Total	1.515			

(6,5)

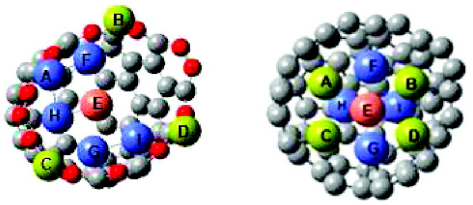

Label	Charge	S. Density	Charge C	
A	0.186	1.98		
B	0.415	2.16	-0.713	-0.642
C	0.326	2.00	-0.413	-0.263
D	0.390	2.08	-0.629	-0.696
E	-0.096	2.01		
F	0.253	1.95	-0.713	
G	0.097	1.94	-0.685	
H	0.191	1.92	-0.430	-0.709
I	0.257	2.00		
Total	2.019			

(7,5)

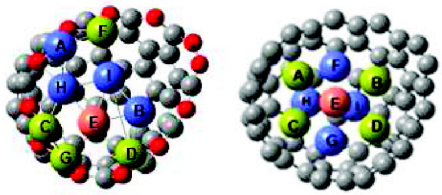

Label	Charge	S. Density	Charge C	
A	0.117	1.92	-0.224	
B	0.139	1.92		
C	0.217	1.67	-0.091	
D	0.423	2.07	-0.874	-0.798
E	-0.238	1.84		
F	0.276	2.02	-0.527	
G	0.484	1.14	-0.581	-0.419
H	0.122	1.87	-0.224	-0.091
I	0.109	1.71		
Total	1.649			

(10,2)

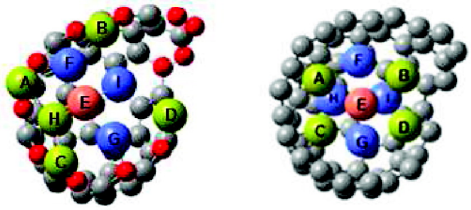

Label	Charge	S. Density	Charge C	
A	0.345	1.99	-0.855	-0.567
B	0.451	2.27	-0.693	
C	0.383	0.12	-0.909	-0.262
D	0.567	2.37	-0.551	
E	-0.043	1.94		
F	-0.016	1.74	-0.720	
G	0.201	2.09	-0.642	
H	0.332	1.79		
I	0.025	1.69		
Total	2.245			

(9,1)

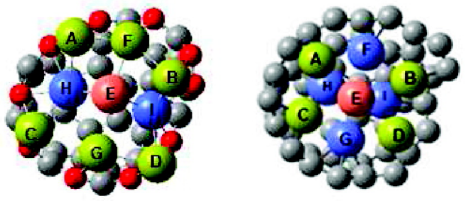

Label	Charge	S. Density	Charge C	
A	0.117	1.92	-0.607	
B	0.139	1.92	-0.503	-0.636
C	0.217	1.67	-0.858	-0.770
D	0.423	2.07	-0.520	
E	-0.238	1.84		
F	0.276	2.02		
G	0.484	1.14	-0.786	
H	0.122	1.87	-0.607	-0.770
I	0.109	1.71		
Total	1.649			

Figure 4-7. Geometric evolution of the cap/cluster systems after optimization (final configurations given by left, initial by right images). The cluster atoms are labeled as in Figure 3-4.The most positively charged atoms are highlighted in yellow, the intermediate positive charges are blue, and light red is used for the negatively charged. Also, in the left image, the red C atoms are those located at the shortest distances from the Co atoms, and their charges are listed in the last two columns. The spin density distribution shows that most of the atoms bear a higher concentration of the majority spin electrons, whereas only the central metal atom (E) carries a negative spin density (indicating predominance of the minority spin) in the more symmetric armchair (6,6) system.

Summarizing the geometrical analysis, the cluster loses its original shape and spreads maximizing its interaction with the caps rims, these geometric changes are more evident in the (6,5). The opening of the cluster reveals that metal/metal interactions are weaker than metal/rim carbon interactions. The weak interaction of the cap body (carbon coordinated to three carbon atoms) with the metal atoms results in the absence of cobalt atoms inside the cap; this feature is consistent with the observed lifting-up of the cap during nanotube growth. Similar results that will be reported elsewhere have been obtained with a larger Co_{15} cluster. The interaction rim/cluster is based on electrostatic attraction between cobalt and carbon atoms. Those carbon atoms are zigzag sites, the strength of this interaction is found to be the largest for (6,5) (10 zigzag sites interacting with the cluster), and the lowest one for (6,6) (which barely has contact with the rim sites).

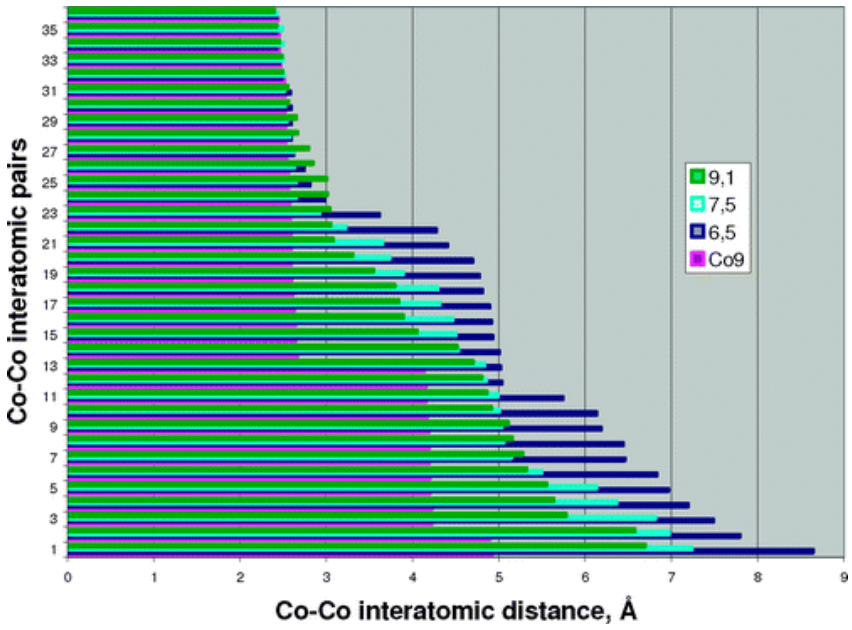

Figure 4-8. Co−Co interatomic distances for all pairs in the original Co_9 cluster (pink bars) are compared with those after the cap-cluster system is coupled. Note that in the original cluster a large number of Co−Co distances are in the range 2.5−2.6 Å (length of the horizontal bars), and significant increases take place after interactions with the caps, the largest differences are found for the near-armchair (6,5) and (7,5) caps.

With the insights gained from the above analyses, we remark that the cluster adopts different shapes to best fit each chirality. Therefore, we suggest that there could be a cluster shape-dependence of the cluster/cap interaction. This aspect can gain relevance in synthesis processes such as CoMoCAT [79], where the size and shape of the metal cluster are believed to be set during the stage of catalyst preparation (calcination, reduction, heating), hence it is likely that those chiral species abundant in the final product are somehow favored by the geometric features that the metal clusters have right in the initial stages (induction period) [80] of the synthesis process.

Another important observation connected to the synthesis process is the general tendency for the cobalt atoms to interact with the cap rear rim sites suggesting the high activity of this zone. Identifying the most active sites of the cap is an important detail that becomes useful when analyzing the kinetic reaction pathway generated by the attack of new species (C, CO, CO_2, Co, C_2, and others). In the armchair caps the rear zone contains sites where the growth can start by forming a new hexagon by attachment of a C_2 radical as shown in Section 3. The set of reactions for the nanotube growth are complex, but taking an overview on electronic distribution and orbital population can give us some useful insights about the reactivity and kinetic of growth, and possible differences among the chiralities, as explained in the next subsection.

4.4.3.4. Orbital analyses

As previously mentioned, the mechanism by which nanotubes grow might vary under certain conditions such as temperature or nature of the reactants. It has been reported that changing the carbon source (methane or carbon dioxide) can alter the selectivity shifting the production from majority near-armchair to majority near-zigzag [20]. Despite mechanistic differences, the orbitals involved in a reaction should still be HOMO and LUMO and their closest ones. The reaction mechanism for nanotube growth might change on the basis of specific localization of the HOMO/LUMO orbitals of the coupled cluster/cap system, and a given mechanism might be more or less favored by specific locations of the frontier orbitals.

Figure 4-9 shows the LUMO and HOMO orbitals for the various cap/cluster pairs. In order to analyze the most important contributions to the frontier orbitals, an isovalue of 0.03 a.u. was used to draw the orbitals. For the chiral caps (no armchair included), the HOMO is localized on the tip of the cap, this localization is more accented in (9,1)/Co_9. Only in the (6,5)/Co_9 and (9,1)/Co_9 pairs is the HOMO partially localized over some of the Co atoms. This might occur because of the small size of (9,1), as shown in **Figure 4-7**, since no rim part is left bare due to the spreading of the Co atoms. Therefore, since the HOMO is located on the tip, overlap with some Co atoms is expected. This does not hold for (6,5) since some part of the rim atoms in the tip are not in contact with Co atoms. It is interesting that despite the presence of the electron cloud typical of metals, the cobalt contribution to the HOMO orbital is very small, as seen for the almost null presence of the HOMO on the cluster (**Figure 4-9**, top); thus, the cluster would be less favorable to nucleophilic reactions. The (6,6)/Co_9 differs from the other pairs in that it is the only one having the HOMO mainly located in the cap rear and specifically on the rim atoms.

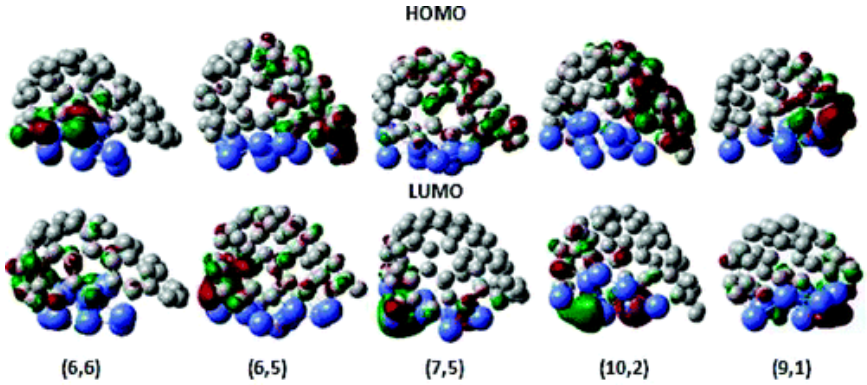

Figure 4-9. LUMO and HOMO orbitals of the coupled system nanotube cap-Co_9. The chirality of the cap at the left is armchair, and the chiral angle decreases toward near zigzag chiralities from left to right.

On the other hand, as the chiral angle increases from zigzag to armchair the observed trend is the change of the LUMO location from the metal cluster to the cap. Under the hypothesis that the growth of the nanotube should occur mainly by adding C_2

radicals to the rim sites, it would be optimum for the LUMO to be localized on a site where the addition of radicals may complete a new hexagonal ring (rear for armchair caps, tip for zigzag caps); thus, the near-armchair caps having a favorable LUMO location would be favored in the C_2-based growth. This advantage would be higher for (6,6) and (6,5) than for (7,5), since on the (7,5) part of the LUMO is localized on the cluster and part located on the rim, close to the site active for C_2 addition (i.e., the site where C_2 completes an hexagon). Thus, it is reasonable to expect that growth would require that neither the LUMO nor the HOMO orbitals would be located on the cluster, since the metal atoms should stay nonreactive in order to avoid the formation of stable carbides or other stable compounds that may hinder nanotube formation. In the (6,6), (6,5), and (7,5) naked caps the LUMO does not locate exactly on the site active for C_2 addition [124], but this mismatching is removed by the presence of the metal atoms and could be one of the many roles of the cluster to facilitate the nanotube growth.

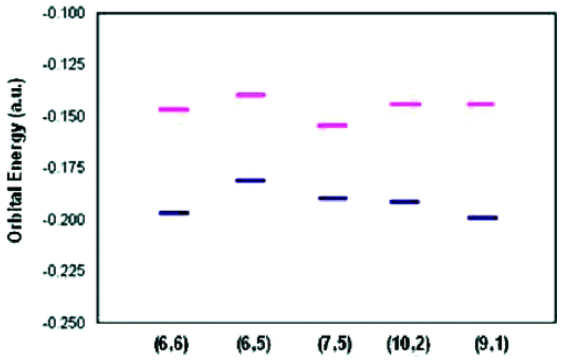

Figure 4-10. Energetics of the HOMO (blue line) and LUMO (pink line) orbital for the systems cap-Co_9 cluster is displayed. The chiral angle decreases from left to right. Notice that the systems with the cap (6,5) and (7,5) have the lowest gap between HOMO and LUMO.

The (6,5) cap has the lowest LUMO among the naked caps, where there is no cluster effect. So if the growth would proceed in absence of the cluster the (6,5) cap appears to have advantage over the other caps for C_2-based growth because the cap-LUMO/C_2-HOMO gap is smaller. However, the (6,5)/Co_9 LUMO appears to be the highest one of the cap/cluster pairs. Their HOMO/LUMO energetics is shown in **Figure**

4-10. Not only has the (6,5)/Co_9 system the highest LUMO but also the highest HOMO. However, in presence of the metal cluster the set of growth reactions and steps should be more complex that just adding C_2 to the cap rim; therefore, it is difficult to know if in the initial steps of the reaction the orbital involved is LUMO or HOMO.

In order to analyze the orbital population and to find chirality-related trends, we discuss the electronic density of states (DOS). **Figure 4-11** displays the DOS for the (6,5)/Co_9, and (10,2)/Co_9as examples of near-armchair and near-zigzag systems. It is found that the partial DOS (dashed line) of the cluster atoms dictates the shape of the total DOS (solid line) (bottom figures). For instance, the α-DOS (blue)/β-DOS (red) shift follows the same pattern as the cobalt atoms partial DOS. This shift is larger than that detected in the naked cap DOS (**Figure 4-2**), and it can be assigned to the much higher spin polarization of the cap/cluster system (17 unpaired electrons) the one for the cap (two unpaired electrons). Although one may expect these unpaired electrons to belong to the cluster, being loose and contributing to the frontier orbitals, **Figure 4-11** reveals that the highest DOS peaks do not correspond to the frontier orbitals, but to the internal orbitals (although the ones close to HOMO and LUMO).

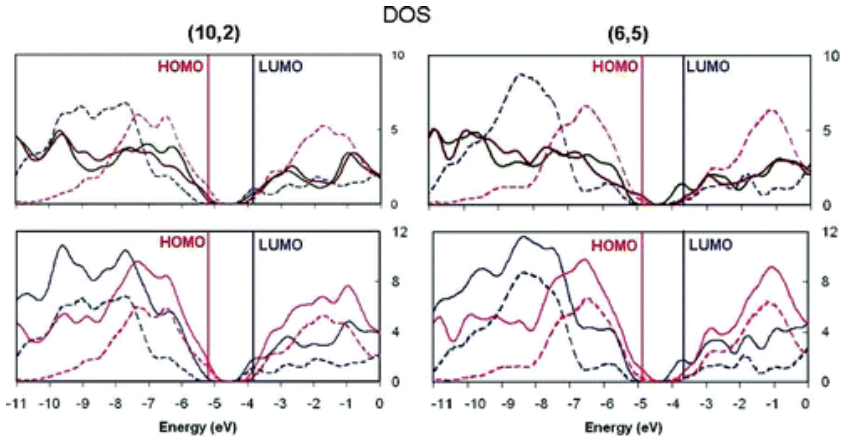

Figure 4-11. Bottom: total (solid line) and partial DOS (dashed line) of cobalt atoms for cap/cluster systems with the (10,2) cap (left) and (6,5) cap (right), α spin in blue and β spin in red. Top: Partial contribution of cobalt (dashed lines, same color code as in bottom figures) and carbon atoms (solid lines, olive green for α spin; maroon for β spin).

Also, the β levels tend to be more energetic than α ones so there is a larger density of high energy levels for the minority spin. Accordingly, the HOMO is a β orbital while the LUMO is a α orbital. One important detail is that the cap rim is still more reactive (despite of the interactions with cobalt) than the cap body since their partial DOS (not shown) reveal a higher contribution of the rim to HOMO/LUMO than those from the cap body (exactly as in the discussion of **Figure 4-3**). A reactive rim supports root-growth mechanism.

In the same line of thought, it is reasonable to expect that during nanotube growth the cap would be more reactive than the cluster (so the cap actually grows). It is interesting that **Figure 4-11** (top) shows that for near zigzag caps (as depicted for (10,2)) the cobalt contribution to the HOMO/LUMO is higher than the respective contribution of carbon atoms, whereas for the near armchair (as illustrated for (6,5)) the carbon atoms contribute more than cobalt. This may be one of the contributing factors for the high abundance of armchair over zigzag tubes. The features of **Figure 4-11** are in agreement to what was observed in **Figure 4-9**, with the location of the LUMO orbital changing toward the rear of the cap as the chiral angle was increasing from ~0° (near-zigzag) to ~30° in the near-armchair.

Finally, we carried out an overlap population DOS (OPDOS) analysis [122, 123] in order to understand the nature of the cobalt/rim interaction. Some examples are displayed in **Figure 4-12** for the (6,5) cap/cluster system, in particular the interaction of the atoms B, A, and E (see **Figure 4-7** for the atom labels) with the rim. Notice that in the HOMO and LUMO zones, the interaction between cobalt and rim atoms does not exist or is negligible. These results suggest that HOMO and LUMO are in fact involved in different functions than the interaction between cobalt and rim atoms; thus, the reactivity of the systems is kept, while the bonding of Co and C atoms is assumed by more internal orbitals. Notice also that the overlapping of β orbitals is stronger than that of α orbitals.

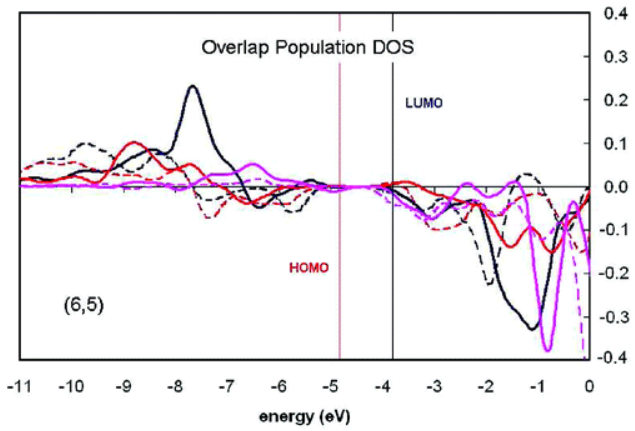

Figure 4-12. Overlap population of the DOS (OPDOS), for the (6,5) cap and selected cobalt atoms: B (blue), A (red), and E (pink); the labels correspond to Figures 4-4 and 4-7. Solid lines correspond to β orbitals, and dashed lines to α orbitals. Positive values denote bonding interactions, negative to antibonding, values very close to zero indicate not interaction at all [122, 123].

4.5. Conclusions

Analyses of the DOS of the naked cap atoms show that the cap rim is the most reactive zone of the cap, which remains true even after the cap interacts with the cluster, supporting root-growth mechanism. The cap/cluster interaction appears to be of electrostatic nature, as suggested by the observed good matching of the electrostatic potential on top of the cluster with that of the interior of the cap.

After the two individual systems are coupled, changes observed in the cluster geometry depend on the cap chirality, which might support the engineering of epitaxial selective nanotube growth since certain chiralities would be favored by particular cluster geometries. Some evidence to support this hypothesis has been recently provided by experimental work [16, 17], and our own computational effort in this direction is in progress.

The metal cluster shows low reactivity, as evidenced by the absence of HOMO/LUMO orbitals located over the cluster atoms; this might facilitate SWCNT growth by promoting the diffusion through instead of reaction of carbon species with the metal cluster. The diffusion of such species is favored by the cluster low cohesive energies, which together with the cap/cluster interaction energy are found to be dependent on the chirality of the cap. The cap/cluster interaction energy was found

larger for (6,5) apparently related to the higher number of zigzag sites interacting with metal atoms; such strong interaction has electrostatic origin.

The spreading of the cluster reveals that metal/metal interactions are weaker than metal/rim carbon interactions, but metal/metal interactions are stronger than metal/body carbon, and this combination should be necessary for lifting of the cap. Analysis of the orbital overlap population shows that such strong $Co{-}C_{rim}$ interactions are dominated by inner rather than by frontier orbitals so the reactivity of the rim atoms for further nanotube growth reactions is maintained.

Common features for all the systems include the oxidation of the cluster atoms, the modification of the 3-D structure of the initial cluster to a 2-D or to a flatter 3-D structure and the correlation of the decrease of the coupled cap/cluster system polarization with the increase of the chiral angle. Considering a C_2-based growth, the LUMO orbital, expected to participate in the C_2 addition reaction for nanotube growth, is located in a more favorable part of the cap rim for near-armchair than for near-zigzag caps, and independently of the reaction mechanism, analysis of the DOS of the coupled system reveals that for the near-zigzag systems the metal atoms contribution to the frontier orbitals is higher than that of the C atoms, and the opposite behavior is found for the near-armchair coupled systems, implying that the C atoms in the near-armchair caps may be have a better predisposition for continuation of the nanotube growth reaction.

In summary, our analysis provides a series of new insights regarding the possible role of the catalyst atoms in the nanotube growth process, suggesting that the armchair and near-armchair systems should be the most favored when the mechanism is dominated by reactions such as C_2 addition to the rim atoms.

5. GROWTH OF CHIRAL SINGLE-WALL CARBON NANOTUBE CAPS IN THE PRESENCE OF A COBALT-CLUSTER*

5.1. Summary

Density functional theory is used to simulate nanotube growth by addition of a pair of carbon atoms to a composite chiral nanotube cap/cobalt cluster system, with caps corresponding to near-armchair (6, 5), (7, 5) and near-zigzag (9, 1) nanotubes. Two different carbon addition processes are evaluated: in the first, the new carbon atoms are located in the vicinity of the armchair site of the cap rim, and thus this process provides insight into the root-growth mechanism; in the second the carbon atoms are initially located under the cobalt cluster, and thus this process helps one to evaluate the dissolution of carbon inside the metal cluster. The geometric evolution and energetics of the system are used to explain features of the mechanism of nanotube growth. The root-growth reaction is shown to occur by displacement of a cobalt atom initially interacting with the armchair site while the added carbon atoms bond to each other forming a new hexagonal ring, whereas the carbon dissolution process shows formation of dimers inside the cluster only for the (6, 5) system. The energetics for both steps reveals that the dissolution stage is probably controlling the overall nanotube growth rate.

5.2. Introduction

Nanotechnology constantly seeks the discovery and development of new materials with potential applications in wide-ranging fields such as medicine, nanoelectronics and energy production. Since their discovery in 1991 [1], carbon nanotubes have shown very interesting mechanical and electronic properties suitable for such applications [89-91, 93, 94, 129], converting them in one of the flags of nanotechnology development [130, 131]. There are many types of nanotubes featuring from single to multiple walls and various degrees of helicity, so during the last decade, research has focused on producing controlled synthesis conditions with the goal of obtaining uniform nanotubes

---

* Diego A. Gomez-Gualdron, and Perla B. Balbuena. "Growth of chiral single-walled carbon nanotube caps in the presence of a cobalt cluster", Nanotechnology, 20, 215601, (2009). DOI:10.1088/0957-4484/20/21/215601. Printed with permission of the Institute of Physics (IOP).

[10, 11, 42, 132, 133]. This objective has been partly achieved, and now several laboratories report the use of carbon vapor deposition (CVD) on catalytic metallic nanoparticles favoring nearly 100% single-walled carbon nanotubes (SWCNT) over multi-walled carbon nanotubes and carbon nanofibers [26, 134-136].

Currently, the bottleneck to the further development of SWCNT technology is the control of the so-called 'chirality' of the nanotubes produced, which itself is hindered by the lack of a thorough and detailed understanding of nanotube growth. Chirality, designated by the chiral indexes (*n,m*) [97], is a very important feature, because the properties of the SWCNTs—in particular electronic and optical properties— strongly depend on it, and therefore its control would lead to a more specialized design of nanodevices. The trial-and-error quest for a selective catalyst—*toward chirality*—has ended up in a few fairly selective processes [44, 137, 138], wherein the CoMoCAT synthesis [79] outstands for its enhanced production of near-armchair (6, 5) nanotubes [20]. Further improvement is expected to be achieved in a more systematic fashion, based upon a better understanding of the nanotubes growth process, which in general terms is believed to include the catalytic decomposition of a C-containing precursor gas, dissolution of carbon in the nanoparticle followed by atomic diffusion leading to a nucleation stage [22, 102, 139] of preliminary C-species over the catalyst prior to sustained nanotube growth.

Even though some experimental studies, especially the use of high resolution microscopy, reveal impressive details on the nucleation stage [17, 38], when chirality selection most likely takes place, understanding the exact SWCNT growth mechanism and its relation to chirality only by experimental tools is difficult because of the small scale of the process and the wide span of involved factors: temperature, pressure, catalyst, substrate, precursor gas, catalyst size, pretreatment, among others. Thus, molecular simulations are valuable tools to obtain additional and complementary details of this stage. In fact, currently some molecular dynamics (MD) codes using reactive force fields are able to reproduce the main qualitative details of the growth process [70, 72, 140, 141]. On the other hand, quantum mechanical density functional theory (DFT)

is useful to study the interplay between the SWCNT's and the metallic catalyst, either represented by a surface [31, 47], a cluster [88, 103, 142] or even a single atom [143].

The main drawback of this more accurate approach is the high computational cost as the simulated system becomes more realistic. Thus, a way around on this problem is breaking the problem into pieces; accordingly, we follow the approach of studying one by one the factors believed to have effect on chirality selection. Recently, we reported the addition of carbon dimers (C_2 radicals) to the smallest structure of a capped SWCNT for which chirality can be assigned—*minimal cap*. We found that besides being more stable, near-armchair caps have intrinsic geometrical features that might make them outgrow near-zigzag caps—under this mechanism, due to increase in the number of sites active for reaction among other factors (Section 3)[124], in agreement with high abundance of near-armchair SWCNT's in some CVD processes [20].

We also investigated (Section 4) [88] the interaction of chiral caps with a cobalt cluster and found that formation of (6, 5) caps during nucleation might outdo the occurrence of other caps because the particular cap/cluster electronic interactions may lead to electronic configurations that favor carbon addition to the rim sites. In the present paper, we make an effort to test a more realistic situation using the knowledge gained in previous studies by performing DFT calculations of the addition of a pair of carbon atoms to a rim armchair (*ac*) site once the cobalt cluster is interacting with a chiral cap, in positions that resemble either the dissolution of carbon inside the nanoparticle or the surface diffusion of carbon over the metal cluster just prior to the addition of a new ring to the nanotube structure. We expect that if we are able to link new theoretical and experimental results that reveal what determines the formation of a chiral tube, we may start to get hints on how chirality might be controlled.

5.3. Computational methods

Full DFT optimizations were performed using the package of programs Gaussian 03 [82]. We used the three-parameter Becke gradient-corrected exchange functional [56, 81] in conjunction with the Lee–Yang–Parr correlation functional [57] (B3LYP), whose

suitability for representing carbon/metal interactions is discussed in Section 4, and [88]. The molecular orbitals are formed by combination of the 6–31g basis set [144] for carbon atoms, and the LANL2DZ for cobalt atoms [60, 61]. The latter includes effective core potentials incorporating the relativistic effect and gives an accurate description of the electronic structure of transition metals [115-117]. A density-based convergence criterion of 10^{-6} was used for the self-consistent-field calculations during optimizations, which were followed by single point calculations using a 10^{-8} threshold.

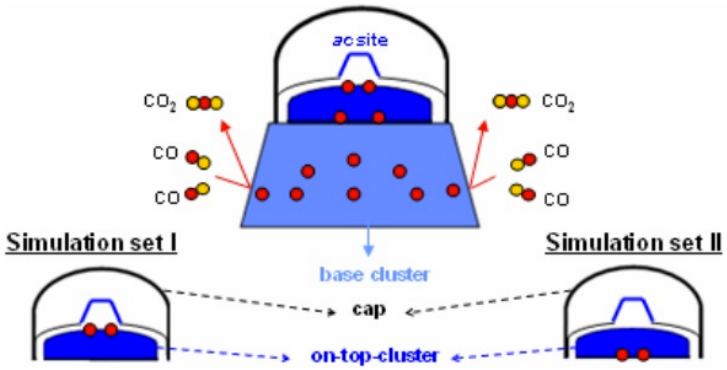

Figure 5-1. Schematic of the reaction mechanism under which our simulations are based. The central figure displays the metal catalyst composed by a base cluster (light blue) and on-top cluster (dark blue). The small on-top cluster contains the active sites where it is assumed that nucleation and growth of the SWCNT takes place. A nascent nanotube cap with an ac site in its rim is shown on top of that cluster. We assume that the CO precursor gas reaches the base cluster where it is decomposed yielding elemental carbon atoms (red spheres) that diffuse through the cluster until they reach the on-top-cluster and pop-up on the surface in the neighborhood of the ac site. Simulation set I focuses on the 'root-growth' reaction, and simulation set II is designed to analyze the dissolution of carbon in the cluster.

The addition of carbon was done to three fully optimized cap/cluster systems selected from our previous work (Section 4) [88]. The criteria for such selection is to examine a highly abundant—(6,5), a somewhat abundant— (7,5), and a scarce chirality—(9,1)—so we can observe how the chiral structure may influence the C addition in our proposed computational experiments. This implies a two-fold strategy: (1) screen the scenarios that are likely to favor nanotube growth, (2) figure out factors relevant to chirality selection. This is done under the premise of a specific reaction

mechanism schematized in **Figure 5-1**, wherein we analyze two specific situations for which simulation sets I and II are prepared.

The initial scenario for our simulations assumes that nucleation has already occurred in a CVD-like process; therefore it comprises the minimal (*n,m*) cap in contact with cobalt atoms. From that point on, the growth of the SWCNT occurs by formation of new hexagonal rings on available rim sites under a root-growth mechanism. Simulation set I tests this hypothesis; two carbon atoms are initially located in the neighborhood of the *ac* site. **Figure 5-2** displays an isolated (6, 5) cap with an *ac* site consisting of four carbon atoms where addition of a carbon dimer creates a new hexagonal ring and one additional *ac* site (or more depending on the chirality) [88].

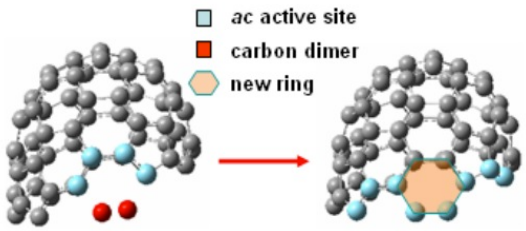

Figure 5-2. An active four-atom-armchair (ac) site in an isolated (6, 5) cap reacts with a carbon dimer (C_2 radical) so a new hexagonal ring is completed. As a result, new ac sites suitable for reaction are created, in this case one at each side of the new ring. In this paper, we analyze the effect of the presence of the catalyst atoms on this reaction.

Here we are interested in analyzing the competition for this *ac* site that may take place between the carbon just added and cobalt atoms of the cluster already interacting with the rim, and if there are specific differences on how this process occurs for distinct chiralities. The size of the present cobalt cluster (nine atoms) does not represent the complete nanoparticle in the experimental process, instead is emulating a small protrusion (on-top cluster in **Figure 5-1**) that appears to nucleate over the nanoparticle (base cluster in **Figure 5-1**), leading to its local deformation, as shown by HRTEM images [17]. This cluster-on-top-of-cluster configuration (**Figure 5-1**) supports the use of only a few metal atoms to study the metal/rim interactions with the nucleating structure.

In simulation set II (**Figure 5-1**) two carbon atoms are initially located underneath the metal cluster, and the objective is to understand how these atoms are dissolved in the on-top cluster already covered by the nascent cap and how this dissolution process is affected by the cap chirality. We note that the size of the nanoparticle does affect the solubility of carbon into the cobalt cluster as it occurs for other carbon– metal systems [36], however in simulation set II there are only two carbon atoms, which should provide a reasonable model for evaluation of their interaction when surrounded by cobalt atoms, and how this interaction is indirectly affected by the cap chirality. This second simulation set intends to reveal insights of the dissolution stage prior to the reaction with the rim. The energetic of carbon addition in simulations sets I and II is calculated in reference to the original cap/cluster system (A) and a carbon dimer (B) using the following equation:

$$E_{bindng} = E_{total} - (E_A + E_B) \qquad (5-1)$$

The use of the energy of a carbon dimer in Equation 5-1 is arbitrary since a dimer is not the initial form of the pair of carbon atoms added, but since the main purpose is comparative this fact does not intervene in our goal of screening differences among the three chiral systems.

5.4. Results and discussion

5.4.1. Geometric evolution of the systems in simulation set I

As previously mentioned, this simulation set is intended to get insights on the hypothetical root-growth mechanism. Under this mechanism the closed-end of the nanotube is free while the open-end is in contact with the metal nanoparticle, the growth occurs at the rim of the open-end as suggested in **Figure 5-2** for the isolated cap, where the (6, 5) chirality was shown to be favored over other chiralities[124]. However, in presence of the metal catalyst, the carbon atoms need to break the carbon–metal (C_{rim}–M) bonds, in particular those close to the *ac* site. The ease for this bond-breaking to happen depends on the relative strengths of the C_{rim}–M and C_{rim}– C interactions and how accessible the *ac* site is while the rim interacts with the cluster; both factors depend on

the cap chirality. For instance, in our simulations, that accessibility depends on the deformation suffered by the cobalt cluster when it gets in contact with the cap.

Such deformation is dictated by the cap chirality and thus on the geometry of the rim, which at the stage of the minimal cap (Section 3) [124] is mainly composed by zigzag (*zz*) sites. We focused attention on the *ac* site based upon the following reasons: (i) addition of two carbon atoms to this site readily completes a new hexagonal ring, (ii) the interaction of *zz* sites and metal are reportedly stronger than the interaction of *ac* sites and metal [103], therefore in *ac* sites it would be easier to break the C_{rim}–M bond. The ideal strength of the carbon/metal interaction for optimal nanotube growth is unknown, therefore understanding its role on specific reaction steps might help clarify the growth mechanism and in turn lead to chirality control.

Figure 5-3 shows the evolution of systems in the simulation set I from their initial molecular geometry (left) to their final one (right). The initial positions of the two new carbon atoms added depend on the position of the cobalt atoms. For instance, on the near-armchair (6, 5) and (7, 5) rims one cobalt atom (Co_{ac}) accommodates in the *ac* site (light blue atoms) forming a planar–pentagonal–heterocyclic ring with their four carbon atoms, the C_{rim}–Co_{ac} bond length being 2 Å and the C_{rim}- C_{rim} bond length 1.5 Å. Thus, we placed the two new carbon atoms (red spheres) one at each side of Co_{ac} equidistantly at 1.4 °A from it and from the closest *ac* C_{rim} atom. The four atoms of the *ac* site, the cobalt atom and the two new carbon atoms (C) initially form a planar seven-member ring (for the two near-armchair cases) that might be regarded as an activated complex. The C–C distance at the beginning of the simulation is 2.7 Å, so initially they are not bonded to each other and the existence of a carbon dimer is not forced in the simulations.

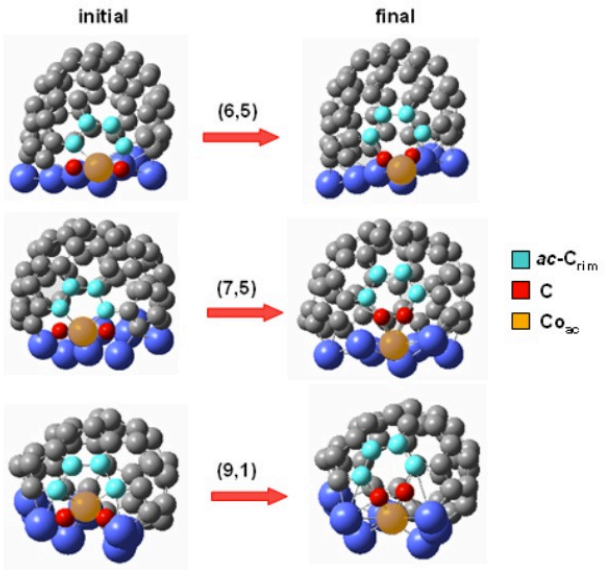

Figure 5-3. Initial and final geometries of the systems in simulation set I. The atoms of the ac active site are highlighted in light blue, the carbon atoms added to the system in red and the cobalt atom initially interacting with the ac site in orange. The other carbon atoms are gray and the other cobalt atoms are blue. The highlighted atoms lay on a common plane, except for (9, 1) where the highlighted cobalt is out-of-plane toward the center of the cap interior.

For (9, 1), the situation is slightly different, the four *ac* C_{rim} atoms and the Co_{ac} form a pentagonal ring in envelope configuration with the Co_{ac} atom in the apex and pointing inward, while the C_{rim}–Co_{ac} bond length is 2.1 Å. This configuration leaves the *ac* site free; however the C atoms were initially located equidistantly at 1.6 Å from the corresponding closest *ac* C_{rim} atom and from the Co_{ac} atom. The initial C–C distance between the two added carbon atoms was 2.1 Å so the new ring is not formed yet. It was not possible to set the initial C–C distance at 2.7 Å as previously done with (6,5) and (7,5) because of C overlap with neighboring Co atoms. The evolution of the described configurations suggests that: (i) there is an equilibrated competition for the new C atoms between the cluster and the *ac* site, (ii) the C atoms initially have clear contact with the cluster reflecting the fact that the cluster acts as carrier and diffusion medium of the carbon species obtained from decomposition of the precursor gas—even for the (9, 1) system, (iii) the formation of a new hexagonal ring is not biased. **Table 5-1** summarizes the change of bond lengths and distances between atoms involved in this root-growth-

like scenario upon optimization of the systems, which complements the visual information from **Figure 5-3**.

Table 5-1. Geometric information of the initial and final configurations of the simulations in set I shown in Figure 5-3.

System	Pair	Initial distance (Å)	Final distance (Å)
(6,5)	C-C	2.7	1.5
	C-C_{rim}	1.4	1.5
	C-Co_{ac}	1.4	2.0
	C_{rim}-Co_{ac}	2.0	3.1
(7,5)	C-C	2.7	1.4
	C-C_{rim}	1.4	1.4
	C-Co_{ac}	1.4	2.0
	C_{rim}-Co_{ac}	2.0	3.3
(9,1)	C-C	2.1	1.4
	C-C_{rim}	1.6	1.5
	C-Co_{ac}	1.6	2.3
	C_{rim}-Co_{ac}	2.1	3.1

One of the interesting findings in these simulations is the formation of the carbon dimer or so-called C_2 radical as the systems are allowed to relax. This occurs in spite of factors such as: (a) the high C–C separation at the beginning of the optimization, (b) the presence of a cobalt atom between the two C atoms as in the (6, 5) and (7, 5) systems, (c) simultaneous interactions with many cobalt atoms as in the (9, 1) system. The mechanism under which this occurs resembles superficial diffusion phenomena that are believed to be important in the nanotube growth process [28, 145]. In the simulations, the formation of the radical occurs simultaneously with the completion of the new hexagonal ring, this shows that even if carbon atoms diffuse individually through or over the nanoparticle, they might merge into a carbon dimer right before reacting with the *ac* site, thus supporting the hypothesis of a reaction mechanism based on the stepwise addition of C_2 radicals to the nanotube rim (Section 3) [124], in agreement with experimental studies suggesting the consumption of two carbon species such as acetylene [146].

It is worth mentioning that the diffusion process that brings together the two carbon atoms takes place at expense of the displacement of cobalt atoms in the cluster whose cohesive energy is debilitated by the strong carbon/metal interactions. It is known that metal nanoparticles have lower melting points than the corresponding bulk metal [36, 37, 147], therefore at the temperatures of the SWCNT growth process (about 1000 K), the nanoparticle is likely in a liquid-like state that allows local deformation of the cluster and enhances diffusion of carbon so the root-growth can occur in a similar fashion as in our simulations where the lack of a supporting structure enhances the 'fluidity' of the cluster.

On the other hand, the simulations show the strength of the carbon/carbon interaction once they have reached the cluster surface, (i.e. when they are no longer solvated by the metal atoms). For instance, **Table 5-1** illustrates that the C–C_{rim} distances kept constant at the beginning and end of the simulations; in fact, tracking this distance during optimization reveals that such distances were indeed unmodified during the geometrical rearrangement. This idea is reinforced by the formation of the carbon dimer. In contrast, **Table 5-1** also shows that the C– Co_{ac} and C_{rim}–Co_{ac} distances increased in all the simulations revealing the relative weakness of the carbon/cobalt bonding.

We note that the C–Co bond length calculated with the same functional/basis set is 1.56 Å. The weak C–Co interaction found in the composite system is explained in the basis of the nature of the carbon/carbon bonding which is covalent and accordingly strong, whereas the carbon/cobalt interaction is based on Coulombic attraction and therefore weaker [88]. This strength difference allows the displacement of the Co_{ac} from its original position interacting with the *ac* site, and the approach of the two carbon atoms forming a carbon dimer—which is evident in **Figure 5-3** for the (6, 5) and (7, 5) systems, and also refrains the redissolution of carbon into the cluster once the C atoms are close to the rim. Sometimes the displacement of the Co_{ac} is so abrupt that this atom is pushed out and even separated from the cluster as shown in **Figure 5-4** for the (6, 5) system.

Also, the increase of the C_{rim}–Co_{ac} distance additionally allows us to observe one important phenomenon for the SWCNT growth process, the lifting-up of the capped structure, which is perhaps more visually evident in the (7, 5) and (9, 1) cases. This phenomenon apparently occurs due to the very weak interactions between the cobalt and carbon atoms not belonging to the cap/nanotube rim. We found that during the addition of the dimer, the electronic charges of the non-rim carbon atoms of the cap are kept very close to zero in contrast to the charges of the rim atoms, in agreement with previous work [88], and validating the hypothesis of carbon/cobalt interaction based on electrostatic forces. The lifting-up observed in our simulations is an important detail for SWCNT growth since it avoids cluster encapsulation and subsequent death of catalytic activity. Therefore, the control and engineering of such electrostatic interactions that could be tuned by appropriate design of the catalytic surface might play a key role in the enhancement of growth for certain chiralities.

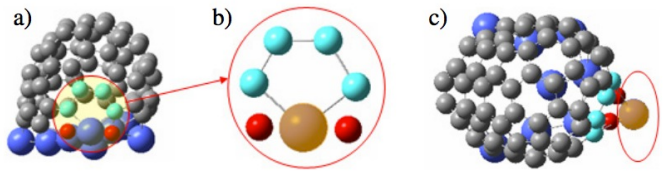

Figure 5-4. The carbon–carbon interaction is stronger than the cobalt–carbon interaction and breaks the Co–C_{rim} bond. For instance, the two newly added carbon atoms –C–(red) in (a) merge into a carbon dimer, complete a new hexagonal ring in the rim of a (6, 5) cap and displace the cobalt atom (orange) that was interacting in (b) with the ac site (light blue), as shown in (c).

Summarizing this subsection, the root-growth mechanism of SWCNT's is shown to occur by formation of carbon dimers in the vicinity of *ac* sites displacing the metal atoms previously interacting with the site, due to the strength of the covalent carbon/carbon interaction being higher than that of the electrostatic-based carbon/cobalt interactions. The accessibility of the *ac* site is dictated by the reshaping of the cluster previous to carbon addition, as determined by the geometric and electronic features of each chiral cap. In (6, 5) and (7, 5) the *ac* site is initially occupied by a metal atom from

the cluster—as opposed to (9, 1), and that metal atom facilitates the migration of the new carbon atoms toward the *ac* site.

5.4.2. Geometric evolution of the systems in simulation set II

As discussed in subsection 5.3, the simulations in this set are intended to gain insights about the dissolution stage and how it is affected by the cap chirality. At this point we have assumed that the catalytic active part of the nanoparticle or base cluster (the one not covered by the nanotube/cap) has already performed its task of decomposing the precursor gas, such as CO, and some elemental carbon is dissolved in the cluster and starts diffusing through it as schematized in **Figure 5-1**. The dissolution and diffusion through the base cluster is unlikely to be affected by the presence of the cap (it could more likely be affected by the nature of the substrate) and it may be analyzed by theoretical studies using metallic structures alone. However, once the carbon atoms reach the small on-top cluster their diffusive behavior is indirectly affected by the cap because of the cap/cobalt cluster interactions. It is at this point where the cap chirality comes into play since it influences the interactions with the metal cluster. Thus, we expect to find different behavior of the two dissolved carbon atoms as the chirality of the cap changes. Moreover, for some of the chiralities, the evolution of the carbon atoms inside the cluster might ultimately enhance the growth rate whereas for other chiralities it might worsen it. If this process is fully understood, it could be modified accordingly (for example modifying the catalyst geometry and/or chemical composition) to tailor the chirality of the nanotubes produced.

Figure 5-5 shows the frontal and bottom view of the initial and final geometries of the simulations in set II. Also, it shows the typical initial local configuration common to all the simulations: the cobalt atoms form a 'bridge' and the dissolved carbon atoms are placed one at each side of the bridge. Simulation set II is designed to get insights on details of the SWCNT process such as whether the carbon atoms dissolved inside the cluster are able to form chains or if they diffuse individually until reaching the nanoparticle surface and only then start forming chains. It is generally believed that the carbon/carbon interactions are debilitated inside the cluster because of screening effects,

in fact some reactive force fields that emulate SWCNT growth specifically damp this interaction when a carbon atom is mainly coordinated by metal atoms [72], however it is important to know if such screening is strong enough as to avoid the formation of carbon dimers, which were shown to be relevant to the growth reaction.

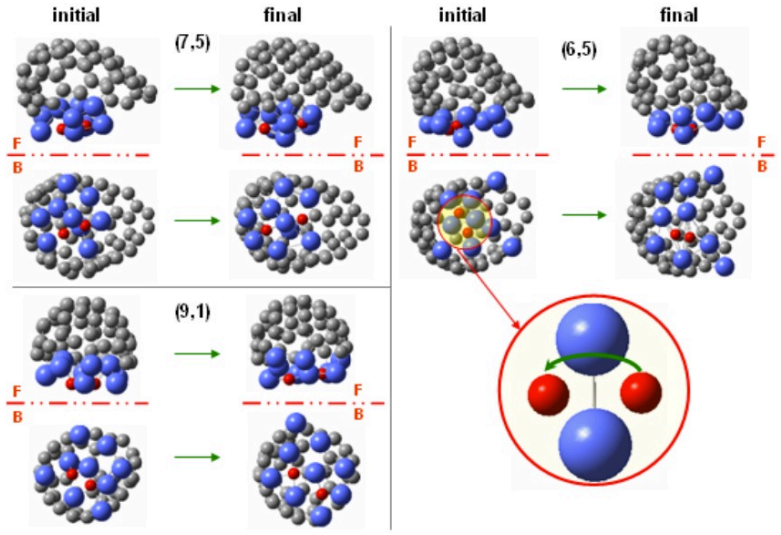

Figure 5-5. Frontal (F) and bottom (B) views of the initial and final geometries of the simulations in set II. Carbon is gray, cobalt blue, and the newly added carbon is highlighted in red. The schematic inside the red circle shows a typical initial local configuration of a simulation in set II, the Co atoms form a bridge, and the two C atoms are placed each at one side. If the C–C interaction is strong enough, the bridge is broken and a carbon dimer is formed as in (6, 5).

Figure 5-1 shows that the two newly added carbon atoms (red) were initially located underneath the small cobalt cluster (on-top cluster); therefore representing those C atoms that have just diffused from the 'base cluster' and enter the zone where the cap effects over the metal atoms are important. Notice, that at this point it does not matter if the carbon was supplied to the base cluster by direct dissociation of the precursor gas, or indirectly supplied by a substrate-like structure beneath the cluster as the molybdenum-carbide present in the CoMoCAT process [79], so our findings might be generalized. After locating the two new carbon atoms (C), and the systems were allowed to relax, we observe that the cluster starts to rearrange its geometry so the carbon atoms find themselves in a mobile environment as it is likely to occur in the actual process. The

visual information grasped with **Figure 5-5** is complemented with geometric data in **Table 5-2**. In an attempt to standardize the simulation all the initial configurations started with the C atoms (red) separated by 2.0 Å, and located in an interstitial position such that the local configuration shown in the inset of **Figure 5-5** is achieved. Also, the carbon atoms locate at a distance (1.5 Å) from the closest cobalt atom, which is generally either atom of the 'bridge', similar to the initial Co_{ac}–C distance in set I. This is done so the C atoms in set I, and set II receive similar influence from their interaction with cobalt. Such influence did not refrained the C atoms from merging each other in set I, however in set II, only in the (6, 5) system the two C atoms managed to merge, whereas they drifted apart in the (7, 5) and (9, 1) systems.

Table 5-2. Geometric information of the initial and final configurations of the simulations in set II. C-Co* corresponds to the distance from C to the closest cobalt atom.

System	Pair	Initial distance (Å)	Final distance (Å)
(6,5)	C-C	2.0	1.3
	C-Co*	1.5	2.0
(7,5)	C-C	2.0	3.2
	C-Co*	1.5	1.9
(9,1)	C-C	2.0	2.9
	C-Co*	1.5	1.8

This shows that the interactions of the cluster with the (6, 5) cap debilitated the Co–Co and Co–C interactions because of the stronger C–C interaction, in agreement with the low cohesive energy of the cluster found after interaction with the (6, 5) cap (Section 4) [88]. This explains the final geometry for the (6,5) in **Figure 5-5**, the low cohesive energy facilitates the breaking of Co–Co of the bridge, which brings the C atoms together (1.3 Å) and opens the cluster structure. On the other hand, it is reasonable to infer that if the Co–Co interaction is weak enough to facilitate the formation of the carbon dimer, then it also facilitates the diffusion of individual carbon atoms. Moreover, the final C–Co distance in the (6,5) system is slightly larger than for the other two, revealing a slightly weaker C–Co interaction in the former, suggesting a higher diffusion coefficient of carbon in cobalt clusters.

The results also suggest that the interactions with the (7, 5) and (9, 1) caps are not able to sufficiently debilitate the cluster, thus the 'screening effect' by the cobalt atoms is still strong enough to weaken the C–C interaction so the C–C distance increases to 3.2 Å and 2.9 Å respectively and the C atoms keep occupying interstitial positions. Also, the Co–C interaction appears to be stronger since the Co–C distances (1.9 and 1.8 Å) are equal to the typical distances of interactions between Co and *zz* sites, which are known to be strong. Thus, the findings in this section can be summarized as follows: the chirality of the cap does indirectly affect the behavior of carbon inside the cluster, the current simulations shows features for the (6, 5) system that likely favor the growth of SWCNT more than the ones found in the (7, 5) and (9, 1), such as formation of carbon species (C_2) directly involved in the growth reaction and suggesting a higher C diffusion rate through the cluster.

Regarding guidelines for chirality control, there seems to be necessary to achieve a balance in the strength of the interactions between the rim carbon atoms and the metal atoms, where the strength has to be high enough for lowering the cohesive energy of the cluster and enhancing diffusion, but also low enough so the displacement of the metal from the *ac* site is not hindered. The engineering of such interaction might be achieved by using distinct metal or metal alloys, but we emphasize that such catalyst design would only emerge from additional theoretical and experimental studies needed to develop a full picture of the role of the metal catalyst on the initial stages of the growth reaction.

5.4.3. Energetics of the systems

In the previous subsections we discussed the geometric rearrangement of the studied systems in simulation sets I and II and related them to the nanotube growth mechanism while pointed out some details probably associated with chirality selection. In this subsection we report the binding energy of the two newly added carbon atoms (C) to the systems as calculated by Equation 5-1. **Figure 5-6** shows a bar diagram with the magnitude of such energies for sets I (coarse-pattern), and II (fine pattern).

The calculated binding energies denote that the addition of the two carbon atoms to all the systems in either scenario (I or II) are energetically favorable. This shows the

viability of such configurations in the actual SWCNT growth process. On the other hand, the higher binding energies suggest that the scenario in set I is more stable than that in set II. Thus, dissolution of carbon inside the cluster is energetically favorable, but once the carbon atoms are inside they will tend to migrate to the surface of the cluster in the vicinity of the *ac* site where their location is the most stable. This difference in binding energies between the two sets is likely to generate a driving force promoting the migration of dissolved carbon toward the reaction sites.

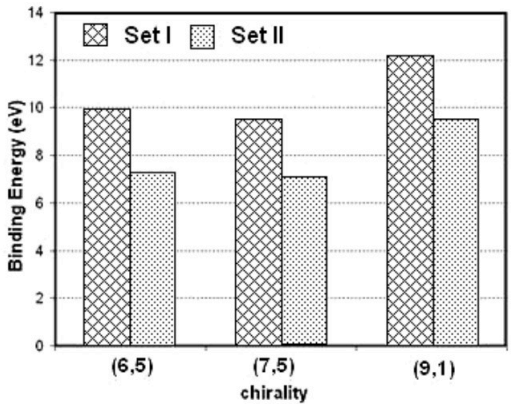

System	$E_{binding}$ (eV)	
	Set I	Set II
(6,5)	-9.7	-7.3
(7,5)	-9.1	-7.1
(9,1)	-12.1	-6.9

Figure 5-6. Bar diagram showing the magnitude of the binding energy calculated with Equation 5-1 for the simulations in set I, and II. Next to the graph, the data used to build the diagram is shown.

Moreover, it is possible (although not proven here) that as the dissolved carbon is closer to the cap–rim/cluster–surface boundary, the C– C_{rim} interactions are less damped by the screening effect of the cobalt atoms than the C–C interactions, so that the migration of dissolved carbon may be facilitated by the stronger interactions of the diffusing carbon atoms with the rim sites. However, the information about the activation barrier must be obtained to better understand the migration process and to find additional differentiating factors in the formation of nanotubes of different chiralities; even though such barriers are likely to be low given that the nanoparticle is in a liquid-like state at the temperature of the process. In the simulation set I, the (9, 1) system possesses the strongest binding energy, followed by (6, 5) and (7, 5). This is because the reorganization of the cobalt atoms before and after the formation of the new hexagonal

ring determines the redistribution of C_{rim}–Co interactions in the final state that enhances the binding energy as calculated by Equation 5-1. Reported data [31, 103] show that *zz* sites interaction with metal atoms is about twice stronger than that of *ac* sites.

Accordingly, we characterized the rim sites as schematically shown in **Figure 5-7**, assigning a reference value of 1 to *ac(1)*, 2 to *ac(2)* and *zz(1)*, and 4 to *zz(2)*, where the numbers in parenthesis indicate the number of Co atoms interacting with a given site. The table in **Figure 5-7** indicates how the number of C_{rim}–Co interactions change after the carbon addition (final state), and the increase of *zz(2)* sites in the (9, 1) systems in agreement with the enhanced binding energy in such system.

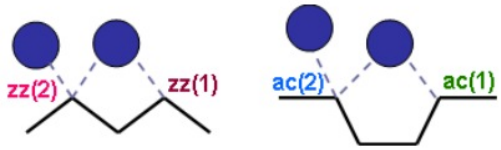

	(6,5)		(9,1)	
Site	initial	final	initial	final
zz(2)	5	3	4	5
zz(1)	2	2	4	3
ac(2)	2	4	2	1
ac(1)	0	0	0	1

Figure 5-7. Topology of the rim/cobalt interactions; the rim sites are named according to the geometry of the site (zz or ac) and the number of atoms it interacts with. Next to the graph, the initial and final number of such sites for the (6, 5), and (9, 1) systems is shown**.**

On the other hand, comparing the (6, 5) and (7, 5) system whose local configurations are identical (**Figure 5-4**b), the (6, 5) has a higher binding energy than the (7, 5) denoting that this reaction step is more favorable for the first system. However, according to our calculations (**Figure 5-6**), the primary step governing the overall growth reaction rate would be the dissolution step based because this step is energetically less favorable than the ring formation step. Accordingly, the overall growth rate might be higher for the (6, 5) chirality, followed by (7, 5) and (9, 1) despite of the high energetic values for the second step of (9, 1).

We finish this subsection by determining the effect of the presence of the cluster on the energetics of completing a new hexagonal ring in the cap rim. **Figure 5-8** compares such values between the simulation set I, and the ones obtained by addition of a carbon dimer to the plain cap in the *ac* site from our previous work (Section 4) [88]

(**Figure 5-2**). As discussed above, (9, 1) is the only system that increases this binding energy in presence of the cluster due to the formation of new C–Co interactions that were absent in the initial system. This does not occur for the (6, 5) and (7, 5) caps, where the binding energy decreases in presence of the metal cluster (as illustrated by **Figure 5-8**); this is expected because of the barrier arisen from the interaction of the new carbon atoms interact with each other and form a new ring with the rim atoms. However, as remarked before, the presence of the metal atom facilitates the carbon migration to the reaction site.

We note that the energetic trend in **Figures 5-6** and **5-8** (for the various chiralities, green bars) suggests also that the interaction energy between the new cap (with the additional ring) and the cluster follows an opposite trend as a function of chirality to the one found in our previous study (Section 4)[88]. The reason for this difference is that the previously reported interaction energy was calculated for the *minimal* (6, 5) and (9, 1) caps, which have identical diameters and almost identical rim configurations: seven (7) *zz* and four (4) *ac* sites in the (6, 5), and 7 *zz* and 3 *ac* sites in the (9, 1); therefore the energies represent the stability of the cap over the cluster in the stage of cap nucleation, with the (6, 5) found more stable than the (9, 1).

However, as soon as the C_2 addition reaction takes place, the rim configuration changes in each successive carbon addition (Section 3) [124], increasing the number of *ac* sites for the near-armchair (6, 5) cap, while keeping approximately the same rim configuration for the (9, 1), and the higher number of *zz* sites enhances the cap/cluster interaction energy of the (9, 1), as discussed above. Thus, once the cap is formed and the nanotube growth starts, a slightly lower cap/cluster interaction energy as found in (6, 5) due to the increase of the number of *ac* sites and decrease of the *zz* sites would favor the breaking of the C_{rim}–Co bond allowing the formation of new rings, and the reorganization of the cluster atoms. This hints that the growth of near-armchair chiralities may be intrinsically favored due to the increase of *ac* sites with weaker interactions with the nanoparticle. On the other hand, this analysis suggests that the less

expensive preliminary studies (without the metal atoms) (Section 3) [124] provide good insights about chirality trends for a given reaction mechanism.

In summary this subsection shows that both of the analyzed SWCNT growth process steps are energetically favorable and the energetic difference between them indicates the existence of a driving force allowing the dissolved carbon to migrate to the surface of the cluster, specifically to the vicinity of the *ac* site. The results also suggest that the dissolution step might control the overall rate of the process, which can be taken advantage of for the design of chiral-selective process.

5.5. Conclusions

Two simulation sets were designed to get insights into the reaction taking place by carbon addition to an armchair site of nanotube caps under the root-growth mechanism (simulation set I) and to examine the dissolution of carbon into the cluster (simulation set II). Our study shows that root-growth might occur by attack of carbon atoms in the vicinity of *ac* sites breaking the interaction between such site and the cobalt atom, due to stronger covalent C–C_{rim} than Coulombic Co_{ac}–C_{rim} interactions. In general terms, the presence of the cluster slightly harms the energetic of such reaction as compared to the formation of a new ring in a plain cap, but facilitates the transport of carbon atom toward the reaction site. On the other hand, the interactions between the cluster and the chiral cap affect the behavior of carbon inside the cluster as only the (6, 5) system was able to form dissolved carbon dimers.

These features hint a higher diffusion rate of carbon inside the cluster when this is interacting with a cap of (6, 5) chirality; the diffusion process is shown likely to be driven by energetic differences between carbon atoms located inside of the cluster and those in most stable positions in the vicinity of the *ac* site. Carbon migration is suggested as the rate-controlling step in the SWCNT growth, premise under which the (6, 5) chirality is predicted to possess a higher growth rate in agreement with experimental results.

We remark that the inability to fully control chirality hinders the development of nanotube technology; however such control can only be achieved if the initial stages of

the growth process are fully understood. In the current work we present bits of the growth process worked in more detail and more realistic ways than reported in the past, and similarities and differences found for different chiralities are pointed out since they may provide useful suggestions to elaborate guidelines for chirality control.

6. NANOCATALYST STRUCTURE AS A TEMPLATE TO DEFINE CHIRALITY OF NASCENT SINGLE-WALLED CARBON NANOTUBES*

6.1. Summary

Chirality is a crucial factor in a single-walled carbon nanotube (SWCNT) because it determines its optical and electronic properties. A chiral angle spanning from 0° to 30° results from twisting of the graphene sheet conforming the nanotube wall and is equivalently expressed by chiral indexes (*n,m*). However, lack of chirality control during SWCNT synthesis is an obstacle for a widespread use of these materials. Here we use first-principles density functional theory (DFT) and classical molecular dynamics (MD) simulations to propose and illustrate basic concepts supporting that the nanocatalyst structure may act as a template to control the chirality during nanotube synthesis. DFT optimizations of metal cluster (Co and Cu)/cap systems for caps of various chiralities are used to show that an inverse template effect from the nascent carbon nanostructure over the catalyst may exist in floating catalysts; such effect determines a negligible chirality control. Classical MD simulations are used to investigate the influence of a strongly interacting substrate on the structure of a metal nanocatalyst and illustrate how such interaction may help preserve catalyst crystallinity. Finally, DFT optimizations of carbon structures on stepped (211) and (321) cobalt surfaces are used to demonstrate the template effect imparted by the nanocatalyst surface on the growing carbon structure at early stages of nucleation. It is found that depending on the step structure and type of building block (short chains, single atoms, or hexagonal rings), thermodynamics favor armchair or zigzag termination, which provides guidelines for a chirality controlled process based on tuning the catalyst structure and the type of precursor gas.

6.2. Introduction

Two distinct approaches are currently used to obtain a homogeneous mixture of single-walled carbon nanotubes (SWCNT's) [148], either post-fabrication separation processes

---

* Reprinted with permission from Diego A. Gomez-Gualdron, Jin Zhao, and Perla B. Balbuena. "Nanocatalyst structure as a template to define chirality of nascent single-walled carbon nanotubes", 134, 014705, (2011). DOI. http://dx.doi.org/10.1063/1.3509387. Copyright 2011, American Institute of Physics

[149-152] or direct control during chemical vapor deposition synthesis [20, 79]. Success in the latter approach would result in nondestructive, scalable, and economical production by the elimination of post-synthesis steps. A chiral angle spanning from 0° to 30° results from twisting of the graphene sheet conforming the nanotube wall and is equivalently expressed by chiral indexes (*n,m*). The chirality [97] of a nanotube of certain diameter belongs to a subset of all the (*n,m*) [153]. Controlling the catalyst nanoparticle size during reaction partially narrows the chirality distribution by restricting the nanotube diameter [138, 154, 155]. A finer control has been achieved for only a few processes. For instance, the CoMoCAT synthesis process [20] produces majority of near-armchair (*6,5*) and not at all near-zigzag (*9,1*), despite the identical diameter of such nanotubes.

But the mechanism under which chirality control has been partially achieved in some processes is not well understood. This is not surprising as the number of variables involved in nanotube synthesis is quite significant (e.g., temperature, pressure, catalyst composition, and nature of feedstock). Consequently, determining the single effect of each variable in order to design a chiral-selective process poses a challenge to the scientific community. The time/scale of the catalyzed synthesis process is very short/small, making experimental observations quite arduous. On the other hand, the same time/scale proves to be beyond the limits of current computational resources used in the first-principles molecular simulations. Therefore, there is a need for interplay between experimental and theoretical work: experiments yielding information to generate simplified, yet accurate, simulation models, which can provide guidelines for a careful, cost-effective selection of experiments. For instance, density functional theory (DFT) studies provide valuable information about molecular structures related to the nanotube growth mechanism, while capturing quantum effects out of the reach of other methods [47, 103, 124, 156-159].

Simulation models have intended to explain experimental trends observed in chiral selectivity during nanotube production. In particular, the abundance of near-armchair nanotubes in nanotube mixtures produced under a number of methods [20, 44,

137, 160, 161] has been attributed to intrinsic characteristics of near-armchair nanotubes during growth such as the increase of active sites in the nanotube rim as growth progresses (Section 3) [124], higher reactivity of their aromatic rings, [156] or to the resemblance between near-armchair rims and screw dislocations [158]. On the other hand, recent experiments have suggested that control over the chirality may be achieved by manipulating other variables such as the structure of the metallic nanoparticle. Using high-resolution transmission electron microscopy and image reconstruction, Zhu *et al* [38] have proposed that there is a correlation between the structure of cobalt nanocatalysts and the chiral angle of the nascent tube.

This might open the possibility of tailoring the nanotube chirality as long as the catalyst structure would be susceptible to control. In fact, by changing the catalyst composition of Ni_xFe_{1-x} nanoparticles, Chiang and Sankaran [48] showed that the alteration of the nanoparticle structure was accompanied by changes in the chiral distribution of the final nanotube sample. Additionally, Harutyunyan *et al* [45] found an apparent correlation between a high production of metallic nanotubes (mostly armchair (*ac*)) and the sharpness of the nanocatalyst structure. Thus, the existence of a relationship between nanocatalyst structure and nascent nanotube chirality seems to emerge from the above-mentioned experiments.

Here we intend to elucidate the nature of such relationship. We first analyze the interactions of small metal clusters with SWCNT caps of three different chiralities and demonstrate the inverse template effect of the carbon network on the structure of a floating metal cluster. Second, we use MD simulations to analyze the template effect that substrates may exert on clusters structure. In subsection 6.4.3 we investigate the existence of a correlation between nascent nanotube chirality and catalyst structure using as building blocks carbon dimers, hexagonal rings, and single carbon atoms on two stepped surfaces: Co(321) and Co(211).

6.3. Computational methods

The nanotube caps used in the calculations of subsection 6.4.1 have been detected experimentally [17, 19], and theoretically [30] during nanotube nucleation stages when chirality may be defined. Nanotube-cap and/or cluster systems were fully optimized using DFT as implemented in Gaussian 03 [82]. The three-parameter Becke gradient-corrected exchange functional [56] in conjunction with the Lee–Yang–Parr [57] correlation functional (B3LYP) was used. The suitability of such functional for representing carbon/metal interactions is discussed elsewhere (Section 4) [88]. The LANL2DZ basis set for the carbon and valence metal atoms.

The effect of additional polarization functions was evaluated with a series of test calculations shown as in *supplementary information* (Tables S1 and S2) in [162]. Specifically, we calculated the interaction energy in the dimers Co–C and Cu–C using the correlation consistent polarized valence triple zeta basis set for the C atoms [163] and the LANL2DZ_mod [164] LANL2tzf, and LANL08f [61, 165, 166] basis sets for the metal atoms, in conjunction with the effective core potentials by Hay and Wadt [60, 61, 167]. Adding polarization functions to C atoms slightly reduces the carbon–metal distance (3% for Co and 8% for Cu) and the atomic charges; while adding also polarization functions to the valence metal basis sets keeps the carbon–metal distance but enhances the electronic charge on the atoms; in both the cases the interaction energy is enhanced (26% in the case of Co and 13% in the case of Cu) with respect to the LANL2DZ results.

Since this analysis indicates that both the relative strength of the carbon–metal interactions and the geometry are reasonably represented by the LANL2DZ results, we report these for the cap–cluster systems. A density-based convergence criterion of 10^{-6} was used for the self-consistent field during optimizations. To increase accuracy in the electronic description, a single point calculation using a 10^{-8} threshold followed the optimizations.

The cobalt (or copper) 15-atom nanoparticles and carbon caps discussed in subsection 6.4.1 were first fully optimized separately, and then brought together and

fully optimized as a complex system. The CC and metal–metal bonding energies were calculated using:

$$E_{bond} = \frac{E_{total} - nE_{atom}}{number\ of\ bonds} \qquad (6-1)$$

The number of bonds was counted for the nanotube caps or the metal cluster using a maximum value of 1.5 Å for carbon and 2.7 Å for metallic atoms. The C–C distance values cover the typical range of C–C bond lengths. The metal–metal maximum distance is slightly elongated with respect to an average value of 2.59 Å in the bare Co_{15} cluster and 2.64 Å in the bare Cu_{15} cluster; however, we account for cluster deformation caused by the contact with the carbon nanostructure, as shown in previous work (Section 4) [88] and discussed here in a later subsection. Likewise, the energy change ΔE_i between clusters and caps was calculated using:

$$\Delta E_i = \frac{E_{total} - E_{cap} - E_{cluster}}{N} \qquad (6-2)$$

The second and third terms in the denominator refer to the cap and cluster energies when optimized separately and N is the number of atoms in the cluster, used as a normalization factor in Equation 6-2. Note that this energy change is due not only to the cap–cluster interaction but also to the changes in energy due to intrinsic cluster deformations.

The DFT calculations on the cobalt and molybdenum-carbide (MoC) discussed in subsections 6.4.2, and 6.4.3 were performed using the Vienna ab-initio simulation package, [168] based on plane-wave basis sets. Electron–ion interactions are described using the projector-augmented wave method [169] using a cutoff energy of 400 eV. Electron exchange and correlation effects were described by the Perdew–Burke–Ernzerhof (PBE) exchange correlation function [170], which uses the generalized gradient approximation. Spin polarization was included in all the simulations. The convergence criterion for the electronic self-consistent iterations was set to 10^{-4} eV, and the energy of the ionic iterations was set 10^{-3} eV. Brillouin zone integration was

performed using a 9 × 9 × 1 Monkhorst–Pack [63] grid (5 × 5 × 1 for MoC systems), and a Methfessel–Paxton [171] smearing of 0.2 eV.

The MoC substrate was chosen to emulate the CoMoCAT process [79]. The tungsten carbide (WC) structured MoC was selected over the β`-Mo_2C phase (also stable in the range of 800–1200 K) because of the high C concentration at the synthesis conditions. The substrate is reproduced by replication of a trigonal cell ($a_1 = a_2 = 2.92$ Å, $c/a_1 = 0.97$). The MoC slab consists of five to seven layers in ABAB stacking sequence (A is a molybdenum layer and B a carbon layer). The cobalt structures are added on top of the MoC and the system is partially allowed to relax with the three bottom layers fixed. The behavior of the cluster was studied by sequentially increasing the number of atoms. First, one cobalt atom was added in different positions to find stable adsorption sites. Then, two cobalt atoms were added at once to observe the dimer formation, and then larger clusters were deposited on the surface.

The Co(211) and Co(321) surfaces were chosen to represent the two nanoparticle structures discussed in subsection 6.4.3. The surfaces were built using slab models with the two bottom layers fixed. A vacuum space of 12 Å is included in the *c* direction to avoid interaction between the slabs. The surface unit cells were built using the CERIUS^2 software by cleavage from bulk fcc cobalt, whose lattice constant was determined as 3.51 Å from the DFT calculations. The Co(321) and Co(211) slabs (1 × 1 unit cells) contain 16 and 24 cobalt atoms, respectively. Additional calculations were performed on larger 2 × 1 unit cells to account for potential surface deformations, as discussed in *supplementary information* (Tables S3 to S8) in [162]. To search for the formation of zigzag (*zz*) and/or armchair chain on the surfaces, two dimers were added to the surfaces in such a way that under periodic boundary conditions a continuous chain was formed. Depending on the location of the dimer the formation of a zigzag or an armchair chain is biased (but not guaranteed) during optimization. In all the cases, the comparison of energies was done for systems with same number of carbon and metal atoms. The different orientations of the ring were achieved by initially locating the carbon atoms

either on bridge or hollow positions, depending on the specific surface and desired orientation (zigzag or armchair), with further relaxation of the system.

The nucleation of carbon structures on the surfaces was also simulated adding one carbon atom at a time to the surfaces, testing all possible positions, and choosing the minimum energy location. Then a new carbon atom was added to the selected system at all possible open positions and the minimum energy location was selected. The criterion for selection is the adsorption energy E_{ad} for the i_{th} addition of carbon, calculated using:

$$\Delta E_{ad} = E_i^* - E_{i-1} - E_C \qquad (6-3)$$

The total energy of the system is E_i. $E_{i-1}{}^*$ is the total energy of the system where the current carbon is added, and E_c is the energy of atomic carbon calculated using the same DFT method (–0.14 eV). Negative values of E_{ad} indicate a favorable (exothermic) adsorption.

Reactive molecular dynamics (RMD) simulations of carbon nanotube growth on a cluster deposited on a substrate, as discussed in subsection 6.4.2, were performed using our molecular dynamics algorithm that allows for instantaneous catalysis of a precursor gas, diffusion of carbon inside of the catalyst particle, and carbon diffusion from the particle interior toward the surface, as well as formation of carbon structures on the surface, nucleation of a cap, and nanotube growth [70]. We use the Tersoff–Brenner potential [73] for C–C interactions, a modification of Tersoff–Brenner for metal reactive carbon interactions, [72] and the many-body Sutton–Chen potential [71] for metal–metal interactions. The interactions between the metal atoms and those of the graphene-like test substrate were described using the same reactive metal–carbon potential [72], with different potential well (E_{adh}) values to simulate variable interaction strengths. Although graphite is not used as a substrate in SWCNT synthesis, it is used here as a model substrate, where we test the variation of the substrate/metal interaction strength on the catalyst shape at the earliest stages of nucleation and during nanotube growth.

The simulated growth was performed at 1000 K. The temperature is kept constant with a simple thermostat where atomic velocities of the precursor phase, the

metal cluster, and the catalyzed carbon are separately rescaled to the target temperature at every step of the simulation. A 0.0005 ps time step was used, and the growth reaction was followed during 6 ns. The reaction growth using the reactive force field was performed on 32-atom metallic cluster, located over the test substrate. The one-layered graphene-like substrate was at the bottom of a ~ 21 × 21 × 82 Å orthorhombic simulation box. Simulation with different cluster/substrate interaction strengths used identical initial cluster geometries. The precursor gas density was kept at 0.5143 kg/m^3 during the simulation. The precursor gas is instantaneously catalyzed (converted into carbon) when it contacts the nanoparticle, and the nanotube growth is monitored. The time evolution of the metallic cluster was followed during the simulated growth.

6.4. Results and discussion

6.4.1. Inverse template effect in floating nanocatalysts

Recent work has shown that catalyst size is critical for nanotube growth [172, 173]. However, during SWCNT synthesis it has been observed that a relatively large nanoparticle may rearrange during reaction having a much smaller catalytically active region[17, 19]. We first present an analysis from non-periodic DFT optimizations of nanotube caps of a given chirality interacting with 15-atom metal clusters. The results obtained in **Figure 6-1**a correspond to the optimization of 15-atom metal clusters interacting with chiral nanotube caps. Although during SWCNT growth, the end termination of the nanotube evolves as the tube grows; such evolution depends on the specific chirality (Section 3) [124]. The caps used here are the smallest possible structures that define a given chirality. They were selected assuming that chirality is defined during the nucleation stage. If several structures of these so-called minimum caps were possible (as for the (7,5) chirality), we used the most stable one, as established through DFT optimization. The initial cluster structure is an optimized geometry (a local minimum) and is the same for all cap chiralities.

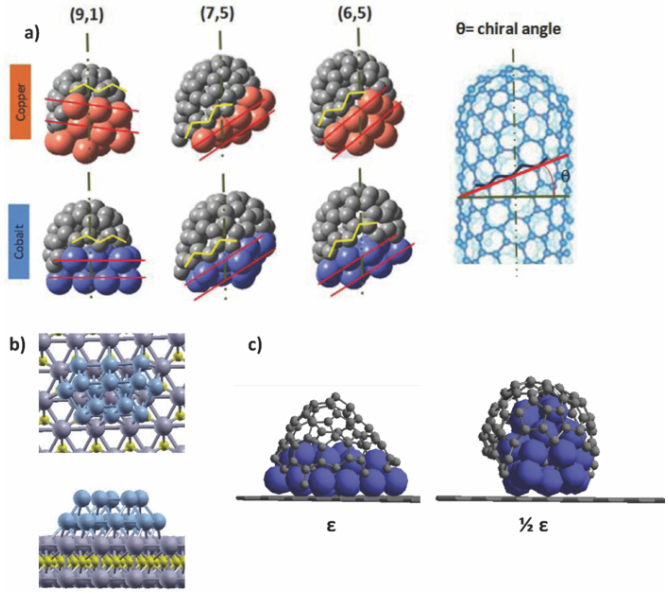

Figure 6-1. a) 15-atom nanoparticles of copper (orange) and cobalt (blue) interacting with nanotube caps of (n, m) chiralities (carbon atoms shown as grey spheres). The angle defined by the highlighted atomic plane (red line) in the nanoparticle and the perpendicular to the nanotube axis, correlates with the chiral angle of the nascent nanotube (cap). The nanotube schematic at the right is introduced to facilitate interpretation. b) Top view (top) and side view (bottom) of the epitaxial matching between a cobalt nanoparticle (blue atoms) and a molybdenum -carbide support (Mo atoms gray, C atoms yellow). c) Structure of a Co nanoparticle (blue) during nanotube growth for strong nanoparticle/substrate interaction E_{adh} (left) and for a weaker interaction (right). E_{adh} is related to the potential well of the metal-substrate potential (see subsection 6.3).

Comparison between the initial and final cap/cluster structures shows negligible changes in the structure of the nanotube caps but clear changes in the cluster structure. (Section 4) [88]. We quantified the deformations in the cluster structure for each case evaluating the differences between the position of each atom and the cluster center of mass before and after the interaction with the cap. These graphs are added as *supplementary information* (Figures S1 and S2 for Co and Cu clusters, respectively in [162]). The root mean squared deviations for each cluster are 0.58, 0.56, and 0.35 Å for (6,5), (7,5), and (9,1) in Co clusters and 1.26, 1.42, and 1.37 Å for (6,5), (7,5), and (9,1) in Cu clusters. In these 0 K DFT optimizations, the cluster deformations are driven by the differences in metal–metal versus carbon–carbon and metal–carbon energies. Our estimates of these bond energies are $E_{cc} = -4.06$ eV > $E_{CoC} = -2.37$ eV > $E_{CuC} = -1.94$ eV > $E_{CoCo} = -0.76$ eV > $E_{Cu-Cu} = -0.75$ eV.

The strongest carbon–metal interactions are expected to be those of the metal atoms interacting with the highly reactive C rim atoms (Section 4) [88] as shown in **Figure 6-1**a by yellow lines. The positioning of the metallic atoms in contact with the rim may induce the remaining cluster structure, leading to the formation of incipient planes in the cluster [red lines in **Figure 6-1**a. The calculated ΔE is similar for the various chiral systems, averaging –1.29 ± 0.031 eV for cobalt and –1.35 ± 0.003 eV for copper; the small energy difference suggests that both metal clusters are stabilized by caps in similar extent and this stabilization may play a significant role in nanotube nucleation [47, 88]. Notice that '$\Delta E_{\text{cap–cobalt}}/\Delta E_{\text{cap–copper}}$' does not correlate to $E_{\text{CuC}}/E_{\text{CoC}}$ possibly due to the contribution of the distinct cluster deformations to ΔE.

The strong cluster deformation noted suggests the existence of an *inverse template effect* of the growing nanostructure on the catalytic nanoparticle. Such an effect supports some known disadvantages regarding chirality selectivity for SWCNT synthesis methods using floating nanoparticles (gas-phase process) as opposed to catalyst nanoparticles supported on a substrate. For example, at the high temperatures of the synthesis (~1000 K) the floating (polydisperse and polymorph) nanoparticles are most likely in a liquid-like state. Thus, the inverse template effect from the nascent carbon structure to the metal particle may exist given the energy differences among the relevant interactions obtained with the 0 K DFT analyses. This inverse template effect is likely present at high temperatures due to the availability of thermal energy in the form of kT (~0.09 eV at 1000 K), which more readily overcomes the nondirectional cohesive forces of metallic bonds ($E_{\text{MM}} \sim -0.76$ eV) than the directional ($E_{\text{CC}} \sim -4.06$ eV) covalent carbon bond forces.

The metal–metal cohesive energies for these small clusters are much weaker than those in bulk due to the cluster size. At 1000 K, even a larger floating cluster of hundreds of atoms is at its melting point, and therefore it is easily deformed by the nascent carbon structure [80, 174]. Reducing the temperature of the process may increase the impact of the metal structure on the chirality distribution; however, a fine control would still be difficult, even more so accounting for diffusion of carbon into the

nanoparticle [24], which may cause a further decrease of the nanoparticle melting point through the formation of an eutectic point [12] and may alter the catalyst structure as well. We come back to this point in subsection 6.4.2, when we discuss the results of classical MD simulations. Using different metals (or alloys) could change the conditions of the eutectic point. Similarly, certain control in the nanostructures may be in part obtained in floating particles by using multimetallic clusters. For instance, alloying two metals having different lattice constants or crystal structures may impart some concentration-dependent structural effect to the nanoparticle, as recently shown [48].

6.4.2. Substrate effect on the catalyst shape

In contrast, the use of an adequate substrate may counterbalance the decrease of the nanocatalyst melting point and help it *acquire* and *keep* the necessary structure to influence the chirality of the resulting nanotubes. Thus, one might control the nanoparticle structure by properly designing the nanoparticle/substrate system to ensure the proper epitaxial matching. Previous work has shown that changing the substrate affects the chiral distribution, possibly by altering the nanoparticle structure [20]. Evidence of this epitaxial matching is shown **Figure 6-1**b by results from periodic DFT optimizations representing sequential growth of a cobalt cluster over a MoC substrate. When the first two cobalt atoms are deposited in alternative pair of sites over the substrate surface, independently of the initial configuration the cobalt atoms, they form a dimer by migrating to neighboring hcp-hollow positions. The same trend is maintained when the number of cobalt atoms is increased, with the cobalt atoms occupying hcp-hollow positions and forming a (111) fcc layer (Figure S1, *supplementary information* in [162]).

Similarly, if a small three-dimensional cluster is deposited on the MoC surface, the cluster bottom layer follows this same epitaxial match with the substrate; the metal atoms occupy hcp-hollow positions, whereas the atoms of the subsequent layer localize on the interstitial positions on top of the bottom layer following the ABC pattern of the fcc structure **Figure 6-1**b. However, the stacking sequence can change with the metal, as recently shown for nickel nanoparticles on magnesium oxide [175]. Earlier

experimental evidence of "contact epitaxy" between the nanoparticles and a substrate was observed for Ag nanoparticles on Cu [176]. More recently, perfectly crystalline Mn-doped germanium nanoparticles (quantum dots) have been synthesized through epitaxy with a Si substrate [177]. A key point is that a strong cluster/substrate interaction should induce epitaxial effects, as well as make the nanoparticle less likely to shape-shift once the nanotube growth reaction starts because of the reduced atomic mobility in the nanoparticle derived from the increase of its melting point [178]. Previous molecular dynamics studies have shown that the melting point of metallic nanoclusters depends on cluster size, shape [80], and presence of a substrate [34, 178, 179]. Reviews on the topic have also been published [174]. We note that the selection of a chemically appropriate substrate is also an important factor, since some substrates may inhibit nanotube nucleation [180].

We illustrate the role of nanoparticle/substrate interaction strength using classical molecular dynamics simulations and a reactive force field that allows bond making and breaking as explained in the Section 2 [72]. We simulated the growth of SWCNTs on a 32-atom metal cluster located over a test substrate at 1000 K. It was observed that for certain (relatively strong) strength of cluster/substrate interactions, the cluster maintained a fairly ordered structure despite temperature, carbon diffusion, and nanotube growth. The bottom layer of the cluster has a clear epitaxial matching with the graphene-like substrate and the subsequent layers packed on top of the bottom one **Figure 6-1**c. The epitaxial behavior is evidenced in that every single atom of the bottom layer occupies a fairly centered hollow position on the substrate (not shown). As the cluster/substrate interaction is weakened, the bottom layer does not perfectly wet the substrate and fewer atoms occupy hollow positions. Further, the metal cluster is barely attached to the substrate and has a more rounded and disordered structure.

To provide additional insights we computed the time evolution of the change in catalyst crystallinity during nanotube growth as the substrate/catalyst interaction weakens, as illustrated in **Figure 6-2**. The catalyst/substrate interaction strengths (E_{adh} in **Figure 6-2)**, range from −1.39 to −0.159 eV. To put these values in context, we

compare with energies of comparable systems (metal clusters over metal-oxide supports) that have been reported in the literature. Ag/MgO interactions range from −0.143 to −0.399 eV/atom [181]; Cu/MgO: −0.36 eV/atom and Ni/MgO: −0.62 eV/atom [182]; and Co/$SrTiO_3$: −2.47 eV/atom. For each interaction strength value indicated in **Figure 6-2**, we have evaluated the density profile of the cluster in a direction perpendicular to the substrate.

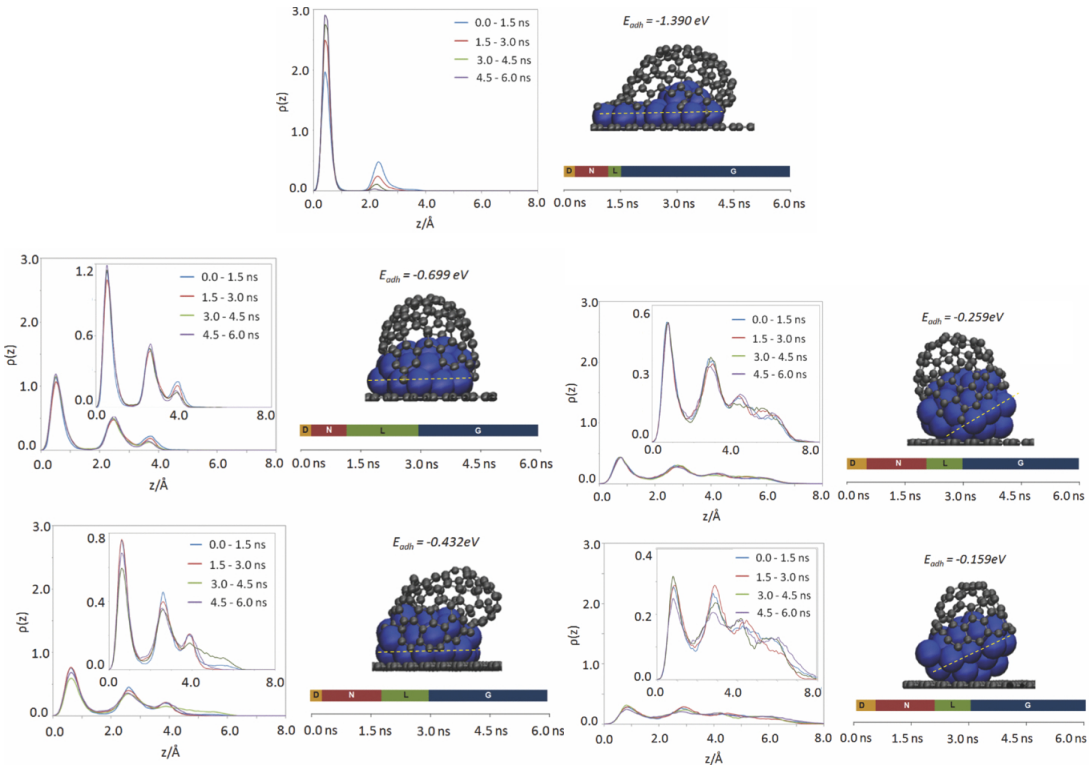

Figure 6-2. Time-evolution of metal density profile in the z direction perpendicular to the substrate, for different metal/substrate interaction strengths (E_{adh}), along with corresponding structures taken at approximately the same stage of nanotube growth. The bar diagrams show the different types of growth through the 6.0 ns of simulation: (D) dissolution (yellow), (N) cap nucleation (red), (L) cap lift-off, and (G) growth (blue). Statistical data for the density profiles are gathered for four time intervals: 0-1.5 ns (blue), 1.5-3.0 ns (red), 3.0-4.5 ns (green), and 4.5-6.0 ns (purple).

At a strong catalyst/substrate interaction (−1.39 and −0.699 eV), the catalyst crystallinity is very well preserved during growth, although some changes are observed in the contact layer due to the catalyst spreading over the substrate. As the

catalyst/substrate interaction becomes weaker (−0.432 eV) we observe more changes in the catalyst that preserves its 3D structure; however, the contact layer structure and orientation are still maintained. At even weaker interaction energies (–0.259 and –0.159 eV) the cluster becomes much more fluid as denoted by the broader and less smooth density profiles and by the changes in the contact layer and orientation as illustrated in **Figure 6-2**.

In the limit of very weak substrate/cluster interactions we expect the impact of the substrate geometry on the nanoparticle to be lost and the behavior of the nanoparticle becoming similar to that when the growth reaction is carried out on the floating nanoparticle. Although during the RMD simulations the grown carbon structures were somewhat defective (due to artificial acceleration imposed to the simulated reaction process), the results illustrate that an adequate nanoparticle/substrate interaction can help to keep the catalyst structure at high temperatures and may alter carbon solubility.

6.4.3. Relationship between nanotube chirality and catalyst structure at early nucleation stage

The role of the step for C adsorption on metal surfaces has been highlighted in several publications [16, 183-186]. A recent paper presents a detailed discussion of graphene growth in relation to the nature of the metal surface [184], and shows that both Ni and Co have the optimum geometry that minimizes the strain in the graphene sheet formed, in contrast to other metals such as Ru, Rh, and strained Ni. We chose the stepped Co(211) and the chiral Co(321) surfaces to model two different structures of the nanoparticle surface (**Figure 6-3**). These cobalt surfaces model an step defect formed on the nanoparticle surface during nanotube growth [17, 19], wherein (fcc) cobalt is chosen based on the lattice matching of Co(111) and graphene [183, 184, 187]. Periodic DFT simulations were performed by adding carbon species near the step since the first carbon species appearing on the nanoparticle surface may concentrate around highly reactive low-coordination sites [16, 183, 184, 186].

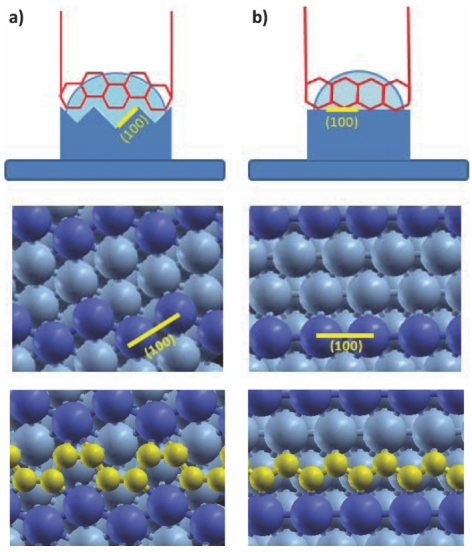

Figure 6-3. The surfaces modeling a step defect in the catalytic nanoparticle. Top: schematic images represent the nanoparticles being modeled. a) The step/terrace structure of the Co(321) surface (middle left image) and the most stable chain structure around the step (bottom, left). b) The step/terrace structure of the Co(211) surface (middle right) and the most stable structure around the step (bottom, right). Co atoms in light blue, C atoms in yellow, step Co atoms in dark blue, and the (100) step is highlighted with the yellow straight line.

The local geometry around the step defect consists of two Co(111) planes connected by a step. The Co(111) planes constitute the majority of exposed facets in the nanoparticle due to its low surface energy but the step exposes Co(100) planes whose orientation depends on the "contact" epitaxial matching between the nanoparticle and the substrate. For instance, a substrate surface having a square-pattern lattice could induce a nanoparticle structure consisting of stacked Co(100) planes parallel to the substrate, so when the step defect is formed, the exposed Co(100) plane is parallel to the substrate as well. Co(211) models a case wherein the exposed Co(100) plane in the step is parallel to the substrate, while Co(321) represents systems having such plane oriented 30° respect to it (*supplementary information* Figure S2 in [162]). Cobalt (211) and (321) surfaces were chosen because of their similar terrace width and simple step geometry.

During SWCNT synthesis, a number of carbon species may be present on the catalyst surface directly from gas decomposition or diffusion from the subsurface. Thus, to account for somewhat different scenarios we calculated the stability of armchair- or

zigzag-related carbon structures using either C (atoms), C_2 (dimers), or C_6 (rings) as building blocks. The probability of occurrence of a given structure *i* can be related to its energy according to $P(i) \sim e^{(-Ei/kT)}$, meaning that highly stable structures are more likely to occur. Thus, during nanotube synthesis, interplay of thermodynamics and kinetic effects would cause that the same thermal energy promoting the formation of less stable carbon structures may allow the most stable configurations to be reached by overcoming energetic barriers.

6.4.3.1. Addition of carbon dimers

The first building blocks used were carbon dimers, which were added near the step, followed by a DFT optimization. Simultaneous addition of two carbon dimers to the Co(211) unit cell stabilized a zigzag carbon chain. This chain is a harbinger of the formation of a *zz* nanotube when the exposed step Co(100) plane in the nanoparticle is parallel to the substrate (**Figure 6-3**). Conversely, the addition of carbon dimers to the Co(321) unit cell (which models the Co(100) plane tilted 30°) stabilizes an armchair chain which hints at the formation of an *ac* nanotube. The stabilization of either chain may originate from the step geometry and the terrace (Co(111)) orientation.

We attempted to obtain the opposite structure in either surface (changing the starting structure for the optimization) to determine the likelihood of growth of alternative configurations. For the (211) surface, the most important finding is that the *zz* configuration is 0.52 eV/surface atom more stable than the *ac* configuration shown in **Figure 6-4**. This shows the stability of the *zz* chain on the Co(211) surface, driven by the strong interaction with the step (whose (100) plane is parallel to the substrate). Interestingly, the *zz* chain (**Figure 6-3b**) is formed by two carbon atoms in hollow positions and other two in top positions, despite all the atoms starting in hollow positions. This is a consequence of an overall relocation of the carbon dimers in an effort to maximize the interaction with the step. A similar relocation was observed in the formation of the *ac* chain from two dimers (**Figure 6-4**a).

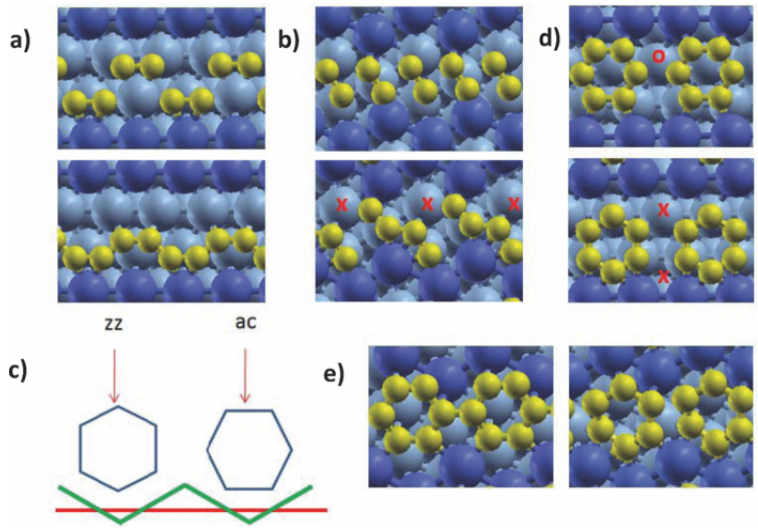

Figure 6-4. (a) Carbon dimers on the Co(211) surface initially located to bias the formation of an armchair chain (top), and the final configuration after optimization (bottom). (b) Carbon dimers on the Co(321) surface initially located to bias the formation of a zigzag chain (top), and the final configuration after optimization (bottom). Addition of carbon in positions denoted with an "*x*" completes a continuous armchair structure. (c) Schematic of armchair (*ac*) and zigzag (*zz*) orientations of a hexagonal ring respect to the step in Co(211) (red line), and Co(321) (green line). (d) Hexagonal rings at different orientations on a Co(211) surface. An "o" denotes a metallic atom halting a carbon–carbon bond (top). Addition of carbon in the positions denoted with an "x" completes a new ring (bottom). (e) Hexagonal rings at different orientations on a Co(321) surface. Color code for the atoms as in Figure 6-3.

On the other hand, on the Co(321) surface, only the armchair chain is a local minimum. This structure only experienced a slight overall shift toward the step to strengthen the interaction (Figures S3 a and b, *supplementary information* in [162]), and the carbon atoms still remained in hollow positions, although not perfectly centered. The four carbon atoms in the unit cell appear to interact strongly with the lowest coordinated cobalt atom of the step. We have previously found this specific configuration, consisting of a cobalt atom symmetrically coordinated with the four atoms of an *ac* site, in cap/nanoparticle simulations where a new carbon ring was formed by addition of two carbon atoms that break up the weaker metal–carbon interaction (Section 5) [188]. It is important to emphasize that these two very different model systems (*ac* site around a step cobalt atom in an extended surface and *ac* site around a cobalt atom from a small metal cluster) reproduce the same physicochemical and geometric features, as confirmed

by analysis of the electronic density distribution (Figures S3c and d, *supplementary information* in [162]).

It is also noteworthy that a stable *zz* structure on the Co(321) surface was not found in spite of the initial positions of the carbon dimers that were biased toward that configuration. Instead, one of the carbon dimers relocated to interact with the kink atom, whereas the other dimer kept its original position (**Figure 6-4**b). Thus, the lowest coordinated atom of the step is interacting with three instead of four carbon atoms and the chain continuity is broken. These two facts may be responsible for the 0.06 eV/surface atom difference between this structure and the *ac* structure; although it is evident from **Figure 6-4**b that addition of a new carbon atom in between the most distanced carbon atoms would produce an armchair-related structure.

In summary, the *ac* chain is very stable on the Co(321) surface and this is associated with the orientation of the (100) step at 30° with respect to the nanoparticle bottom layer. In addition, the calculations show that it is more likely to obtain an *ac* chain when the (100) step runs parallel to the substrate than a *zz* chain when the (100) step runs oblique to the substrate, since at least the former is a local minimum. Even in absence of specific control of the nanoparticle catalyst structure on a substrate, this would be one of the several reasons for the relative abundance of near-armchair nanotubes previously mentioned.

6.4.3.2. Formation and orientation of graphene on Co(211) and Co(321)

Because of the high reactivity of carbon atoms, they could rapidly form sp^2 structures on the nanoparticle surface. Thus, an additional set of simulations was designed to prove the formation/orientation of graphene structures on the stepped surfaces, using C_6 rings as building blocks. We analyzed the properties of a hexagonal carbon ring adjacent to the surface step and arranged in two different orientations rotated 30° respect to each other. These arrangements reflect the orientation that the rings in the nanotube wall would have with respect to the nanoparticle surface for different nanotube chiral angles. For chiral angle 0^o, we model the nanotube wall/nanoparticle surface interaction of a *zz* nanotube when a ring apex points toward the step **Figure 6-4**c. Similarly, the *ac* case (chiral angle

= 30^{o}) is modeled when the CC bond is parallel to the direction of the step **Figure 6-4**c. The carbon ring is initially located on the surfaces according to the expected epitaxy with the cobalt surface [187].

The results show that for an hexagonal ring on the Co(211) surface, the *ac* orientation is 0.55 eV/surface atom *more favorable* than the *zz* one. Although in the *zz* orientation the ring carbon atoms were initially located at the most stable (hollow) positions for adsorption of one carbon atom (Figure S4, *supplementary information* in [162]) the optimized structure shows an overall relocation of the carbon ring structure toward the step, similar to the behavior of the carbon chains. Thus, only one carbon atom ends up adsorbed on the step hollow site, whereas its two neighboring carbon atoms, as well as that located in the opposite position, adsorb on top sites (**Figure 6-4**d). The two remaining carbon atoms occupy hollow positions, but different to the starting ones. Adding periodic images, it is clear that on the Co(211) surface the *zz* arrangement appears *suitable for formation of the graphene sheet*, since a perfect graphene lattice is easily completed by addition of two new carbon atoms, without generating strain [184] in the structure (**Figure 6-4**d, bottom).

In the more stable *ac*-ring adsorption, a similar ring relocation toward the step occurs, and the carbon atoms end up occupying hollow positions (Figure S4-b, *supplementary information* in [162]) where two C atoms per ring-interaction are located at the most favorable step locations. However, the location of the ring in *ac* orientation on the (211) surface is not optimal for the formation of the graphene lattice, since the two carbon atoms that should be forming a bond are 1.66 Å apart (obtained using a larger 2 × 1 supercell, see Table S6, *supplementary information* in [162]), and at either side of a cobalt atom (shown by adding periodic images, (**Figure 6-4**d-top). In summary, the (211) surface simulations modeling the (100) step parallel to the substrate show that the *ac* configuration is favored because of enhanced interactions of carbon atoms with step metal atoms, although the *zz* arrangement appears more suited for formation of the graphene lattice.

Simulations of the Co(321) surface (**Figure 6-4**e) also show that the *ac* orientation is 0.24 eV/surface atom *more stable* than the *zz* one. Once again, there was a displacement of the initial structures in order to enhance the interaction with the step atoms. In the *ac*-oriented ring, the ring atoms originally occupied hollow positions (Figure S5, *supplementary information* in [162]), and only one was at a short interaction distance from the step metal atoms. During optimization, the ring changed its position, with two carbon atoms strongly interacting with the step atoms, and making a moiré pattern with the cobalt atoms beneath (**Figure 6-4**e-left). Adding periodic images it is found that the *formation of an armchair-oriented graphene lattice is favorable* on the Co(321) surface since the carbon–carbon bond length between rings in adjacent unit cells is 1.41 Å. Also, there is a carbon configuration around the lowest coordinated step atom similar to the one described for the *ac* chain. As shown in previous work, (Section 5) [188] this configuration appears suitable for nanotube growth under the root-growth mechanism.

On the other hand, the *zz*-oriented ring moved toward the step such that three carbon atoms end up strongly interacting with the step (Figure S5-b, *supplementary information* in [162]). Nonetheless, the *zz* orientation is less stable than the *ac* one due to the distorted geometry of the ring caused by the interaction with the step. Adding periodic images reveals that formation of a graphene layer on the Co(321) surface is *not favored* at all when the ring is in *zz* orientation. The spacing between rings in continuous unit cells is not suitable for the formation of a new hexagonal ring, but rather a squared ring or perhaps a pentagonal one, and in any case introducing a defect to the graphene lattice. Thus, simulations on the Co(321) surface modeling the (100) step at 30° show that the *ac* configuration is favored over the *zz* one and such *ac* orientation of the ring is better suited for the formation of the graphene lattice.

In summary, on both the stepped surfaces *ac* ring orientation is preferred in agreement with previous findings [31]. However, only *ac*-terminated graphene formation is favorable on (321) surfaces whereas only *zz*-terminated graphene is found on (211) surfaces.

6.4.3.3. Sequential addition of single C atoms

The last question we address is about *nucleation* of carbon structures on a step defect of each surface, *by sequential adsorption of single carbon atoms* on the surface. The simulation is carried out by adding one carbon atom to the surface, and allowing the system to find an energy minimum. Different initial positions are tested to find the most stable local minimum, and then the procedure is repeated with successive additions of a single carbon atom (see methods). It is assumed that each added carbon atom comes from the catalytic decomposition of the precursor gas or comes out from the nanoparticle subsurface and diffuses along the surface (using thermal energy to hop from site to site) to find its preferred position. Although at high temperatures thermal energy may allow nucleation through other chemically allowed paths, the minimum energy path is the less energetically demanding route.

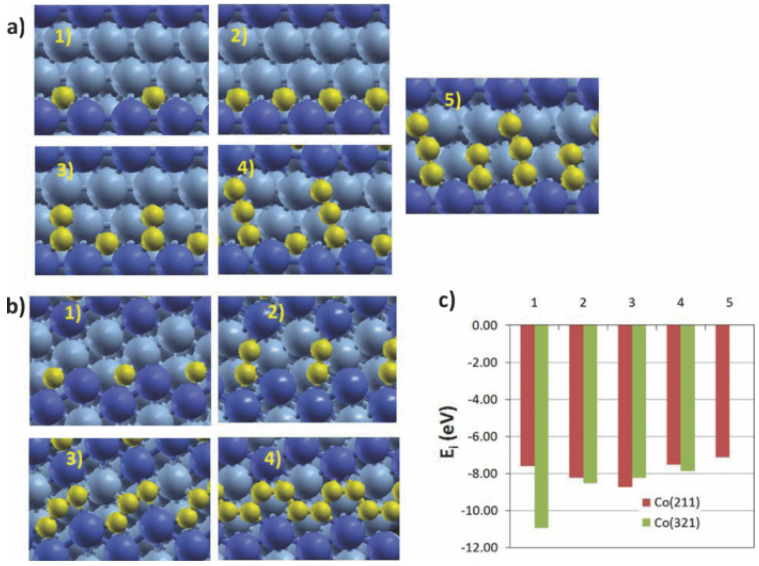

Figure 6.5. (a) Carbon nucleation by sequential addition of single C atoms on the step of Co(211). (b) Successful armchair carbon chain nucleation sequence on the step of Co(321). (c) Carbon adsorption energy diagram during the nucleation steps in (a) and (b).

On the Co(321) surface, nucleation starts (**Figure 6-5**b) with adsorption of one carbon atom on the step (100) hollow site (adsorption energy $E_i = -10.94$ eV). This is followed by formation of a carbon dimer due to adsorption of a second carbon atom on

the closest hollow-hcp site (E_i = −8.51 eV). The next carbon atom is adsorbed on the neighbor hollow-fcc site adjacent to the site where the previous adsorption occurred leading to the formation of a carbon trimer chain along the (100) step (E_i = −8.22 eV). Finally, a new carbon atom is added in a nearby hollow-hcp position (E_i = −7.87 eV). This would be expected to form a linear tetramer chain, but the chain folds around the lowest-coordinated atom of the step yielding an armchair carbon chain that is visualized in **Figure 6-5**b after applying periodic images. It is noteworthy that the nucleation occurred around the lowest coordinated cobalt atom of the step, acting as an anchorage point for newly added carbon atoms and facilitating the formation of the armchair structure.

On the Co(211) surface **Figure 6-5**a, the nucleation also starts with carbon adsorption on one of the (100) sites on the steps, but with much weaker adsorption energy (E_i = −7.60 eV) than on the Co(321) step site. This is followed by a new adsorption on the neighboring (100) site of the step. The adsorption of the second carbon is stronger (E_i = −8.23 eV) than the first one, and despite of both carbon atoms occupying adjacent sites a dimer is not formed yet. However, the next carbon adsorbed on a nearby hollow-hcp site forms a dimer (E_i = −8.73 eV) with one of the carbon atoms adsorbed on the step. This dimer becomes a trimer (E_i = −8.57 eV) following the adsorption of carbon on a neighbor site. At this point, the trimer points away from the step, without harbinger of zigzag (or armchair) structure formation; contrary to the nucleation on the Co(321) structure where, at this stage, the armchair chain is already formed.

A new carbon atom was added intending to obtain a zigzag-related structure, but instead a dimer was formed (E_i = −7.12 eV) with the remaining carbon atom on the step, arranged parallel to the trimer previously formed (**Figure 6-5**a). It is very likely that annealing the system at a higher temperature, a *zz*-related structure does form (as it does in presence of dimers), but in contrast, the easiness of formation of the *ac* chain in the Co(321) surface is striking under this mechanism.

6.5. Conclusions

An inverse template effect may occur on floating nanocatalysts where the metal nanoparticle adopts variable shapes determined by the growing carbon structure. On the other hand, we postulate that under strong metal/substrate interactions, a catalyst may grow epitaxially with well-defined structures that in contact with the nascent cap, can determine its chirality. Here we test this hypothesis by analysis of early nucleation stages using a variety of building blocks, including single C atoms, dimers, and hexagons on two different stepped surfaces: Co(211) models a case wherein the exposed Co(100) plane in the step is parallel to the substrate, while Co(321) represents systems having such plane oriented 30° respect to it.

It is important to point out similarities between the nucleation of carbon on both surfaces under sequential addition of single carbon atoms. First, no adsorption of carbon on other sites occurs until all the possible (100) step sites are occupied. At that point, the formation of a carbon dimer is favored over the scattered adsorption of carbon. Then, subsequent additions of monoatomic carbon elongate the nascent chain until either an obstacle is reached or the initial chain merges another chain. We note that sequential addition of carbon atoms is only one of many possible growth mechanisms, since catalyzed decomposition of a C-containing precursor gas yields several products such as C, C_2, C_3, and some growth processes may involve combinations of these species.

Here we have shown the preferential formation of *zz* carbon chains on the (211) surfaces under simultaneous adsorption of C dimers, whereas *ac* chains are preferentially formed on the (321) stepped surfaces under two different mechanisms: simultaneous adsorption of dimers and sequential addition of single carbon atoms. In addition, our DFT studies revealed that rings adsorb preferentially with their *ac* edges interacting with the most favorable step locations on both surfaces, while there is a preferred orientation for graphene formation on each surface: rings are *zz*-terminated on the (211) and *ac*-terminated on the (321) surface. Thus, we have observed trends that demonstrate that the geometry of the catalytic structure can influence the chirality of growing carbon structures.

Our conclusions regarding chirality selectivity result from a combination of thermodynamic stability and kinetic driving forces. At the high temperatures of the synthesis process a floating metal nanoparticle of the order of 1 nm is at its melting point; thus kinetic effects determine nanotube growth with negligible chirality selectivity. In contrast, for a supported nanoparticle having a strong substrate–particle interaction the melting point can be significantly increased. Thus, we suggest that a sufficiently strong metal–substrate interaction keeps the crystallinity of the metal catalyst limiting the diffusion of carbon inside of the nanoparticle and especially favoring the growth of carbon structures that follow a template given by the metal surface. Thus, in this case thermodynamic stability may dictate the growth of specific nucleation patterns with carbon diffusion playing a less important role.

Previously we had shown the kinetically preferred growth of armchair nanotubes derived from a reaction mechanism based on addition of C_2 radicals (Section 3) [124]; this kinetic factor may enhance growth, once the proper nucleation seeds are induced by the template structure. However, even if the substrate may impart the needed control of the catalyst structure, we acknowledge that at the relatively elevated temperatures used for nanotube synthesis, many nucleation processes could be activated resulting in the growth of a range of chiralities; although the template effect would significantly narrow the chiral angle range. In the current work we are analyzing cluster/substrate structures using other substrate stepped-surfaces. These analyses indicate that other stepped surfaces can be used to induce specific chiral angles (intermediate between 0^o and 30^o). Further studies will be focused toward implementing these results for design of specific catalyst/substrate systems that may produce majority of *ac*- or *zz*-type nanotubes.

7. DYNAMIC EVOLUTION OF SUPPORTED METAL NANOCATALYST/CARBON STRUCTURES DURING SINGLE-WALLED CARBON NANOTUBE GROWTH*

7.1. Summary

Single-walled carbon nanotubes (SCWNTs) have outstanding properties that depend on structural features such as their chirality. Thus, developing a strategy to control chirality during SWCNT synthesis is critical for the exploitation of nanotube-based technologies in fields such as electronics and biomedicine. In response to this need, tuning the nanocatalyst structure has been envisioned as a means to control the nanotube structure. We use reactive classical molecular dynamics to simulate nanotube growth on supported Ni_{32}, Ni_{80}, and Ni_{160} nanoparticles at various metal/support interaction strengths (E_{adh}). The initial carbon ring formation is shown to correlate to the nanoparticle surface structure, demonstrating the existence of a "template effect" through a dominant occupation of hollow sites. The E_{adh} strength alters the dynamic/structural behavior of the nanoparticle, in turn influencing the interplay between nanotube and nanoparticle structures. For example, the contact region between the nanoparticle surface and the growing nanotube decreases as E_{adh} increases because capillary forces that raise the metal into the nanotube are counteracted by the strong metal/support interaction. The nanoparticle mobility decreases as E_{adh} increases, eliminating a possible inverse template effect but hindering defect annealing in detriment of the nanotube/nanoparticle structural correlation. On the other hand, the contact between the nanoparticle and the nanotube increases with nanoparticle size. However, the heterogeneity of the nanoparticle structure increases with size, reducing the structural correlation. These results suggest that an appropriate combination of

* Reprinted with permission from Diego A. Gomez-Gualdron, Gilbert D. McKenzie, Juan F. J. Alvarado, "Dynamic Evolution of Supported Metal Nanocatalyst/Carbon Structure during Single-Walled Carbon Nanotube Growth", 6, pp 720-735, (2011). DOI. 10.1021/nn204215c. Copyright 2011 American Chemical Society

nanoparticle size and strength of the catalyst/support interaction may enhance the desired template effect and bias formation of specific nanotube chiralities.

7.2. Introduction

For about two decades, carbon nanotubes have been envisioned as one of the most promising materials in nanotechnology [4, 189, 190]. In particular, SWCNTs possess a number of astounding electrical, optical, and mechanical properties [90] with the potential to revolutionize several fields such as electronics, materials science, and medicine through their implementation in sophisticated devices (*e.g.* single-electron transistors) [2], nanocomposite structures (*e.g.*, nanotubes in polymeric matrices) [191], and new diagnosis and therapeutic procedures (*e.g.* nanotube-based biosensors) [192]. Geometrically, a carbon nanotube is obtained by bringing together two points in a graphene sheet, rolling it into tubular form. Selection of different points results in different helical patterns of the nanotube wall [153]. A way to describe this helicity is with the *chiral angle*, which spans values from 0 to 30°. The lowest value corresponds to a *zigzag* nanotube and the highest to an *armchair* nanotube. Interestingly, the properties of the nanotubes are found to depend on their chiral angle and their diameter (or alternatively on their chiral indexes (*n*,*m*)) [153], opening the possibility of selecting the most appropriate type of nanotube for a given application (*e.g.*, selecting a given band gap). Unfortunately, nanotubes are usually synthesized in bundles [193, 194] containing different *chiralities*, wherein their outstanding properties are lost. Thus additional steps are required to separate the nanotubes [149, 150], increasing the production cost and decreasing the viability of application.

Accordingly, there is a huge interest in controlling the chirality of the nanotubes *during* synthesis to allow the exploitation of carbon-nanotube-based technologies. Throughout the past decade, some processes such as CoMoCAT (majority of (6,5) and (7,5) nanotubes) [20] were known to produce SWCNTs with a relatively narrow chiral distribution. This process used a bimetallic cobalt–molybdenum catalyst on different supports (SiO_2 and MgO), wherein change in the support was one of the factors shown to alter the chiral distribution. Using cobalt supported on TUD-1 (an ordered

mesoporous silica) [195], a majority of (9,8) nanotubes were produced instead [21], also suggesting that the catalyst support can indirectly influence nanotube chirality. In addition to changing the support, the catalyst/support interaction has also been changed by using different metals. For instance, He *et al* produced majority of (6,5) using both cobalt [196] and nickel [18], but the abundance of secondary (7,5), (7,6), and (8,4) was altered by the use of either metal. Similarly, altering the interaction with the support using a bimetallic Fe–Cu catalyst, He *et al* were able to produce (6,5) majority on a MgO catalyst, [43] overcoming the inactivity of monometallic Cu and the selectivity of Fe toward multi-walled carbon nanotube formation on that substrate.

On the other hand, in recent years, theoretical and experimental work has suggested that the structure of the nanoparticle directly affects the resulting chiral distribution. For instance, Zhu *et al* [38] used HRTEM images to show a correlation between the chirality of the nanotube and the structure of the catalytic nanoparticle. Also, Chiang and Sankaran [48] demonstrated that structural changes in bimetallic Ni–Fe nanoparticles caused changes in the resulting chiral distribution. On the other hand, Harutyunyan *et al* [45] showed that the production of ~90% of metallic nanotubes was connected with a specific shape adopted by the Fe nanocatalyst during catalyst preparation. Similarly, in previous work, we used various theoretical methods to perform simulations aimed to prove the nanoparticle template effect hypothesis (Section 6) [162]. However, a major concern is the occurrence of an inverse template effect which results from the much stronger C–C bond in comparison to C–M and M–M bonds. Moreover, some recent experiments [17, 33] have shown the restructuring of the nanoparticle during nanotube growth, thus suggesting the liquid-like state of the nanoparticle as a possible obstacle to the use of the nanoparticle structure for controlling the nanotube chirality. Nevertheless, it is possible that through a careful selection of catalyst material, support material, nanoparticle size, and temperature—to mention a few factors—an adequate interplay among these factors can create the necessary conditions for the template effect to occur.

In this work, our goal is to use our simulations as a theoretical microscope to carefully investigate the dynamics between carbon and metal at the atomistic level, while trying to understand the influence (or lack thereof) of the nanoparticle structure on the nascent carbon structure(s). Thus, to explore the relation between the structure of the nascent nanotube and that of the catalytic nanoparticle at different conditions, we simulate the growth of carbon nanotubes using various nanoparticle/support interaction strengths and three different nanoparticle sizes. Five simulations are performed at each condition to account for the statistical nature of the nanotube growth. First, the simulation trajectories are carefully analyzed to determine general trends common to three nanoparticle sizes and various nanoparticle/support interaction strengths. Second, the chiral angle θ_c at the end of the simulations is determined to be either high (near-armchair) or low (near-zigzag), thus allowing one to evaluate whether a connection of chirality with the nanoparticle size, shape, or nanoparticle/support interaction exists.

We follow with an analysis of the dynamics connecting the nanoparticle structure and the nascent carbon structures at the nucleation stage. This is done with the purpose of understanding epitaxial effects between metal and carbon and structural evolution of the metal nanoparticle at typical conditions of temperature and pressure of the synthesis. This analysis is carried out by determining the type of sites on the nanoparticle surface preferentially occupied by carbon atoms, while attempting to evaluate the extent at which the geometry of early carbon structures is influenced by the continuously evolving nanoparticle surface. This is analyzed across the different simulation conditions to find whether a "template effect" or an "inverse template effect" appears to dominate at the nucleation stage. We then extend our analysis to later times in the simulation trajectories to determine whether a correlation between the nanoparticle structure and the nanotube exists once factors such as lattice mismatching and lattice defects start to play a more significant role. We also study how the dynamic evolution of the nanoparticle structure may affect the existence of such correlation for different simulation conditions.

We use a classical reactive force field [72] that allows performing a comparatively large number of simulations, while successfully modeling nanotube

growth [70, 80, 104, 197, 198]. This allows somewhat accounting for the statistical nature of nanotube growth due to high temperature, different initial catalyst structures, and different adsorption sites. Thus, we expect our simulations to complement other more rigorous, but computationally more demanding, theoretical approaches [25, 30, 102, 142, 199, 200]. On the other hand, our force field readily permits modification of factors such as metal–carbon, carbon–support, and metal–support interaction strengths, thus enabling an extensive study on how different conditions affect the nanotube growth [173, 201, 202].

7.3. Computational methods

Classical reactive molecular dynamics using the SIMCAT code is used to simulate the growth of carbon nanotubes on supported nanoparticles [33]. Three metallic clusters, namely, Ni_{32}, Ni_{80}, and Ni_{160}, were used to study the influence of the nanoparticle size. Magic size clusters characterized for their unusually high cohesive energy and highly symmetric structure have been reported for 13, 55, and 147 atoms in unsupported nickel clusters, while 32, 81, and others are secondary magic sizes [203]. However, for supported nanoparticles, the interaction with the substrate may alter the given sizes as reported in the literature [204, 205]. In the present work, the clusters display different structural behavior for the various values of E_{adh}, but they never appear to adopt perfectly symmetric geometries, thus behaving as regular clusters.

The nanoparticles are placed on a model substrate, whose interaction with the nanoparticle can be modified through the increase or decrease of a damping factor in the force field. The force field describes the most relevant interactions in the nanotube growth including: (1) metal–metal (MM) interactions, represented using the Sutton Chen potential [71]; (2) carbon–carbon (CC) interactions, characterized by a modified potential [33] inspired in the second generation reactive empirical bond order (REBO) Brenner potential [73]; (3) metal–carbon (MC) interactions, described using a Tersoff–Brenner scheme, [33] wherein the strength of the interaction depends on the hybridization of the carbon atoms and the local geometry of the metal atoms; for instance, on the basis of density functional theory (DFT) calculations, [33]the interaction

between carbon atoms at the nanotube tip (sp^2 atoms) and metal is modeled weaker than the interaction between carbon atoms at the nanotube rim (sp atoms) and metal; (4) carbon–substrate interactions are described using equivalent expressions to those for CC interactions, but using a different damping factor; (5) metal–substrate interactions are described using equivalent expressions to those for MC interactions, but different parameterization. A detailed description of the force field equation can be found elsewhere [33]. This force field has been proven useful to get insights on the nanotube growth and to determine how the interplay of the different interactions promotes either nanotube growth or encapsulation for supported and unsupported nanoparticles as a function of temperature, nanoparticle size, and strength of metal–substrate interactions [173, 201, 202].

At the beginning of the simulations, the nanoparticle is located at the center of a tetragonal simulation box, whose dimensions are c = 84.0 Å and $a = b$ = 25.0 Å for Ni_{32} and Ni_{80}, and 39 Å for Ni_{160}. Precursor atoms initially appear in the gas phase at random positions according to the desired density (0.0001 atoms/Å^3). The number of precursor atoms is such that a preset gas density is maintained, and they move inside the simulation box according to the simulation temperature. When "by chance" a precursor atom contacts the nanoparticle, it is instantaneously converted into a carbon atom and new precursor atoms appear at a random position in the gas phase. Thus, there is neither a predetermined carbon addition rate of carbon nor predetermined addition sites on the nanoparticle. There are no interactions between a precursor atom and either metal, carbon, or substrate atoms. However, when a precursor atom travels closer than 1.0 Å to a metal atom, it irreversibly transforms into a carbon atom whose interactions with the rest of the system are described accordingly. For all sizes, the number of carbon atoms dissolved inside the nanoparticle reaches a maximum within 500 ps. However, it must be noted that segregation to the surface was observed before this "supersaturation" occurs.

This algorithm models an instantaneous irreversible catalysis, thus accelerating the growth with respect to experimental rates [206]. The temperature is set at 1000 K,

which is representative of CVD growth [20, 21, 137], and separately rescaled to the target temperature for each species. The parameters used in our simulations result in the following interaction energies: (i) carbon–carbon ~ −5.0 eV, (ii) sp^2-carbon–metal ~ −0.10 eV, (iii) sp-carbon–metal ~ −2.78 eV, (iv) carbon–substrate ~ -1×10^{-5} eV, (v) metal–substrate interaction E_{adh} takes different values, namely, −0.10, −0.16, −0.43, −0.70, and −1.39 eV. Typical values for E_{adh} range from −0.14 to −0.62 eV for metal supported on MgO and −2.47 eV for metal supported on $SrTiO_3$ [181, 182]. We note that a number of factors can affect the interaction strength between nanoparticle and substrate. For instance, E_{adh} can change with the nanoparticle size/shape in a nonmonotonic fashion [207], and can be affected by structural defects on the support [208], or by the presence of functional groups on the support surface [209].

However, some trends can be observed for commonly utilized supports such as silica, magnesia, and graphene. Namely, adsorption on silica tends to be stronger than on magnesia but weaker than on graphene, as revealed by E_{adh} values (per contact atom) of −1.1 [207], −0.23 [210], and −2.07 eV [208] for Au_5 clusters on silica, magnesia, and graphene, respectively. On the other hand, calculation of E_{adh} for *one* metal atom on silica[211] shows Ni (E_{adh} = −1.90 eV) to adsorb more strongly than Fe (E_{adh} = −1.70 eV), but more weakly than Co (E_{adh} = −2.20 eV). However, on magnesia [212], Ni adsorbs more strongly (E_{adh} = −1.32 eV) than both Fe (E_{adh} = −0.91 eV) and Co (E_{adh} = −0.81 eV). Increasing the number of metal atoms, the value of E_{adh} (per contact atom) decreases. In silica, the trend is maintained with E_{adh} = −0.62 and −0.34 eV for Co and Ni, respectively [213], but not so in magnesia with E_{adh} ~ −0.67 and −0.63 eV for Co and Ni, respectively [175].

On the other hand, the relative values of CC and MC interactions agree well with previous DFT calculations (Section 6) [162]. The length of each simulation is 5.0 ns, which allows one to observe the stages of dissolution, cap nucleation, and cap lift-off. A simulation step of 0.5 fs is used. The trajectory is saved so each trajectory frame represents 0.5 ps of simulation. The trajectories were analyzed using VMD [214].

For each determination of chiral angle, the axial direction of the growing carbon nanotube is first established using VMD [214]. The final trajectory frame is rotated to obtain the "best" view of the nanotube cross section. Then a straight line passing through two axis points is drawn, and the system is rotated to obtain the true length view of this line. Finally, according to the orientation of the hexagonal pattern of the growing nanotube relative to this line, the chiral angle (θ_c) is estimated as high (between 15 and 30°) or low (between 0 and 15°). On the other hand, to count the number of C atoms occupying a given surface site type, a utility program was created to identify the atoms on the surface and classify them using the carbon–metal coordination number as criteria. For instance, carbon atoms with one metal neighbor are said to occupy *top* sites, whereas those with two metal neighbors occupy *bridge* sites, or those with three or four metal neighbors occupy *hollow* sites.

The simulation statistics were improved by using different initial conditions for the catalytic nanoparticle; the different initial structures were varied as a function of five distinct annealing times (t_a). During the catalyst preparation in CVD growth, usually a precursor oxide undergoes a calcination/reduction/annealing process, which generates the metallic nanoparticles that catalyze the nanotube growth. The time frames utilized in these stages can be controlled in order to modify the catalyst characteristics. For instance, the catalyst precursor can be partially reduced to control the particle size [196]. In a CVD experiment, the structure/diameter of the reduced nanoparticles, before growth, is unlikely to be identical. Thus, here the different annealing times are used *only* to represent the diversity of initial catalytic structures.

7.4. Results and discussion

7.4.1. General growth trends

Inspection of 75 simulation trajectories shows the nanotube growth to occur through the following steps: *1)* carbon dissolution into the metal nanocatalyst particle; *2)* carbon segregation to the nanoparticle surface; *3)* formation of carbon nanostructures on the metal surface identified as (a) chains, (b) isolated rings (usually branched), and (c) concatenated rings (usually branched); *4)* "merging" of carbon nanostructures to form a

nanotube cap; *5)* lifting-off of the nanotube cap; and *6)* incorporation of carbon to the nanotube rim/nanoparticle surface interface (length increase). In general, the onset of chain formation occurs earlier than that for ring formation, while the onset for ring formation occurs earlier than that for concatenated ring formation. Nevertheless, the onset of a latter substage does not necessarily coincide with the end of an earlier substage since in a number of instances the formation of chains (or rings) may occur after some rings (or concatenated rings) have already been formed. This sort of scenario was more apparent for larger nanoparticle sizes due to the surface area increase. Additionally, formation of rings (or concatenated rings) was observed while the formation of chains (or rings) was dominant, but such rings (or concatenated rings) appeared to be less stable—having lifetimes of a few picoseconds.

On the other hand, as the metal–substrate interaction E_{adh} decreases, the number of carbon structures (chains, rings, and concatenated rings) on the nanoparticle surface for a particular surface carbon concentration increases. For example, on a Ni_{32} particle initially annealed for 0.5 ns, 15 carbon atoms are found to form two chains (C_{11} and C_4) when $E_{adh} = -1.39$ eV, whereas the same number of atoms form three chains (C_6, C_5, and C_4) at a weaker $E_{adh} = -0.16$ eV for the same initial conditions of the nanoparticle. This could be related to a higher mobility of the metal atoms at weaker E_{adh} that may increase the number of favorable nucleation points on the nanoparticle surface. We come back to this point in a later subsection when discussing the relative occupancies of surface sites by C atoms.

Snapshots in **Figure 7-1** illustrate typical appearances of nascent nanotubes after 5 ns of simulation. Although the presented snapshots are only for one set of initial conditions ($t_a = 0.10$ ns), representative trends observed in the analysis of all simulation trajectories can be summarized as follows: *1)* A correlation between nanotube diameter (d) and nanoparticle size is apparent[20, 215-217] with the change in particle size from Ni_{32} through Ni_{160} (at constant E_{adh}), and with the variation of E_{adh} from −0.16 through −1.39 eV (at constant particle size). *2)* Cap lift-off occurs faster when E_{adh} is stronger. As cap lift-off starts, the separation between the nanotube cap and the nanoparticle

becomes apparent, with the nanotube rim region keeping the contact with the nanocatalyst. Carbon atoms are incorporated to the nanotube through this contact region, thus allowing the growth of the nanotube *via* a root-growth mechanism [22].

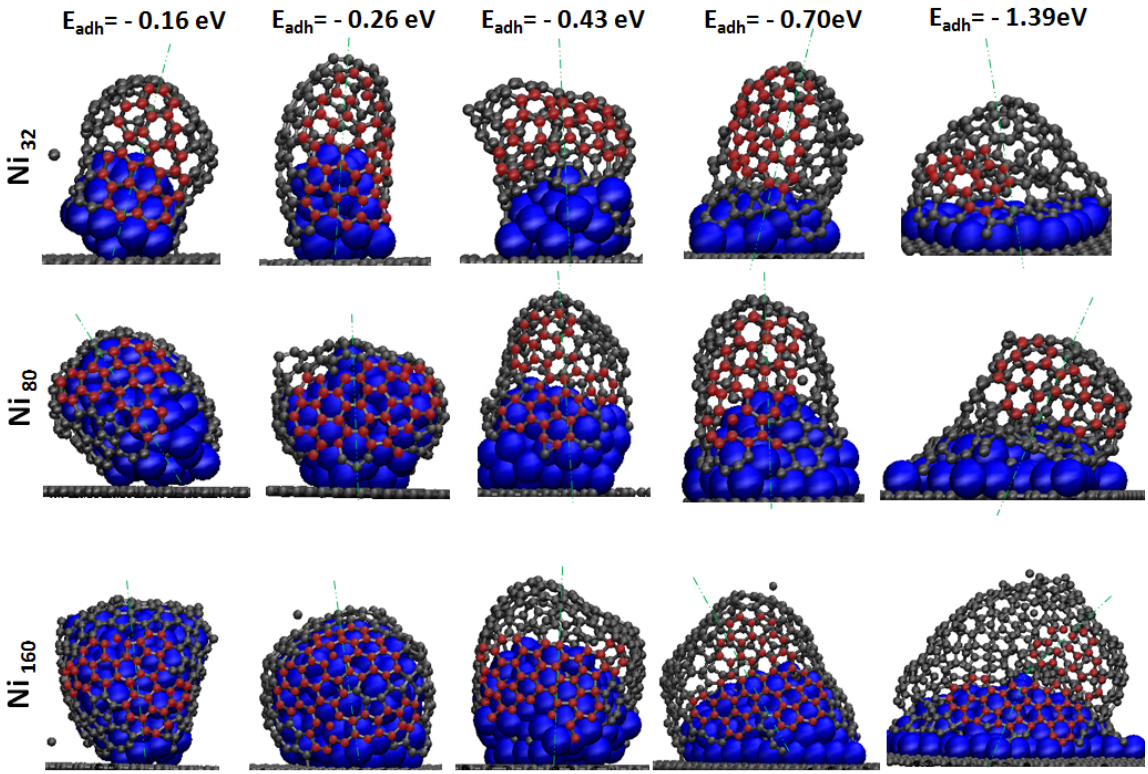

Figure 7-1. Snapshots after 5.00 ns of simulated growth showing the nascent nanotube structure (red and gray atoms) on a supported metallic nanoparticle (blue atoms). The metal/substrate interaction strength increases from left to right, while the nanoparticle size increases from top to bottom; the annealing time before growth was 0.10 ns. Carbon atoms used in assessing the chiral angle appear in red. Green dash-dotted lines are used to indicate the axial direction.

It was apparent that the number of carbon atoms involved in this contact region decreases as E_{adh} increases. It is noteworthy that regions of the nanotube not contacting the nanoparticle do not show major restructuration during growth (*i.e.*, bond rearrangement seldom occurs), thus the probability of healing existing defects or creating new ones appears to be very low. On the other hand, the contact region is observed to continuously reconstruct mediated by the dynamics of metal atoms, thus facilitating defect healing and formation. This is in agreement with previous studies

suggesting the importance of the metal for defect annealing [199, 218]. These phenomena are revisited in a later subsection discussing its impact for controlling the nanotube structure. During cap lift-off, the nanoparticle is observed to periodically change its shape. The effect is more noticeable for weak E_{adh} values, as revealed by the change in height of the nanoparticle mass center (NP_{mc}), with respect to the substrate position, during the simulation. For strong E_{adh}, the cap-lift occurs as the height of the NP_{mc} decreases, involving flattening of the nanoparticle. This process has been recently discussed from an energetic point of view [219].

The acceleration of cap lift-off at stronger E_{adh} occurs because a stronger attraction of the substrate to the metal atoms allows counteracting the capillary forces that tend to raise the metal into the nanotube [17, 33]. For weak E_{adh}, when the cap starts lifting-off, the (relatively) "fluid" nanoparticle elongates in the direction of growth, thus increasing the time that the cap and the nanoparticle are in contact. Moreover, the wetting angle ω of the nanoparticle on the substrate is *always* larger when growth is occurring, in agreement with a growth-induced effect. In a previous study [202], it was shown that such effect can be as strong as to detach the nanoparticle from the substrate as occurs for a tip-growth mechanism [220]. *3)* A stronger E_{adh} typically results in lower angles (φ_G) of the nanotube growth direction (axial direction) with respect to the substrate, whereas weaker E_{adh} strengths result in variable φ_G (*i.e.*, growth direction oscillates during the simulation), and moderate E_{adh} typically results in upright growth ($\varphi_G \approx 90°$). *4)* Although the nanotubes grown during the simulation possess a number of defects, typically pentagonal and heptagonal rings, it is possible to recognize defect-free regions in their walls large enough to determine whether their chiral angle is low ($0° < \theta_c < 15°$) or high ($15° < \theta_c < 30°$).

We recognize that defect healing could somewhat alter θ_c and d, thus we refrain from determining the exact (n,m) indexes, from their connection to θ_c and d, and rather focus our analysis on whether near-zigzag (low θ_c) or near-armchair (high θ_c) nanotubes are favored for a particular combination of nanoparticle size and E_{adh}. It is noted that, for a particular simulation, the region highlighted in **Figure 7-1** is not the only defect-free

region on the nanotube, but it is selected to show the relative orientation of the nanotube wall with respect to the surface and the nanotube axial direction used in the characterization of θ_c summarized in **Figure 7-2**.

7.4.2. Chirality trends

Varying the pre-growth nanoparticle annealing time, t_a, results in different initial catalyst structures to simulate the nanotube growth on Ni_{32}, Ni_{80}, and Ni_{160} nanoparticles at various values of E_{adh}. However, due to the relatively short annealing times, the difference among initial structures for a particular combination of catalyst size and E_{adh} is rather subtle; for instance, their density profiles are similar. Thus, the main purpose of evaluating different t_a values was to introduce higher statistical significance to the chiral angle analysis.

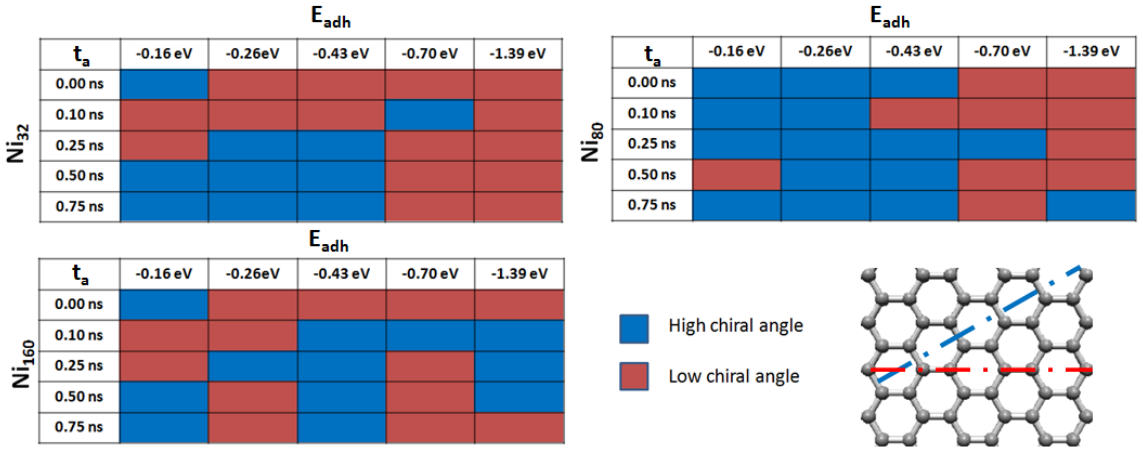

Figure 7-2. Schematics showing the classification of the nascent nanotube into a high (~30°) or a low (~0°) chiral angle structure after 5.00 ns of simulated growth. Each cell corresponds to a particular set of metal/substrate interaction strength (E_{adh}), catalyst size, and annealing time (t_a) before growth (hence different initial catalyst structure). The chiral angle is determined according to the relative orientation of the nanotube graphene network (red atoms in Figure. 7-1) and the axial direction (green dash-dotted line in Figure 7-1) according the schematics in the lower-right corner.

From the data in **Figure 7-2**, the following observations are drawn: *1)* relatively weak metal–substrate interaction strengths (-0.16 eV $\leq E_{adh} \leq -0.43$ eV) tend to favor near-armchair nanotubes for the smaller particle sizes (Ni_{32} and Ni_{80}) for values. In this E_{adh} range, 60.0% of the Ni_{32} simulations resulted in near-armchair nanotubes and 40.0% in

near-zigzag nanotubes. Also, within this E_{adh} range, 83.3% of the simulations with shorter pre-growth annealing times ($t_a \leq 0.1$ ns) resulted in near-zigzag nanotubes, and 88.8% of the simulations with larger pre-growth annealing times ($t_a \geq 0.25$ ns) resulted in near-armchair nanotubes. *2)* In contrast, at higher metal–substrate interaction strengths (-0.70 eV $\leq E_{adh} \leq -1.39$ eV), 90.0% of the simulations using Ni_{32} resulted in near-zigzag nanotubes. It must be noted that the quality of the nanotubes produced in this range was much lower than those produced at lower values of E_{adh}; this aspect is further discussed in a later subsection when referring to the interplay between metal surface reorganization and carbon nanostructure rearrangements. *3)* It is also apparent that some of the chirality trends observed for the smallest Ni_{32} are better defined in the intermediate sized Ni_{80} nanoparticle. For instance, for Ni_{80}, 86.6% of simulations in the -0.16 eV $\leq E_{adh} \leq -0.43$ eV yielded near-armchair nanotubes, and in the -0.70 eV $\leq E_{adh} \leq -1.39$ eV range, 80.0% resulted in near-zigzag nanotubes. *4)* In contrast to Ni_{32}, no connection was found between the annealing times t_a and the resulting chiral angle for Ni_{80} possibly due to the lesser impact of a particular annealing time on the structure of the intermediate sized Ni_{80} compared to the smaller Ni_{32}. *5)* The trends observed for Ni_{32} and Ni_{80} disappeared in the simulations of the larger Ni_{160} nanoparticle where a clear chirality trend could not be found. For example, 53.3% of the simulations in the -0.16 eV $\leq E_{adh} \leq -0.43$ eV range produced near-armchair nanotubes, and 60.0% of the simulations in the -0.70 eV $\leq E_{adh} \leq -1.39$ eV range produced near-zigzag nanotubes.

These observations suggest that increasing the nanoparticle size beyond a certain size could be detrimental for controlling the nanotube chiral angle since the distribution for Ni_{160} presented a larger random character than those for Ni_{32} and Ni_{80}. It must be noted that the set of (n,m) indexes that fit a particular nanotube diameter d increases in size as d increases. On the other hand, our simulations reveal that the final nanotube diameters were 0.2–0.4 nm larger than their corresponding nanoparticle. Accordingly, since Ni_{160} has a larger diameter than Ni_{80} and Ni_{32}, there is a larger number of (n,m) nanotubes potentially fitting Ni_{160} in comparison to either Ni_{32} or Ni_{80}, thus increasing the difficulty to impose chirality control [20, 215]. As a quantitative example, we note

that the final average diameters for Ni_{32}, Ni_{80}, and Ni_{160} for $E_{adh} \leq -0.26$ eV were found to be ~0.5, ~0.9, and ~1.2 nm, whereas their corresponding nanotubes were found to be ~0.9, ~1.1, and ~1.5 nm in diameter. On the basis of these diameters [90], the number of (n,m) nanotubes fitting a particular nanoparticle approaches seven for Ni_{32}, nine for Ni_{80}, and 13 for Ni_{160}, which implies an increase of 28% from Ni_{32} to Ni_{80}, but one of 85% from Ni_{32} to Ni_{160}.

A potential scenario is proposed linking the structures of the nascent nanotube and that of the evolving nanoparticle [38, 45, 48, 162], where subtle differences in the structural behavior of Ni_{160} compared to Ni_{80} and Ni_{32} could hinder the appearance of chiral distribution trends for the largest nanoparticle. For instance, as the nanoparticle size increases it is easier to detect (on the same nanoparticle) surface regions with different structural and dynamic behavior facilitated by the increased surface area and the high reaction temperature. In particular, sometimes it is noted a desynchronization in the orientation of neighbor surface "domains", which is disadvantageous under the premise that the orientation of the nanoparticle surface could be connected to the nanotube chirality through epitaxial matching. This matching has been proposed to occur between the energetically favored (111) facets in fcc nanoparticles and the hexagonal lattice of the nanotube wall [38, 162, 183, 184, 187]. Since, for a particular simulation time, the Ni_{160} surface often shows neighbor (111) domains with conflicting orientation, the metal surface influence on the nanotube structure is unclear. We emphasize that although conflicting regions also are observed for Ni_{80} and Ni_{32} the ratio of desynchronized/synchronized regions is perceived to be smaller.

On the basis of the previous discussion, it is interesting to note that the simulations of Ni_{80} presented somewhat more defined trends than the Ni_{32} ones. Although this could be an artifact of the relatively small population sample (five simulations for each nanoparticle size and E_{adh}), it could also suggest that a moderately small nanoparticle could be optimal for chirality control [20, 21, 48]. It is possible that although the number of (n,m) nanotubes fitting Ni_{32} is 23% smaller than that for Ni_{80}, it is more difficult for the smallest nanoparticle to clearly impose its structure on the

nascent nanotube. For instance, for the smallest particle and relatively weak $E_{adh} \leq -0.43$ eV, the nanoparticle diameter is within the 0.5–0.8 nm range, wherein other factors such as curvature energies can have an important effect on the nanotube [99, 173]. On the other hand, although for $E_{adh} \geq -0.70$ eV the diameter is within the 0.9–1.1 nm range, the contact between the nanotube wall and the nanoparticle decreases since cap lift-off is accelerated (see **Figure 7-1**), which hinders epitaxy. On the contrary, Ni_{80} features a similar diameter range (0.9–1.2 nm) for $E_{adh} \leq -0.43$ eV, while showing a good contact between the nanotube wall and the nanoparticle. At larger diameters (1.3–1.6 nm $E_{adh} \geq -0.70$ eV), this contact decreases, but it is still better than for Ni_{32}.

In addition, given the available thermal energy, a nanoparticle can evolve from one local minimum structure to another. For smaller nanoparticles, local minima are closer in energy [221], thus an easier transition from minimum to minimum may occur, with Ni_{32} and Ni_{80} readily moving from one minimum to another at a rate related to E_{adh}. Conversely, local minima for larger nanoparticles are more scattered [221], so such transition in Ni_{160} does not occur as easily. Accordingly, Ni_{160} shows irregular transition structures for longer times than Ni_{32} and Ni_{80}, thus negatively affecting a possible template effect. On the other hand, the faster dynamics in Ni_{32} may also hinder a template effect because nucleation of carbon structures has to continuously adapt to structural changes as Ni_{32} switches among different local minimum structures. In this scenario, Ni_{80} perhaps offers the best compromise for a template effect to occur, among the three studied sizes.

7.4.3. Interplay between evolving nanoparticle structure and nascent carbon nanostructures

It has been assumed in the preceding discussion that epitaxy between the nanotube and the nanoparticle does indeed occur. Although some authors have presented evidence correlating the structure of the nanoparticle of the nanotubes [38, 45, 48], it is still debatable whether the nanoparticle imposes its structure on the nascent nanotube (direct template effect) or the nanotube conditions the structure of the nanoparticle (inverse template effect) due to factors such as the higher strength of C–C bonds *versus* M–M

bonds (Section 6) [162, 172], and the melting point depression of metallic nanoparticles [35]. We had previously suggested the use of a supported nanoparticle on a substrate with an adequate E_{adh} to solve this issue (Section 7) [162]. We had also demonstrated through DFT calculations that if the fcc(111) facet is oriented such that the [110] direction (or the (100) plane) is at a 30° with respect to the substrate, carbon rings (and other structures) preferably adopted the armchair configuration but preferred the zigzag configuration when the angle is 0° (Section 7) [162]. Trajectory analysis of our current simulations shows that, when the wetting is poor, the [110] direction is *usually* at 30° with respect to the substrate but *usually* at 0° when the wetting is good. Notice that a good wetting is caused by strong E_{adh}, which results in the nanoparticle featuring a *flat* "frozen" (111) epitaxial contact layer [202], thus the natural packing sequence of the upper layers results in the formation of a (111) facet with the [110] direction parallel to the substrate.

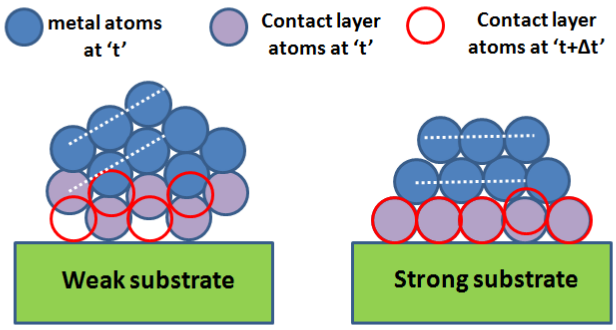

Figure 7-3. Side-view schematics capturing the most typical behavior of the nanoparticle structure for a weak interaction with the support and poor wetting (left) and a strong interaction with the support and good wetting (right). Metal atoms of the 'contact layer' are represented by filled purple circles; regular metal atoms are represented by filled blue circles. The position of the atoms in the contact layer (unfilled red circles) after 'Δt' picoseconds denotes a fast dynamics for the 'weak substrate' and a slow dynamics for the 'strong substrate'. The white dash line corresponds to the [110] direction of the (111) facet shown.

On the other hand, weak E_{adh} values result in poor wetting and an *uneven* mobile contact layer due to the up-and-down motion of the contact layer atoms. This behavior is somewhat transmitted to the upper layers, resulting in the [110] direction at an angle with the substrate. It must be noted that, due to the non-equilibrium nature of the

nanotube growth process, this is only a general outline of the overall behavior of the nanoparticle during growth (schematized in **Figure 7-3**). Thus the nanoparticle can display "transient structures" contradicting the outlined trends. Nevertheless, according to the observed nanoparticle structural/dynamic trends and our previous DFT studies, we expect the probability for production of near-armchair nanotubes to increase at weaker values of E_{adh} and the probability for production of near-zigzag to increase at stronger values of E_{adh}, assuming upright growth ($\varphi_G \sim 90°$). Interestingly, such trends appeared to be reproduced by Ni_{32} and Ni_{80}, although $\varphi_G \neq 90°$ throughout most of the simulations, thus indicating the need of a more detailed analysis.

It is useful to point out that, for the smallest particles, as E_{adh} increases, the shape of the nanoparticle changes from rounded (high wetting angle) to a flatter shape (low wetting angle). In the flatter shape (strong E_{adh}), the contact layer is flat and relatively still, with the atoms in upper layer positioning on the hollow sites of the layer underneath, favoring fcc packing, and the (110) surface direction parallel to the substrate (**Figure 7-3**, right). In the rounded shape (weak E_{adh}), the influence of the substrate is weaker, with a much more dynamic contact layer (**Figure 7-3**, left). Thus, the nanoparticle seems to adopt a structure of polyhedral character. This structural transition is evident for Ni_{32} at $E_{adh} = -0.70$ and -1.39 eV. The influence of E_{adh} on this polyhedron fcc transition has been previously discussed [36]. Notice that the interaction with the support alters the nanoparticle structure, thus creating different scenarios for nanotube growth. Additionally, the same values of E_{adh} that favor fcc structures also notably slow down the nanoparticle dynamics, decreasing the rate of metal-mediated defect annealing, thus hindering a possible template effect.

Although weaker values of E_{adh} result in wetting values $\omega > 90°$ that, in principle, favor a nanoparticle structure adequate for near-armchair growth for growing directions $\varphi_G = 90°$, they also result in more mobile metal atoms than those found for stronger values of E_{adh}. Therefore, at weaker values of E_{adh}, the nanoparticle is expected to be more susceptible to inverse template effects than at stronger values of E_{adh}. Since it has been suggested that near-armchair nanotubes are favored thermodynamically and

kinetically over near-zigzag ones, (Section 3 and [76, 124, 157]) besides analyzing the existence of a substrate-assisted template effect, we also discuss whether such majority of near-armchair nanotubes found at weaker values of E_{adh} may result from such effect. This is carried out through a careful analysis of the simulation trajectories to correlate the nanoparticle structure and the nascent carbon structure, eventually, nanotube structure.

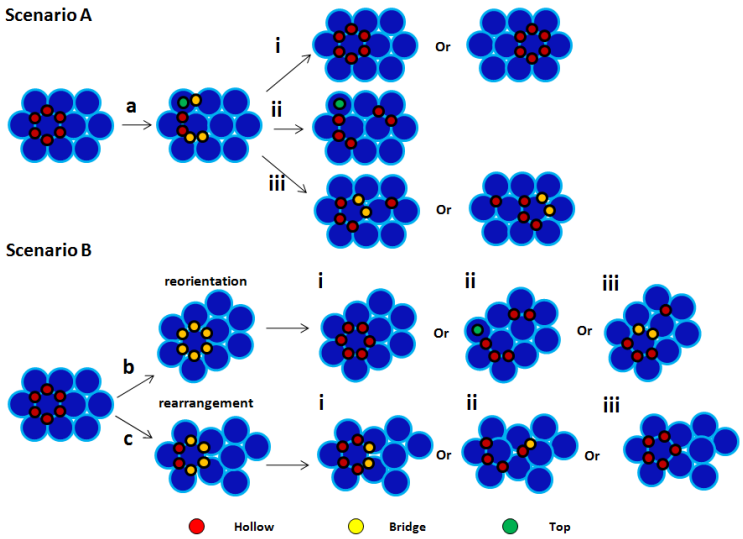

Figure 7-4. Schematics of a typical surface region in the nanoparticle, exemplifying general trends regarding the type of sites occupied and the correlation between the nanoparticle structure and the early formation of carbon rings. In scenario A (top), within a time interval Δt, the surface pattern and the matching ring are stable, *then* the ring breaks down (*a*). In scenario B (bottom), within a time interval Δt the surface pattern and the matching ring are stable, *then* the surface pattern undergoes either a reorientation (*b*) or a rearrangement (*c*). Panels *i* through *iii* schematize typical configurations observed after either event *a*, or *b*, or *c*, occur.

It has been demonstrated through DFT calculations (T = 0 K) that three-fold hollow sites on fcc(111) facets and four-fold hollow sites in fcc(100) facets are the most stable sites for carbon adsorption on transition metals such as Ni, Co, and Fe [222-225]. It follows that the systematic occupation of these sites results in the formation of a graphene monolayer correlated to the underlying facet structure. Such correlation is the foundation for a potential template effect of the nanoparticle upon the nascent nanotube [38, 162, 184]. However, it is important to recognize that at higher temperatures (T =

1000 K) this correlation could be hindered because carbon atoms possess enough energy to overcome diffusion barriers and are able to occupy other less preferred sites (*e.g.*, bridge and top sites). Additionally, at higher temperatures, the surface of the nanoparticle is continuously evolving. Thus, a less optimal scenario for epitaxy than that modeled in DFT calculations occurs. We begin the analysis of this high-temperature scenario looking at the interplay between the surface structure and the early formation of carbon rings (at simulation times $t < 1.0$ ns) on Ni_{32}, Ni_{80}, and Ni_{160} across various values of E_{adh} since E_{adh} affects the nanoparticle dynamics.

Figure 7-4 displays a summary representing some general trends gathered from the visual analysis of the trajectories. The figure is organized to demonstrate two different scenarios: the first (scenario A) where the surface is relatively stable and the carbon nanostructure needs to relocate for maximizing the occupancy of the most stable sites; in the second (scenario B), the surface is able to restructure and rearrange and the carbon nanostructures follow these motions. The main observations are as follows: *1)* Early rings displayed short lifetimes τ ($\tau < 25.0$ ps), wherein pentagonal rings *generally* appear earlier but have shorter lifetimes than hexagonal ones. *2)* Both hexagonal and pentagonal rings display higher stability (*i.e.*, longer lifetimes) when such rings match the underlying surface structure, with a *perfect* matching corresponding to all of the ring atoms occupying hollow positions (**Figure 7-4**) and a *good* matching still occurring when more than half of the ring atoms occupy hollow positions. The interaction of the nanoparticle with these hollow atoms appears to determine the orientation of the ring on the nanoparticle surface (*e.g.*, **Figure 7-4** sA,a-i, where the nomenclature indicates scenario A as sA and the respective pathway a-i). Thus, hexagonal rings usually are centered on metal atoms possessing six surface nearest neighbors, such as in a fcc(111) facet (*e.g.*, **Figure 7-4** sA,a-i), whereas pentagonal rings tend to do so on metal atoms possessing five surface nearest neighbors (*e.g.*, **Figure 7-4** sB,c-iii). *3)* There are time intervals of steady regions, wherein the nanoparticle surface region maintained its structure, and a hexagonal or pentagonal ring is able to match the underlying surface pattern (*i.e.*, most atoms occupying hollow positions). Due to thermal fluctuations, this

carbon structure may be altered, and the ring breaks down, with *most* carbon atoms *no longer* occupying hollow positions (**Figure 7-4** sA,a) for a *few* picoseconds (*e.g.*, $\tau < 3$ ps). This is followed by any of the following events as pictured in **Figure 7-4** sA: (i) the original ring is recovered on the original (or a different) surface location (**Figure 7-4** sA,a-i); (ii) the carbon atoms rearrange into a chain(s), with *most* of them occupying hollow positions (Figure7-4 sA,a-ii); or (iii) the original hexagonal (or pentagonal) ring is not recovered, but a new pentagonal (or hexagonal) ring is formed on the original (or a different) surface location, with *most* atoms occupying hollow positions (**Figure 7-4** sA,a-iii). *4)* A different scenario (**Figure 7-4** sB) occurs when the matching between the surface and the ring is altered because of changes of the surface structure, instead of the ring being broken down. Nonetheless, this surface restructuring destabilizes the ring since most of its carbon atoms are no longer occupying hollow sites (*i.e.*, matching no longer occurs) as a result of either surface reorientation (**Figure 7-4** sB,b) or rearrangement (**Figure 7-4** sB,c). Thus the ring structure only holds for a short time (*e.g.*, $\tau < 3$ ps) before any of the following events occurs: (i) the ring *does not* break down but reorients to match the new surface orientation (**Figure 7-4** sB,b/c-i); or (ii) the ring *does* break down with the carbon atoms rearranging into structures matching the new surface geometry (**Figure 7-4** sB,b/c-ii/iii).

It must be noted that, due to the effect of E_{adh} on the nanoparticle mobility, scenario A (**Figure 7-4**) was observed to dominate at stronger E_{adh} and larger nanoparticle sizes, whereas scenario B (**Figure 7-4**) was observed to dominate at weaker E_{adh} and smaller nanoparticle sizes. It is also noteworthy that, in similar way as carbon structures that matched the underlying surface appeared to be more stable than the ones that did not, nanoparticle (surface) regions supporting matching structures appeared to be more stable (and better defined) than those that did not. This was evidenced in the simulations through observation of the behavior of "carbon-free" surface regions in comparison to "carbon-covered" surface regions during time intervals where epitaxial matching occurred. This may be interpreted as a cooperative effect between carbon and metal, wherein the *template effect* contributes to the stability of carbon structures,

whereas the *inverse template effect* contributes to the stability of metal surface regions. It follows from the mobility–E_{adh} relation that this cooperative effect is more important at weaker E_{adh} and smaller nanoparticles. However, notice that (at least) at this early stage the template effect dominates since analysis of the simulation trajectories shows that the carbon atoms usually rearrange following pattern changes in the nanoparticle surface but seldom vice versa.

7.4.4. Template effect at high temperatures

Figure S5 (*supplementary information* in [226]) and **Figure 7-5** (top) illustrate combinations of the scenarios described in **Figure 7-4** for relatively low E_{adh} values. A first case involves Ni_{32} and E_{adh} = −0.16 eV (Figure S5 in [226]), where an existing Y-shaped C_6 chain rearranges to form a pentagonal ring (branched) on a *defective* fcc(111) facet. Since the matching was non-optimal, a sequence of events consistent with scenarios A and B illustrates the cooperative stabilization between carbon nanostructures and the metal surface with the formation of a hexagonal ring accurately matching a *perfect* fcc(111) facet. This is maintained despite the reorientation of the latter, consistently with scenario B-b in **Figure 7-4.**

At the slightly higher E_{adh} = −0.26 eV (**Figure 7-4**, top) an H-shaped C_{11} chain preceded the formation of a four-branched pentagonal ring. This ring, centered on a five-coordinated metal atom (see **Figure 7-4** sB,c-iii), was shortly destabilized due to thermal fluctuations but recovered and stabilized during 10.0 ps (scenario A,a-i in **Figure 7-4**). However, when a surface rearrangement no longer favors the pentagonal ring, a hexagonal one is formed instead (scenario B,c-iii in **Figure 7-4**), with 4/6 of the ring atoms in hollow positions, exemplifying how the carbon nanostructures try to follow the evolving surface structure. Also notice that for both E_{adh} values, configurations dominated by occupation of hollow sites last longer (τ > 15.0 ps) than those where this does not occur (τ < 3.0 ps).

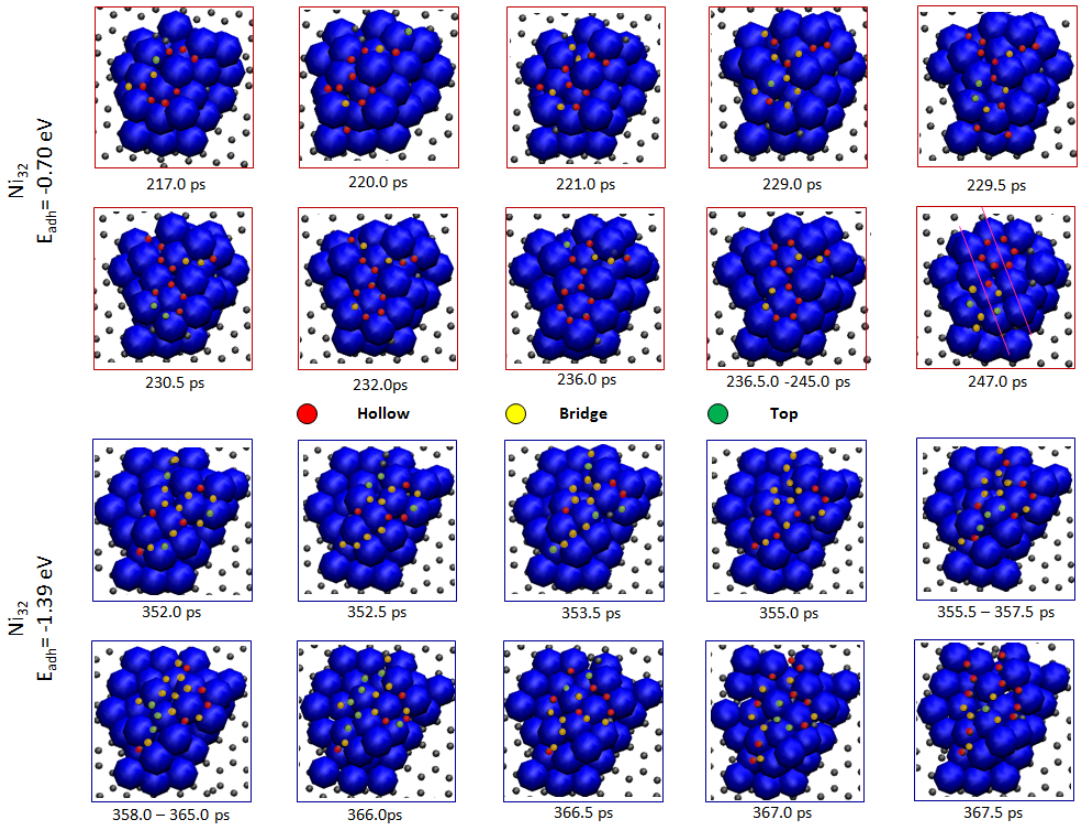

Figure 7-5. Simulation frames showing the initial formation of ring structures on a supported Ni_{32} nanoparticle for three different metal/substrate interactions: E_{adh} = -0.26 eV (top), E_{adh} = -0.70 eV (middle) and E_{adh}= -1.39 eV (bottom). The relevant carbon atoms are colored according to the type of site they occupy on the nanoparticle surface: hollow (red), bridge (yellow), or top (green).

The described scenarios (**Figure 7-4**) can also be mapped onto the actual nanoparticle surfaces for stronger interactions for which the metal atoms appear less mobile. For E_{adh} = −0.43 eV (Figure S5 in [226]) and −0.70 (**Figure 7-5**), H-shaped C_9 and C_{12} chains preceded the ring formation, respectively. For the former case, the surface did not show major changes for 29.5 ps, thus stabilizing a branched hexagonal ring, with carbon atoms preferably occupying hollow sites (scenario A). Moreover, new atoms are incorporated to the ring branches without destabilizing the existing matching. After this time, the surface rearranged, disrupting the matching and breaking the ring (scenario B,c-ii in **Figure 7-4**). For E_{adh} = −0.70 eV (**Figure 7-5**, middle), the surface mobility is further reduced, which allows a strained fcc(111) region to survive for 12.0 ps, supporting a moderately matching branched pentagonal ring for 7.0 ps, after which a

hexagonal ring is formed. The strained region evolves into a fcc(111) region, finally allowing the ring to fully occupy hollow sites. Notice that the preference of ring atoms for hollow sites is observed even during the short-lived (τ = 2.0 ps) transitional five-fold surface configuration. Interestingly, the formation of an additional ring was also observed, which can be related to the formation of the graphene network. Initially, the ring was a pentagonal one following the pattern of the surface but morphed into a hexagonal one following a surface pattern rearrangement.

It must be noted that all of the atoms of the newly formed ring were located in hollow sites, but as a result, since the two rings are connected, the five atoms of the first ring previously occupying hollow sites were displaced. This exemplifies how *lattice mismatching* between the metal and graphene walls can *prevent a dominant occupation of hollow sites* as the graphene network starts to form. Nonetheless, it must also be noted that, despite the resulting offset of the first ring with respect to the surface pattern, the zigzag direction of both rings and the fcc ⟨110⟩surface direction appeared aligned. This suggests that a template effect could occur without the occupation of hollow sites being absolutely dominant. Nonetheless, the occupation of hollow sites still appears to be a key factor because the orientation of the graphene network is to be influenced by the orientation of individual rings adsorbing on hollow sites since carbon atoms attach more strongly to the surface on such sites.

Although a strong metal/substrate interaction reduces the mobility of the surface, for the simulations using the strongest values of E_{adh} (−1.39 eV), it was more difficult to observe the correlation between the surface pattern and the early ring formation. **Figure 7-5** (bottom) shows that a C_{16} structure containing a heptagonal ring preceded the formation of a pentagonal ring. Such ring formed concatenated to the heptagonal ring. In a short time span ($\tau \approx$ 10.0 ps), an additional (concatenated) ring is formed and transformed into a hexagonal ring. However, during this time span, the occupation of hollow sites does not dominate since there is a similar occupation of bridge sites and hollow sites. Interestingly, after this time, the pentagonal and hexagonal rings break

down, whereas the heptagonal ring was observed to remain stable, demonstrating the difficulty in annealing this kind of defects if E_{adh} is too strong.

7.4.5. Dynamics of the adsorption occupancies at nucleation stages

Similar findings to the ones described for Ni_{32} are also encountered for Ni_{80} and Ni_{160}, such as the involvement of a larger number of atoms for the formation of the first ring as E_{adh} increases, and the important role of the occupation of hollow sites in the correlation between the surface structure and the nascent carbon nanostructure. **Figure 7-6** shows the number of carbon atoms occupying hollow, bridge, and top sites at various E_{adh} values for Ni_{32}, Ni_{80}, and Ni_{160} during the initial 1000 ps of simulation. According to the analyses of the simulation trajectories, this time interval corresponds to the formation of the nanotube cap preceding the lift-off. It can be observed that the occupation of hollow sites dominates in the initial stages of the simulations, wherein ~70% of the atoms adsorbed on the surface occupy hollow sites, whereas the remaining ~30% adsorb typically on bridge sites and to a lesser extent on top sites. This is in agreement with the relative adsorption site preference calculated by DFT [222-225].

In an ideal scenario, 100% of the atoms would adsorb on hollow sites in such a way that the pattern of the hollow sites on the surface would determine the geometry of the nascent carbon nanostructures. However, this does not occur due to the high temperature, which allows carbon atoms to occupy a variety of sites, and because of the dynamic structure of the nanoparticle, which does not *rigorously* match the graphene wall of the nanotube due to curvature effects, a time-dependent surface structure, surface imperfections, and lattice mismatching.

Nevertheless, **Figure 7-6** shows an initial ~70% occupancy of hollow sites, indicating that there still is an important influence of the nanoparticle on the geometry of nucleating structures. After a certain time, the percentage of atoms in hollow, bridge, and top positions becomes equal, ~33%. This transition to a more random distribution occurs at earlier times as the value E_{adh} increases and as the nanoparticle size decreases. For instance, for Ni_{32}, this occurs after ~600 ps for E_{adh} = −0.16 and −0.43 eV, whereas it occurs after ~300 ps for E_{adh} = −1.39 eV, in agreement with the results discussed in

Figure 7-5, and Figure S5 in [226]. On the other hand, for E_{adh} = −1.39 eV, this transition occurs after ~300 ps for Ni_{32}, after ~800 ps for Ni_{80}, and after~1000 ps for Ni_{160}.

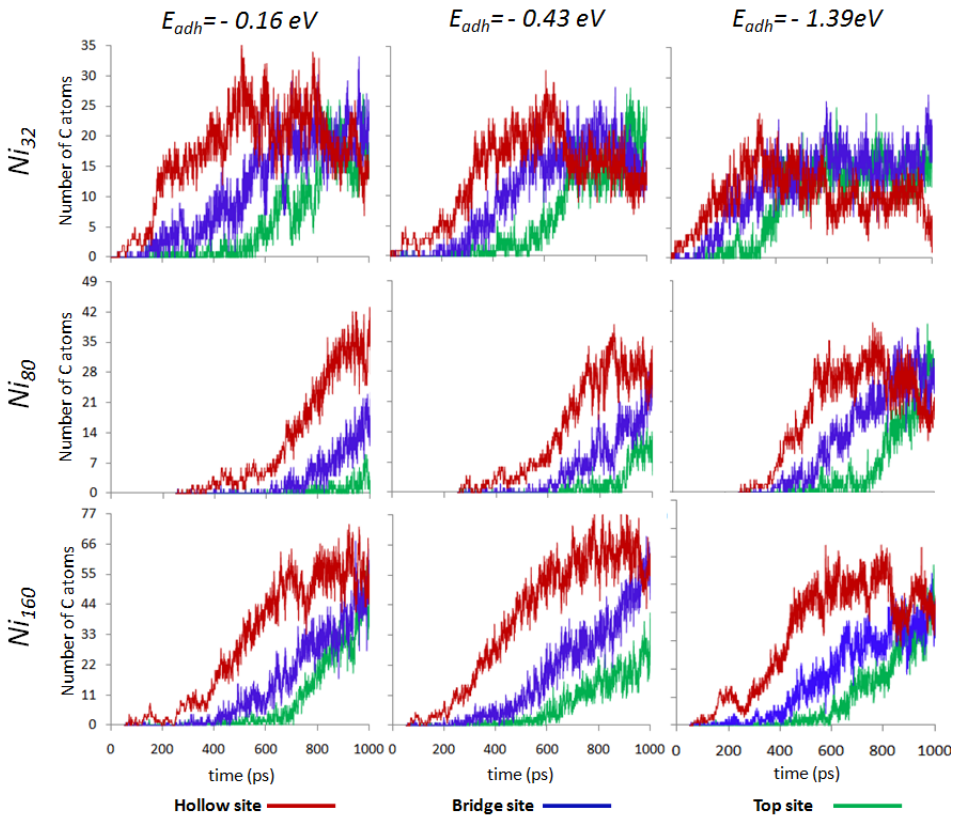

Figure 7-6. Plots showing the number and/or percentile occupation of each type of site on the nanoparticle surface vs. time.

Observation of the simulation trajectories at the transition times shows that such transition to a random distribution of site occupancies coincides with the formation of a graphene network on the surface. This is consistent with the occurrence of lattice mismatching, as discussed for E_{adh} = −0.70 eV in **Figure 7-5**. The results presented in **Figure 7-5** and **7-6** also demonstrate the importance of atom mobility for the growth of defect-free matching structures as occurs for the growth on thin films [227]. If the conditions are such that carbon atoms are not very mobile, it is more difficult for the atoms to move toward the most stable sites, thus facilitating the formation of carbon

nanostructures not matching the underlying surface. These structures tend to be defective. For instance, we noticed that the formation of rings with more than six atoms (*e.g.*, a decagonal ring) became more common as E_{adh} approached −1.39 eV. Moreover, the reduced mobility also hinders the annealing of these defective rings, therefore decreasing the quality of the nanotube structure. On the other hand, the presence of defective rings in the graphene network amplifies the lattice mismatching further hindering the occurrence of a template effect.

7.4.6. Correlation between facet structure and nanotube rim structure at end of nucleation/beginning of carbon nanotube growth

Although lattice mismatching may occur, as the decrease in occupation of hollow sites at the end of nucleation shows in **Figure 7-6**, there may still be a correlation between the structures of the nanoparticle and the nascent nanotube, as shown in **Figure 7-5** for E_{adh}= −0.70 eV. Accordingly, we observed the simulation trajectories to analyze whether such correlation was found or not. The results of Ni_{32} simulations are shown in **Figure 7-7** (Ni_{80} and Ni_{160} cases are shown in Figures S6 and S7 in [226]) for various E_{adh} values at different times. The ⟨110⟩ direction on the nanoparticle surface is denoted by a white solid line. It is observed that the orientation of such direction can vary during the simulation in a manner consistent with scenario B,b in **Figure 7-4**. Although not clearly seen in **Figure 7-7** due to the limited number of simulation frames shown, analysis of the trajectories reveals that the⟨110⟩direction is frequently parallel to the substrate for stronger E_{adh} values, whereas such direction is frequently found at ~30° with respect to the substrate for weaker E_{adh} values. This correlates well with the change in the wetting pattern with E_{adh}. It must be noted that the change in orientation of the ⟨110⟩ direction occurs faster for weaker E_{adh} values due to a higher atom mobility.

Additionally, **Figure 7-7** suggests that indeed there seems to be a correlation between the orientation of the ⟨110⟩direction of the surface and the zigzag direction on the graphene wall. This occurs with some of the rings having their atoms occupying hollow sites, whereas adjacent rings have their atoms occupying other sites, or even not clearly occupying a specific site. It is apparent that the rings matching the surface

pattern through occupation of hollow sites strongly influence the orientation of the graphene network.

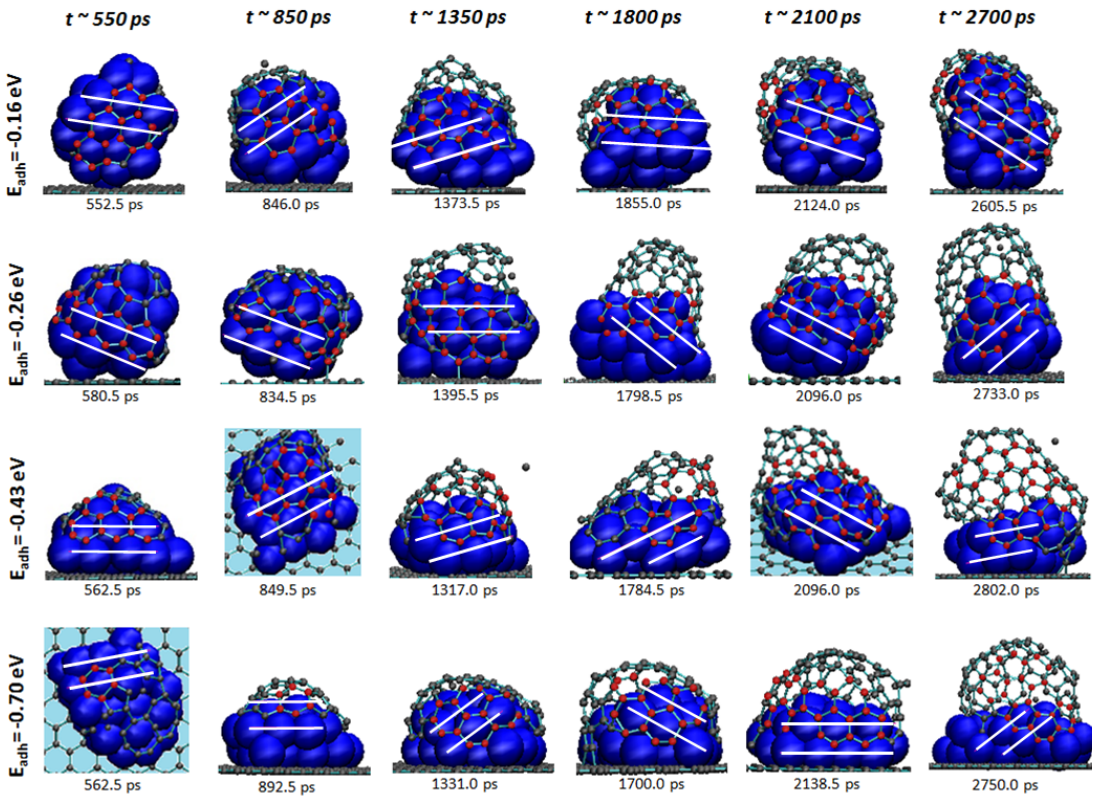

Figure 7-7. Snapshots showing the correlation between the <110> direction in the Ni_{32} nanoparticle and the orientation of the nascent nanotube graphene network at different simulation times.

Broadening the analysis of early ring formation further in the simulation, it is found that scenarios analogous to those discussed in **Figure 7-4** are also encountered once the graphene network has formed. For instance, the graphene network may temporarily mismatch the underlying surface but return to a matching position after a short time (scenario A). Also, the underlying surface may change, resulting in a temporary mismatch, which makes the network to reorient in order to maintain the matching (scenario B). However, it is important to recognize that, as the nanotube cap forms and the graphene network grows in size, the events occurring in one nanoparticle

region are connected to those occurring elsewhere. For instance, matching of a region of nascent graphene network with a nanoparticle region may conflict with matching with another region. Thus the matching in one region may be lost to accommodate matching on another one depending on which one is more energetically favorable. Therefore, it can be inferred in agreement with DFT results [223-225] that the graphene network is oriented to increase the number of atoms occupying hollow sites.

As a result of the nanotube/nanoparticle dynamics, there are time intervals where matching between the nanotube and the nanoparticle becomes unclear, even when these time frames are located between intervals where the correlation is apparent. It must be noted that the correlation between the hexagonal graphene network and the nanoparticle surface also suffers due to the presence of pentagonal or heptagonal (and other) rings, which tend to align their center on top of a metal atom, but preventing neighbor hexagonal rings to orientate "correctly". Since increasing E_{adh} results in nanotubes of lesser quality, it is also observed that the nanotube/nanoparticle correlation is more difficult to observe for stronger E_{adh} values.

In **Figure 7-7**, it can be observed for $t \sim 550$ ps that the number of hexagonal rings matching the surface decreases from four to one as E_{adh} changes from −0.16 to −0.70 eV. As the simulations progress, some of these defects heal, but with more difficulty as E_{adh} increases, as previously discussed. Thus, the intervals during which the correlation can be observed are longer as E_{adh} is decreased. Similar trends are observed for simulations of Ni_{80} and Ni_{160} (Figures S6 and S7 in [226]). Notice that, since the size of the graphene network increases with the nanoparticle size, the percentage of carbon atoms that clearly matches the surface decreases because the number of defects increases (given that for the same time scale it is easier to anneal a smaller network). Similarly, although a larger nanoparticle offers more contact area, it also increases the probability of existence of conflicting regions (due to high temperature dynamics) for the graphene network to match. Thus, for Ni_{160}, the intervals at which the correlation is observed are noticeably shorter than for Ni_{32} and Ni_{80}.

It also follows from the previous discussion that for a particular time not all of the entire graphene network matches the nanoparticle structure (due to either the graphene structure or the nanoparticle structure). On the other hand, as mentioned earlier, the graphene region around the nanotube rim is observed to be very dynamic regarding bond breaking and formation mediated by the dynamics of metal atoms. This occurs in such a way that the rim region constantly follows the nanoparticle surface pattern in a similar way as observed for early ring formation. This means that the rim region is continuously rearranging in an effort to match the underlying structure even though this may cause a mismatch elsewhere.

This is explained on the basis of the lower coordination of the rim atoms, requiring less bonds to be rearranged in order to modify their positions, and to the stronger interaction of these carbon atoms with metal atoms according to DFT calculations and incorporated into the force field used in the simulation [72]. Thus, it is inferred that, energetically, a good matching around the rim, but not optimal elsewhere, is preferred over a good matching elsewhere, but not optimal around the rim. Therefore, the contact between the nanotube rim region and the nanoparticle appears to play an important role for both template effect and defect annealing. Accordingly, the lower number of atoms involved in the nanotube/nanoparticle matching as E_{adh} increases may result from the comparatively poorer contact between the nanotube rim and the nanoparticle. Also, the poorer contact of the rim region with the nanoparticle as E_{adh} increases may hinder the influence of the catalyst structure on that of the nanotube. On the other hand, decreasing E_{adh} may increase the effect of the nanoparticle structure provided that such metal/substrate interaction is strong enough to hinder an inverse template effect.

7.5 Conclusions

Instantaneous catalysis accelerated simulated nanotube growth, reducing the quality of the nanotubes grown, but allowed us to perform a large number of simulations at reasonable computational times. Analyses of the simulation trajectories showed nanotube growth to occur through the stages of (i) carbon dissolution, (ii) carbon

segregation, (iii) formation of chains and rings, (iv) cap formation, (v) cap lift-off, and (vi) growth. Cap lift-off appeared to occur faster for strong E_{adh} values because capillary effects (*i.e.*, nanoparticle stretching inside the nanotube) were not as important as for weak E_{adh} values. Also, at strong E_{adh} values, the nanotubes appeared to grow more defective, which is consistent with lower atom mobility hindering annealing. The growth direction tended to be at a low angle with respect to the substrate for strong E_{adh} values, at a right angle for moderate, and at varying angle for weak E_{adh}.

The final nanotube structures were analyzed to evaluate the chiral angle θ_c, which was determined to be high (near-armchair) or low (near-zigzag). The largest nanoparticles did not present a clear trend regarding θ_c *versus* E_{adh}, but the smallest and the intermediate size did. Interestingly, the intermediate size presented a more defined trend than the smallest one. This suggested a compromise between reducing the nanoparticle size to limit the number of possible chiralities (*i.e.*, indirect chiral control) and increasing the nanoparticle size to improve contact with the nanotube walls, thus resulting in an optimum intermediate nanoparticle size for chirality control. Further details regarding the effect of the nanoparticle structure were explored through analysis of the formation of early rings and the correlation of the <110> surface direction and the nascent nanotube (graphene) wall orientation.

The occupation of hollow sites on the nanoparticle surface appeared as a key factor for establishing a nanotube/nanoparticle structural correlation. Our analysis showed a preference for this site despite the available thermal energy and the nanoparticle dynamics. This was clear during the early ring formation, wherein near 70% of the carbon atoms were shown to occupy such sites. It was shown that early carbon structures attempt to follow the underlying surface structure, even for weak E_{adh} values, as described by scenarios A and B. Nevertheless, a cooperative dynamics between the nascent structures and the nanoparticle was observed where the template effect stabilized the nascent structures and the inverse template effect stabilized the underlying surface, even though the former was observed to dominate.

Upon cap nucleation, lattice mismatching effects become important, and the occupation of hollow sites drops. However, it was still possible to correlate the structures of the nascent network/nanotube and the nanoparticle (**Figure 7-6** and Figures S6 and S7 in [226]). This correlation was more difficult to observe as E_{adh} increased because of more defective network (due to low mobility and more difficult annealing) and poorer contact (decrease of capillary effects). On the other hand, this correlation was easier to observe in the intermediate nanoparticle because of a better contact with the nanotube than that of the smallest nanoparticle and a less conflictive matching than that offered by the largest one (due to conflicting domains orientation on the nanoparticle surface). Additionally, the nanotube rim region in contact with the nanoparticle appears more active than other nanotube regions since it was observed to continuously anneal in an effort to follow the nanoparticle structure (*i.e.*, occupy hollow sites), thus impacting the orientation of the graphene network in rest of the tube. These results support the hypothesis that the catalyst structure affects the nanotube structure, thus encouraging further experimental and theoretical efforts to find the conditions at which this effect can be maximized.

8. EVIDENCE OF SURFACE DIFFUSION AS THE DOMINANT CARBON TRANSPORT MECHANISM DURING SINGLE-WALLED CARBON NANOTUBE GROWTH ON SUPPORTED METAL NANOPARTICLES

8.1 Summary

One of the outstanding questions about synthesis of single-walled carbon nanotubes is what is the role and mechanism of carbon diffusion during chemical vapor deposition synthesis. Examination of individual trajectories of all carbon atoms involved in reactive molecular dynamics simulated growth of single-walled carbon nanotubes on supported nanoparticles identifies carbon atoms involved in surface diffusion, bulk diffusion, and carbide formation. We show that transitions between induction, nucleation, and growth are denoted by saturation of the nanoparticle and by changes in the catalytic regime. It is found that nucleation and dissolution may occur simultaneously, with pre-saturation nucleation driven by the low-energy barrier for surface diffusion. It is concluded that for 'carbonphilic' catalysts, induction and nucleation periods are usually governed by bulk diffusion, while the growth period is dominated by surface diffusion. Surface diffusion control during growth is in agreement with successful nanotube growth on metals such as copper and gold, which do not dissolve carbon. In the range studied, C solubility decreases with particle size, and the Ni/C ratios found coincide with stoichiometries of known Ni carbides.

8.2. Introduction

Single-walled carbon nanotubes (SWCNTs) are an allotropic tubular form of carbon having properties [228] that confer them the potential to revolutionize electronics [3] and other fields [5]. In particular, whether a nanotube is metallic or semiconductor (and its associated band gap) depends on their structure and chirality [6]. Currently, the heterogeneity (chirality-wise) of as-synthesized nanotubes is the main obstacle for full exploitation of nanotube-based technologies due to the application-dependent requirement of either metallic or semiconducting nanotubes [228]. In this regard, tailoring nanotubes via control of the nanocatalysts structure is among the proposed

strategies to achieve chirality control during chemical vapor deposition (CVD) synthesis. [20, 24, 45, 48, 88, 162, 226]

Nonetheless, a rational approach to chirality control requires a thorough understanding of the still under debate nanotube growth mechanism [7, 8, 13, 14, 16, 23-25, 28, 30, 145, 217, 229, 230]. As pointed out in recent reviews [8, 217, 230], the vapor-liquid-solid mechanism (VLS) [22] despite criticisms [16, 17, 28, 231], and despite successful nanotube synthesis in challenging conditions [26, 27, 232] is surprisingly accepted as the prevalent growth mechanism at least for *typical* synthesis conditions using metallic nanoparticles. Central to the VLS model [22] is the dissolution of carbon by a liquid nanoparticle and nanotube growth controlled by carbon bulk diffusion. In this context, whether the dissolved carbon forms a carbide is subject to debate [7, 24, 25, 231, 233, 234].

The liquid nanoparticle hypothesis is based on nanoparticle melting point depression [39, 235], eutectic formation due to carbon dissolution [36], and in lesser extent to nanoparticle deformation during growth [17, 33, 226] which can be explained via a creep mechanism. On the other hand, the bulk diffusion hypothesis can be based on growth activation energies [13, 15], detection of carbon inside the nanoparticle [13, 14, 24, 234], diffusion-dependent growth models [18, 39] and carbon solubility values of typical metal catalysts. Regarding the last point, although Takagi *et al* [26] have synthesized nanotubes on copper and gold, which negligibly dissolve carbon in bulk form, a later work by the same group suggests that such nanoparticles do dissolve carbon [23].

Density functional theory (DFT) calculations show that surface-diffusion (or sub-surface diffusion) shows a lower energy barrier than bulk-diffusion on stable solid metal slabs [28, 29] (T = 0K), but do not capture the structural evolution of the nanoparticle during nanotube growth (T~1000 K) [16, 17, 33, 219, 226]. Density functional tight binding molecular dynamics DFTB-MD simulations (T = 1500 K) by Morokuma *et al* [30] have shown that carbon structures can nucleate on a Fe_{38} without carbon dissolution (although with a high carbon feeding rate). However, more recent efforts from

Morokuma *et al* [25] (T=800-2000 K) show the depletion of initially dissolved carbon in M_xC_y unsupported nanoparticles consistent with the VLS mechanism. Although valuable since they account for electronic effects (while less computationally expensive than DFT), DFTB-MD simulations currently yield piecewise information of nanotube growth limited to a ~500 ps time window, which prevents from obtaining a continuous picture of nanotube growth. Thus, considering the vast nanotube growth parameter space, reactive classical MD is a valuable alternative for its exploration.

In this contribution, we determine the trajectory of all carbon atoms in a series of simulations of nanotube growth (T=1000 K) on supported nickel. Simulations are done at various nanoparticle sizes, and varying the interaction between the nanoparticle and an immobilized model support to directly explore the carbon transport mechanism and potential carbide formation through a continuous picture of nanotube growth. We select nickel because of its prominence as nanotube growth catalyst, and its capacity to form carbides. Also, we chose to support the nanoparticles due to the potential relevance of supported systems to chiral control strategies [20, 45, 162, 226], and to the possibility of altering the nanoparticle mobility with the nickel/support interaction (an effect similar to lowering temperature) to explore its effect on carbon transport.

Recently, Maruyama *et al* [236] calculated the rate growth of individual nanotubes of different chiralities, using ethylene (a C(2) type gas) as precursor gas and iron as catalyst, demonstrating that near-armchair nanotubes grow faster than near-zigzag ones (T~1360 K) in agreement with our previous work (Section 3) [124]. We predicted that under a C_2-based mechanism, nanotubes should grow faster from near-armchair caps than from near-zigzag due to the formation of a higher number of active sites in near-arm chair caps at each successive C_2 addition. However, as pointed out by Ding *et al* [32], this implies that bulk-diffusion may not be the controlling step in nanotube growth, suggesting that the energy barrier for addition of carbon to the nanotube rim (0.9 eV for CH_4, and 1.3 eV for C_2H_2) may control growth.

Upon analysis of growth rates, dissolution curves, carbon atom trajectories (and their dissolution residence times in the nanoparticle) we show that surface diffusion may

increasingly contribute more carbon atoms to the nanotube structure than bulk diffusion, as nanotube formation advances through induction, nucleation and growth stages. This is true even at a high temperature (T=1,000 K), effects of metal/support interaction strengths and a material that readily dissolves carbon (nickel). Since diffusion through the nanoparticle is initially observed but decreases with time, we propose that dissolution follows a simple model based on the difference between the carbon content of the nanoparticle and the expected saturation value, which we observed to be dependent on nanoparticle size. Based on dissolution residence times we identify carbon atoms that hint a stabilization of the M_xC_y nanoparticle that we suggest to be a harbinger of carbide formation later in the growth stage although at times beyond the current simulation times.

8.3. Computational methods

We use our reactive classical molecular dynamics code, SIMCAT [72], to simulate nanotube growth on nickel nanoparticles supported on a graphene support, where the metal/support interaction is artificially varied through the parameter α in Equation 8-1. Metal/metal (MM) interactions are described by the Sutton Chen potential [71], carbon/carbon (CC) interactions by a modified Brenner potential [72], and metal/carbon (MC) (and metal/support interactions (MS)) by a reactive bond order (REBO) potential with a general form given by Equation 8-1, where the values of α depend on coordination numbers and on whether the carbon atoms belong to the support. The force field parameterization accounts for the screening of CC interactions within the nanoparticle.. Although electronic effects are not included explicitly in our potential, these are implicitly included in the DFT-derived parameters. On the other hand, adjustable parameters such as α are convenient to explore regions of the nanotube growth parameter space as shown in [201, 202].

$$E_{ij} = \alpha V_{repulsion}(r_{ij}) - \alpha^{1.1} V_{attraction}(r_{ij}) \qquad (8-1)$$

A detailed description and parameterization of this force field is described in a previous work [72]. For MS interactions, varying α results in different values of energy of adhesion E_{adh}, which we estimated calculating the total energy of a single-layer support slab (E_S), a single-layer metal slab (E_M), and the two slabs together (E_{MS}) for their use in Equation 8-2 (n_m is the number of metal atoms in the slab).

$$E_{adh} = (E_{MS} - E_M - E_S)/n_m \qquad (8 - 2)$$

The outcome consisted of five values of E_{adh}, namely, -0.16 eV, -0.26 eV, -0.43 eV, -0.70 eV, and -1.39 eV. The comparison of these values with experimental data for some metal/support systems has been reported in Section 7 and [226]. The first two E_{adh} values are weak interactions, and the last two are strong ones. A temperature of 1000 K selected based on typical CVD processes was controlled using a Langevin thermostat [237]. The carbon feeding process was modeled using a C(1) precursor gas maintained at $P_{gas} \sim 11$ atm. The motion of gas molecules is determined by a 1000 K velocity distribution. When a gas molecule impinges a free catalyst site, catalysis (conversion to a C atom) occurs according to a conversion factor *f*. While simple, this scheme eliminates bias in the initial positions of carbon on the catalyst. We use $f=1.0$ to accelerate growth. The three stages of growth are obtained in 5.0 ns of simulation, with the catalytic activity depending exclusively on the number of free catalyst sites and precursor gas pressure [201]. The simulation step was 0.5 fs, and configurations are collected every 0.5 ps producing simulation trajectories of 10,000 frames.

To identify the carbon atoms we use their index *n*, which corresponds to the catalysis sequence. Thus carbon atom *n+1* was produced after *n*, and the atom indexes can be used to indicate the progress of the simulation. Carbon atom *n* throughout the simulation was classified as: (0) uncatalyzed, (1) dissolved, and (-1) not dissolved, based on the calculation of the number of metallic nearest neighbors (MNN) using a 2.5 Å cutoff around it. A dissolved carbon atom has MNN $\geq$ 5, whereas MNN < 5 corrresponds to a non-dissolved atom. The cutoff was calibrated to reproduce standard manual counts of dissolved atoms. The cutoff is 0.6 Å larger than typical NiC distances

in carbides ~1.9 Å [238]; the difference accounts for nanoparticle thermal fluctuations and dynamic reconstruction. It must be noted that due to such reconstruction MNN = 5 is a borderline case, with surface carbon atoms *occasionally* having five metal neighbors. Moreover, due to this reconstruction, the nanoparticle diameter and height vary with time and $E_{adh.}$ Thus the nanoparticles used in this study are identified as Ni_{32}, Ni_{80}, Ni_{160}, but their geometrical parameters will be discussed through subsection 8.3. We select reduced nanoparticles (M^0) to start our simulations based on the usual detection (and observation) of reduced metal pre-growth [17, 20, 231].

8.4. Results and Discussion

8.4.1. Precursor catalysis and carbon dissolution

Figure 8-1a shows representative *catalysis curves* displaying the number of carbon atoms generated by precursor decomposition versus simulation time for Ni_{32}, Ni_{80}, and Ni_{160} (E_{adh} = -0.70 eV). As the nanocatalyst size increases, the number of carbon atoms generated by catalysis increases. During 5,000 ps, simulations on Ni_{32} generated 175-179 carbon atoms; on Ni_{80}, 241-282 carbon atoms; and on Ni_{160}, 398-505 carbon atoms, with the highest number corresponding to the strongest E_{adh}'s. The slope of the catalysis curves (**Figure 8-1**) yields the catalysis rate, with the observed change in slope at time t_t signifying a change in catalytic regime (indicated by vertical dashed lines in **Figure 8-1**a). The catalysis rates for regime I ($0 < t < t_t$), and regime II ($t_t < t < 5.0$ ns) are given by $R_c(I)$ and $R_c(II)$, respectively. **Table 8-1** reports $R_c(I)$, $R_c(II)$ and t_t values for all our simulations, where it is apparent that the highest catalysis rate occurs before t_t. Observation of **Figure 8-2** (snapshots of representative simulations at various times) reveals that at $t=t_t$ the nanoparticle becomes considerably covered by an incipient carbon cap, thus explaining the regime transition (and catalysis rate decrease) on the basis of the lower number of free catalyst active sites. Before $t=t_t$, the nanoparticle is sparsely covered (**Figure 8-2** – $t = t_s$) so $R_c(I)$ increases with size, as the latter correlates with the number of surface sites. Due to higher wetting of the support, an increase in E_{adh} strength increases the nanoparticle surface/volume ratio, but some of the gained surface is lost in the metal/support interface, thus there is not a clear correlation between $R_c(I)$

and E_{adh}. On the contrary, R_c(II) shows an unclear correlation to size (a larger nanoparticle results in the nucleation of a correspondingly larger cap), but a clear correlation with E_{adh} because as the latter increases, the nanotube/nanoparticle contact decreases leaving comparatively more free active sites on the surface. This is due to the lower impact of capillary forces on the nanoparticle shape as the strength of E_{adh} increases. As **Figure 8-2** shows comparatively for E_{adh} values of -0.26 eV and -0.70 eV for t=t* and t=5.0 ns, the cap lift-off is more difficult for a weaker interaction (-0.26 eV), with more metal atoms drawn into the nanotube interior. Accordingly, after $t=t_t$, more free active sites are found for the stronger E_{adh} (-0.70 eV). Observation of the system at $t=t_t$ shows a correlation between the regime transition and the end of *cap nucleation.*

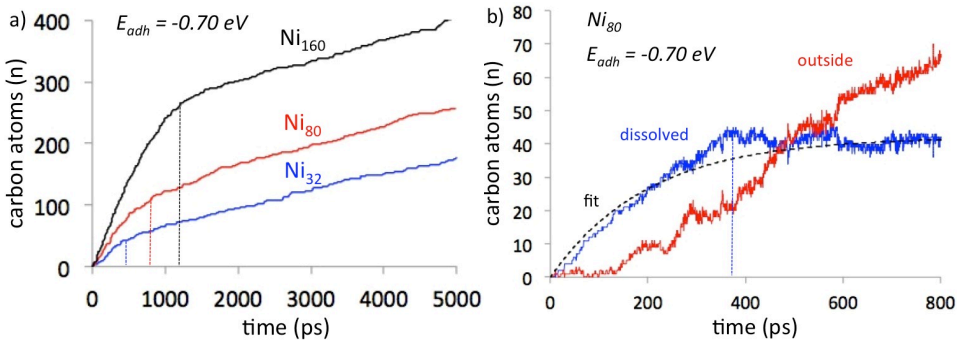

Figure 8-1. a) Number of carbon atoms yielded from catalysis of the precursor gas as a function of time, wherein the slope corresponds to the catalytic rate R_c [=] n_c/ps. Two precursor decomposition (catalytic) regimes can be observed, a fast regime early in the simulation (I), and a slow one (II) after a time indicated by the vertical dashed lines. Plot corresponds to catalysis on Ni_{32} (blue), Ni_{80} (red) and Ni_{160} (black) nanoparticle with an interaction with the support given by E_{adh} = -0.70 eV. b) Number of carbon atoms dissolved (blue) and outside (red) the nanoparticle as a function time during the fast catalytic regime on a Ni_{80} nanoparticle (for E_{adh} = -0.70 eV). The vertical dashed line indicates the point of maximum solubility. A fit to the dissolution curve according to Equation 8-4 is shown in (black) dashed line.

Figure 8-1b shows the dissolution curve (dissolved carbon versus time) and growth curve (non-dissolved carbon versus time) for a representative case (Ni_{80}, E_{adh} = -0.70 eV) during regime I (i.e. nucleation). Non-dissolved (carbon) atoms may be part of isolated C_n chains on the nanoparticle surface, or part of the nanotube (nascent structures). The slope of the *dissolution* curve represents the *net dissolution rate*. This

curve also shows a transition from a fast (dissolution) regime to a notoriously slow one, with the transition time t_s indicated by a vertical dashed line.

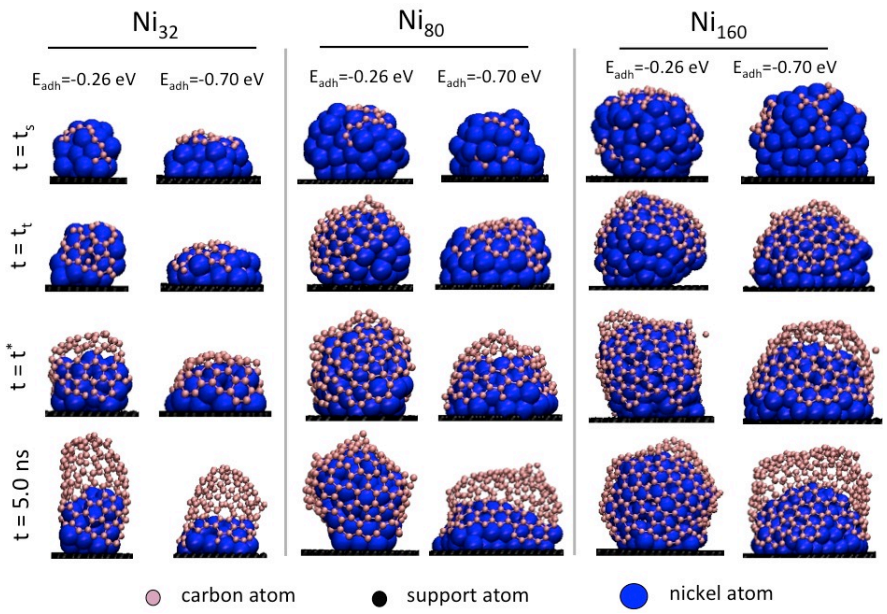

Figure 8-2. Snapshots showing the progress of simulated nanotube growth for Ni_{32}, Ni_{80}, and Ni_{160} and interactions with the support given by values of E_{adh} of -0.26 eV and -0.70 eV. Topmost-row snapshots correspond to the moment the nanoparticle reaches saturation ($t = t_s$). Second-row snapshots correspond to the moment the catalytic regime transitions from fast to slow ($t = t_t$). Third-row snapshots correspond to the moment the nucleated cap starts lifting-off from the nanoparticle ($t^* \sim 1.5$ ns for Ni_{32}, $t^* \sim 2.0$ ns for Ni_{80}, $t^* \sim 3.0$ ns for Ni_{160}). Nickel atoms are represented with blue spheres, support atoms with black atoms, and carbon atoms with pink spheres.

Table 8-1 reports the values of t_s, the number of dissolved atoms at t_s ($n_d(t_s)$), and the average number of dissolved atoms from t_s until t_t ($n_d(I)_{av}$). Comparison between $n_d(ts)$ and $n_d(I)_{av}$ reveals a moderate nanoparticle supersaturation (20.0-27.0% for Ni_{32}, 12.5-22.0% for Ni_{80}, and 5.0-8.0% for Ni_{160}) under these conditions. Nonetheless, the black dashed (fitted) curve in **Figure 8-2**b shows that the dissolution process is controlled by mass transfer [239], thermodynamically driven by the difference (n_d^{sat}-n_d) where n_d^{sat} is a saturation value dependent on size, shape, and material of the nanoparticle; and n_d is the number of carbon atoms 'currently' dissolved. Thus the dissolution rate is given by Equation 8-3, where the proportionality constant k' is an overall mass transfer coefficient accounting for kinetic parameters including diffusion

activation energies. We must note that although the energy barrier for surface diffusion is smaller than for bulk diffusion [28, 29] dissolution is a more favorable process than surface diffusion, at least until an incipient cap is formed (since the presence of the nanotube rim modifies the potential of the surface) [16, 32].

$$\frac{dn_d}{dt} = k'\left(n_d^{sat} - n_d\right) \tag{8 - 3}$$

Integration with the initial conditions $n_d = 0$ for $t = 0$ results in a dissolution curve given by Equation 8-4:

$$n_d = n_d^{sat}\left(1 - e^{-k't}\right) \tag{8 - 4}$$

Table 8-2 shows the fitting parameters corresponding to the dissolution curves of all our simulations based on Equation 8-4; the correlation factor *r*, and the standard deviation between the model and simulation data; and nanoparticle geometrical parameters during nucleation. It is apparent that the saturation value n_d^{sat} increases with nanoparticle size, and decreases as the strength of E_{adh} is increased. The effect of relatively weak E_{adh} values of -0.16 eV and -0.26 eV determined nanoparticles with an aspect ratio close to one (during nucleation), and a Ni/C ratio (based on n_d^{sat}) of ~2.9 for Ni_{32}, ~1.95 for Ni_{80}, and ~ 1.53 for Ni_{160}, which resemble known carbide stoichiometries Ni_3C, Ni_2C and Ni_3C_2 [238]. We must note that these ratios may be compatible with the coexistence of M_3C and M_xC_y discussed by Curtarolo *et al* [240], with the solubility of the M_xC_y phase decreasing as the particle size is reduced (as observed here). Stronger E_{adh} values -0.43 eV and -0.70 eV produce more flattened nanoparticles, with the Ni/C ratio slightly increased to ~3.5 for Ni_{32}, but approximately maintained for Ni_{80} and Ni_{160}. However, the strongest E_{adh}, -1.39 eV, did significantly change nanoparticle shape and solubility, with Ni_{32} featuring a Ni/C ratio of 5.3; Ni_{80} one of 2.5, and Ni_{160} one of ~5.0.

Table 8-1. Characterization of the growth process on Ni_{32}, Ni_{80}, and Ni_{160} nanoparticles with different interactions with the support E_{adh} (eV). [a] time t_s (ps) corresponds to the moment of maximum carbon dissolution. [b] $n_d(t_s)$ and $n_o(t_s)$ are the number of carbon atoms dissolved and outside of the nanoparticle at $t=t_s$, respectively. [c] $n_d(I)_{av}$ is the (rounded) average of n_d for $t_s < t < t_t$. [d] time t_t corresponds to the moment of transition from a fast to a slow catalytic regime. [e] $n_{cut}(t_t)$ is the number of carbon atoms yielded from catalysis at $t = t_t$. [f] $R_c(I)$ and $R_c(II)$ are the catalytic rates for the fast and slow (II) regimes (n_c/ps), respectively. [g] n_d corresponds to the (rounded) average of n_d for 3.0 ps < t < 4.0 ps.

E_{adh}	t_s [a]	$n_d(t_s)$ [b]	$n_o(t_s)$ [b]	$n_d(I)_{av}$ [c]	t_t [d]	$n_c(t_t)$ [e]	$R_c(I)$ [f]	$R_c(II)$ [ff]	$n_d(II)_{av}$ [h]
				Ni_{32}					
-0.16	220	14	12	11	1000	78	0.081	0.021	8
-0.26	280	14	14	11	500	52	0.092	0.025	11
-0.43	150	12	16	10	500	49	0.096	0.024	9
-0.70	380	12	25	10	500	44	0.097	0.028	8
-1.39	280	9	18	-	1500	90	0.055	0.025	-
				Ni_{80}					
-0.16	313	45	24	39	1500	186	0.123	0.016	39
-0.26	490	47	26	40	1500	162	0.108	0.021	40
-0.43	380	43	43	40	800	130	0.165	0.023	39
-0.70	360	45	24	40	800	107	0.139	0.034	33
-1.39	530	39	30	31	1000	103	0.108	0.044	18
				Ni_{160}					
-0.16	520	107	73	101	1200	278	0.242	0.025	94
-0.26	650	105	77	99	1200	273	0.222	0.026	92
-0.43	450	101	25	96	1200	273	0.237	0.029	93
-0.70	440	93	44	90	1200	262	0.225	0.033	85
-1.39	600	94	93	87	1200	269	0.225	0.061	65

We infer that reducing atom mobility through the interaction with the support causes a reduction on solubility (i.e. n_d^{sat}) similar to that expected by a decrease in temperature. The volume/surface ratio decreases from Ni_{160} to Ni_{32}, accompanied by solubility decreases. At constant number of (metal) atoms, the particle shape affects solubility due to the effect of the former on the particle volume/surface ratio. Accordingly, during the growth stage (after nucleation), the value of n_d^{sat} may be reduced and restablished

periodically as the nanoparticle also periodically elongates and recovers its shape [16, 17, 33, 219] due to competition of MM, MS, and nanotube-particle interactions.

Table 8-2. Fitting parameters n_d^{sat} and k' (ps^{-1}) according to the dissolution rate model given by Equations 8-3 and 8-4; and the correlation factor r and standard deviation S between the model and the simulation data for different nanoparticle sizes and interactions E_{adh} with the support. Diameter d and height h of the nanoparticle are also included.

	Ni_{32}					**Ni_{80}**					**Ni_{160}**				
	-E_{adh} (eV)														
	0.16	***0.26***	***0.43***	***0.70***	***1.39***	***0.16***	***0.26***	***0.43***	***0.70***	***1.39***	***0.16***	***0.26***	***0.43***	***0.70***	***1.39***
n_d^{sat}	11	11	9	9	6	42	41	41	41	32	104	105	101	96	90
k'(10^{-3})	12.0	16.0	23.0	7.0	25.0	7.5	6.0	6.8	6.0	7.3	3.8	4.0	4.0	4.0	5.0
r	0.90	0.91	0.81	0.94	0.81	0.98	0.98	0.99	0.98	0.97	0.99	0.99	1.00	0.99	0.99
S	1.09	1.04	0.97	1.08	1.89	3.92	2.90	2.86	3.12	3.45	7.99	5.16	6.16	6.57	6.53
d(nm)	1.0	1.0	1.2	1.2	1.3	1.3	1.3	1.5	1.5	1.6	1.6	1.6	1.8	1.8	2.0
h(nm)	1.0	1.0	0.5	0.5	0.4	1.2	1.2	1.1	1.1	0.7	1.4	1.4	1.4	1.4	1.0

As an example, for weak interactions (E_{adh} = -0.16 and -0.26 eV), Ni_{32} periodically elongates 0.2 nm while reducing its diameter in 0.3 nm. For stronger interactions, (E_{adh} = -0.43 and -0.70 eV), only a 0.1 nm elongation was observed in Ni_{32}. For the strongest E_{adh} = 1.39 eV, nanotube growth promotes wetting, permanently changing the nanoparticle shape (a 2D cluster for Ni_{32}) and reducing C solubility. Nevertheless, our dissolution model describes well the dissolution process as shown by the correlation factor r and standard deviation S.

According to our model and simulations, at the beginning of nanotube synthesis (induction period), the driving force for dissolution is comparatively high with respect to later stages since the nanoparticle is initially carbon-free, and then saturates (the actual driving force depends on the material solubility at the conditions of synthesis). However, we must note that formation of chains and condensation of rings on the particle surface can occur before saturation takes place as observed in **Figure 8-2** for t_s.

This pre-saturation nucleation occurs due to the low-energy-barrier surface diffusion allowing a random walk of carbon atoms on the particle surface before they dissolve. If during their random walk carbon atoms meet each other, they can no longer dissolve without a bond dissociation energy penalty. We infer that an increase in C solubility (material/conditions-dependent) hinders pre-saturation nucleation, which can be favored by an increase in carbon feeding rate (although a too fast rate may result in catalyst poisoning by amorphous carbon since the healing of defects depends on the feeding rate [218]).

8.4.2. Trajectory of carbon atoms

Figure 8-3 shows representative trajectories of more than 3,000 carbon atom trajectories determined in this study. The graphs represent the 'status' of the relevant carbon atom (0 = uncatalyzed, 1 = dissolved, and -1 = nondissolved) versus time. In **Figure 8-3**a the relevant carbon atom is uncatalyzed at point *1*, and catalyzed on the particle surface at point *2*, and remains nondissolved throughout the simulation (e.g. point *3*). Thus, such type of trajectory necessarily corresponds to an atom subject to *surface diffusion* (SD carbon). **Figure 8-3**b corresponds to a carbon atom that upon catalysis (point *2*) dissolves, emerging later to the surface (point *4*) and remaining nondissolved from then on; thus representing an atom subject to *bulk diffusion.* Finally, **Figure 8-3**b shows an atom that upon catalysis (point *2*) remains dissolved throughout the simulation (points *3*, *4*, *6*, *7*, and *9*), although ephemeral appearances may occur on the surface – typically on the surface region below the lifted-off cap – (points *5* and *8*). From a kinetic point of view, even if the carbide is the stable phase, its formation requires longer times, so only carbon atoms with longer residence times may be involved in carbide formation. Moreover, it has been stated that diffusion of carbide carbon atoms is relatively slow [14]. Thus, within the limitation of simulation time, the type of trajectory in **Figure 8-3**c corresponds to an atom *candidate* for *carbide formation* (CF carbon).

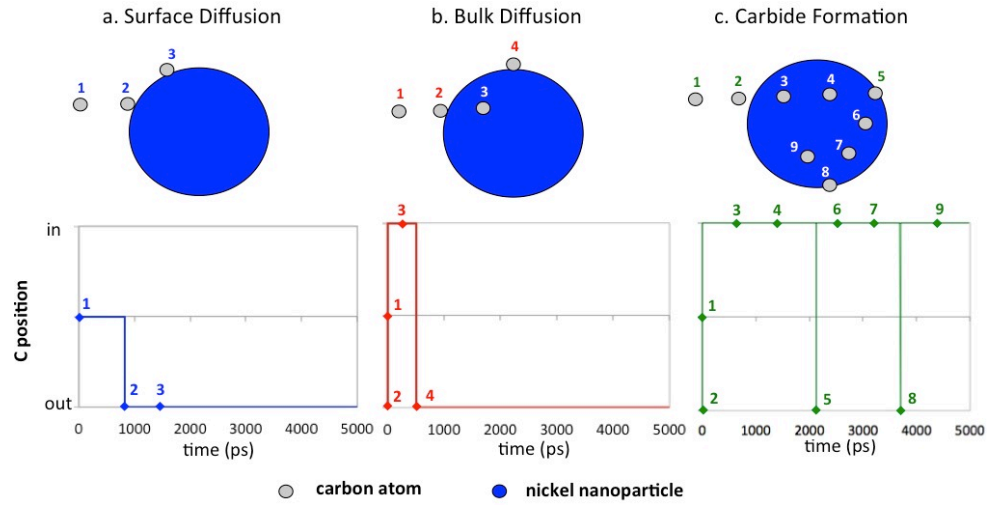

Figure 8-3. Representative trajectories of carbon atoms a) undergoing surface diffusion, or b) bulk diffusion, or c) suitable for carbide formation. Trajectories correspond to carbon atoms 53, 3, and 4, respectively, for nanotube growth simulated on Ni_{32} (E_{adh}=-0.70 eV).

The period of time during which a carbon atom remains dissolved according to its calculated trajectory is the *dissolution residence time* τ_D. Collecting this information from all carbon atom trajectories we constructed the histograms shown in **Figure 8-4**, which display the distribution of carbon atoms (distributed by simulation cases) based on the values of τ_D. We only include atoms whose dissolution residence time τ_D is 1 ps and above, thus the histograms only include atoms that either undergo bulk diffusion (BD) or are candidates for carbide formation (CF).

The distributions in **Figure 8-4**a-c are typically concave, with a minimum at an intermediate τ_D range, and two boundary maxima at τ_D=1-1,000 ps, and τ_D=4,000-5,000 ps (with somewhat more atoms in the 1-1,000 ps range than in the 4,000-5,000 ps one). Such bimodal distribution clearly denotes the existence of one group of atoms that dissolves and migrates to the surface comparatively fast and another that tends to remain dissolved. The latter group is compatible with a *potential* carbide formation (CF), because longer dissolution times can facilitate the stabilization of the carbide. The former group, on the other hand, is compatible with bulk-diffusion (BD), wherein more than 50% of all atoms with τ_D in the 1-1,000 ps range having a τ_D smaller than 250 ps.

An inspection of their distance to the particle center of mass reveals that these BD carbon atoms typically do not migrate very deep into the particle.

Notice that there are atoms that remained dissolved throughout the simulation, but have dissolution times noticeably smaller than 5,000 ps due to the limit imposed by the simulation time. For instance, a carbon atom catalyzed at 2,000 ps can have maximum dissolution time of 3,000 ps. In our analysis we established a 3,000 ps threshold in τ_D to determine whether a carbon atom tends to remain dissolved hence having potential to form a carbide phase (i.e. CF carbon), since the τ_D minima is typically located at this value. We must also note that the population of atoms with τ_D in the 3,000-5,000 ps range is dominated by atoms with τ_D > 4,000 ps. The number of CF carbon atoms determined with this criterion agrees well with the number determined with a one-by-one inspection of trajectories for three selected cases (Ni_{32}, Ni_{80} and Ni_{160} at E_{adh} -0.16 eV). We must emphasize that although we identify carbon atoms whose dynamics suggests carbide formation, conclusively determining carbide formation requires further analysis of the particle structure and dynamics and simulation of more advanced growth stages.

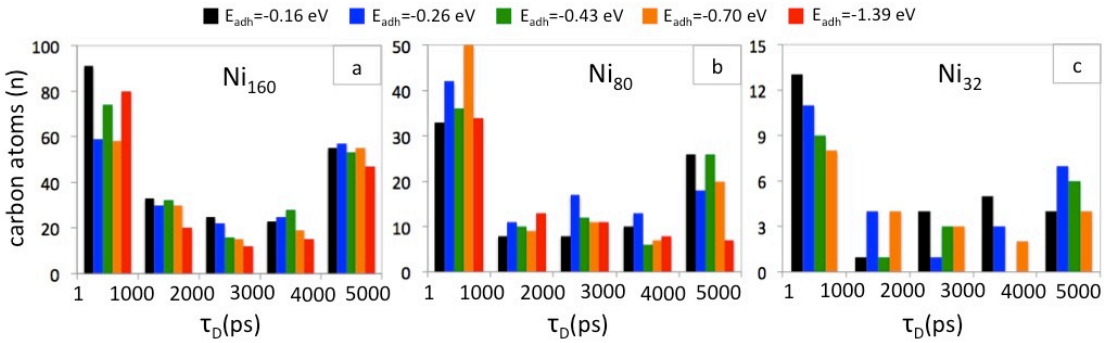

Figure 8-4. Histograms showing the distribution of carbon atoms according to their dissolution residence times (τ_D). Each panel shows the distribution for different values of E_{adh} (see color code on top) for a particular nanoparticle size. a) Distribution for Ni_{32}, b) Distribution for Ni_{80}, and c) Distribution for Ni_{160}.

Since after t_s (and t_t) the *dissolution curve* (**Figure 8-1**b) is approximately constant, the plot of non-dissolved carbon versus time (*growth curve*) (**Figure 8-1**b), and the *catalysis curve* (**Figure 8-1**a) have nearly identical slopes. Thus after nucleation (t >

t_t) (steady state growth) the nanotube growth rate (R_G) is given by R_c(II) in **Table 8-1**. We use these data to analyze the impact of a carbon atom according to its dissolution time on the overall growth. The *average* catalytic/growth rate in our simulations (0.0268 C atoms/ps) estimates that, in average, one carbon atom is added to the nanotube every 37.3 ps. Thus 6-7 carbon atoms have been added to the nanotube structure before a carbon atom with τ_D = 250 ps (BD carbon) becomes part of the nanotube. This number increases to 26-27 atoms for a carbon atom with τ_D=1,000 ps, and to 53-54 atoms for one with τ_D =2,000 ps. For CF carbon, this number is 80-81 atoms for τ_D=3,000 ps, and 107-108 atoms for τ_D=4,000 ps, thus these atoms contribute only to ~1% of the nanotube structure, hence their dynamics are rather disconnected from nanotube growth.

It is noteworthy that the number of carbon atoms with τ_D > 4,000 ps corresponds to 50% and up of the average solubility $n_d(II)_{av}$ (**Table 8-1**). Thus 50% and up of the atoms that appeared dissolved at the end of our simulations did so before nucleation was finished ($t < t_t$). Interestingly, the Ni:C ratio is close to the Ni_3C stoichiometry (for instance, for Ni_{160} this ratio varies from 2.9 to 3.4 as the strength of E_{adh} is increased), whereas the ratio of nickel to dissolved carbon is close to Ni_2C and Ni_3C_2 for Ni_{80} and Ni_{160}, as previously discussed.

8.4.3. Dominant carbon transport mechanism

In our simulations, the ratio of the number of atoms undergoing surface diffusion to those that dissolve: $N_{SD}/(N_{BD}+N_{CF})$ falls in the 5.5-7.8 range for Ni_{32}, 0.96-2.82 range for Ni_{80}, and 0.74-1.93 range for Ni_{160}. Thus, in most cases the amount of carbon atoms undergoing surface diffusion is either comparable or large than that of carbon atoms dissolving. This ratio increases as the strength of E_{adh} increases, and as particle size decreases (incidentally, this is the same trend that facilitates cap lift-off). Despite the high $N_{SD}/(N_{BD}+N_{CF})$ ratio, visualization of the simulation trajectories shows that, at the early stages, dissolution dominates in agreement with the dissolution model proposed here. Thus, it is inferred that a switch in the dominant diffusion mechanism occurs at some moment in the simulation. Accordingly, in order to explore the dominant diffusion mechanism as a function of time (at least indirectly), we create groups of 20 carbon

atoms (with each group representing a time window in the simulation) and determine the percentage of atoms determined as SD carbon, BD carbon, or CF carbon (according to the established τ_D-based criteria) within each group.

Figure 8-5 shows representative results of this analysis for the three particle sizes with a weak (-0.16 eV) and a strong (-0.70 eV) E_{adh}. Group *a* is constituted by carbon atoms indexed 1 through 20 (see subsection 8.3), group *b* by atoms indexed 21 through 40, and so forth. Thus as the group index increases, a later simulation interval is represented.

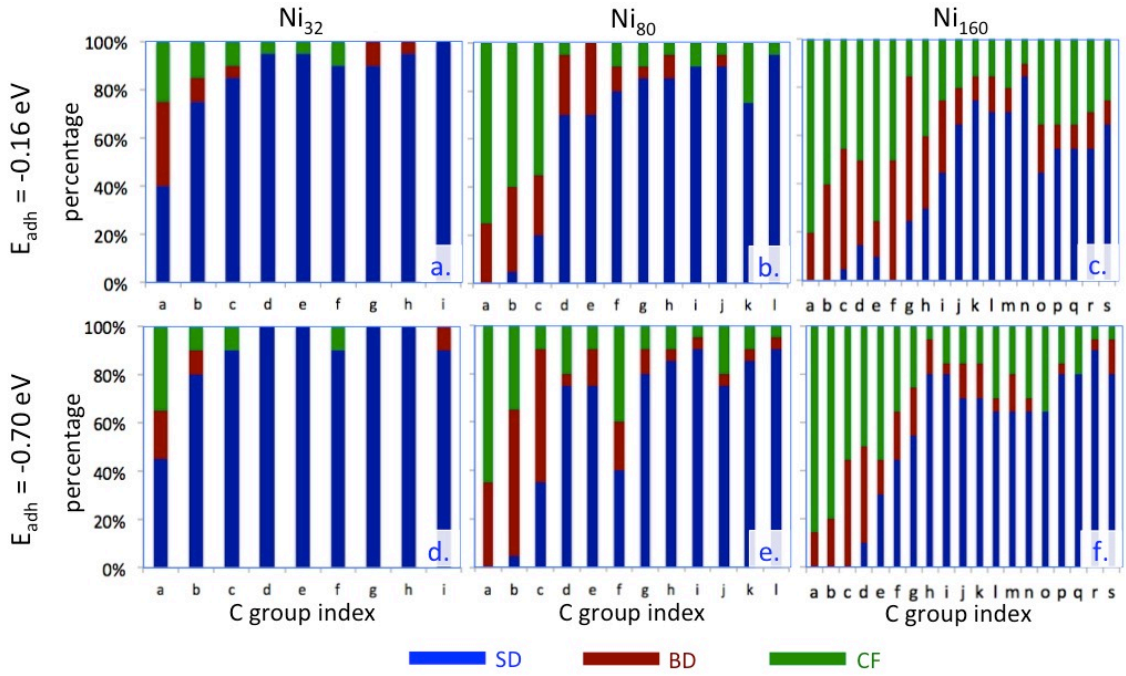

Figure 8-5. Percentage of carbon atoms undergoing either surface diffusion (SD), bulk diffusion (BD), or suitable for carbide formation (CF) as nanotube growth progresses on Ni_{32}, Ni_{80} and Ni_{160} nanoparticles for E_{adh}=-0.16 eV (top row), and E_{adh}=-0.70 eV (bottom row). Group *a* corresponds to carbon atoms with label numbers in the range 1-20, group *b* to carbon atoms with label number in the range 21-40, and so on.

For all nanoparticle sizes, it is apparent that the percentage of atoms classified as SD, BD, or CF changes as nanotube growth progresses. Early in the growth process, dissolution (BD and CF) dominates, consistent with the large driving force existing when the particle is well below the saturation point (Equations 8-3 – 8-4). A steeper

decrease in the dissolution driving force with respect to the number of catalyzed carbon occurs as the particle size decreases. For Ni_{32} the solubility (n_d^{sat}) is well below 20 carbon atoms, so the driving force is expected to steeply decrease within the time interval represented by group *a* (since most of these atoms are dissolving). In contrast, for Ni_{160} the solubility is around 100 atoms, so up to group *f* the driving force is expected to be high. Accordingly, dissolution (BD and CF) shows a steeper decrease (group-wise) as the particle size decreases. Also, a significant number of early dissolved carbon atoms are *candidates* for *potential* carbide formation, and as mentioned in subsection 8.4.2 they constitute a significant part of the carbon dissolved in the nanoparticle making plausible the hypothesis that the particle is slowly evolving into a carbide phase.

In a trend contrary to that of BD carbons and CF carbons, the percentage of atoms undergoing surface diffusion (SD carbon) increases group-wise (and thus with the simulation time) with earlier onsets (group-wise) as particle size decreases and E_{adh} increases. **Figure 8-5** shows that the first atoms undergoing surface diffusion belong to group *a* for Ni_{32}, group *b* for Ni_{80}, and group *c-d* for Ni_{160}. This result is understandable on the basis of the proposed dissolution model (Equations 8-3 - 8-4): the faster the particle saturates, the faster the dissolution driving force decreases and consequently a random-walk of the carbon atom most likely maintains the atom on the surface because the energy barrier for surface diffusion is lower than that for bulk-diffusion. Moreover, with the formation of the nanotube rim, a driving force for surface diffusion is created (since the rim acts as a sink for carbon atoms, and surface diffusion conclusively takes over bulk diffusion).

We must note that although surface diffusion dominates in the growth stage (~90% for Ni_{32}, ~70% for Ni_{80}, and~60% for Ni_{160}) bulk-diffusion still contributes (albeit in lesser extent) to nanotube growth. As discussed in subsection 8.4.1, the particle periodic reconstructions can cause a momentaneous reduction in solubility (n_d^{sat}) leading to the expulsion of carbon atoms, with some of them becoming incorporated to the nanotube. This incorporation leaves the particle undersaturated once the shape is recovered (and its inherent n_d^{sat}), thus a small driving force for dissolution is

restablished, leading to some bulk-diffusion from newly catalyzed atoms. The observed reconstruction also plays against a potential carbide stabilization since a carbide particle should be more rigid than a metallic one [14], although a fluctuating carbide has also been proposed [24].

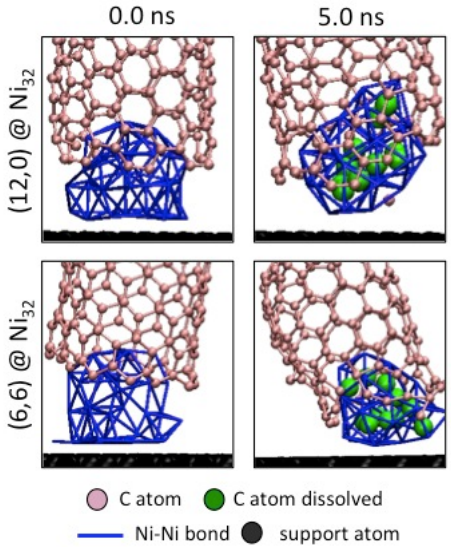

Figure 8-6. Snapshots showing (re)dissolution of carbon and nanoparticle saturation after 5.0 ns of precursor-free simulation (P_{gas} = 0 atm) of either an armchair(ac) or zigzag(zz) on a Ni_{32} nanoparticle. Carbon atoms are represented by pink spheres, but dissolved carbon atoms are represented by green spheres. Blue sticks represent nickel-nickel bonds in the nanoparticle. A similar process is observed in the presence of the precursor gas (P_{gas} ~5 atm) (see Table 8-3).

In order to further test that as long as a dissolution driving force exists dissolution, bulk-diffusion, and (potentially) carbide formation can occur even with a low barrier for surface diffusion (and the rim acting as a sink), we performed 5 ns simulations starting with a seed of either an armchair (6,6) or a zigzag (12,0) nanotube on Ni_{32} both in the presence and absence of precursor gas. Ni_{32} was selected based on the dominance of surface diffusion for these cases, and tube chiralities were selected to fit the nanoparticle diameter. **Figure 8-6** shows that in the absence of precursor the dissolution driving force leads to detachment of carbon atoms from the nanotube rim and migration to the nanoparticle inside. The values in **Table 8-3** for detached and dissolved carbon at P_{gas} = 0 atm correlates well with the values for n_d^{sat} in **Table 8-2**. A similar

situation was observed for the simulations in the presence of precursor gas (5=atm) with similar saturation levels being reached. For P_{gas}= 5 atm, **Table 8-3** identifies the amount of carbon atoms dissolved that originated from the nanotube seed (n_d^{CNT}), and those that originated from precursor catalysis. It is observed that the majority of carbon atoms dissolved originated from the precursor and only a minority from the nanotube seed. Thus, even for a particle size where surface diffusion was observed to clearly dominate once the particle saturated, dissolution (BD and CF) was observed from the newly catalyzed atoms when a significant difference ($n_d^{sat} - n_d$) was artificially created in advanced stages of growth.

Table 8-3. Number of carbon atoms dissolved, n_d, during 5.0 ns of simulation of an armchair (ac) or a zigzag (zz) nanotube on a Ni_{32} nanoparticle in the absence (P_{gas} =0 atm) or in the presence (P_{gas} ~5 atm) of precursor gas for various values of interaction with the support E_{adh}. For cases in the presence of precursor gas, the number of dissolved atoms provided by the nanotube, n_d^{CNT}, is specified.

	E_{adh}			
	-0.16 eV	**-0.26 eV**	**-0.43 eV**	**-0.70 eV**
$\mathbf{n_d}$ (ac, P_{gas} = 0 atm)	12	12	10	10
$\mathbf{n_d}$ (zz, P_{gas} = 0 atm)	11	11	9	4
$\mathbf{n_d}$ (ac, P_{gas} = 5atm)	8	10	7	8
$\mathbf{n_d^{CNT}}$(ac, P_{gas} = 5atm)	2	1	4	0
$\mathbf{n_d}$ (zz, P_{gas} = 5atm)	11	11	7	7
$\mathbf{n_d^{CNT}}$(zz, P_{gas} = 5atm)	2	2	1	1

8.4.4 Nanotube growth outline

Based on the analysis performed in this work we present an outline for nanotube growth schematized in **Figure 8-7**. Initially the nanoparticle is carbon-free, and highly catalytically active since all the (active) surface sites are available, thus precursor decomposition occurs rather fast (regime I). The carbon atoms generated from the precursor at this stage are subject to a high dissolution driving force if the material has high carbon solubility at the synthesis conditions. In the case of nickel studied here, the majority of carbon atoms readily dissolve into the nanoparticle early in the simulation. Nevertheless, due to the comparatively lower energy barrier for surface diffusion, a

fraction of the generated carbon atoms randomly walk on the particle surface finding other carbon atoms (before they manage to dissolve) and start the process of chain/ring formation and ring condensation. This process has a lower probability to occur for materials with higher solubility, and a higher probability for higher catalysis (carbon feeding) rates. We emphasize that the initiation of this process is independent of the moment when the particle is saturated, although a saturated particle may facilitate it, because it eliminates the dissolution driving force that establishes the competition between chain/ring formation and dissolution. We identify the time elapsed from the introduction of precursor gas to the system until the particle is saturated as the *induction period*.

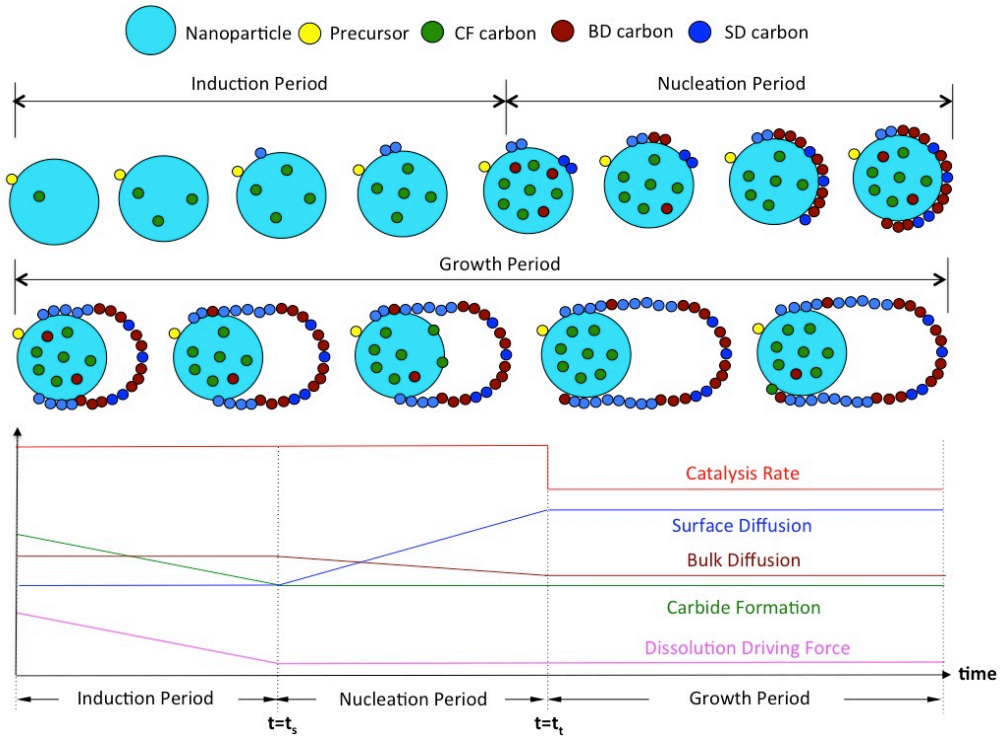

Figure 8-7. At the top, schematic outline of nanotube growth on nickel nanoparticles based on our analysis of carbon atom trajectories. The large sphere represents a nickel nanoparticle with a value of n_d^{sat} equal to nine. Small spheres represent carbon atoms, with the color indicating their trajectory-based classification. At the bottom, a simplified diagram representing the variation of catalysis rate (red line), dissolution driving force (pink line), fraction of atom undergoing surface diffusion SF (blue line), bulk diffusion BD (maroon line), and suitable for carbide formation (CF).

In **Figure 8-5**, the induction period spans groups *a-b* for Ni_{32}, groups *a-d* for Ni_{80}, and groups *a-g* for Ni_{160}. The majority of carbon atoms dissolved during this period tends to remain dissolved within the nanoparticle; thus they may be involved in the stabilization of a carbide structure. Moreover, the majority of atoms identified as candidates for carbide formation are dissolved during the induction period. When the induction period finishes any existing driving force for dissolution is significantly reduced due to particle saturation. This accelerates the nucleation of incipient graphene structures into a carbon cap, because the saturation of the particle allows new carbon atoms generated from catalysis to readily stay on the particle surface and incorporate into the nascent carbon cap. Moreover, the process is further facilitated because the nascent cap acts as a sink creating a driving force guiding the migration of carbon atom toward its rim, and growing until the cap covers most of the particle surface.

This covering of the particle reduces the catalysis rate and indicates the end of the *nucleation period* (from t_s to t_t). We observe that nucleation and dissolution processes compete and take place simultaneously. Thus nucleation can occur without dissolution or in materials/conditions with no carbon solubility, as long as there is catalytic activity (or a carbon species is fed to the system by some means). Nonetheless, it is important to note that for successful SWCNT growth, the conditions (e.g. temperature, feeding rate) must facilitate the formation of graphene-like networks that can detach from the particle, or else the formation of amorphous carbon can poison the catalyst. During the *induction* and *nucleation* periods, the dissolution of carbon accelerates the dynamics of the particle, and some dissolved carbon atoms segregate via bulk-diffusion driven by the presence of the nascent carbon structures on the particle surface. More details about the nucleation process have been discussed in Section 7 and in [226].

With the end of nucleation, the *growth period* begins (from t_t until growth is terminated) with a comparatively slow catalysis rate, and negligible dissolution driving force. Most of generated carbon atoms readily undergo surface diffusion and incorporate to the cap/nanotube. For supported-particle systems a competition between

the interactions between the particle and the support, the particle and the nanotube (with the nanotube inducing capillary forces), and among the particle atoms, and fluctuations in the particle shape are observed. Since these fluctuations affect the particle carbon solubility, they can lead to periodic segregation of carbons via bulk-diffusion, and further C dissolution (with the reappearance of a dissolution driving force). However, this process is not very significant, and during the growth period the Ni_xC_y particle has a dynamics relatively independent of the growth process (with the exception of the cited shape fluctuations that are more susceptible to occur to weak particle/support interactions), which may plausibly lead to the stabilization of a particle carbide in more advanced stages of growth.

8.5. Conclusions

Reactive classical molecular dynamics was performed to obtain a continuous picture of nanotube growth regarding carbon dissolution process, carbon transport mechanism (surface diffusion and bulk diffusion), potential carbide formation, and catalysis rate for systems with various particle sizes and interactions with the support (affecting solubility and mobility). A dissolution model based in a thermodynamic driving force was proposed and shown to agree well with the dissolution process observed in the simulation. Carbon solubility was shown to decrease with particle size in the range studied, with Ni/C ratios compatible with stoichiometries of common nickel carbides. Surface diffusion was directly shown to be dominant during *growth* stage, whereas bulk diffusion was more important during *induction* and *nucleation.* Nucleation of carbon structures on the particle surface, and carbon dissolution were shown to be two competing, but ultimately independent processes. During the growth process, the Ni_xC_y nanoparticle (core) dynamics was shown to be rather independent of the growth process suggesting conditions that may lead to carbide formation.

9. METAL NANOCATALYST STATE AND PRECURSOR EFFECTS DURING SINGLE-WALLED CARBON NANOTUBE GROWTH

9.1. Summary

The catalyst nanoparticle structure has been proposed as a potential template to guide nanotube growth toward desired chiralities. However, exploitation of such effect depends understanding the state of the nanocatalyst throughout the various stages of nanotube growth for different reaction conditions. Here we show that during nucleation there is a high carbon transport activity through the nanoparticle, but eventually a nickel-carbon core is stabilized. Furthermore, the nickel-carbon stoichiometry of the nanoparticle corresponds to known carbide compositions, with such composition varying with nanoparticle size. The calculated self-diffusion coefficients of nickel atoms are consistent with viscous solid nanoparticles, with the solid character of the nanoparticle increasing with the strength of metal/support interaction. Nanophase metal-carbon separation was observed due to the association of carbon within the nanoparticle, although the extent of this effect depends on the type of precursor (C(1)- or C(2)-type) used. Additionally, the type of precursor was also found to have an effect on the quality of the nanotubes produced in our simulations, as well on the bias toward the formation of high-chiral angle nanotubes. In particular, the use of a C(2)-type precursor moderately increased the formation of high-chiral angle nanotubes.

9.2. Introduction

The electronic and optical properties of single-walled carbon nanotubes (SWCNTs) make this carbon material a particularly attractive candidate to revolutionize a number of technological fields including biomedicine [241], and electronics [3, 5]. It must be noted, however, that a particular application demands nanotubes of either semiconductor or metallic character. On the other hand, the electronic character of a SWCNT is connected to structural features such as nanotube chirality [6]. Accordingly, controlling the nanotube structure/chirality during synthesis to produce selectively either metallic or semiconductor nanotubes is one of the most sought-after goals in nanotechnology. However, a thorough and comprehensive experimental exploration of conditions that

may lead to chiral selectivity is a challenging task due to the notoriously wide parameter space of nanotube growth.

Among the parameters that can affect nanotube growth, the nanoparticle structure has been proposed to play a role in strategies to achieve chiral/structural control of the nanotube during chemical vapor deposition (CVD) synthesis [45, 48, 100, 162, 226]. Both computational work and experimental work have explored this possibility, finding evidence suggesting a link between the structures of the nanotube and the nanoparticle. However, one important step in trying to exploit this effect is to understand the state of the nanoparticle during nanotube growth. The two main points under debate related to the use of metallic catalysts is whether the metallic nanoparticle is in a liquid, solid, or 'fluctuating' state, and whether a particle metal-carbide is formed or not during (or before) nanotube growth.

A liquid nanoparticle is proposed by the vapor-liquid-solid (VLS) mechanism of Gavillet *et al* [22], with the melting point depression of nanoparticles [35], the observed change of the nanoparticle shape during growth [33], and the exothermic character of hydrocarbon decomposition (which would help liquefaction) supporting this hypothesis [8]. However, observation of crystallinity of the particle even during drastic changes in shape has led some researchers to propose a 'fluctuating' nanoparticle [17, 24], wherein the particle may be in a solid state, but fluctuates shapes based on a creep mechanism governed by nanotube-induced capillary forces. On the other hand, a solid nanoparticle is proposed as plausible since nanotube growth have been demonstrated on nanoparticle of ceramic or semiconductor materials with high melting points [27, 217]. Furthermore, a solid nanoparticle has been associated with the occurrence of nanotube 'bamboo growth' [14, 242].

Carbide formation, on the other hand, is a controversial topic, wherein research work claiming both proving [24, 25] and disproving the presence of the carbide is found in the literature [16, 231]. It has been pointed that an inherent difficulty in determining whether the nanoparticle structure corresponds to that of a carbide or not is the similarity of lattice constants between the pure metal and some of its carbides [8]. Also, distortion

effects that are bound to occur in the nanoparticle due to size effects may hinder distinction between the two structures. Additionally, conflicting evidence showing that the metal-carbide nanoparticle is inactive or active for nanotube growth have been presented. Most recently, a reconciliatory position has been presented, wherein nanotube growth occurs both from metal and metal-carbide nanoparticles, although at different growth rates –and potentially, mechanisms [14].

Other strategies to grow preferentially, for instance, semiconductor nanotubes over metallic ones consist in the use of specific mixture of precursor gases such as methanol and ethanol or isopropyl alcohol that result in semiconductor/metallic selectivities higher than 90% [49, 50]. On the other hand, other works report changes in nanotube chiral distribution when the precursor gas is changed for instance from carbon monoxide to methane/hydrogen [20]. Also, as discussed in the computational work presented in Section 3, growth based on C_2 dimers is expected to favor formation of near-armchair nanotubes in agreement with recent experimental work. Accordingly, these results illustrate the potential role of different reactive species in the selection of nanotube chirality.

In this Section, the catalyst nanoparticle state, and precursor effects on such state and on the growth mechanism are investigated during the simulated nanotube growth on supported nickel nanoparticles using RMD. It is shown that the initial dissolution of carbon during the induction/nucleation stage enhances the dynamics of the nanoparticle, but precedes the stabilization of a nickel-carbon core enclosed by a nickel shell. Calculation of density profiles suggests an intercalated carbon-nickel layered structure, and an analysis of the carbon association within the nanoparticle suggests carbon-nickel nanophase separation. As a first approximation, application of a regular solution model shows that such separation should not occur, thus its occurrence is attributed to kinetic effects. These kinetic effects are shown to depend on the type of precursor gas (i.e. C(1) or C(2) type) because, using a C(2) precursor gas, additional energy barriers may slow down dissolution. Additionally, a C(2) precursor gas was shown to be more efficient in the formation of hexagonal rings on Ni_{32} and Ni_{80} nanoparticles, and show a moderate

effect favoring the formation of near-armchair nanotubes. On the other hand, the calculated nickel self-diffusion coefficients are consistent with a nanoparticle viscous state. The particle state is shown to have a more liquid character during nucleation, and then a more solid character during the growth stage. The more solid the character of the particle, a higher probability for occurrence of bamboo growth is observed.

9.3. Computational methods

We use our reactive classical molecular dynamics code, SIMCAT [72], to simulate nanotube growth on nickel nanoparticles supported on a graphene support, where the metal/support interaction is artificially varied through the parameter α in Equation 9-1. Metal/metal (MM) interactions are described by the Sutton Chen potential [71], carbon/carbon (CC) interactions by a modified Brenner potential [72], and metal/carbon (MC) (and metal/support interactions (MS)) by a reactive bond order (REBO) potential. Electronic effects are implicitly included in the DFT-derived parameters including the screening of CC interaction inside the nanoparticle. The adjustable parameters of the developed force field are utilized to manipulate relevant interactions such as metal/support interaction (E_{adh}) to explore different regions of the nanotube growth parameter space [201, 202].

$$E_{ij} = \alpha V_{repulsion}(r_{ij}) - \alpha^{1.1} V_{attraction}(r_{ij}) \qquad (9-1)$$

A detailed description and parameterization of this force field is described in Section 2 and [72]. The variation of the parameter α in Equation 9-1 for MS interactions, result in five different values of energy of adhesion E_{adh}, namely, -0.16 eV, -0.26 eV, -0.43 eV, -0.70 eV, and -1.39 eV. The comparison of these values with experimental data for some metal/support systems has been reported in Section 7 and [226]. The first two E_{adh} values are weak interactions, and the last two are strong ones.

The simulations presented here are performed at the typical CVD temperature of 1000 K, and controlled using Langevin dynamics [237]. The carbon feeding process was modeled using either a C(1) precursor gas maintained at P_{gas} ~ 11 atm, or a C(2)

precursor at either P_{gas} ~ 11 atm or ~5 atm. The motion of the precursor gas is determined by a 1000 K velocity distribution. When a gas molecule impinges a free catalyst site, catalysis (conversion to a C atom) occurs according to a conversion factor *f* (*f* = 1.0 is used in this work). If the precursor is modeled as a C(1) precursor, catalysis generates a single atom at the location the precursor gas impinges the nanoparticle If the precursor is modeled as a C(2) precursor, catalysis generates a carbon dimer at the location the precursor impinges on the nanoparticle. At the moment of creation, the velocity vectors of both carbon dimers point in the same direction to avoid prematurely splitting the dimer, and rather leave the dynamics of the nanoparticle dictate how the breaking occurs. The simulation step was 0.5 fs, and configurations are collected every 0.5 ps producing simulation trajectories of 10,000 frames. Identification of carbon atoms as surface diffusion atoms (SD), bulk diffusion atoms (BD), and atoms suitable for carbide formation (CF) for the visualization of trajectories is done as described in Section 8.

A clustering algorithm is used to determine the association of carbon atoms within the nanoparticle. Using a cutoff of 1.7 Å, an initial carbon atom is assigned the class 1, the number and identity (index) of carbon atoms bonding the class 1 atom is determined and assigned the class 2; then the number and identity of carbon atoms bonding the class 2 atoms are determined, and assigned the class 3; and so forth until no more atoms bonding other atoms in the previous classes are found, with the total of number of atoms associated this way corresponding to the 'length' *i* of species C_i. This procedure is repeated for atoms not included in previous iterations, until the number of each species C_i is determined.

Identifying the atoms dissolved and non-dissolved within the nanoparticle is based on the metal coordination number around carbon atoms N_{MC}. When this number is larger than five (5), the corresponding carbon atom is determined to be a dissolved carbon, and non-dissolved otherwise. Analysis of the particle structure, and atom mobility are done calculating radial distribution functions, density profiles, and self-diffusion coefficients derived from calculated mean square displacement curves.

9.4. Results and discussion

9.4.1. Stabilization of a nickel-carbon core

Figure 9-1 shows a sequence of snapshots for simulated nanotube growth (using a C(1) precursor on a Ni_{80} particle with a E_{adh} value of -0.43 eV), with carbon atoms color-coded according to its dissolution residence time. (It must be noted that the color of any particular carbon atom remains unchanged during visualization.) Classifying carbon atoms according to this criteria results in *surface diffusion* (SD) atoms, *bulk diffusion* (BD) atoms, and atoms suitable for *carbide formation* (CF), as discussed in Section 8. To facilitate the visualization of carbon atoms within the nanoparticle, the spheres representing nickel were reduced in size, whereas those representing CF atoms were increased. It must be noted that although it corresponds to a particular case, **Figure 9-1** is representative of the observations done for all the simulation trajectories.

It can be observed that as growth progresses the nanoparticle steadily fills with carbons that were deemed suitable for carbide formation (CF carbon). Such atoms do not all necessarily dissolve immediately after they are generated through precursor catalysis, and can even temporarily contribute to the formation of chains on the nanoparticle surface. Although not captured in **Figure 9-1**, it is apparent from visualization of simulation trajectories (for all cases) that the time elapsed (~ 1-200 ps) on the particle surface by CF carbons depends on several factors. 1) On the amount of carbon inside the nanoparticle, thus CF carbon generated earlier in the simulation dissolves faster. 2) On their integration or not to chains or other structures nucleating on the particle surface, with CF atoms readily dissolving when they are isolated on the particle surface, but remaining longer on the surface as part of a carbon structure (typically, CF carbon atoms are observed at the end of chains from which they detach to dissolve into the nanoparticle). 3) On the particle size, with CF carbon dissolving more readily into Ni_{160} than into Ni_{80} and Ni_{32}. 4) On the interaction with the support E_{adh}, with CF carbon dissolving more readily for weaker interactions.

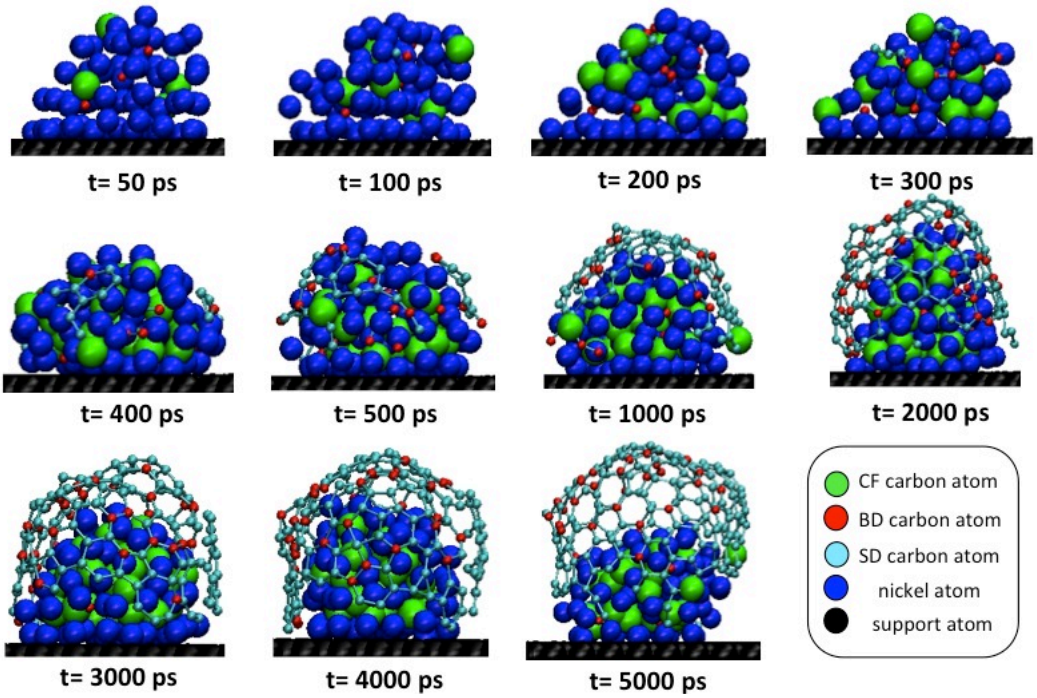

Figure 9-1. Snapshots of a nanotube growth simulation trajectory (Ni_{80}, E_{adh}=-0.43 eV, C(1) precursor gas). For visualization purposes, carbon atoms are colored according to their dissolution residency time, with the color of a particular carbon atom not being changed during the trajectory visualization. Carbon atoms with $\tau_D > 3.0$ ns (carbon atoms candidate for carbide formation: CF carbon atom) are colored green; those with $\tau_D < 3.0$ ns (carbon atoms undergoing bulk diffusion: BD carbon atom) are colored red; those with $\tau_D < 1.0$ ps (carbon atoms undergoing surface diffusion: SD carbon atom) are colored light blue. Nickel and support atoms are colored blue and black, respectively.

To understand the observations presented in numerals *1* though *4* it must be noted that the rate at which any process occurs depends both on a thermodynamic driving force (i.e. the differences in free energy between relevant states), and on relevant kinetic energy barriers. According to the dissolution model proposed in Section 8, the driving force for dissolution is proportional to the difference between the current concentration of carbon in the particle and the concentration of C at saturation ($n_d^{sat} - n_d$), whereas relevant kinetic energy barriers are those for surface diffusion, bulk diffusion, and CC bond breaking. Early in the simulation, the dissolution driving force is large, thus thermal energy is used to overcome the bulk diffusion barrier, and thus carbon readily dissolves. It must be noted that as carbon dissolves and accommodates within the nanoparticle, the dynamics of the particle is affected, becoming more mobile than in the absence of growth (i.e. precursor gas is not added to the simulation box), thus

the bulk diffusion barrier may be lower than that estimated through zero K DFT calculations [28, 31]. In fact, this high mobility and rearrangement dynamics leads to some dissolved atoms to reappear on the particle surface (BD carbon atoms).

The interplay between dissolution driving force, and the energy barrier for bulk diffusion may determine the *typical* time in which a single carbon atom remains on the surface before dissolving. During its time on the surface, a carbon atom may bond another carbon atom or structure, in which case its time on the surface increases, because it cannot dissolve until it splits from the structure (which incurs in an energy penalty to break CC bonds). As a matter of fact, CF carbon atoms in the simulations using a C(2) precursor remain on the surface longer than those using a C(1) precursor, because the former produce dimers that have to be split to allow carbon atoms to dissolve. On the other hand, the nanoparticle size affects the dissolution driving force ($n_d^{sat} - n_d$), with the particle carbon solubility increasing with size (within the size range studied here), whereas the value of E_{adh} affects both carbon solubility, and possibly the energy barrier for bulk diffusion (due to effect of E_{adh} on metal atom mobility).

Observing the growth sequence in **Figure 9-1** up to 400 ps, it is apparent that most carbon atoms generated early in the simulation are identified as CF carbon, and once they dissolve the majority remain within the nanoparticle throughout the simulation. Notice that after 5000 ps only *two* CF carbon atoms were incorporated into the nanotube structure. Thus it is observed that after a given time depending on the growth conditions (e.g. particle size, precursor type, E_{adh}), the nanoparticle essentially forms a (CF) carbon-nickel core enclosed by a nickel shell (surface atoms). Although dynamically evolving during growth (at a rate depending on temperature and E_{adh}), the nanoparticle outer shell retains the crystallographic characteristics of fcc nickel, thus arranging into a combination of (111) and (100) planes.

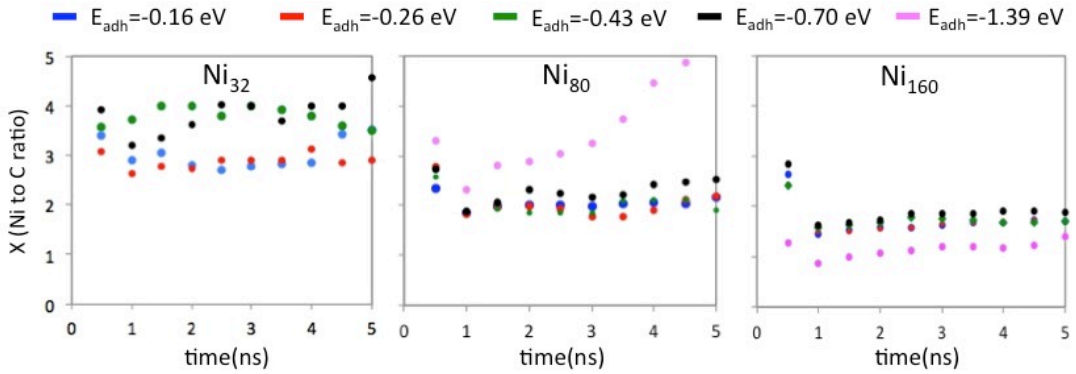

Figure 9-2. Nickel-to-carbon stoichiometric ratio (X) of the nanoparticle (Ni_XC) versus nanotube growth (1000K) simulation time for three nanocatalyst sizes (Ni_{32}, Ni_{80}, Ni_{160}) and different metal/support adhesion energies (E_{adh}). Each point plotted is calculated averaging the value of X from (t – 0.5 ns) to t.

Once the nickel-carbon core is formed, the nucleation of the cap becomes more effective, because carbon atoms generated after the formation of such core are bound to join preexisting carbon structures on the particle surface before managing to dissolve, due to the interplay between a low dissolution driving force and a comparatively low energy barrier for surface diffusion. **Figure 9-2,** which shows the average stoichiometry of the nanoparticle (Ni_xC) during growth (in 0.5 ns intervals), suggests that the nanoparticle stoichiometry (hence the nickel-carbon core) is stabilized within the first nanosecond of simulation. The presented cases correspond to the use of a C(1) precursor, but similar trends are observed with the use of a C(2) precursor.

It appears that the stoichiometry of Ni_{32} is more sensitive to variations in E_{adh}. For weak E_{adh} values (-0.16 and -0.26 eV) the stoichiometry is Ni_3C, but for stronger values (-0.43 and -0.70 eV) the nickel/carbon ratio 'x' increases to about four (4). However, such increase is explained on the basis of the comparatively higher sensitivity of the shape of the Ni_{32} nanoparticle to E_{adh}. As the latter (E_{adh}) becomes stronger, the wetting angle is reduced resulting in a 'hat-shaped' particle (or a 2D cluster as for E_{adh} = -1.39 eV), wherein the 'brim' region does not dissolve carbon (because is a one-atom thick layer), but the 'crown' region does with a nickel/carbon stoichiometry corresponding to Ni_3C. In the case of Ni_{80}, only the strongest E_{adh} (-1.39 eV) seems to have a markedly different stoichiometry, which is also related to a 'hat-shaped' nanoparticle. Interestingly, the 'crown' is determined to have a Ni_2C stoichiometry

instead of a Ni_3C one as for Ni_{32}. For Ni_{160} (as for Ni_{80}), only the strongest E_{adh} value (-1.39 eV) results in a nickel/carbon stoichiometry different to that obtained with other E_{adh} values. Such nickel/carbon stoichiometry is ~NiC for E_{adh} -1.39 eV, and ~Ni_3C_2 for other cases.

9.4.2. Structure and dynamics of carbon and nickel in the nanoparticle

It is apparent that the value of E_{adh} and the nanoparticle size affect C solubility (stoichiometry) due to their effect on nanoparticle shape and dynamics, which in turn affects the processes of carbon dissolution, nucleation, and growth. On the other hand, the nanoparticle shape has been observed to change periodically in our simulations, thus the dynamics of carbon transport in and out of the nanoparticle, which can in turn affect the dynamics of the nanoparticle (i.e. metal atoms), can also vary periodically during growth. **Figure 9-3** shows representative graphics showing the dynamics of carbon going into (dissolution) and out (precipitation) of the nanoparticle. Each bar represents the frequency with which carbon atoms are detected leaving the nanoparticle (blue bar), or entering the nanoparticle (black bar) in a 0.5 ns interval. This is done by comparing the indexes of the carbons atoms dissolved in the nanoparticle between consecutive configurations.

Observation of **Figure 9-3** shows that the period of higher dissolution/precipitation activity corresponds to the first nanosecond (1.0 ns), which corresponds to the nucleation stage, and the stabilization of the nickel-carbon core. During this period (which corresponds to 1000 configurations), nearly 90 dissolution and 80 precipitation events were detected for Ni_{32} (E_{adh} = -0.43 eV), with the difference (10) expectedly agreeing with the corresponding carbon solubility for Ni_{32}. Similarly the difference between dissolution and precipitation events for Ni_{80} (~40) and Ni_{160} (~100) also agrees with their corresponding carbon solubilities.

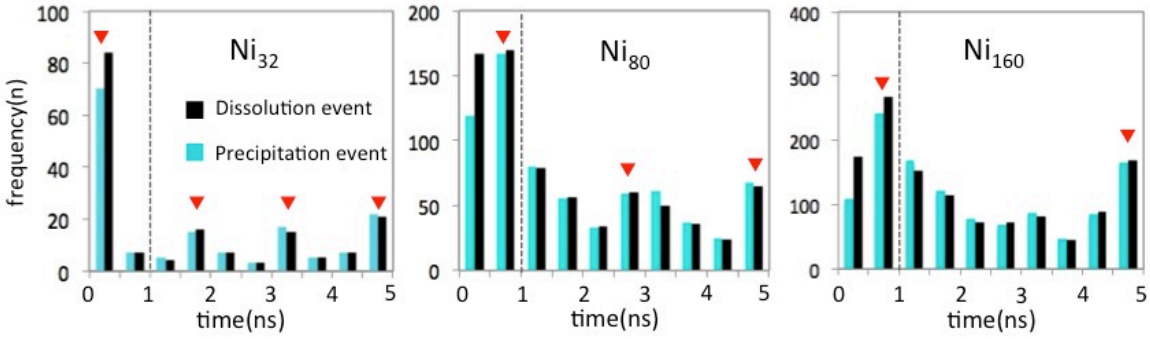

Figure 9-3. Exemplary bar diagrams (E_{adh}= -0.43 eV, C(1) precursor) showing the number of dissolution and precipitation events within a time interval of 0.5 ns as simulated nanotube growth at 1000 K progresses on three nanocatalyst sizes (Ni_{32}, Ni_{80}, Ni_{160}). At each time the carbon atoms dissolved in the nanocatalyst are identified and listed by their unique indexes; comparison of lists for 't – 0.5 ps' and 't' allows identifying dissolution events (atoms listed in 't', but *not* in 't – 0.5 ps'), and precipitation events (atoms *not* listed in 't + 0.5 ps', but in 't'). Triangular markers are used to indicate peaks in dissolution/precipitation activity. Vertical dashed line denotes the limit between the nucleation and growth stages.

It must be noted, however, that often carbon atoms may be detected to enter and leave the nanoparticle multiple times, thus n dissolution (or precipitation) events do not necessarily correspond to n different carbon atoms. This becomes more apparent for Ni_{80}, and Ni_{160} for which the number of dissolution (or precipitation) events exceeds the number of catalysis events. Moreover, trajectory visualization (e.g. **Figure 9-1**) discards a continuous flow of carbon through the nanoparticle (i.e. n atoms are generated, n atoms enter, n atoms leave) since some atoms are involved in formation of the nickel/carbon core, others in surface diffusion, and others in bulk diffusion (which requires entering and leaving the nanoparticle).

Based on these observations, it is concluded that during the induction/nucleation stage the dynamics of the nanoparticle is enhanced as a result of the continuous rearrangement of the nanoparticle structure to accommodate the carbon atoms that are being dissolved. This rearrangement and enhanced dynamics results in some carbon atoms precipitating to the surface, wherein they may be incorporated to a nucleating structure, or redissolve due to the current dissolution driving force ($n_d^{sat} - n_d$). It is noteworthy that in agreement with the dissolution model proposed in Section 8, DFT calculations on nickel slab models show that (before saturation) carbon atoms are more

stable dissolved than adsorbed (on the surface). Thus, before a noticeable carbon structure is nucleated on the surface, the precipitation of carbon to the surface is not a driven process, but the result of random motions due to the nanoparticle structural rearrangement.

Figure 9-3 also shows that after nucleation/induction is finished, and the nickel-carbon core is formed, the dissolution/precipitation activity greatly decreases, and the number of dissolution and precipitation events for subsequent intervals are essentially identical. For the representative cases, there is an average ten-fold, five-fold, and three-fold reduction in activity, with spikes in activity nearly every 1.5 ns, 2.0 ns, and 4.0 ns for Ni_{32}, Ni_{80}, and Ni_{160}, respectively. These spikes in activity may be related to periodic changes in shape observed in the nanoparticle, wherein upon shape changes some carbon atoms are 'expelled' from the nanoparticle, and redissolved as the nanoparticle recovers its shape. However, if an 'expelled' carbon appears on the surface nearby the nanotube rim, it may incorporate into the nanotube instead.

The final configuration at the end of simulated growth consists of a single-wall carbon nanotube (SWCNT) on a nanoparticle that consists of nickel-carbon core enclosed on a nickel shell. In order to investigate the stability of the nanoparticle and its structure, the final nanotube structure and carbon atoms adsorbed on the particle surface were removed, and additional 2.0 ns of dynamics of the particle were simulated in the absence of precursor gas. **Figure 9-4**b shows representative nanoparticle structures after these additional 2.0 ns. Remarkably, no carbon atoms precipitate from the nanoparticle nickel-carbon core to the nanoparticle surface, thus denoting the *stability of the nanoparticle nickel-carbon core*, and also in agreement with DFT calculations showing that carbon is more stable dissolved than adsorbed on the surface (up to saturation).

These results are seemingly in contrast with DFTB-MD simulations performed by Morokuma *et al* [25] where the dynamics of metal nanoparticles initially filled with carbon was simulated. In their work, carbon atoms precipitated to the surface, and started the nucleation of a carbon cap. It must be noted, however, that the initial configuration may be significantly supersaturated, thus the energy of the system is

reduced by moving atoms from inside the nanoparticle to its surface (i.e. there is a driving force for precipitation).

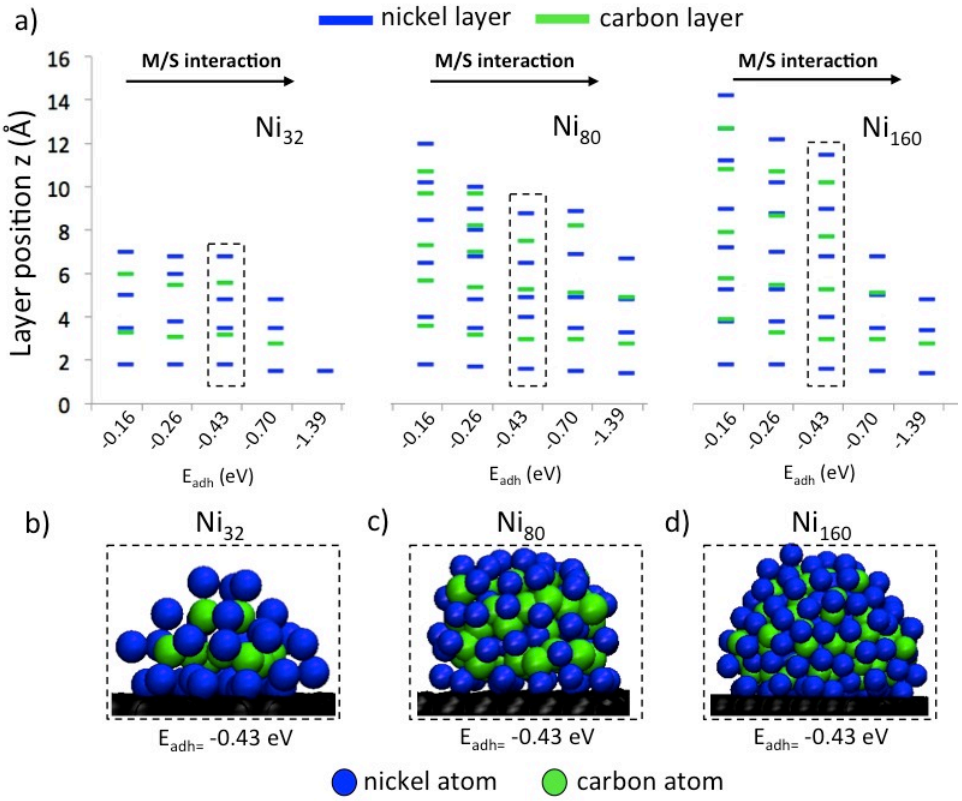

Figure 9-4. a) Plots describing the peak positions (atomic layer positions) in the calculated 'carburized' nanocatalyst density profiles along the direction normal to the support, for three nanoparticles sizes (Ni_{32}, Ni_{80}, and Ni_{160}) across metal/support adhesion energies (E_{adh}) from 0.16 eV to -1.39 eV. Green lines are used to denote peak positions in density profiles of carbon, and blue lines for those of nickel. Relevant density profiles are calculated on the 'carburized' nanocatalyst stripped of the nanotube, and equilibrated for 1.0 ns at 1000 K. b)-d) Snapshots of 'carburized' nanocatalyst Ni_{32} – Ni_{160} at E_{adh}=-0.43 eV after 1.0 ns of precursor-free simulation. Carbon and nickel atoms are represented in green and blue, respectively.

Radial distribution functions (RDFs) to investigate the coordination of nickel atoms around carbon atoms (Ni-C), carbon atoms around carbon atoms (C-C), and nickel atoms around nickel atoms (Ni-Ni) were calculated along with nickel and carbon *density profiles* along the direction normal to the support. The schematic in **Figure 9-4**a summarizes the information corresponding to peak position in the calculated density profiles. For instance, for Ni_{32} and E_{adh} = -0.16 eV, the blue lines denote that there are four (4) *nickel peaks* centered at 1.8 Å, 3.5 Å, 5.0 Å, and 7.0 Å, and the green lines

denote that there are two (2) *carbon peaks* are centered at 3.3 Å, and 6.0 Å. This shows that the nanoparticle structure for this case consists of four (4) nickel layers and two (2) carbon layers in a Ni-C-Ni-Ni-C-Ni sequence. However, it must be noted that for this weak MS interaction these layers are not as well defined, as the breadth of the density profiles peaks for this case reveals (**Figure 9-4**a does not contain information about the peaks definition). However, better defined peaks are obtained for stronger MS interactions such as E_{adh}= -0.43 eV, wherein for Ni_{32} four well-defined *nickel peaks* (at 1.5 Å, 3.5 Å, 4.8 Å, and 6.8 Å), and two well-defined *carbon peaks* (at 3.2 Å, and 5.6 Å) are observed denoting a Ni-C-Ni-Ni-C-Ni layered structure as well. Further increases in E_{adh}, decreases the number of peaks (layers), but increases the definition of each peak (layer). For instance, for Ni_{32} and E_{adh} = 0.70 eV, there are three *nickel peaks* (1.5 Å, 3.5 Å, and *carbon peak* (2.8 Å) in a Ni-C-Ni-Ni layered structure.

A common observation from the density profiles for all sizes and nickel/support interaction strengths is the detection of carbon layers intercalated between nickel layers, wherein the definition of these layers is improved with increases in the strength of E_{adh}. Furthermore, increases in the strength of E_{adh} also give way to a more regular interlayer spacing, which oscillates between 1.5 Å and 2.0 Å for weak metal/support interactions, and between 1.8 Å and 2.0 Å for strong ones. However, for either case, the interlayer separation is more irregular than for the pure nickel particles whose density profiles denoted a regular 2.0 Å separation, which corresponds to the interlayer distance between (111) planes in nickel. Thus it is apparent that the formation of the nickel-carbon core has only a small effect in the interlayer separation, with the nickel atoms approximately retaining their fcc arrangement. Notably, no significant differences were found between Ni_{32}, Ni_{80}, and Ni_{160} despite their different Ni_XC stoichiometry.

Further comparison of the 'carburized' nanoparticle with the pure nickel nanoparticle is done through the corresponding Ni-Ni RDFs. The relative positions of the peaks corresponding to the first coordination shell of nickel around nickel shows a reduction in the Ni-Ni bond from 2.35 Å (or 2.45 Å) for the pure case to 2.25 Å (2.35 Å) for the 'carburized' case. The distances between parentheses correspond to the cases

with strongest interaction with the support, which seem to induce a slight bond length increase involving the atoms in the nanoparticle contact layer (with the support). On the other hand, the average number of nickel atoms in the first coordination shell around nickel is reduced due to the carburization. These results suggests that 1) the Ni-Ni interaction is strengthened due to the presence of carbon, and 2) although nickel atoms tend to maintain their characteristic fcc interlayer separation, the coordination shell around nickel is distorted by the presence of carbon. Comparison of RDFs between the 'carburized' particle and carbide models [238] shows that the Ni-Ni bond distance in the 'carburized' particle (2.25 Å) is shorter than that for carbide models: Ni_2C-*Pnnm* (2.55 Å), Ni_2C-*Pbcn* (2.65 Å), Ni_3C-*Pnma* (2.55 Å), Ni_3C-*P6₃22* (2.75 Å), and NiC-*Fmmm* (2.55 Å).

In the carbide models mentioned above, carbon atoms possess a coordination shell composed of six (6) nickel atoms, typically corresponding to carbon atoms in octahedral positions, and a Ni-C distance typically in the 1.85–2.05 Å range. Preference for octahedral positions was also determined through DFT calculations determining the most stable position for carbon dissolution in nickel slab models. Nonetheless, although the Ni-C distance was estimated to be 1.85 Å, the C-Ni RDFs do not show this type of coordination around carbon for the 'carburized' particles presented here. Moreover, the C-C RDFs reveal that carbon atoms can be as close as 1.25 Å, denoting CC bond formation within the nanoparticle. It must be noted that this happens despite the force field DFT-based parameterization being designed to screen C-C interactions within the nanoparticle.

9.4.3. Precursor effects on the association of carbon inside the nanoparticle

To analyze the bonding of carbon atoms within the nanoparticle, a clustering algorithm is utilized to determine the number of C_1, C_2, C_3, C_4, and C_5 chains inside the nanoparticle for each of the 10,000 configurations constituting a simulation trajectory. The ratio between the frequency with which n C_i chains are observed within the nanoparticle and the number of observations (10,000) gives the empirical probability $P(n)$ that n C_i chains are observed in a randomly selected configuration. Each cell in the

charts in **Figure 9-5**a shows the most probable value of *n* (i.e. the mode) of a given C_i chain for each combination of particle size (i.e. Ni_{32}, Ni_{80}, or Ni_{160}) and E_{adh}. According to the side color scale, the color of the cell is correlated to the probability P(*n*) of the *mode*. **Figure 9-5**b complements these charts, and shows the maximum number N_{max} of C_i that are observed within the nanoparticle. No dependence on E_{adh} is shown in **Figure 9-5**b, because N_{max} did not show dependence on the nickel/support interaction.

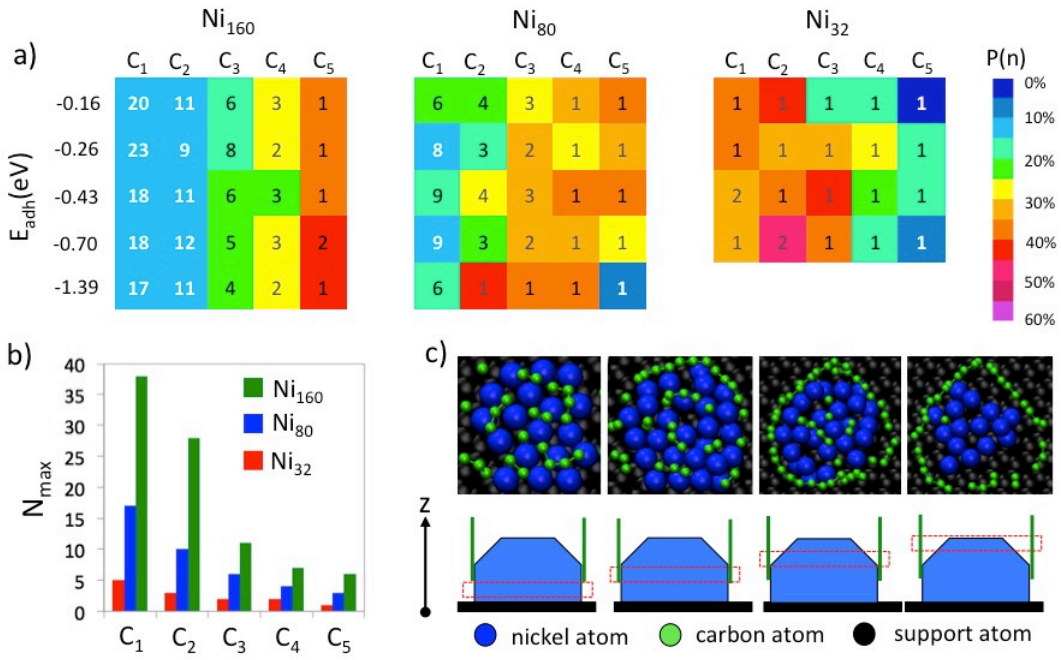

Figure 9-5. a) Exemplary colored charts for Ni_{32}, Ni_{80} and Ni_{160} based on probability distribution histograms of the number of C_1, C_2, C_3, C_4, and C_5 chains inside the nanocatalyst during simulated nanotube growth (1000 K). The *empirical probability* P(n) is calculated as the ratio between the *absolute frequency* that *n* units of C_i were detected and the total number of observations. The number in each square corresponds to the *most probable* number *n* of C_i chains (i.e. the mode) for a given E_{adh}, wherein the color correspond to the probability associated with that *n*. b) Exemplary bar diagram showing the *maximum* number *n* of C_i chains detected inside Ni_{32}, Ni_{80}, and Ni_{160} nanoparticle during simulated nanotube growth (1000 K). c) Exemplary cross-sectional scanning showing slices of the nanoparticle structure (Ni_{80}, E_{adh} = -0.43 eV) along the direction normal to the support. Carbon, nickel, and support atoms are green, blue, and black, respectively. The large carbon 'chain' surrounding the particle belongs to the nanotube structure.

Figure 9-5a-b corresponds to simulation cases using a C(1) precursor, (but the observed trends also apply to simulation cases using a C(2) precursor) and in agreement with the CC RDFs shows that there is a noticeable formation of carbon chains within the nanoparticle. It is apparent from **Figure 9.5**a that the *mode* value for a carbon chain C_i

decreases as *i* increases. This result is expected because carbon atoms enters the nanoparticle in 'monomer' form (i.e. C_1), and have to find each other and bond to form larger chains, a process that is hindered due to the screening of CC interactions within the nanoparticle. The mode probabilities for C_1 and C_2 decrease as the particle size increases (up to 10% for Ni_{160}, up to 20 % for Ni_{80}, and up to 50% for Ni_{32}), because the larger the nanoparticle the broader and flatter the probability distribution is. On the other hand, the mode probabilities for C_5 increase with the particle size (up to 15% for Ni_{32}, up to 35 % for Ni_{80}, and up to 45% for Ni_{160}) because the larger the particle the more carbon available to make larger chains. The mode probabilities for C_3 and C_4, however, show their higher values for the intermediate Ni_{80} size. There is not a clear correlation with E_{adh} because higher metal atom mobility (weak E_{adh}) facilitates carbon diffusion within the nanoparticle so carbon atoms can find each other, but also facilitates CC bond breaking due to structural/shape fluctuations. On the other hand, lower metal atom mobility (strong E_{adh}) hinders carbon diffusion within the nanoparticle, but also hinders CC bond breaking due to higher structural stability.

It must be noted that the value of N_{max} for C_1 (for each nanoparticle size) is less than half the value of carbon solubility determined for each particle in Section 8. Thus it follows that *at least* half of the carbon atoms dissolved in the nanoparticle *must* be in the form of dimers (C_2), trimers (C_3), tetramers (C_4), and pentamers (C_5) (or even larger chains). **Figure 9-5**c shows a scan of the nanoparticle structure for a selected case (Ni_{80}, E_{adh}= -0.43) during nanotube growth. For visualization purposes, the nanoparticle is cut in slices in the direction parallel to the support. In the left-most panel it is possible to observe the nickel contact layer with a rather clear (111) configuration; and on top, the carbon being detected as a layer at 3.0 Å in the corresponding density profile (**Figure 9-4**). Notice that at the moment of observation this 'layer' was composed of three (3) dimers, two (2) tetramers, one (1) tetramer, and one (1) monomer. The subsequent panels show nanoparticle slices farther form the support, wherein is apparent the increasing disorder of the metal layers, and the association of carbon atoms. Besides some disorder, large vacancies are observed in the metal layers, which are in fact

occupied by C_1, C_2, C_3, C_4, and C_5 chains. This confers each section an appearance similar to that of microphase separation in polymers, and it will be referred here as *nanophase separation*.

This nanophase separation may be responsible for the observation of the layered structure observed in the analysis of the nanoparticle density profiles. However, it also indicates that within the limitation of simulation time carbide formation is *not yet* observed; although the formation of the nickel-carbon core, the observed layered structure, and the particle stoichiometry may suggest that carbide formation is plausible at more advanced simulation times. However, it is noteworthy that the force field used in these simulations has not been fine-tuned to reproduce carbide formation within the nanoparticle, although all the parameters have been derived based on DFT calculations. Under the regular solution model, if the interaction between carbon atoms *is not* screened, then $\varepsilon_{NiNi} + \varepsilon_{CC} > 2\varepsilon_{NiC}$ (with $\varepsilon_{NiNi} \sim 0.70$ eV, $\varepsilon_{CC} \sim 4.0$ eV, and $\varepsilon_{NiC} \sim 2.3$ eV according to typical values for MM, MC, CC interactions calculated in Section 6), and nanophase separation should be expected. However, the interaction between carbon atoms in the presented simulation is screened so $\varepsilon_{NiNi} + (\varepsilon_{CC})_{in} < 2\varepsilon_{NiC}$ (with $(\varepsilon_{CC})_{in} \sim 0.4$ eV), and nanophase separation should not be expected. Nonetheless, it must be noted that the nanotube growth process is a non-equilibrium process, and the observed state of the system is susceptible to kinetic factors.

As a matter of fact, **Figure 9-6** shows differences in the state of carbon association within the nanoparticle depending on the type of precursor used, wherein the type of precursor affects the rate at which carbon is dissolved into the nanoparticle. The histograms in **Figure 9-6** are constructed by determining the most abundant (number-wise) type of C_i chain within the nanoparticle for each of the 10,000 configurations constituting a simulation trajectory. The ratio between the frequency with which C_i chains are determined to be the most abundant/dominant carbon species and the number of observations (10,000) gives the empirical dominance probability DP(i) of C_i chains. **Figure 9-6** shows that, for Ni_{32}, carbon dimers C_2 have the highest dominance probability when a C(1) precursor is used independently of E_{adh}. But when a C(2)

precursor is used instead, the dominance probability of C_1, DP(1) increases with the strength of E_{adh}, and the dominance probability of C_2, DP(2), decreases with increases in the strength of E_{adh}.

When a C(1) precursor is used, a monomer C_1 is generated in the surface, and only the bulk diffusion energy barrier needs to be overcome to dissolve carbon into the nanoparticle. Thus the dissolution process occurs comparatively fast, facilitating the association of carbon within the nanoparticle. On the other hand, when a C(2) precursor is used, a dimer C_2 is generated in the surface, and both the CC bond breaking energy penalty, and the bulk diffusion energy barrier must be overcome to dissolve carbon into the nanoparticle. Thus in the second case the process occurs comparatively slow, hindering the association of carbon within the nanoparticle. A weak E_{adh} results in higher atom mobility that both *facilitates* the splitting of the dimer and the dissolution of carbon, whereas a strong E_{adh} results in lower atom mobility that both *hinders* the splitting and the dissolution of dimer. Thus, in the confined volume of Ni_{32}, using a C(2) precursor, a weak E_{adh} ($|E_{adh}| \leq 0.26$ eV) results in dominance of dimers, whereas a strong E_{adh} ($|E_{adh}| \geq 0.43$ eV) results in dominance of monomers. However, in the relatively larger volume of Ni_{80}, and Ni_{160}, the use of the C(1) and C(2) precursor always results in the dominance of dimers, and monomers, respectively.

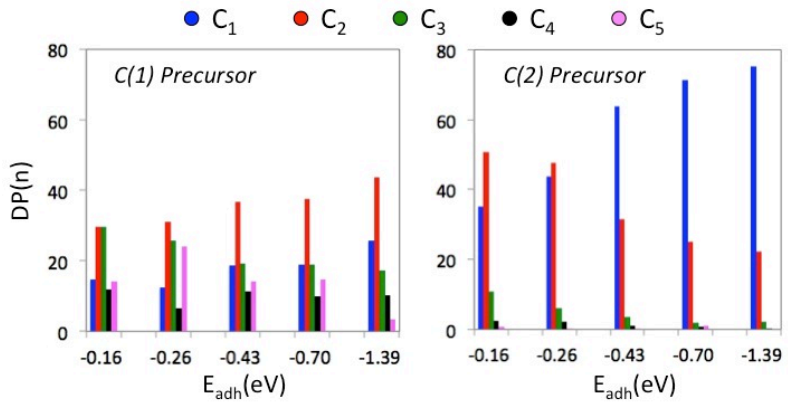

Figure 9-6. Representative *empirical* dominance probability (%) of species C_n *within* the nickel nanoparticle (DP(n)) calculated for catalytic decomposition of either a C(1)- or C(2)-type precursor varying the strength of the metal/support interaction (E_{adh}). Results shown correspond to Ni_{32}, and P_{gas} = 11 atm. DP(n) corresponds to the ratio between the *absolute frequency* that C_n was found to be the most abundant carbon species within the nanoparticle and the total number of observations.

Figure 9-7a-b shows a typical sequence of events for catalysis and subsequent carbon dissolution upon the first catalytic event (when dissolution driving force is highest) using a C(1) and a C(2) precursor, respectively. In both cases the newly generated carbon atom(s) is (are) colored in red. For the C(1) precursor case is observed that the newly generated atom lasted less than 10.0 ps. Within that time, the adsorption site for that atom (initially a (111) configuration), changed to a (100) configuration leading to the dissolution of the relevant carbon atom before the latter would have the time to diffuse around the particle surface.

For the C(2) precursor case, it is observed that during the first 20.0 ps the dimer diffuses around the surface before it is split into two carbon atoms. Then the adsorption site of each carbon atom changed to a (100) configuration preceding carbon dissolution at t ~30.0 ps. Thus carbon dissolution using a C(2) precursor was roughly three times slower than when using a C(1) precursor. This behavior affects the competition between dissolution and nucleation as shown in **Figure 9-7**c. The latter figure shows the growth curve (carbon non-dissolved vs. time), and the dissolution curve (carbon dissolved vs. time), wherein is apparent that the nucleation outpaces dissolution when a C(2) precursor is used. For the C(1) precursor case in **Figure 9-7**c, at the moment the particle saturates there are 12 carbon atoms inside the nanoparticle, and 9 atoms outside (on the surface) the nanoparticle giving a C_{out}/C_{in} ratio of 0.75, whereas for the C(2) precursor the C_{out}/C_{in} ratio is 3.60.

This ratio is displayed for other Ni_{32} cases in **Figure 9-7**f to show the combined effect of precursor type and metal interaction with the support, E_{adh}, on the nucleation/dissolution competition. Overall, it is apparent that increases in the strength of E_{adh} increase the C_{out}/C_{in} ratio, and thus increase the preference for nucleation over dissolution. Also, it is clear that a C(2) precursor increases the preference for nucleation as well, as indicated C_{out}/C_{in} ratio, which is always larger than 1.0 when using such type of precursor. Nucleation is favored when carbon atoms are present on the surface long enough so they can find and bond other carbon atoms (or C structures). In the current cases, this is achieved by increasing the catalysis rate (thus increasing the probability of

finding other carbon atoms before dissolving), or using a C(2) precursor (thus imposing an additional energy penalty –*bond breaking* – to the dissolution process). Regarding the latter point, notice that the C_{out}/C_{in} ratio obtained with a C(2) precursor at $P_{gas} \sim 5$ atm is always larger than that obtained with a C(1) precursor at $P_{gas} \sim 11$ atm despite the higher catalysis rate R_c for the latter during nucleation as indicated in **Figure 9-7**d. Regarding the former point, notice that the C_{out}/C_{in} ratio obtained with a C(2) precursor at $P_{gas} \sim 11$ atm is much larger than that obtained with a C(2) precursor at $P_{gas} \sim 5$ atm in agreement with the relative catalysis rates during nucleation (**Figure 9-7**d).

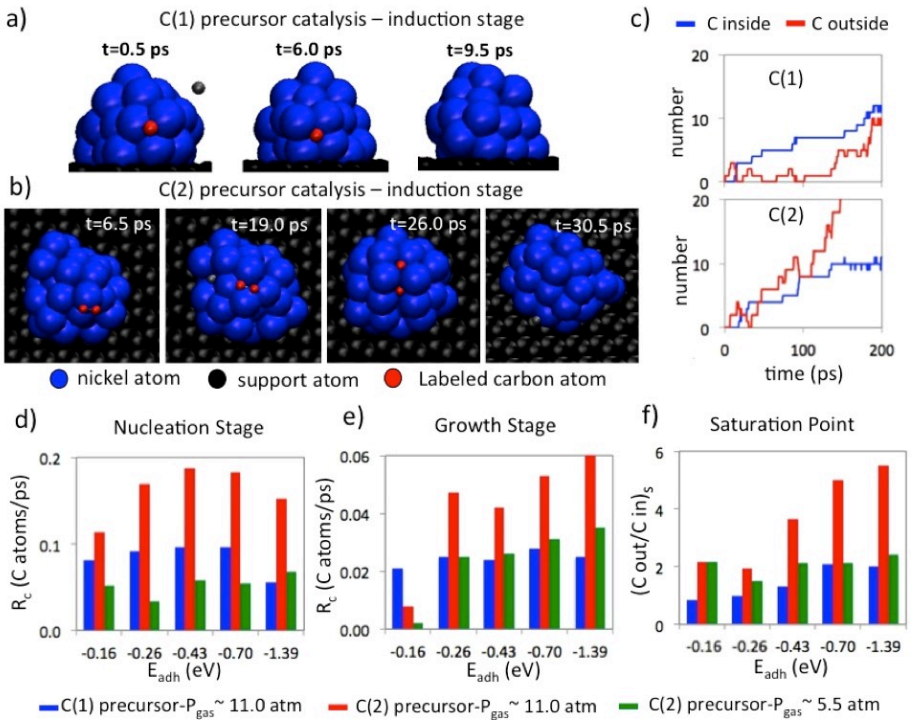

Figure 9-7. a) Sequence demonstrating the typical precursor catalysis and subsequent carbon dissolution with a C(l) precursor gas. b) Sequence demonstrating the typical precursor catalysis and subsequent carbon dissolution with a C(2) precursor gas. For a) and b), nickel, and support atoms are colored blue and black. Carbon atoms are gray, but those of interest are colored in red. c) Representative dissolution (carbon inside nanoparticle) and growth (carbon outside nanoparticle) curves for a C(1) precursor (top) and a C(2) precursor (bottom). d) Bar diagram showing the catalysis rate (R_c) during the *nucleation stage* for simulated nanotube growth on Ni_{32}, using either C(1) or C(2) precursor gas. e) Bar diagram showing the catalysis rate (R_c) during the *growth stage* for simulated nanotube growth on Ni_{32}, using either C(1) or C(2) precursor gas. f) Bar diagram showing the ratio of carbon outside the nanoparticle to carbon dissolved at the moment of nanoparticle saturation during simulated nanotube growth on Ni_{32} using either C(1) or C(2) precursor gas.

9.4.4. Mobility of nickel atoms and effect on nanotube growth

To complement the analysis of the nanoparticle state during nanotube growth, the nickel self-diffusion coefficients D_{Ni} are calculated based on the application of the Einstein equation to the mean square displacement vs. time curves obtained from the simulations. No significant impact of the precursor type was found on D_{Ni}, thus only results for the C(1) precursor case are shown in **Figure 9-8**. The self-diffusion coefficient for each combination of nanoparticle size and E_{adh} strength was calculated in four time intervals. The blue bar corresponds to the value of D_{Ni} calculated on the equilibrated structure of the pure nickel particle on the support (at the corresponding E_{adh}) in the absence of precursor gas. The red bar corresponds to the value of D_{Ni} calculated within the first nanosecond of simulation, which corresponds to the nucleation stage. The green bar corresponds the value of D_{Ni} within the last nanosecond of simulation, which corresponds to the growth stage. Finally, the black bar corresponds to the D_{Ni} value of the 'carburized' particle utilized to calculate the density profiles in **Figure 9-4**. That is, it corresponds to the value of D_{Ni} within the additional 2.0 ns of dynamics performed on the nanoparticle once the latter was stripped of the carbon nanotube grown during the original 5.0 ns of simulation.

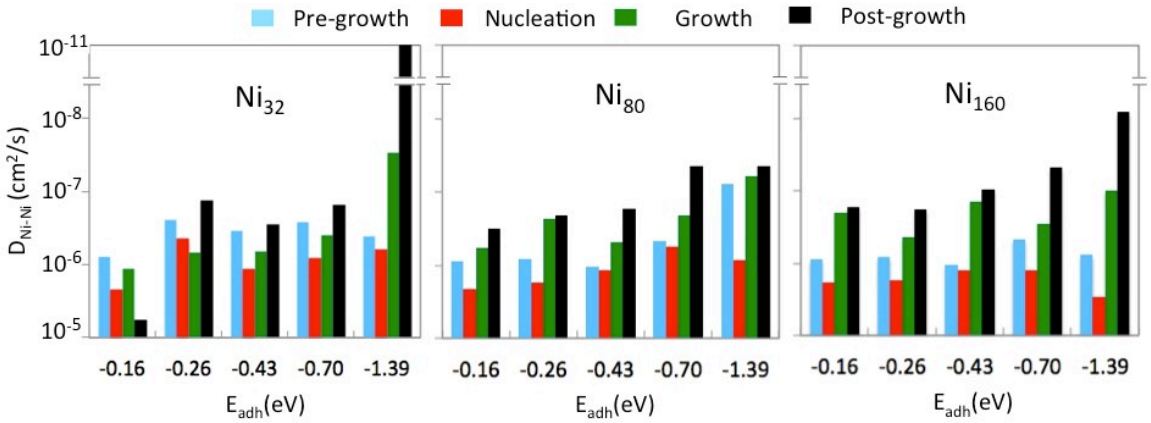

Figure 9-8. Inverse-scale logarithmic bar diagram showing the calculated self-diffusion coefficient of nickel (D_{Ni-Ni}) for Ni_{32}, Ni_{80} and Ni_{160} nanocatalysts across metal/support adhesion energies (E_{adh}) from -0.16 eV to -1.39 eV. Coefficients are calculated for the equilibrated nanocatalyst structure pre-growth (blue bar), for the nucleation stage (t < 1.0 ns) (red bar), for the growth stage for t > 4.0 ns (green bar), and for the 'carburized' nanocatalyst stripped of the nanotube (black bar).

The vertical scale is an inverted logarithmic scale with the base line corresponding to 10^{-5} cm^2/s, which corresponds to typical values for self-diffusion coefficients in liquids [243]. Thus, the shorter the D_{Ni} bar, the more it denotes a liquid behavior of the nanoparticle. On the other hand, self-diffusion coefficients for solids are in the order of 10^{-9} cm^2/s and smaller [244]. Thus, the taller the D_{Ni} bar, the more it denotes a solid behavior of the nanoparticle. It is apparent that in all cases the nanoparticle starts with a D_{Ni} in the 1×10^{-7} - 1×10^{-6} cm^2/s range, which is in the frontier between liquid and solid behavior. Also, in all cases, the dissolution of carbon during the nucleation stage gives a more liquid-like behavior during this stage. This is consistent with the enhanced dynamics observed during this stage through trajectory visualization, and the higher dissolution/precipitation activity shown in **Figure 9-3**.

On the other hand, the relative stabilization of the nanoparticle (and the nickel-carbon core) during the growth stage is denoted by the reduction of D_{Ni} during the growth stage in comparison to the nucleation stage (green bar taller than red bar). For Ni_{80} and Ni_{160}, this reduction of the particle liquid character results in a stronger particle solid character than even the corresponding one for the pure nickel particle. This behavior may be due to a thermodynamic factor such as the particle carbon stoichiometry being near a eutectic point for large part of the nucleation, and beyond the eutectic point during the growth stage, or a harbinger of the formation of a high melting point carbide within the nanoparticle. However, it must be noted that this cannot be asserted until further exploration of metal-carbon phase diagrams at the nanoscale is done. On the other hand, the reduction of the particle dynamics due to the reduction of carbon transport in and out of the nanoparticle is also a suitable explanation.

Interestingly, stripping the particle of the nanotube results in a further increase of the particle solid character. This confirms the fluctuating behavior of the nanoparticle observed experimentally being due to the presence of the nanotube. During nanotube growth there is a competition between metal/support (MS) interactions, metal/metal (MM) interaction, and metal/nanotube (MC_{SWCNT}) interactions. The MC_{SWCNT} interactions tend to create capillary effects that elongate the nanoparticle into the nanotube, whereas

the MS interactions tend to increase the support wetting by the nanoparticle. Since the nanotube is continuously growing, the MC_{SWCNT} interactions continuously evolve, also modifying the particle structure. Thus, stripping the nanotube from the nanoparticle allows the nanoparticle to stabilize, reducing D_{Ni}. For stronger values of E_{adh}, the MC_{SWCNT} are not strong enough to elongate the nanoparticle into the nanotube, thus hindering the contact between the nanotube and the particle. This typically resulted in 'bamboo growth' as reported in **Table 9-1**, which shows a higher tendency toward this type of growth as the strength of E_{adh} increases, and the particle size decreases (both of which are consistent with decreasing the nanotube/particle contact).

Table 9-1. Information regarding the observation (O), or not (X) of 'bamboo' growth for simulated growth on nickel nanoparticles varying size and interaction with the support E_{adh} at conditions: ***A***= [C(1), P_{gas} =11 atm]; ***B*** = [C(2), P_{gas} = 5 atm]; ***C***=[C(2), P_{gas} = 11 atm]

	Ni_{32}					**Ni_{80}**					**Ni_{160}**				
	-E_{adh} (eV)														
	0.10	***0.14***	***0.20***	***0.28***	***0.42***	***0.10***	***0.14***	***0.20***	***0.28***	***0.42***	***0.10***	***0.14***	***0.20***	***0.28***	***0.42***
A	X	X	O	O	O	X	X	X	O	O	X	X	X	X	O
B	X	X	X	O	O	X	X	X	O	O	X	X	X	X	O
C	X	X	X	O	O	X	X	X	O	O	X	X	X	X	X

In the nanotube literature, 'bamboo growth' (the growth of nanotubes that under TEM observation show stripes perpendicular to the nanotube axis) has been associated with growth on solid nanoparticles, which is consistent with the association of bamboo growth with stronger E_{adh} presented in **Table 9-1**. The mechanism of the formation the 'carbon membrane' perpendicular to the axis is schematized in **Figure 9-9**a-b. The left-most panel shows a normal configuration of the nanotube supported on the nanoparticle, and a good nanotube/nanoparticle contact. In the subsequent panel, the nanotube keeps growing and try to lift-off from the nanoparticle. If E_{adh} is weak, the nanoparticle be elongates as the nanotube try to lift-off, thus maintaining a good nanotube/nanoparticle contact. However, if E_{adh} is strong, the nanoparticle/support interaction does not allow dewetting from the support, and nanoparticle elongation; thus failing to maintain a good nanotube/nanoparticle contact. This leads to a region of the nanotube wall bending

inwards (second-to-left panel). If precursor decomposition generates carbon around this region, the nanotube/nanoparticle contact is reconstituted, but the region originally bending inwards keeps growing utilizing bulk-diffusing carbon to form a secondary carbon structure (second-to-right panel). While nanotube growth continues, eventually the secondary structure evolves into a carbon membrane (right-most panel).

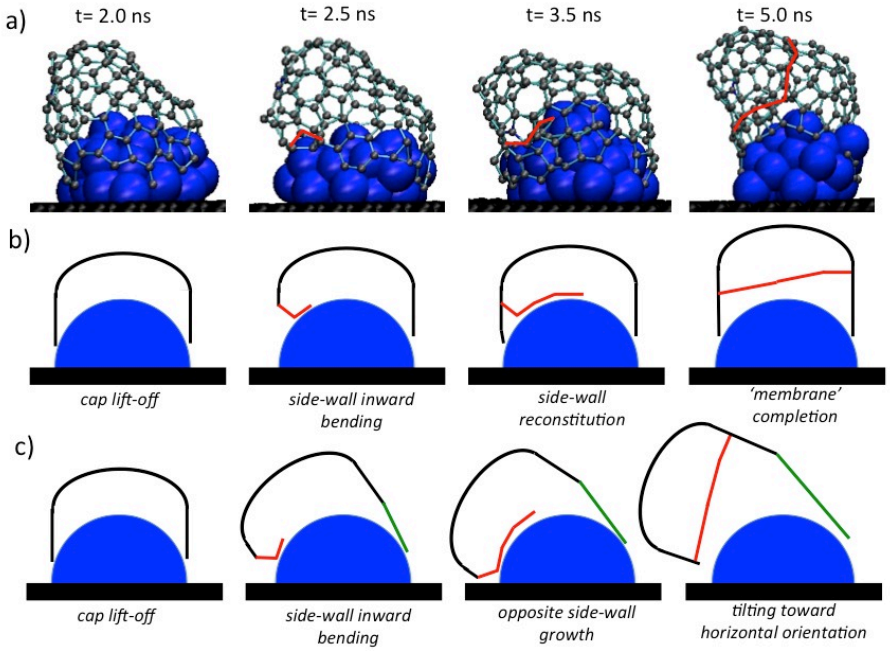

Figure 9-9. a)-b) Snapshots and schematics of simulated nanotube growth on a Ni_{32} nanoparticle (C(1) precursor, E_{adh} = -0.20 eV) as an example of 'bamboo' growth, and its mechanism. c) Related growth mechanism for 'horizontal' growth observed in simulated nanotube growth.

A variation of this mechanism has been observed in a number of simulations of that have resulted in horizontal nanotube growth. This is schematized in **Figure 9-9**c wherein the left-most and second-to-left panels are identical to those in **Figure9-9**b. However, if precursor decomposition generates carbon in the opposite side to where the nanotube wall inward bending occurred, the nanotube wall keeps growing in the opposite site, leading to and overall tilting of the growing structure (second-to-right panel). This tilting reduces the accessibility of precursor gas to reconstitute the nanotube wall in the bent region, but favors the growth of the nanotube on the opposite site,

further increasing the nanotube tilting (right-most panel). As this tilting occur, the carbon membrane is completed, and the latter was detected in the totality of simulations where nanotubes grew horizontally. It is plausible that strong enough support/nanotube (SC_{SWCNT}) interactions are necessary to maintain the horizontal tilting of the nanotube.

9.4.5. Precursor effects on carbon transport, and nanotube quality and chirality

In Section 8, it was shown that (using a C(1) precursor) as nanotube growth progresses surface diffusion progressively takes over bulk diffusion. This dominance of surface diffusion is, however, less pronounced as the nanoparticle size increases from Ni_{32} to Ni_{160}. On the other hand, using a C(2) precursor has been shown to slow down carbon dissolution in comparison to using a C(1) precursor. Thus, expectedly the dominance of *surface diffusion increases with the use of a C(2) precursor*. Furthermore, during the growth stage, the generated carbon dimers *very rarely* split or dissolve before incorporating into the rim of the nascent nanotube structure. As an example, **Figure 9-10**a-h shows the incorporation of a sequence of eight consecutively generated dimers through catalysis on Ni_{160} (each dimer is identified with a different color). In some cases, the addition of the dimers to the rim completes a hexagonal ring (panels *g* and *h*), whereas in other cases the dimer incorporates as a dangling chain in the nanotube rim (panels *a*, *c*, and *e*), or completing other *n*-membered rings.

Once incorporated into the nanotube structure, the two atoms originally forming the dimer typically split due to the continuous annealing/rearrangement of the rim. Thus the more stable is the local structure they form when joining the rim, the higher probability that they remain bonded. For instance, carbon atoms involved in the formation of a hexagonal ring remain together longer (e.g. green atoms in *d* are still together in *e*, and blue atoms in *g* are still together in *h*) than carbon atoms involved in other structures (e.g. orange atoms in *a* are split in *b*). It must be noted that C_1 and C_2 combine differently with different local rim geometries. For instance, an *ac* rim site (as described in Section 3) approached by C_1 forms a pentagon, but approached by C_2 forms a hexagon.

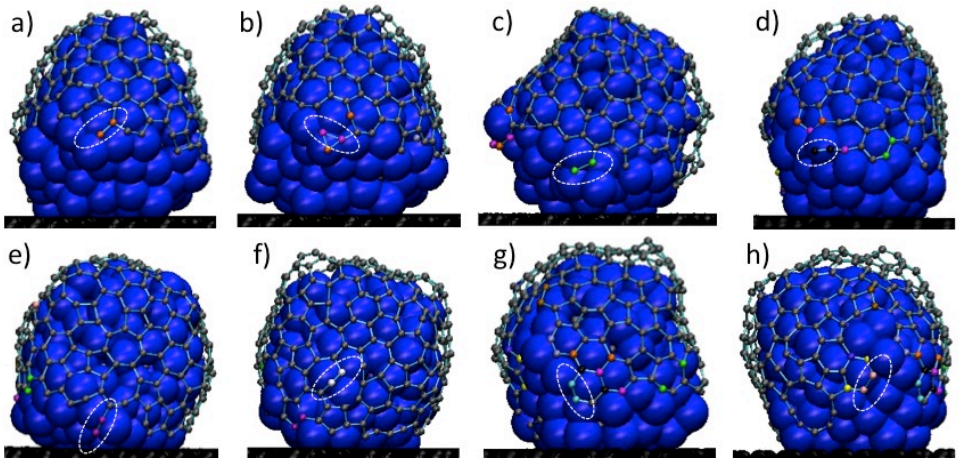

Figure 9-10. Representative sequential incorporation (panels *a* through *h*) of carbon dimers (generated through catalysis of a C(2) precursor) into the nascent nanotube structure. Each carbon dimer is identified with a color. Nickel atoms are blue, 'regular' carbon atoms are gray, and support atoms are black.

Figure 9-11 shows representative plots of the number of hexagonal rings formed in relation to the number of carbon atoms outside the nanoparticle (which during the growth stage roughly corresponds to the number of atoms in the nanotube structure). The number of carbon atoms outside the nanoparticle increases with the simulation time, thus it can be used as a measure of nanotube growth progress. Notice that due to the continuous rearrangement/annealing of the nanotube structure (in particular in the rim region) a particular number of *n* carbon atoms can be associated with different numbers of hexagonal rings. It seems from the presented plots that using a C(2) precursor (red and green curves) on a Ni_{32} or Ni_{80} nanoparticle, there is a more efficient formation of hexagonal rings than using a C(1) precursor. For instance, in the plot for Ni_{32}, a nanotube structure of 150 atoms is related to an *average* of 26.5 hexagonal rings, using a C(2) precursor; and to an *average* of 20.1 hexagonal rings using a C(1) precursor. Similarly, in the plot for Ni_{80}, a nanotube structure of 200 atoms is related to an *average 49.6* hexagonal rings; and to an *average* of 35.4 hexagonal rings using a C(1) precursor.

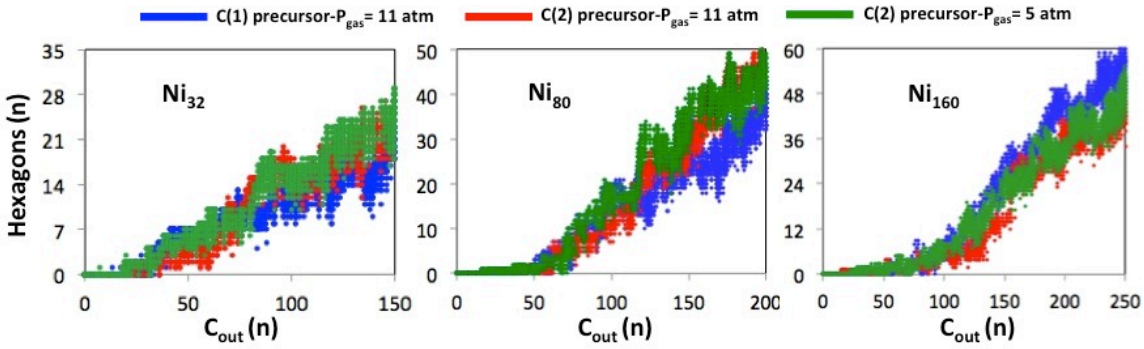

Figure 9-11. Representative plots showing the number of hexagons formed vs. the number of carbon atoms outside the nanoparticle for Ni_{32}, Ni_{80}, and Ni_{160}.

Interestingly, the observed trend for Ni_{32}, and Ni_{80} is reversed on the Ni_{160} nanoparticle. In the plot for Ni_{160}, a nanotube structure of 250 atoms is related to an *average* of 42.94 hexagonal rings, using a C(2) precursor; and to an *average* 54.1 hexagonal rings, using a C(1) precursor. It has been noted that the catalysis or carbon feeding rate impacts the healing of nanotube defects, and hence on the quality of its structure. In fact, the typical quality ratio $N_{hexagons}/(N_{hexagons}+N_{pentagons}+N_{Heptagons})$ in the 0.5–0.7 range in our simulations has been attributed to accelerated nanotube growth due to instantaneous catalysis (f=1.0). However, it must be noted that the efficiency of hexagonal ring formation using a C(2) precursor is similar using a gas pressure P_{gas} of either 5 atm or 11 atm, despite the notably different catalysis rates R_c during the growth stage as shown in **Figure 9-7**e. Furthermore, considering all cases, not a clear correlation between the relative catalysis rates and the relative efficiencies for formation of hexagonal rings is found. Thus it can be inferred that the observed difference may be due to differences in the steps leading to the formation of hexagonal rings due to the different types of carbon species approaching the rim.

Finally, the chiral angle analysis strategy utilized in Section 7 (**Figure 7-2**) is used to analyze potential effects of the precursor gas on the nanotube chirality as shown in **Figure 9-12**. It must be noted only one simulation is performed for each combination of particle size, interaction with the support, precursor gas type, and gas pressure. The use of a C(2) precursor gas resulted in several cases where the nanotube clearly

presented different chiralities (either a change in chiral angle or diameter) in the top and bottom part of the nanotube (corresponding to the diagonally split cells in **Figure 9-12**).

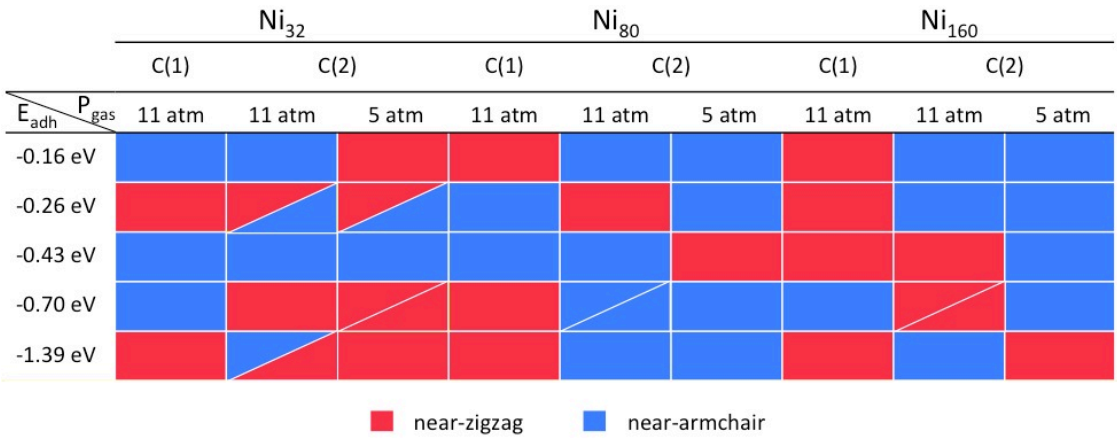

Figure 9-12. Chiral angle analysis after 5.0 ns of simulated growth for different combinations of particle size, interaction with the support, precursor gas type, and gas pressure. Diagonally split cells correspond to cases where the top and bottom part show distinct chiralities (either a change in chiral angle or diameter).

Analysis of the relevant simulation trajectories shows that these changes in chirality are associated with noticeable changes in the nanoparticle shape (e.g. diameter) in agreement with the effect particle structure on chirality. Considering all cases, ~70% of the cases with comparatively weak interaction with the support ($|E_{adh}| \leq 0.43$ eV) resulted in near-armchair tubes, and ~55% of the cases with comparatively strong interaction with the support ($|E_{adh}| \geq 0.70$ eV) resulted in near-zigzag tubes. On the other hand, only considering the C(2) precursor cases ~77% of the weak interaction cases resulted in near-armchair tubes, and ~50% of the strong interaction cases resulted in near-zigzag tubes. Thus, a moderate increase in the tendency to form near armchair tubes was observed with the use of the C(2) precursor.

9.5 Conclusions

It was shown that the initial dissolution of carbon during the induction/nucleation stage enhances the dynamics of the nanoparticle, but precedes the stabilization of a nickel-carbon core enclosed by a nickel shell. Calculation of density profiles suggests an

intercalated carbon-nickel layered structure, and an analysis of the carbon association within the nanoparticle suggests carbon-nickel nanophase separation. Application of a regular solution model shows that such separation should not occur, thus its occurrence is attributed to kinetic effects. These kinetic effects are shown to depend on the type of precursor gas (i.e. C(1) or C(2) type) because, using a C(2) precursor gas, additional energy barriers may slow down dissolution. Additionally, a C(2) precursor gas was shown to be more efficient in the formation of hexagonal rings on Ni_{32} and Ni_{80} nanoparticles, and show a moderate effect favoring the formation of near-armchair nanotubes. On the other hand, the calculated nickel self-diffusion coefficients are consistent with a nanoparticle viscous solid state. The particle state is shown to have a more liquid character during nucleation, and then a more solid character during the growth stage. The more solid the character of the particle, a higher probability for occurrence of bamboo growth is observed.

10. CONCLUSIONS AND RECOMMENDATIONS

Density functional theory and reactive molecular dynamics simulations were used to investigate the growth mechanism of single-walled carbon nanotubes, and the viability of using the nanoparticle structure as a template to guide nanotube growth toward desired chiralities.

The rim was determined as the most reactive region of the nanotube. Thus, it was concluded that C_2-based growth should proceed faster from high chiral angle caps due to the larger number of *armchair* active sites in their rim (addition of C2 to such sites completes a hexagonal ring). Furthermore, since armchair sites interact less strongly with the catalyst than zigzag sites, displacement of metal atoms interacting with the rim thus allowing addition of carbon to the rim should occur more easily in high chiral angle nanotubes.

Charge transfer between nanotube rim atoms and metal atoms in the catalyst dominates the nanotube/catalyst interactions, wherein carbon atoms in the peaks of rim zigzag sites are negatively charged, whereas the catalyst is in an oxidized state. Orbital overlap analyses reveal a negligible covalent character of such interactions. The nanocatalyst was observed to modify its structure maximizing its interaction with the nanotube rim. Moreover, the calculated nanotube/catalyst interaction energy correlates well with the number of metal-carbon (MC) interactions involving rim zigzag sites.

The interaction with nanotube zigzag rim sites gives way to a chiral angle-dependent modification of the crystallographic orientation/structure of unsupported metal nanoparticles. Since the nanoparticle structure was imposed by the nanotube geometry, this effect is coined as an *inverse template effect*, and shows the correlation between the structures of the nanotube and the catalyst. The inverse template effect occurs due to the relative bond strengths which decreases as CC > MC > MM. On these grounds, supporting the nanoparticle on an adequate support (i.e. adequate geometry, and adequate metal/support interaction) is proposed as a strategy to control nanoparticle structure, and achieve a *direct template effect.*

Accordingly, the impact of nanoparticle size, and metal/support interaction on the effectiveness of the direct template effect was investigated. DFT and RMD simulations demonstrates that such direct template effect is driven by maximization of occupation of catalyst surface hollow sites by carbon atoms, which minimizes the energy of the system. A non-monotonic relation between nanoparticle size (or metal/support interaction) and the template effect effectiveness was found. Increasing nanoparticle size increases the nanotube/catalyst contact, but decreases the homogeneity of the catalyst surface. Increasing the metal support interaction increases the stability of the nanoparticle, but reduces nanotube/catalyst contact, and decrease defect annealing due to reduced atom mobility. These observations show the necessity for fine-tuning reaction conditions to maximize such direct template effect.

Such fine-tuning requires finding an overlap between conditions that allow for nanoparticle stability while also allowing for high quality nanotube growth. Insights in the nanotube growth mechanism were obtained that provide useful information to delineate a region within the parameter space where nanotube growth is possible. During the induction/nucleation stage bulk-diffusion and carbon dissolution were dominant in agreement with a high dissolution driving force. Upon nanoparticle saturation, the dissolution driving force decreases and surface-diffusion becomes dominant, and sustains nanotube growth. Thus it is inferred that bulk diffusion is not necessary for nanotube growth. Furthermore, nucleation of carbon structures is observed on the particle surface before saturation occurs, thus demonstrating that nucleation and dissolution are simultaneous competing processes.

For carbonphilic materials such as nickel, a metal-carbon core was stabilized after the induction/nucleation stage was finished. The stoichiometry (carbon solubility) of the nanoparticle was found to depend on nanoparticle size (and to a lesser extent on the metal/support interaction), and to be consistent with stoichiometry of known M_3C, M_2C, and M_3C_2 carbides. However, formation of carbide was not conclusively determined during the simulations. In fact, carbon-metal nanophase separation was observed within the nanoparticle at an extent depending on the type of precursor gas

used. Association of carbon atoms within the nanoparticle decreases with the use of a C(2) precursor gas due to the slower carbon dissolution.

Calculated self-diffusion coefficients demonstrate that the nanoparticle is in a viscous solid state through the various stages of nanotube growth. The solid character of the nanoparticle decreases with the dissolution of carbon during induction/nucleation, with the nanoparticle probably being at pre-eutectic compositions. The nanoparticle solid character increases once nucleation is finished and the metal-carbon core is stabilized with a composition corresponding to a carbide. Thus it is inferred that carbonphilic nanoparticles are less suitable to act as templates during nucleation.

Based on the work presented in this dissertation, a general recommendation is to explore both theoretically and experimentally the growth of SWCNTs on supported nanoparticles at conditions that hinder carbon dissolution, but favor carbon surface diffusion under a vapor-solid-solid (VSS) mechanism, with the goal of studying templated nanotube growth. Specific recommendations for future work are outlined as follows:

- Implementation of enhanced sampling techniques such as temperature-accelerated dynamics in the SIMCAT program. This will allow the annealing of defects within the nanotube structure, which in turn will allow the formation of high-quality nanotubes that will facilitate studying the dependence of chirality on different parameters of growth with higher accuracy.
- Derivation and implementation of a force field that enables the formation of a carbide structures for metal-carbon systems. Such force field can then be implemented in the SIMCAT program for carbon atoms dissolved within the nanoparticle. This will enable to both study more accurately the potential formation of a metal carbide during nanotube growth, as well as to explore nanotube growth using carbide particles as the initial catalyst.
- Expanding the capabilities of the SIMCAT program to the simulation of nanotube growth on selected materials also requires an accurate description of the relative catalytic capabilities of each material to obtain at least semi-

quantitative comparison of the performance of each material at similar reaction conditions. DFT calculations and the nudge elastic band (NEB) method can be used to determine the relevant energy barriers for the decomposition of various precursor gases on the surface of selected materials. This information can be translated into values of conversion factors characteristic of each selected material.

- Bimetallic nanoparticles are expected to play a significant role in fine-tuning reaction conditions to exploit the template effect, and guide nanotube growth toward desired chiralities. Growth parameters such as the overall interaction with the support, and the overall catalytic activity of the catalyst can be fine-tuned based on the nature and relative concentration of the bimetallic nanoparticle selected components. Additional effects can also be expected (and investigated) such as changes in the nanoparticle structure (e.g. lattice constant), and in the stability of potential metal carbides (changes in phase diagrams).
- Metal carbides may play a significant role in the growth of carbon nanotubes, but may be also important for catalysis of other industrially important reactions. Therefore, a DFT-based study of these materials is of broad interest. Such DFT studies should start with the determination of the stability of different carbides for different sizes. For this the so-called pressure-size approximation may be implemented to simulate size effects in bulk/slab models. The surface energy of different carbide facets for different sizes should also be determined to study the decomposition of hydrocarbons and reactants of interest on the most stable facets. For nanotube synthesis is also of interest to understand the diffusion of carbon through, or on the surface of these materials, by identifying relevant dissolution driving forces, and kinetic barriers. Also, determining the epitaxial matching and binding energy of graphene layers on these materials may be relevant to understanding cap lift-off, and potential template effects on carbide particles.

- In the general area of nanotube growth, the synthesis of either vertical (forest growth) or horizontal (carpet growth) dense nanotube arrays is becoming increasingly important for the potential implementation of SWCNTs in electronic devices. Coarse-grained reactive molecular dynamics may be a suitable alternative to study the growth of such large systems. Each nanotube may be simulated as chain of coarse-grained beads, whereas the support may be discretized as a grid. Interactions between beads corresponding to the same nanotube may be modeled with a harmonic potential, whereas interactions between beads of different nanotubes, and between nanotube beads and the support may be modeled as Van der Waals interactions. A scheme must be devised to add new beads to each growing nanotube, and to assign chirality to the first nanotube bead (subsequent beads should have the same chirality). Information about the chiral dependent interactions of the nanotube with the support, and other nanotubes, must be obtained through DFT calculations.
- In recent efforts to synthesize majority of semiconducting nanotubes, the hypothesis that metallic nanotubes are etched away by some of the reactants species has gained strength. Thus, it may be useful to use DFT calculations to identify reactant species that can be created through different hydrocarbon (or other gases) decomposition paths. Then, the attack on chiral nanotubes by a selection of identified species (chosen based on their potential to etch the nanotube) can be studied to identify the most effective/selective species, and their etching mechanism to gain the base knowledge for a rationale optimization of this etching effect.

REFERENCES

1. Iijima, S., Helical microtubules of graphitic carbon. *Nature*, 1991. 354(6348): p. 56-58.

2. Postma, H.W.C., T. Teepen, Z. Yao, M. Grifoni, and C. Dekker, Carbon nanotube single-electron transistors at room temperature. *Science*, 2001. 293(5527): p. 76-79.

3. Franklin, A.D., M. Luisier, S.-J. Han, G. Tulevski, C.M. Breslin, et al., Sub-10 nm carbon nanotube transistor. *Nano Letters*, 2012. 12(2): p. 758-62.

4. Polizu, S., O. Savadogo, P. Poulin, and L.H. Yahia, Applications of carbon nanotubes-based biomaterials in biomedical nanotechnology. *Journal of Nanoscience and Nanotechnology*, 2006. 6(7): p. 1883-904.

5. Heller, D.A., G.W. Pratt, J. Zhang, N. Nair, A.J. Hansborough, et al., Peptide secondary structure modulates single-walled carbon nanotube fluorescence as a chaperone sensor for nitroaromatics. *PNAS*, 2011. 108: p. 8544-49.

6. Saito, R., G. Dresselhaus, and M.S. Dresselhaus, Trigonal warping effect of carbon nanotubes. *Physical Review B*, 2000. 61(4): p. 2981-90.

7. Esconjauregui, S., C.M. Whelan, and K. Maex, The reasons why metals catalyze the nucleation and growth of carbon nanotubes and other carbon nanomorphologies. *Carbon*, 2009. 47(3): p. 659-69.

8. Kumar, M. and Y. Ando, Chemical vapor deposition of carbon nanotubes: A review on growth mechanism and mass production. *Journal of Nanoscience and Nanotechnology*, 2010. 10(6): p. 3739-58.

9. Born, M. and R. Oppenheimer, Zur quantentheorie del molekeln. *Ann. Phys (Leipzig)*, 1927. 84(20): p. 457-84

10. Journet, C., W.K. Maser, P. Bernier, A. Loiseau, M.L. de la Chapelle, et al., Large-scale production of single-walled carbon nanotubes by the electric-arc technique. *Nature*, 1997. 388(6644): p. 756-58.

11. Journet, C. and P. Bernier, Production of carbon nanotubes. *Applied Physics a-Materials Science & Processing*, 1998. 67(1): p. 1-9.

12. Curtarolo, S., N. Awasthi, W. Setyawan, A. Jiang, K. Bolton, et al., Influence of Mo on the Fe : Mo : C nanocatalyst thermodynamics for single-walled carbon nanotube growth. *Physical Review B*, 2008. 78(5): p. 051045 1-8

13. Anisimov, A.S., A.G. Nasibulin, H. Jiang, P. Launois, J. Cambedouzou, et al., Mechanistic investigations of single-walled carbon nanotube synthesis by ferrocene vapor decomposition in carbon monoxide. *Carbon*, 2010. 48(2): p. 380-88.

14. He, Z., J.-L. Maurice, A. Gohier, C.S. Lee, D. Pribat, et al., Iron catalysts for the growth of carbon nanofibers: Fe, fe3c or both? *Chemistry of Materials*, 2011. 23(24): p. 5379-87.

15. Baker, R.T.K., M.A. Barber, P.S. Harris, F.S. Feates, and R.J. Waite, Nucleation and growth of carbon deposits from the nickel catalyzed decomposition of acetylene. *Journal of Catalysis*, 1972. 26(1): p. 51-62.

16. Helveg, S., C. Lopez-Cartes, J. Sehested, P.L. Hansen, B.S. Clausen, et al., Atomic-scale imaging of carbon nanofibre growth. *Nature*, 2004. 427(6973): p. 426-29.

17. Hofmann, S., R. Sharma, C. Ducati, G. Du, C. Mattevi, et al., In situ observations of catalyst dynamics during surface-bound carbon nanotube nucleation. *Nano Letters*, 2007. 7(3): p. 602-08.

18. He, M., A.I. Chernov, E.D. Obraztsova, J. Sainio, E. Rikkinen, et al., Low temperature growth of swnts on a nickel catalyst by thermal chemical vapor deposition. *Nano Research*, 2011. 4(4): p. 334-42.

19. Zhu, H.W., K. Suenaga, A. Hashimoto, K. Urita, K. Hata, et al., Atomic-resolution imaging of the nucleation points of single-walled carbon nanotubes. *Small*, 2005. 1(12): p. 1180-83.

20. Lolli, G., L.A. Zhang, L. Balzano, N. Sakulchaicharoen, Y.Q. Tan, et al., Tailoring (n,m) structure of single-walled carbon nanotubes by modifying reaction conditions and the nature of the support of Co-Mo catalysts. *Journal of Physical Chemistry B*, 2006. 110(5): p. 2108-15.

21. Wang, H., B. Wang, X.-Y. Quek, L. Wei, J. Zhao, et al., Selective synthesis of (9,8) single walled carbon nanotubes on cobalt incorporated TUD-1 catalysts. *Journal of the American Chemical Society*, 2010. 132(47): p. 16747-49.

22. Gavillet, J., A. Loiseau, C. Journet, F. Willaime, F. Ducastelle, et al., Root-growth mechanism for single-wall carbon nanotubes. *Physical Review Letters*, 2001. 87(27): p. 275504 1-4.

23. Takagi, D., Y. Kobayashi, H. Hibino, S. Suzuki, and Y. Homma, Mechanism of gold-catalyzed carbon material growth. *Nano Letters*, 2008. 8(3): p. 832-35.

24. Yoshida, H., S. Takeda, T. Uchiyama, H. Kohno, and Y. Homma, Atomic-scale in-situ observation of carbon nanotube growth from solid state iron carbide nanoparticles. *Nano Letters*, 2008. 8(7): p. 2082-86.

25. Page, A.J., H. Yamane, Y. Ohta, S. Irle, and K. Morokuma, Qm/md simulation of swnt nucleation on transition-metal carbide nanoparticles. *Journal of the American Chemical Society*, 2010. 132(44): p. 15699-707.

26. Takagi, D., Y. Homma, H. Hibino, S. Suzuki, and Y. Kobayashi, Single-walled carbon nanotube growth from highly activated metal nanoparticles. *Nano Letters*, 2006. 6(12): p. 2642-45.

27. Takagi, D., H. Hibino, S. Suzuki, Y. Kobayashi, and Y. Homma, Carbon nanotube growth from semiconductor nanoparticles. *Nano Letters*, 2007. 7(8): p. 2272-75.

28. Hofmann, S., G. Csányi, A.C. Ferrari, M.C. Payne, and J. Robertson, Surface diffusion: The low activation energy path for nanotube growth. *Physical Review Letters*, 2005. 95(3): p. 036101 1-4.

29. Yazyev, O.V. and A. Pasquarello, Effect of metal elements in catalytic growth of carbon nanotubes. *Physical Review Letters*, 2008. 100(15): p. 156102 1-4.

30. Ohta, Y., Y. Okamoto, A.J. Page, S. Irle, and K. Morokuma, Quantum chemical molecular dynamics simulation of single-walled carbon nanotube cap nucleation on an iron particle. *ACS Nano*, 2009. 3(11): p. 3413-20.

31. Yazyev, O.V. and A. Pasquarello, Carbon diffusion in CVD growth of carbon nanotubes on metal nanoparticles. *Physica Status Solidi B-Basic Solid State Physics*, 2008. 245(10): p. 2185-88.

32. Yuan, Q., H. Hu, and F. Ding, Threshold barrier of carbon nanotube growth. *Physical Review Letters*, 2011. 107(15): p. 156101 1-5.

33. Moseler, M., F. Cervantes-Sodi, S. Hofmann, G.b. Csányi, and A.C. Ferrari, Dynamic catalyst restructuring during carbon nanotube growth. *ACS Nano*, 2010. 4(12): p. 7587-95.

34. Huang, S.P. and P.B. Balbuena, Melting of bimetallic cu-ni nanoclusters. *Journal of Physical Chemistry B*, 2002. 106(29): p. 7225-36.

35. Qi, W.H., Size effect on melting temperature of nanosolids. *Physica B-Condensed Matter*, 2005. 368(1-4): p. 46-50.

36. Jiang, A., N. Awasthi, A.N. Kolmogorov, W. Setyawan, A. Börjesson, et al., Theoretical study of the thermal behavior of free and alumina-supported fe-c nanoparticles. *Physical Review B*, 2007. 75(20): p. 205426 1-12.

37. Lopeandia, A.F. and J. Rodriguez-Viejo, Size-dependent melting and supercooling of ge nanoparticles embedded in a sio2 thin film. *Thermochimica Acta*, 2007. 461(1-2): p. 82-87.

38. Zhu, H., K. Suenaga, J. Wei, K. Wang, and D. Wu, A strategy to control the chirality of single-walled carbon nanotubes. *Journal of Crystal Growth*, 2008. 310(24): p. 5473-76.

39. Nasibulin, A.G., P. Queipo, S.D. Shandakov, D.P. Brown, H. Jiang, et al., Studies on mechanism of single-walled carbon nanotube formation. *Journal of Nanoscience and Nanotechnology*, 2006. 6(5): p. 1233-46.

40. Komatsu, N. and F. Wang, A comprehensive review on separation methods and techniques for single-walled carbon nanotubes. *Materials*, 2010. 3(7): p. 3818-44.

41. Yao, Y., C. Feng, J. Zhang, and Z. Liu, "Cloning" of single-walled carbon nanotubes via open-end growth mechanism. *Nano Letters*, 2009. 9(4): p. 1673-77.

42. Farhat, S., M.L. de La Chapelle, A. Loiseau, C.D. Scott, S. Lefrant, et al., Diameter control of single-walled carbon nanotubes using argon--helium mixture gases. *The Journal of Chemical Physics*, 2001. 115(14): p. 6752-59.

43. He, M., A.I. Chernov, P.V. Fedotov, E.D. Obraztsova, J. Sainio, et al., Predominant (6,5) single-walled carbon nanotube growth on a copper-promoted

iron catalyst. *Journal of the American Chemical Society*, 2010. 132(40): p. 13994-96.

44. Miyauchi, Y.H., S.H. Chiashi, Y. Murakami, Y. Hayashida, and S. Maruyama, Fluorescence spectroscopy of single-walled carbon nanotubes synthesized from alcohol. *Chemical Physics Letters*, 2004. 387(1-3): p. 198-203.

45. Harutyunyan, A.R., G. Chen, T.M. Paronyan, E.M. Pigos, O.A. Kuznetsov, et al., Preferential growth of single-walled carbon nanotubes with metallic conductivity. *Science*, 2009. 326(5949): p. 116-20.

46. Zhu, Z., H. Jiang, T. Susi, A.G. Nasibulin, and E.I. Kauppinen, The use of NH_3 to promote the production of large-diameter single-walled carbon nanotubes with a narrow (n,m) distribution. *Journal of the American Chemical Society*, 2010. 133(5): p. 1224-27.

47. Reich, S., L. Li, and J. Robertson, Epitaxial growth of carbon caps on Ni for chiral selectivity. *Physica Status Solidi B-Basic Solid State Physics*, 2006. 243(13): p. 3494-99.

48. Chiang, W.-H. and R.M. Sankaran, Linking catalyst composition to chirality distributions of as-grown single-walled carbon nanotubes by tuning Ni_xFe_{1-x} nanoparticles. *Nature Materials*, 2009. 8(11): p. 882-86.

49. Ding, L., A. Tselev, J. Wang, D. Yuan, H. Chu, et al., Selective growth of well-aligned semiconducting single-walled carbon nanotubes. *Nano Letters*, 2009. 9(2): p. 800-05.

50. Che, Y., C. Wang, J. Liu, B. Liu, X. Lin, et al., Selective synthesis and device applications of semiconducting single-walled carbon nanotubes using isopropyl alcohol as feedstock. *ACS Nano*, 2012. 6(8): p. 7454-62.

51. Schrödinger, E., Quantisierung als eigenwertproblem. *Annalen der Physik*, 1926. 385(13): p. 437-90.

52. Hohenberg, P. and W. Kohn, Inhomogeneous electron gas. *Physical Review*, 1964. 136(3B): p. B864-71.

53. Roothaan, C.C.J., New developments in molecular orbital theory. *Reviews of Modern Physics*, 1951. 23(2): p. 69-89.

54. Perdew, J.P., K. Burke, and M. Ernzerhof, Generalized gradient approximation made simple. *Physical Review Letters*, 1996. 77(18): p. 3865-68.

55. Perdew, J.P., J.A. Chevary, S.H. Vosko, K.A. Jackson, M.R. Pederson, et al., Atoms, molecules, solids, and surfaces: Applications of the generalized gradient approximation for exchange and correlation. *Physical Review B*, 1992. 46(11): p. 6671-87.

56. Becke, A.D., A new mixing of hartree--fock and local density-functional theories. *The Journal of Chemical Physics*, 1993. 98(2): p. 1372-77.

57. Lee, C., W. Yang, and R.G. Parr, Development of the colle-salvetti correlation-energy formula into a functional of the electron density. *Physical Review B*, 1988. 37(2): p. 785-89.

58. Kohn, W., Analytic properties of Bloch waves and Wannier functions. *Physical Review*, 1959. 115(4): p. 809-21.

59. Slater, J.C., Atomic shielding constants. *Physical Review*, 1930. 36(1): p. 57-64.

60. Hay, P.J. and W.R. Wadt, Ab initio effective core potentials for molecular calculations - potentials for K to Au including the outermost core orbitals. *Journal of Chemical Physics*, 1985. 82(1): p. 299-310.

61. Hay, P.J. and W.R. Wadt, Ab initio effective core potentials for molecular calculations - potentials for the transition-metal atoms Sc to Hg. *Journal of Chemical Physics*, 1985. 82(1): p. 270-83.

62. Blöchl, P.E., Projector augmented-wave method. *Physical Review B*, 1994. 50(24): p. 17953-79.

63. Monkhorst, H.J. and J.D. Pack, Special points for Brillouin-zone integrations. *Physical Review B*, 1976. 13(12): p. 5188-92.

64. Rahman, A., Correlations in the motion of atoms in liquid argon. *Physical Review*, 1964. 136(2A): p. A405-A11.

65. Verlet, L., Computer "experiments" on classical fluids. I. Thermodynamical properties of lennard-jones molecules. *Physical Review*, 1967. 159(1): p. 98-103.

66. Hermansson, K., G.C. Lie, and E. Clementi, On velocity scaling in molecular dynamics simulations. *Journal of Computational Chemistry*, 1988. 9(3): p. 200-03.

67. Berendsen, H.J.C., J.P.M. Postma, W.F. van Gunsteren, A. DiNola, and J.R. Haak, Molecular dynamics with coupling to an external bath. *The Journal of Chemical Physics*, 1984. 81(8): p. 3684-90.

68. Hoover, W.G., Canonical dynamics: Equilibrium phase-space distributions. *Physical Review A*, 1985. 31(3): p. 1695-97.

69. Adelman, S.A. and J.D. Doll, Generalized Langevin equation approach for atom/solid-surface scattering: General formulation for classical scattering off harmonic solids. *The Journal of Chemical Physics*, 1976. 64(6): p. 2375-88.

70. Zhao, J., A. Martinez-Limia, and P.B. Balbuena, Understanding catalysed growth of single-wall carbon nanotubes. *Nanotechnology*, 2005. 16(7): p. S575-81.

71. Sutton, A.P. and J. Chen, Long-range finnis–sinclair potentials. *Philosophical Magazine Letters*, 1990. 61(3): p. 139-46.

72. Martinez-Limia, A., J. Zhao, and P.B. Balbuena, Molecular dynamics study of the initial stages of catalyzed single-wall carbon nanotubes growth: Force field development. *Journal of Molecular Modeling*, 2007. 13(5): p. 595-600.

73. Brenner, D.W., O.A. Shenderova, J.A. Harrison, S.J. Stuart, B. Ni, et al., A second-generation reactive empirical bond order (REBO) potential energy expression for hydrocarbons. *Journal of Physics-Condensed Matter*, 2002. 14(4): p. 783-802.

74. Saito, R., G. Dresselhaus, and S. Dresselhaus, Physical properties of carbon nanotubes,1998, London, Imperial College Press.

75. Brinkmann, G., P.W. Fowler, D.E. Manolopoulos, and A.H.R. Palser, A census of nanotube caps. *Chemical Physics Letters*, 1999. 315(5–6): p. 335-47.

76. Reich, S., L. Li, and J. Robertson, Structure and formation energy of carbon nanotube caps. *Physical Review B*, 2005. 72(16): p. 165423 1-8.

77. Ebbesen, T.W. and P.M. Ajayan, Large-scale synthesis of carbon nanotubes. *Nature*, 1992. 358(6383): p. 220-22.

78. Lamouroux, E., P. Serp, and P. Kalck, Catalytic routes towards single wall carbon nanotubes. *Catalysis Reviews*, 2007. 49(3): p. 341-405.

79. Resasco, D.E., W.E. Alvarez, F. Pompeo, L. Balzano, J.E. Herrera, et al., A scalable process for production of single-walled carbon nanotubes (SWNTs) by catalytic disproportionation of CO on a solid catalyst. *Journal of Nanoparticle Research*, 2002. 4(1-2): p. 131-36.

80. Balbuena, P.B., J. Zhao, S.P. Huang, Y.X. Wang, N. Sakulchaicharoen, et al., Role of the catalyst in the growth of single-wall carbon nanotubes. *Journal of Nanoscience and Nanotechnology*, 2006. 6(5): p. 1247-58.

81. Becke, A.D., Density-functional thermochemistry. III. The role of exact exchange. *The Journal of Chemical Physics*, 1993. 98(7): p. 5648-52.

82. Frisch, M.J.T., G. W.; Schlegel, H. B.; Scuseria, G. E.; Robb, M. A.; Cheeseman, J. R.; Montgomery, J. A.; Vreven, T.; Kudin, K. N.; Burant, J. C.; Millam, J. M.; Iyengar, S. S.; Tomasi, J.; Barone, V.; Mennucci, B.; Cossi, M.; Scalmani, G.; Rega, N.; Petersson, G. A.; Nakatsuji, H.; Hada, M.; Ehara, M.; Toyota, K.; Fukuda, R.; Hasegawa, J.; Ishida, M.; Nakajima, T.; Honda, Y.; Kitao, O.; Nakai, H.; Klene, M.; Li, X.; Knox, J. E.; Hratchian, H. P.; Cross, J. B.; Bakken, V.; Adamo, C.; Jaramillo, J.; Gomperts, R.; Stratmann, R. E.; Yazyev, O.; Austin, A. J.; Cammi, R.; Pomelli, C.; Ochterski, J. W.; Ayala, P. Y.; Morokuma, K.; Voth, G. A.; Salvador, P.; Dannenberg, J. J.; Zakrzewski, V. G.; Dapprich, S.; Daniels, A. D.; Strain, M. C.; Farkas, O.; Malick, D. K.; Rabuck, A. D.; Raghavachari, K.; Foresman, J. B.; Ortiz, J. V.; Cui, Q.; Baboul, A. G.; Clifford, S.; Cioslowski, J.; Stefanov, B. B.; Liu, G.; Liashenko, A.; Piskorz, P.; Komaromi, I.; Martin, R. L.; Fox, D. J.; Keith, T.; Al-Laham, M. A.; Peng, C. Y.; Nanayakkara, A.; Challacombe, M.; Gill, P. M. W.; Johnson, B.; Chen, W.; Wong, M. W.; Gonzalez, C.; Pople, J. A., Gaussian 03, revision c.02, 2004, Gaussian, Inc.: Wallingford CT.

83. Arepalli, S. and C.D. Scott, Spectral measurements in production of single-wall carbon nanotubes by laser ablation. *Chemical Physics Letters*, 1999. 302(1–2): p. 139-45.

84. Zhu, H.W., C.L. Xu, D.H. Wu, B.Q. Wei, R. Vajtai, et al., Direct synthesis of long single-walled carbon nanotube strands. *Science*, 2002. 296(5569): p. 884-86.

85. Hata, K., D.N. Futaba, K. Mizuno, T. Namai, M. Yumura, et al., Water-assisted highly efficient synthesis of impurity-free single-walled carbon nanotubes. *Science*, 2004. 306(5700): p. 1362-64.

86. Zhang, L., Y. Tan, and D.E. Resasco, Controlling the growth of vertically oriented single-walled carbon nanotubes by varying the density of Co-Mo catalyst particles. *Chemical Physics Letters*, 2006. 422(1–3): p. 198-203.

87. Laidler, K.J., Chemical kinetics. 3rd ed, 1987, New York, Harper Collins.

88. Gomez-Gualdron, D.A. and P.B. Balbuena, Effect of metal cluster-cap interactions on the catalyzed growth of single-wall carbon nanotubes. *Journal of Physical Chemistry C*, 2009. 113(2): p. 698-709.

89. Dresselhaus, S., G. Dresselhaus, and P. Avouris, Carbon nanotubes: Synthesis, structure, properties, and applications, 2001, Berlin, Springer.

90. Dresselhaus, S., G. Dresselhaus, and P.C. Eklund, Science of fullerenes and carbon nanotubes, 1996, New York, Academic Press.

91. Dresselhaus, M.S., Nanotubes - Burn and interrogate. *Science*, 2001. 292(5517): p. 650-51.

92. Bachtold, A., P. Hadley, T. Nakanishi, and C. Dekker, Logic circuits with carbon nanotube transistors. *Science*, 2001. 294(5545): p. 1317-20.

93. Collins, P.C., M.S. Arnold, and P. Avouris, Engineering carbon nanotubes and nanotube circuits using electrical breakdown. *Science*, 2001. 292(5517): p. 706-09.

94. Ouyang, M., J.L. Huang, C.L. Cheung, and C.M. Lieber, Energy gaps in "metallic" single-walled carbon nanotubes. *Science*, 2001. 292(5517): p. 702-05.

95. Strano, M.S., C.A. Dyke, M.L. Usrey, P.W. Barone, M.J. Allen, et al., Electronic structure control of single-walled carbon nanotube functionalization. *Science*, 2003. 301(5639): p. 1519-22.

96. LeMieux, M.C., M. Roberts, S. Barman, Y.W. Jin, J.M. Kim, et al., Self-sorted, aligned nanotube networks for thin-film transistors. *Science*, 2008. 321(5885): p. 101-04.

97. Dukovic, G., M. Balaz, P. Doak, N.D. Berova, M. Zheng, et al., Racemic single-walled carbon nanotubes exhibit circular dichroism when wrapped with DNA. *Journal of the American Chemical Society*, 2006. 128(28): p. 9004-05.

98. Zheng, M., A. Jagota, M.S. Strano, A.P. Santos, P. Barone, et al., Structure-based carbon nanotube sorting by sequence-dependent DNA assembly. *Science*, 2003. 302(5650): p. 1545-48.

99. Kunstmann, J., A. Quandt, and I. Boustani, An approach to control the radius and the chirality of nanotubes. *Nanotechnology*, 2007. 18(15): p. 155703 1-3.

100. Reich, S., L. Li, and J. Robertson, Control the chirality of carbon nanotubes by epitaxial growth. *Chemical Physics Letters*, 2006. 421(4–6): p. 469-72.

101. Papadimitrakopoulos, F. and S.-Y. Ju, Materials science: Purity rolled up in a tube. *Nature*, 2007. 450(7169): p. 486-87.

102. Amara, H., C. Bichara, and F. Ducastelle, Understanding the nucleation mechanisms of carbon nanotubes in catalytic chemical vapor deposition. *Physical Review Letters*, 2008. 100(5): p. 056105 1-4.

103. Ding, F., P. Larsson, J.A. Larsson, R. Ahuja, H. Duan, et al., The importance of strong carbon-metal adhesion for catalytic nucleation of single-walled carbon nanotubes. *Nano Letters*, 2008. 8(2): p. 463-68.

104. Ding, F., A. Rosen, and K. Bolton, Molecular dynamics study of the catalyst particle size dependence on carbon nanotube growth. *Journal of Chemical Physics*, 2004. 121(6): p. 2775-79.

105. Carneiro, J.W.d.M. and M.T.d.M. Cruz, Density functional theory study of the adsorption of formaldehyde on Pd-4 and on Pd-4/γ-Al_2O_3 clusters. *Journal of Physical Chemistry A*, 2008. 112(38): p. 8929-37.

106. Cruz, M.C.T.D.M., J.W.D.M. Carneiro, D.A.G. Aranda, and M. Buehl, Density functional theory study of benzene adsorption on small Pd and Pt clusters. *Journal of Physical Chemistry C*, 2007. 111(29): p. 11068-76.

107. Ghosh, M., S. Sproules, T. Weyhermueller, and K. Wieghardt, (α-diimine)chromium complexes: Molecular and electronic structures; a combined experimental and density functional theoretical study. *Inorganic Chemistry*, 2008. 47(13): p. 5963-70.

108. Jacob, T. and W.A. Goddard, Chemisorption of (CH_X and C_2H_Y) hydrocarbons on Pt(111) clusters and surfaces from DFT studies. *The Journal of Physical Chemistry B*, 2004. 109(1): p. 297-311.

109. Longo, R.C., M.M.G. Alemany, B. Fernández, and L.J. Gallego, Comment on "Ground-state geometry of small Ni-C clusters". *Physical Review B*, 2003. 68(16): p. 167401 1-3.

110. Lundin, A., I. Panas, and E. Ahlberg, Quantum chemical modelling of ethene epoxidation with hydrogen peroxide-role of catalytic sites. *Physical Chemistry Chemical Physics*, 2007. 9(45): p. 5997-6003.

111. Pakiari, A.H. and Z. Jamshidi, Interaction of amino acids with gold and silver clusters. *The Journal of Physical Chemistry A*, 2007. 111(20): p. 4391-96.

112. Polestshuk, P.M., P.I. Demyanov, and I.G. Ryabinkin, The electronic structure and energetics of v[sup +]-benzene half-sandwiches of different multiplicities: Comparative multireference and single-reference theoretical study. *The Journal of Chemical Physics*, 2008. 129(5): p. 054307-13.

113. Tanaka, H., H. Mori, H. Seino, M. Hidai, Y. Mizobe, et al., DFT study on chemical N_2 fixation by using a cubane-type $RuIr_3S_4$ cluster: Energy profile for binding and reduction of N_2 to ammonia via $Ru{-}N{-}NH_x$ ($x = 1{-}3$) intermediates with unique structures. *Journal of the American Chemical Society*, 2008. 130(28): p. 9037-47.

114. Shibuta, Y. and S. Maruyama, Bond-order potential for transition metal carbide cluster for the growth simulation of a single-walled carbon nanotube. *Computational Materials Science*, 2007. 39(4): p. 842-48.

115. Freedman, T.B., X.L. Cao, D.A. Young, and L.A. Nafie, Density functional theory calculations of vibrational circular dichroism in transition metal complexes: Identification of solution conformations and mode of chloride ion association for (+)-tris(ethylenediaminato)cobalt(iii). *Journal of Physical Chemistry A*, 2002. 106(14): p. 3560-65.

116. Balbuena, P.B., D. Altomare, L. Agapito, and J.M. Seminario, Theoretical analysis of oxygen adsorption on Pt-based clusters alloyed with Co, Ni, or Cr embedded in a Pt matrix. *Journal of Physical Chemistry B*, 2003. 107(49): p. 13671-80.

117. Balbuena, P.B., P.A. Derosa, and J.M. Seminario, Density functional theory study of copper clusters. *Journal of Physical Chemistry B*, 1999. 103(15): p. 2830-40.

118. Stewart, J.J.P., Optimization of parameters for semiempirical methods v: Modification of NDDO approximations and application to 70 elements. *J Mol Model*, 2007. 13(12): p. 1173-213.

119. Stewart, J.J.P., MOPAC2007, 2007, Stewart Computational Chemistry, Colorado Springs, CO, USA, http://openmopac.net.

120. Besler, B.H., K.M. Merz, and P.A. Kollman, Atomic charges derived from semiempirical methods. *Journal of Computational Chemistry*, 1990. 11(4): p. 431-39.

121. Mulliken, R.S., Electronic population analysis on lcao [single bond] Mo molecular wave functions. I. *The Journal of Chemical Physics*, 1955. 23(10): p. 1833-40.

122. Gorelsky, S.I., AOMIX: Program for molecular orbital analysis, 2007: University of Ottawa, ON, Canada, http://www.sg-chem.net/aomix.

123. Gorelsky, S.I. and A.B.P. Lever, Electronic structure and spectral, of ruthenium diimine complexes by density functional theory and indo/s. Comparison of the two methods. *Journal of Organometallic Chemistry*, 2001. 635(1-2): p. 187-96.

124. Gomez-Gualdron, D.A. and P.B. Balbuena, The role of cap chirality in the mechanism of growth of single-wall carbon nanotubes. *Nanotechnology*, 2008. 19: p. 485604 1-7.

125. Fox, S. and H.J.F. Jansen, Total energy of trigonal and tetragonal cobalt. *Physical Review B*, 1999. 60(7): p. 4397-400.

126. Kitakami, O., H. Sato, Y. Shimada, F. Sato, and M. Tanaka, Size effect on the crystal phase of cobalt fine particles. *Physical Review B*, 1997. 56(21): p. 13849-54.

127. Owen, E.A. and D.M. Jones, Effect of grain size on the crystal structure of cobalt. *Proceedings of the Physical Society. Section B*, 1954. 67(6): p. 456-66.

128. Kittel, C., Introduction to solid state physics, 1986, New York, John Wiley & Sons.

129. Tománek, D. and R.J. Enbody, Science and application of nanotubes, 2000, New York, Kluwer Academic/Plenum Publishers.

130. Hafner, J.H., C.L. Cheung, and C.M. Lieber, Growth of nanotubes for probe microscopy tips. *Nature*, 1999. 398(6730): p. 761-62.

131. Rueckes, T., K. Kim, E. Joselevich, G.Y. Tseng, C.L. Cheung, et al., Carbon nanotube-based nonvolatile random access memory for molecular computing. *Science*, 2000. 289(5476): p. 94-97.

132. Takikawa, T., M. Ikeda, K. Hirahara, Y. Hibi, Y. Tao, et al., Fabrication of single-walled carbon nanotubes and nanohorns by means of a torch arc in open air. *Physica B-Condensed Matter*, 2002. 323(1-4): p. 277-79.

133. Junzo, Y., M. Takeji, N. Yuzo, S. Shuichi, S. Takeshi, et al., Present status of swcnt mass production & future problems, *Fullerene, Nanotubes General Symposium*, 2007. 32(1): p. 4-9.

134. Nikolaev, P., M.J. Bronikowski, R.K. Bradley, F. Rohmund, D.T. Colbert, et al., Gas-phase catalytic growth of single-walled carbon nanotubes from carbon monoxide. *Chemical Physics Letters*, 1999. 313(1-2): p. 91-97.

135. Kitiyanan, B., W.E. Alvarez, J.H. Harwell, and D.E. Resasco, Controlled production of single-wall carbon nanotubes by catalytic decomposition of CO on bimetallic Co-Mo catalysts. *Chemical Physics Letters*, 2000. 317(3-5): p. 497-503.

136. Zhou, W., Z. Han, J. Wang, Y. Zhang, Z. Jin, et al., Copper catalyzing growth of single-walled carbon nanotubes on substrates. *Nano Letters*, 2006. 6(12): p. 2987-90.

137. Bachilo, S.M., M.S. Strano, C. Kittrell, R.H. Hauge, R.E. Smalley, et al., Structure-assigned optical spectra of single-walled carbon nanotubes. *Science*, 2002. 298(5602): p. 2361-66.

138. Jeong, G.-H., A. Yamazaki, S. Suzuki, H. Yoshimura, Y. Kobayashi, et al., Production of single-walled carbon nanotubes with narrow diameter distribution

using iron nanoparticles derived from DNA-binding proteins from starved cells. *Carbon*, 2007. 45(5): p. 978-83.

139. Fan, X., R. Buczko, A.A. Puretzky, D.B. Geohegan, J.Y. Howe, et al., Nucleation of single-walled carbon nanotubes. *Physical Review Letters*, 2003. 90(14): p. 145501 1-4.

140. Ding, F., K. Bolton, and A. Rosén, Nucleation and growth of single-walled carbon nanotubes: A molecular dynamics study. *The Journal of Physical Chemistry B*, 2004. 108(45): p. 17369-77.

141. Esfarjani, K., N. Gorjizadeh, and Z. Nasrollahi, Molecular dynamics of single wall carbon nanotube growth on nickel surface. *Computational Materials Science*, 2006. 36(1–2): p. 117-20.

142. Raty, J.Y., F. Gygi, and G. Galli, Growth of carbon nanotubes on metal nanoparticles: A microscopic mechanism from ab initio molecular dynamics simulations. *Physical Review Letters*, 2005. 95(9): p. 096103 1-4.

143. Deng, W.-Q., X. Xu, and W.A. Goddard, A two-stage mechanism of bimetallic catalyzed growth of single-walled carbon nanotubes. *Nano Letters*, 2004. 4(12): p. 2331-35.

144. Dunning Jr, T.H. and P.J. Hay, in Modern theoretical chemistry, H.F. Schaefer, 1976, Plenum Press: New York. p. 1-28.

145. Bartsch, K., K. Biedermann, T. Gemming, and A. Leonhardt, On the diffusion-controlled growth of multiwalled carbon nanotubes. *Journal of Applied Physics*, 2005. 97(11): p. 114301-7.

146. Eres, G., A.A. Kinkhabwala, H. Cui, D.B. Geohegan, A.A. Puretzky, et al., Molecular beam-controlled nucleation and growth of vertically aligned single-wall carbon nanotube arrays. *The Journal of Physical Chemistry B*, 2005. 109(35): p. 16684-94.

147. Sun, J. and S.L. Simon, The melting behavior of aluminum nanoparticles. *Thermochimica Acta*, 2007. 463(1-2): p. 32-40.

148. Hersam, M.C., Progress towards monodisperse single-walled carbon nanotubes. *Nature Nanotechnology*, 2008. 3(7): p. 387-94.

149. Zheng, M., A. Jagota, E.D. Semke, B.A. Diner, R.S. McLean, et al., DNA-assisted dispersion and separation of carbon nanotubes. *Nature Materials*, 2003. 2(5): p. 338-42.

150. Krupke, R., F. Hennrich, H. von Lohneysen, and M.M. Kappes, Separation of metallic from semiconducting single-walled carbon nanotubes. *Science*, 2003. 301(5631): p. 344-47.

151. Arnold, M.S., A.A. Green, J.F. Hulvat, S.I. Stupp, and M.C. Hersam, Sorting carbon nanotubes by electronic structure using density differentiation. *Nature Nanotechnology*, 2006. 1(1): p. 60-65.

152. Tu, X., S. Manohar, A. Jagota, and M. Zheng, DNA sequence motifs for structure-specific recognition and separation of carbon nanotubes. *Nature*, 2009. 460(7252): p. 250-53.

153. Wilder, J.W.G., L.C. Venema, A.G. Rinzler, R.E. Smalley, and C. Dekker, Electronic structure of atomically resolved carbon nanotubes. *Nature*, 1998. 391(6662): p. 59-62.

154. Li, Y.M., W. Kim, Y.G. Zhang, M. Rolandi, D.W. Wang, et al., Growth of single-walled carbon nanotubes from discrete catalytic nanoparticles of various sizes. *Journal of Physical Chemistry B*, 2001. 105(46): p. 11424-31.

155. Cheung, C.L., A. Kurtz, H. Park, and C.M. Lieber, Diameter-controlled synthesis of carbon nanotubes. *Journal of Physical Chemistry B*, 2002. 106(10): p. 2429-33.

156. Zhao, J. and P.B. Balbuena, Effect of nanotube length on the aromaticity of single-wall carbon nanotubes. *Journal of Physical Chemistry C*, 2008. 112(10): p. 3482-88.

157. Ding, F., A.R. Harutyunyan, and B.I. Yakobson, Dislocation theory of chirality-controlled nanotube growth. *Proceedings of the National Academy of Sciences of the United States of America*, 2009. 106(8): p. 2506-09.

158. Wang, J.-T., C. Chen, K. Ohno, E. Wang, X.-L. Chen, et al., Atomistic nucleation and growth mechanism for single-wall carbon nanotubes on catalytic nanoparticle surfaces. *Nanotechnology*, 2010. 21(11) 1-5.

159. Wang, Q., M.-F. Ng, S.-W. Yang, Y. Yang, and Y. Chen, The mechanism of single-walled carbon nanotube growth and chirality selection induced by carbon atom and dimer addition. *Acs Nano*, 2010. 4(2): p. 939-46.

160. Hirahara, K., M. Kociak, S. Bandow, T. Nakahira, K. Itoh, et al., Chirality correlation in double-wall carbon nanotubes as studied by electron diffraction. *Physical Review B*, 2006. 73(19): p. 195490 1-11.

161. Paillet, M., J.C. Meyer, T. Michel, V. Jourdain, P. Poncharal, et al., Selective growth of large chiral angle single-walled carbon nanotubes. *Diamond and Related Materials*, 2006. 15(4-8): p. 1019-22.

162. Gomez-Gualdron, D.A., J. Zhao, and P.B. Balbuena, Nanocatalyst structure as a template to define chirality of nascent single-walled carbon nanotubes. *The Journal of Chemical Physics*, 2011. 134(1): p. 014705-11.

163. Kendall, R.A., T.H. Dunning, and R.J. Harrison, Electron-affinities of the 1st-row atoms revisited - systematic basis-stes and wave-functions. *Journal of Chemical Physics*, 1992. 96(9): p. 6796-806.

164. Couty, M. and M.B. Hall, Basis sets for transition metals: Optimized outer p functions. *Journal of Computational Chemistry*, 1996. 17(11): p. 1359-70.

165. Roy, L.E., P.J. Hay, and R.L. Martin, Revised basis sets for the lanl effective core potentials. *Journal of Chemical Theory and Computation*, 2008. 4(7): p. 1029-31.

166. Ehlers, A.W., M. Bohme, S. Dapprich, A. Gobbi, A. Hollwarth, et al., A set of f-polarization functions for pseudo-poetntial basis sets of transition metals sc-cu, y-ag, and la-au. *Chemical Physics Letters*, 1993. 208(1-2): p. 111-14.

167. Wadt, W.R. and P.J. Hay, Ab initio effective core potentials for molecular calculations - potentials for main group elements na to bi. *Journal of Chemical Physics*, 1985. 82(1): p. 284-98.

168. Kresse, G. and J. Furthmuller, Efficient iterative schemes for ab initio total-energy calculations using a plane-wave basis set. *Physical Review B*, 1996. 54(16): p. 11169-86.

169. Kresse, G. and D. Joubert, From ultrasoft pseudopotentials to the projector augmented-wave method. *Physical Review B*, 1999. 59(3): p. 1758-75.

170. Perdew, J.P., K. Burke, and M. Ernzerhof, Generalized gradient approximation made simple. *Physical Review Letters*, 1997. 78(7): p. 1396-96.

171. Methfessel, M. and A.T. Paxton, High-precision sampling for brullouin zone integration in metals. *Physical Review B*, 1989. 40(6): p. 3616-21.

172. Zhu, W., A. Borjesson, and K. Bolton, DFT and tight binding Monte Carlo calculations related to single-walled carbon nanotube nucleation and growth. *Carbon*, 2010. 48(2): p. 470-78.

173. Burgos, J.C., H. Reyna, B.I. Yakobson, and P.B. Balbuena, Interplay of catalyst size and metal-carbon interactions on the growth of single-walled carbon nanotubes. *Journal of Physical Chemistry C*, 2010. 114(15): p. 6952-58.

174. Baletto, F. and R. Ferrando, Structural properties of nanoclusters: Energetic, thermodynamic, and kinetic effects. *Reviews of Modern Physics*, 2005. 77(1): p. 371-423.

175. Ferrando, R., G. Rossi, F. Nita, G. Barcaro, and A. Fortunelli, Interface-stabilized phases of metal-on-oxide nanodots. *Acs Nano*, 2008. 2(9): p. 1849-56.

176. Yeadon, M., M. Ghaly, J.C. Yang, R.S. Averback, and J.M. Gibson, "Contact epitaxy" observed in supported nanoparticles. *Applied Physics Letters*, 1998. 73(22): p. 3208-10.

177. Xiu, F., Y. Wang, J. Kim, A. Hong, J. Tang, et al., Electric-field-controlled ferromagnetism in high-curie-temperature $Mn_{0.05}Ge_{0.95}$ quantum dots. *Nature Materials*, 2010. 9(4): p. 337-44.

178. Huang, S.P., D.S. Mainardi, and P.B. Balbuena, Structure and dynamics of graphite-supported bimetallic nanoclusters. *Surface Science*, 2003. 545(3): p. 163-79.

179. Huang, S.P. and P.B. Balbuena, Platinum nanoclusters on graphite substrates: A molecular dynamics study. *Molecular Physics*, 2002. 100(13): p. 2165-74.

180. Homma, Y., Y. Kobayashi, T. Ogino, D. Takagi, R. Ito, et al., Role of transition metal catalysts in single-walled carbon nanotube growth in chemical vapor deposition. *Journal of Physical Chemistry B*, 2003. 107(44): p. 12161-64.

181. Robach, O., G. Renaud, and A. Barbier, Structure and morphology of the ag/mgo(001) interface during in situ growth at room temperature. *Physical Review B*, 1999. 60(8): p. 5858-71.

182. Pacchioni, G. and N. Rosch, Supported nickel and copper clusters on mgo(100): A first-principles calculation on the metal/oxide interface. *Journal of Chemical Physics*, 1996. 104(18): p. 7329-37.

183. Bengaard, H.S., J.K. Norskov, J. Sehested, B.S. Clausen, L.P. Nielsen, et al., Steam reforming and graphite formation on Ni catalysts. *Journal of Catalysis*, 2002. 209(2): p. 365-84.

184. Saadi, S., F. Abild-Pedersen, S. Helveg, J. Sehested, B. Hinnemann, et al., On the role of metal step-edges in graphene growth. *Journal of Physical Chemistry C*, 2010. 114(25): p. 11221-27.

185. Nikolla, E., J. Schwank, and S. Linic, Promotion of the long-term stability of reforming Ni catalysts by surface alloying. *Journal of Catalysis*, 2007. 250(1): p. 85-93.

186. Stolbov, S., F. Mehmood, T.S. Rahman, M. Alatalo, I. Makkonen, et al., Site selectivity in chemisorption of C on Pd(211). *Physical Review B*, 2004. 70(15). 155410 1-8

187. Swart, J.C.W., E. van Steen, I.M. Ciobica, and R.A. van Santenc, Interaction of graphene with fcc-co(111). *Physical Chemistry Chemical Physics*, 2009. 11(5): p. 803-07.

188. Gomez-Gualdron, D.A. and P.B. Balbuena, Growth of chiral single-walled carbon nanotube caps in the presence of a cobalt cluster. *Nanotechnology*, 2009. 20(21): p. 215601 1-9.

189. Cohen, M.L., Nanotubes, nanoscience, and nanotechnology. *Materials Science and Engineering: C*, 2001. 15(1–2): p. 1-11.

190. Baughman, R.H., A.A. Zakhidov, and W.A. de Heer, Carbon nanotubes - the route toward applications. *Science*, 2002. 297(5582): p. 787-92.

191. Byrne, M.T. and Y.K. Gun'ko, Recent advances in research on carbon nanotube-polymer composites. *Advanced Materials*, 2010. 22(15): p. 1672-88.

192. Yu, X., B. Munge, V. Patel, G. Jensen, A. Bhirde, et al., Carbon nanotube amplification strategies for highly sensitive immunodetection of cancer biomarkers. *Journal of the American Chemical Society*, 2006. 128(34): p. 11199-205.

193. Ajayan, P.M., J.M. Lambert, P. Bernier, L. Barbedette, C. Colliex, et al., Growth morphologies during cobalt-catalyzed single-shell carbon nanotube synthesis. *Chemical Physics Letters*, 1993. 215(5): p. 509-17.

194. Thess, A., R. Lee, P. Nikolaev, H.J. Dai, P. Petit, et al., Crystalline ropes of metallic carbon nanotubes. *Science*, 1996. 273(5274): p. 483-87.

195. Telalovic, S., A. Ramanathan, G. Mul, and U. Hanefeld, TUD-1: Synthesis and application of a versatile catalyst, carrier, material. *Journal of Materials Chemistry*, 2010. 20(4): p. 642-58.

196. He, M., A.I. Chernov, P.V. Fedotov, E.D. Obraztsova, E. Rikkinen, et al., Selective growth of swnts on partially reduced monometallic cobalt catalyst. *Chemical Communications*, 2011. 47(4): p. 1219-21.

197. Shibuta, Y. and S. Maruyama, Molecular dynamics simulation of formation process of single-walled carbon nanotubes by ccvd method. *Chemical Physics Letters*, 2003. 382(3-4): p. 381-86.

198. Ding, F., A. Rosen, and K. Bolton, Dependence of swnt growth mechanism on temperature and catalyst particle size: Bulk versus surface diffusion. *Carbon*, 2005. 43(10): p. 2215-17.

199. Page, A.J., Y. Ohta, S. Irle, and K. Morokuma, Mechanisms of single-walled carbon nanotube nucleation, growth, and healing determined using qm/md methods. *Accounts of Chemical Research*, 2010. 43(10): p. 1375-85.

200. Neyts, E.C., Y. Shibuta, A.C.T. van Duin, and A. Bogaerts, Catalyzed growth of carbon nanotube with definable chirality by hybrid molecular dynamics-force biased monte carlo simulations. *Acs Nano*, 2010. 4(11): p. 6665-72.

201. Ribas, M.A., F. Ding, P.B. Balbuena, and B.I. Yakobson, Nanotube nucleation versus carbon-catalyst adhesion--probed by molecular dynamics simulations. *The Journal of Chemical Physics*, 2009. 131(22): p. 224501-7.

202. Burgos, J.C., E. Jones, and P.B. Balbuena, Effect of the metal-substrate interaction strength on the growth of single-walled carbon nanotubes. *Journal of Physical Chemistry C*, 2011. 115(15): p. 7668-75.

203. Hu, W.J., L.M. Mei, and H. Li, Simulation of ground state structure of nickel clusters ($n \leq 40$). *Solid State Communications*, 1996. 100(2): p. 129-31.

204. Zhang, P., Y. Xie, W. Zhang, X. Ning, and J. Zhuang, Different magic number behaviors in supported metal clusters. *Journal of Nanoparticle Research*, 2011. 13(4): p. 1801-07.

205. Rossi, G., L. Anghinolfi, R. Ferrando, F. Nita, G. Barcaro, et al., Prediction of the structures of free and oxide-supported nanoparticles by means of atomistic approaches: The benchmark case of nickel clusters. *Physical Chemistry Chemical Physics*, 2010. 12(30): p. 8564-70.

206. Yao, Y., R. Liu, J. Zhang, L. Jiao, and Z. Liu, Raman spectral measuring of the growth rate of individual single-walled carbon nanotubes. *Journal of Physical Chemistry C*, 2007. 111(24): p. 8407-09.

207. Veith, G.M., A.R. Lupini, S. Rashkeev, S.J. Pennycook, D.R. Mullins, et al., Thermal stability and catalytic activity of gold nanoparticles supported on silica. *Journal of Catalysis*, 2009. 262(1): p. 92-101.

208. Pulido, A., M. Boronat, and A. Corma, Theoretical investigation of gold clusters supported on graphene sheets. *New Journal of Chemistry*, 2011. 35(10): p. 2153-61.

209. Meyer, R., Q. Ge, J. Lockemeyer, R. Yeates, M. Lemanski, et al., An ab initio analysis of adsorption and diffusion of silver atoms on alumina surfaces. *Surface Science*, 2007. 601(1): p. 134-45.

210. Molina, L.M. and B. Hammer, Theoretical study of CO oxidation on Au nanoparticles supported by MgO(100). *Physical Review B*, 2004. 69(15): p. 155424 1-22.

211. Ma, Q.S., K. Klier, H.S. Cheng, and J.W. Mitchell, Interaction between catalyst and support. 4. Periodic trends and patterns in interactions of first-row transition metals with the silica surface. *Journal of Physical Chemistry B*, 2002. 106(39): p. 10121-27.

212. Fernandez, S., A. Markovits, and C. Minot, Adsorption of the first row of transition metals on the perfect and defective MgO(100) surface. *Chemical Physics Letters*, 2008. 463(1-3): p. 106-11.

213. Ma, Q.S., K. Klier, H.S. Cheng, J.W. Mitchell, and K.S. Hayes, Interaction between catalyst and support. 3. Metal agglomeration on the silica surface. *Journal of Physical Chemistry B*, 2001. 105(38): p. 9230-38.

214. Humphrey, W., A. Dalke, and K. Schulten, VMD: Visual molecular dynamics. *Journal of Molecular Graphics & Modelling*, 1996. 14(1): p. 33-38.

215. Bandow, S., S. Asaka, Y. Saito, A.M. Rao, L. Grigorian, et al., Effect of the growth temperature on the diameter distribution and chirality of single-wall carbon nanotubes. *Physical Review Letters*, 1998. 80(17): p. 3779-82.

216. Okamoto, A. and H. Shinohara, Control of diameter distribution of single-walled carbon nanotubes using the zeolite-CCVD method at atmospheric pressure. *Carbon*, 2005. 43(2): p. 431-36.

217. Rummeli, M., A. Bachmatiuk, F. Borrnert, F. Schaffel, I. Ibrahim, et al., Synthesis of carbon nanotubes with and without catalyst particles. *Nanoscale Research Letters*, 2011. 6(1): p. 303 1-9.

218. Page, A.J., Y. Ohta, Y. Okamoto, S. Irle, and K. Morokuma, Defect healing during single-walled carbon nanotube growth: A density-functional tight-binding molecular dynamics investigation. *Journal of Physical Chemistry C*, 2009. 113(47): p. 20198-207.

219. Pigos, E., E.S. Penev, M.A. Ribas, R. Sharma, B.I. Yakobson, et al., Carbon nanotube nucleation driven by catalyst morphology dynamics. *ACS Nano*, 2011. 5(12): p. 10096-101.

220. Bower, C., O. Zhou, W. Zhu, D.J. Werder, and S.H. Jin, Nucleation and growth of carbon nanotubes by microwave plasma chemical vapor deposition. *Applied Physics Letters*, 2000. 77(17): p. 2767-69.

221. Doye, J.P.K. and F. Calvo, Entropic effects on the structure of lennard-jones clusters. *Journal of Chemical Physics*, 2002. 116(19): p. 8307-17.

222. Jiang, D.E. and E.A. Carter, Carbon atom adsorption on and diffusion into Fe(110) and Fe(100) from first principles. *Physical Review B*, 2005. 71(4): p. 045402 1-6.

223. Cinquini, F., F. Delbecq, and P. Sautet, A DFT comparative study of carbon adsorption and diffusion on the surface and subsurface of Ni and Ni_3Pd alloy. *Physical Chemistry Chemical Physics*, 2009. 11(48): p. 11546-56.

224. Ramirez-Caballero, G.E., J.C. Burgos, and P.B. Balbuena, Growth of carbon structures on stepped (211)Co surfaces. *Journal of Physical Chemistry C*, 2009. 113(35): p. 15658-66.

225. Wang, Q., K.H. Lim, S.-W. Yang, Y. Yang, and Y. Chen, Atomic carbon adsorption on Ni nanoclusters: A DFT study. *Theoretical Chemistry Accounts*, 2011. 128(1): p. 17-24.

226. Gómez-Gualdrón, D.A., G.D. McKenzie, J.F.J. Alvarado, and P.B. Balbuena, Dynamic evolution of supported metal nanocatalyst/carbon structure during single-walled carbon nanotube growth. *ACS Nano*, 2011. 6(1): p. 720-35.

227. Park, S., B.L. Clark, D.A. Keszler, J.P. Bender, J.F. Wager, et al., Low-temperature thin-film deposition and crystallization. *Science*, 2002. 297(5578): p. 65-65.

228. Bandaru, P.R., Electrical properties and applications of carbon nanotube structures. *Journal of Nanoscience and Nanotechnology*, 2007. 7(4-5): p. 1239-67.

229. Kukovitsky, E.F., S.G. L'Vov, and N.A. Sainov, VLS-growth of carbon nanotubes from the vapor. *Chemical Physics Letters*, 2000. 317(1–2): p. 65-70.

230. Hong, G., Y. Chen, P. Li, and J. Zhang, Controlling the growth of single-walled carbon nanotubes on surfaces using metal and non-metal catalysts. *Carbon*, 2012. 50(6): p. 2067-82.

231. Lin, M., J.P. Ying Tan, C. Boothroyd, K.P. Loh, E.S. Tok, et al., Direct observation of single-walled carbon nanotube growth at the atomistic scale. *Nano Letters*, 2006. 6(3): p. 449-52.

232. Hofmann, S., C. Ducati, J. Robertson, and B. Kleinsorge, Low-temperature growth of carbon nanotubes by plasma-enhanced chemical vapor deposition. *Applied Physics Letters*, 2003. 83(1): p. 135-37.

233. Kim, H. and W. Sigmund, Iron particles in carbon nanotubes. *Carbon*, 2005. 43(8): p. 1743-48.

234. Ni, L., K. Kuroda, L.-P. Zhou, K. Ohta, K. Matsuishi, et al., Decomposition of metal carbides as an elementary step of carbon nanotube synthesis. *Carbon*, 2009. 47(13): p. 3054-62.

235. Buffat, P. and J.P. Borel, Size effect on the melting temperature of gold particles. *Physical Review A*, 1976. 13(6): p. 2287-98.

236. Rao, R., D. Liptak, T. Cherukuri, B.I. Yakobson, and B. Maruyama, In situ evidence for chirality-dependent growth rates of individual carbon nanotubes. *Nat Mater*, 2012. 11: p. 213-16.

237. Grest, G.S. and K. Kremer, Molecular dynamics simulation for polymers in the presence of a heat bath. *Physical Review A*, 1986. 33(5): p. 3628-31.

238. Josh, S.G., U. Jamal, R.C. Thomas, K.B. Nelli, and K.W. Angela, First-principle study of structure and stability of nickel carbides. *Journal of Physics: Condensed Matter*, 2010. 22(44): p. 445503 1-7.

239. Sun, H., Factors influencing dissolution of carbonaceous materials in liquid iron. *Metallurgical and Materials Transactions B*, 2005. 36(6): p. 893-94.

240. Harutyunyan, A.R., N. Awasthi, A. Jiang, W. Setyawan, E. Mora, et al., Reduced carbon solubility in Fe nanoclusters and implications for the growth of single-walled carbon nanotubes. *Physical Review Letters*, 2008. 100(19): p. 195502 1-4.

241. Welsher, K., S.P. Sherlock, and H. Dai, Deep-tissue anatomical imaging of mice using carbon nanotube fluorophores in the second near-infrared window. *PNAS*, 2011. 108(17): p. 8943-48

242. Wu, J., B. El Hamaoui, J. Li, L. Zhi, U. Kolb, et al., Solid-state synthesis of "bamboo-like" and straight carbon nanotubes by thermolysis of hexa-peri-hexabenzocoronene–cobalt complexes. *Small*, 2005. 1(2): p. 210-12.

243. Holz, M., S.R. Heil, and A. Sacco, Temperature-dependent self-diffusion coefficients of water and six selected molecular liquids for calibration in accurate 1h nmr pfg measurements. *Physical Chemistry Chemical Physics*, 2000. 2(20): p. 4740-42.

244. Butrymowicz, D.B., J.R. Manning, and M.E. Read, Diffusion in copper and copper alloys. Part i. Volume and surface self-diffusion in copper. *Journal of Physical and Chemical Reference Data*, 1973. 2(3): p. 643-56.